UAB
Universitat Autònoma de Barcelona

Mathematical modelling of angiogenesis as an integrated multicellular process

PhD Thesis

AUTHOR: DARIA STEPANOVA

SCIENTIFIC ADVISORS: TOMÁS ALARCÓN COR

HELEN M. BYRNE

PHILIP K. MAINI

ACADEMIC TUTOR: LLUÍS ALSEDÀ SOLER

Universitat Autònoma de Barcelona (UAB)

Centre de Recerca Matemàtica (CRM)

Doctorate Programme in Mathematics

February 2022

A dissertation submitted in partial fulfillment

of the requirements for the degree of

Doctor of Philosophy in Mathematics

at the

Universitat Autònoma de Barcelona

February 2022

To my parents.

Acknowledgments

This thesis would have not been possible without the support and guidance of my supervisors, Tomás Alarcon, Helen Byrne and Philip Maini. I would like to thank you for encouraging me to do this work, for your patience and kindness. It has been been an invaluable experience to learn from you. I also would like to express my gratitude to Lluís Alsedà for his belief in me and support during my years at the CRM.

I would like to acknowledge La Caixa Foundation that supported my studies as a part of the Collaborative Mathematics programme. I also would like to extend my gratitude to Fundació Ferran Sunyer i Balaguer for funding my research stay at the Mathematical Institute, University of Oxford.

I am deeply grateful to my parents and family for their love and support. Finally, thanks to my friends, especially to Núria Folguera, Lucía Vicens and Marcos Tenesa, and to my partner for being by my side.

Declaration

I declare that this thesis has been composed by myself under the guidance of my supervisors, Tomás Alarcon, Helen Byrne and Philip Maini, unless otherwise stated by reference or acknowledgment. This thesis has not been submitted, in whole or in part, in any previous application for a degree.

A version of Chapter 2 has been published in *PLoS Computational Biology 17.1 (2021): e1008055*, entitled 'A multiscale model of complex endothelial cell dynamics in early angiogenesis' by D. Stepanova, H. M. Byrne, P. K. Maini, & T. Alarcón.

A version of Chapter 3, entitled 'A method to coarse-grain multi-agent stochastic systems with regions of multistability' by D. Stepanova, H. M. Byrne, P. K. Maini, & T. Alarcón, has been accepted for publication in *SIAM Multiscale Modelling & Simulation (MMS)* and is expected to be published in February 2022.

We plan to submit for publication the work contained in Chapter 1 as a review on mathematical and computational modelling of angiogenesis.

We also plan to submit for publication the work contained in Chapter 4 as an extension of our multiscale model of angiogenesis presented in Chapter 2.

Abstract

Angiogenesis, the formation of new blood vessels from pre-existing ones, is essential for normal development and plays a crucial role in such pathologies as cancer, diabetes and atherosclerosis. In spite of extensive research, many of aspects of how new vessels sprout from existing vasculature remain unclear. Recent experimental results indicate that endothelial cells, lining the inner walls of blood vessels, rearrange within growing vessels and that sprout elongation is dominated by cell mixing during the early stages of angiogenesis. Cell rearrangements have been shown to be regulated by dynamic adaptation of cell gene expression, or cell phenotype. However, most theoretical models of angiogenesis do not account for these phenomena and instead assume that cell positions are fixed and cell phenotype is irreversible during sprouting.

In this thesis, we formulate a multiscale model of angiogenic sprouting driven by dynamic cell rearrangements. Our model accounts for cell mixing which is regulated by a stochastic model of subcellular signalling linked to phenotype switching. We initially focus on early angiogenic sprouting when the effects of cell proliferation are negligible. We validate our model against available experimental data. We then use it to develop a measure to quantify the amount of cell rearrangement that occurs during sprouting and investigate how the branching structure of vascular networks changes as the level of cell mixing varies. Our results suggest that cell shuffling directly affects the morphology of growing vasculatures. In particular, rearrangements of endothelial cells with distinct phenotypes can drive changes in the network structure since cell phenotype adaptation is slower than cell migration. Cell mixing also contributes to remodelling of the extracellular matrix which, in turn, guides vascular growth.

In order to investigate the effects of cell proliferation, which operates on longer timescales than cell migration, we first develop a method, based on large deviation theory, which allows us to reduce the computational complexity of our hybrid multiscale model by coarse-graining the internal dynamics of its cell-agents. The coarse-graining (CG) method is applicable to systems in which agent behaviour is described by stochastic systems with multiple stable steady states. The CG technique reduces the original stochastic system to a Markov jump process on the space of its stable steady states. Our CG method preserves the original description of agent states (instead of converting them to discrete ones) and stochastic transitions between them, while considerably reducing the computational complexity of model simulations.

After formulating the CG method for a general class of hybrid models, we illustrate its potential by applying it to our model of angiogenesis. We coarse-grain the subcellular model, which determines cell phenotype specification. This substantially reduces the computational cost of simulations. We then extend our model to account for cell proliferation and validate it using available experimental data. This framework allows us to study network growth on timescales associated with angiogenesis *in vivo* and to investigate how varying the cell proliferation rate affects network growth.

Summarising, this work provides new insight into the complex cell behaviours that drive angiogenic sprouting. At the same time, it advances the field of theoretical modelling by formulating a coarse-graining method, which paves the way for a systematic reduction of hybrid multiscale models.

Contents

Chapter 1

Introduction

1.1   Motivation

Angiogenesis is the growth of new blood vessels from a pre-existing vascular network. During this process, quiescent endothelial cells (ECs), forming the inner layer of blood vessels, become activated in response to signalling cues generated by insufficiently oxygenated (i.e. hypoxic) tissues. Activated ECs migrate from the pre-existing vascular bed by forming sprouts. Sprouts branch and fuse with neighbouring vessels to form a new vascular network. Angiogenic sprouting occurs in physiological (such as embryonic development) and pathological conditions (such as cancer, diabetes and atherosclerosis [1], [2]). While it has been extensively investigated in recent years [3]–[12], our understanding of the complex behaviour of ECs involved in angiogenesis remains incomplete. Mathematical and computational modelling represent a natural alternative to experimental studies, which are often challenging to perform.

This thesis aims to use mathematical and *in silico* modelling to investigate how (recently discovered [4], [9]) cell rearrangements impact sprouting angiogenesis and the structure of the growing vascular networks. Until recently, it was assumed that ECs positioned at the sprout tips guide sprout elongation towards the source of signalling cues, and that the ECs positioned behind the leading cell trail and maintain sprout integrity via proliferation. This

assumption has been termed the 'snail-trail' model of angiogenesis. However, recent experimental observations reveal that ECs can overtake each other within growing sprouts [4], [9]. This phenomenon has been termed *cell mixing* or *cell rearrangement*. Its functionality and effects on the morphology of vascular networks remain unclear [3], [4], [9]. Many existing mathematical and computational models of angiogenesis are based on the snail-trail assumption (see section 1.5) and, thus, are unable to provide insight into how EC rearrangements influence vasculature growth.

The work presented in this thesis was inspired by experiments by Arima and coworkers [4]. They developed a technique to visualise ECs in real time during *in vitro* sprouting from aortic ring assays embedded in collagen matrix and stimulated by externally supplied vascular growth factor (VEGF). Their methodology was based on computationally assisted time-lapse microscopy, which allowed them to monitor trajectories of individual cells and to quantify their complex behaviour. The authors demonstrated that ECs move forwards and backwards within growing sprouts, and can overtake each other. Arima and colleagues' analysis of their experimental data demonstrated that cell rearrangements contribute to sprout elongation and that only a small proportion of cells proliferate. They concluded that sprout extension during early (on a timescale of hours) angiogenesis is dominated by cell migration. These observations were strengthened by *in vivo* experiments of murine retina vascularisation, which demonstrated that cell overtaking also occurs *in vivo* [4]. These findings reveal that EC behaviour is more complex than was previously believed and that the snail-trail assumption is unable to resolve this level of detail. They also show that vascular network growth can occur in uniform VEGF concentrations, whereas many theoretical models of angiogenesis assume that a VEGF gradient is necessary for sprout elongation (see section 1.5).

Arima and coworkers [4] showed that cell mixing depends on intracellular communication via VEGF-Delta-Notch signalling. A similar conclusion was obtained by Jakobsson et al. [9]. They used mosaic sprouting assays to investigate EC overtaking *in vitro* and *in vivo* [9]. Their findings reveal that the ability of ECs to overtake and occupy the leading position at

the sprout tip depends on their gene expression profile. In particular, ECs with higher Delta levels seem to be better able to shuffle up to the sprout tip.

The importance of cell rearrangements for the growth of blood vessels was shown in recent work by Angulo-Urarte et al. [3]. However, the functional role of cell mixing in angiogenic sprouting is poorly understood.

Existing mathematical and computational models of angiogenic sprouting do not account for phenotype-dependent (i.e. regulated by cell gene expression profile) cell rearrangements. A new modelling framework is required to investigate the phenomenon of cell mixing and its effects on vascular morphology. In this thesis, we use a multiscale framework to formulate a model, validated against experimental data, which captures this complex EC behaviour during angiogenic sprouting.

The remainder of this introductory chapter is organised as follows. In section 1.2, we provide a biological background to angiogenesis. We then briefly review mathematical approaches for modelling random cell migration and hybrid (multiscale) modelling in sections 1.3 and 1.4, respectively. Section 1.5 provides an overview of existing mathematical and computational models of angiogenesis. Finally, section 1.6 outlines the main goals of this work and explains the structure of the thesis.

1.2 Biological background of angiogenesis

1.2.1 Angiogenesis is a process of vasculature outgrowth

Blood vessels play a pivotal role in delivering oxygen and nutrients and removing waste products in all tissues in the body. The formation and maintenance of vascular networks is essential for maintaining homeostasis in living systems. During early development, a primitive vascular plexus forms *de novo* through a process termed vasculogenesis. Endothelial progenitor cells aggregate to form primitive tube-like structures of initial capillary networks
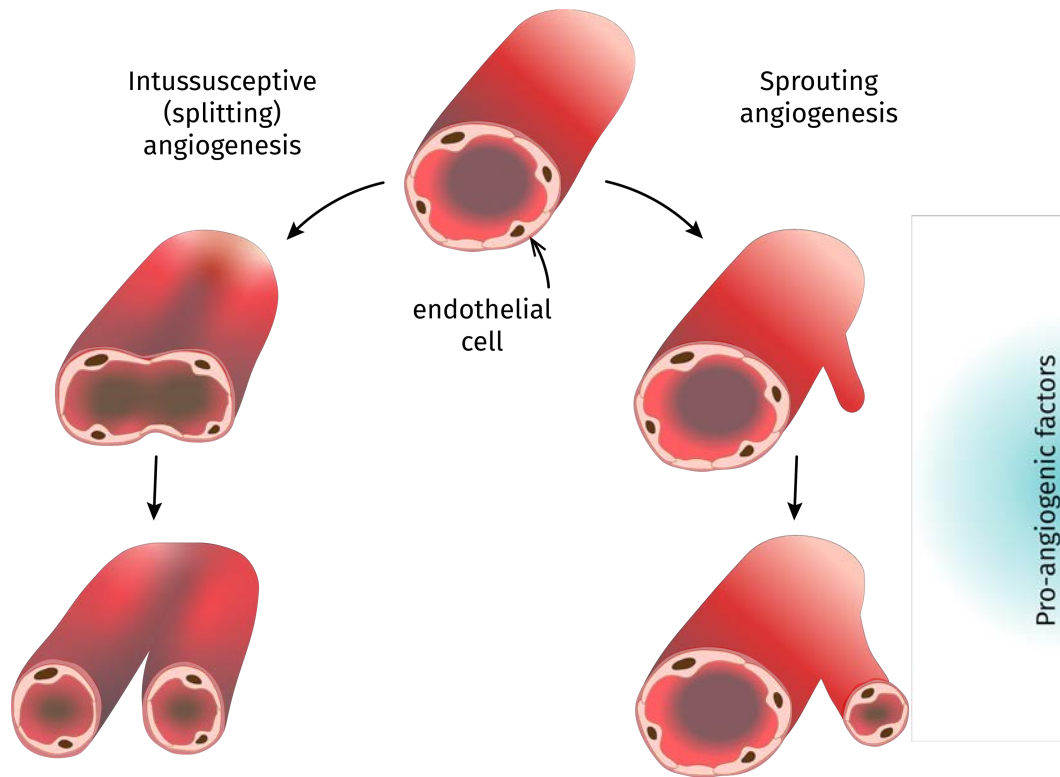
Figure 1.1. A cartoon illustrating two types of angiogenesis. Intussusceptive, or splitting, angiogenesis (left branch) is a process in which a capillary splits into two adjacent vessels [13], [14]. In sprouting angiogenesis (right branch), pro-angiogenic factors secreted by hypoxic tissues activate ECs lining the nearest vessel. This induces formation of new sprouts via EC migration and proliferation towards the source of angiogenic stimuli.

[15]. Further growth of vascular networks occurs by generating new capillaries from pre-existing vessels, a phenomenon called angiogenesis. Two types of angiogenic vessel formation have been distinguished: intussusceptive (or splitting) and sprouting angiogenesis (see Figure 1.1). The former type is characterised by splitting of a capillary into two vessels: ECs lining the blood vessel connect with ECs on the opposite wall of the capillary, the vascular membrane splits and the capillary separates into two adjacent vessels [14] (see Figure 1.1, left branch). Vascular intussusception was first described at the end of the 20th century [13] but its study has been hindered by difficulties visualising it using traditional light microscopy [14]. Further research is needed to better understand its role and significance in vascular

network formation [13], [14].

More extensive research has been focused on the second type of angiogenesis, in which new blood vessels form by sprouting from pre-existing vessels (see Figure 1.1, right branch). One of the most best-known pro-angiogenic cues is vascular endothelial growth factor (VEGF). VEGF is secreted by cells under hypoxia and diffuses towards the nearest vascular bed where it activates ECs lining the vessels by binding to receptors on their membranes. Upon activation, ECs degrade the basement membrane (BM) surrounding the vessel and sprout towards the source of the pro-angiogenic factors [16]–[18]. *In vivo* and *in vitro*, coordinated migration is guided by local chemical and mechanical cues [19]–[21]. ECs can rapidly switch from a quiescent state into active migratory and proliferative phenotypes which facilitate rapid expansion of a new vascular network in order to restore the supply of oxygen and nutrients to hypoxic tissues [6]. Sprouting angiogenesis occurs both in physiological and pathological conditions. For example, it plays an important role in wound healing, diabetes, atherosclerosis and tumour growth [1], [2]. Given its importance in disease, there has been much interest in investigating the mechanisms that underpin angiogenesis and therapeutic strategies for manipulating angiogenesis in order to treat diseases.

During the early stages of vascular formation an initial branching network forms which usually contains many immature and blind-ended vessels [22]. During the later stages of angiogenesis, the provisional network is remodelled by other cell types (such as pericytes) and in response to stimuli such as wall shear stress due to blood flow to create a stable functional vasculature [2], [8], [23], [24]. In this work, we focus on early angiogenesis, i.e. initial expansion of vascular networks via sprouting.

1.2.2   Phenotype specification of endothelial cells

During the early stages of angiogenesis, ECs migrate towards the source of a stimulus which activates them (e.g. growth factors expressed by hypoxic tissues). EC behaviours are heterogeneous, depending on the gene expression patterns, or phenotype, of each cell [5], [9].
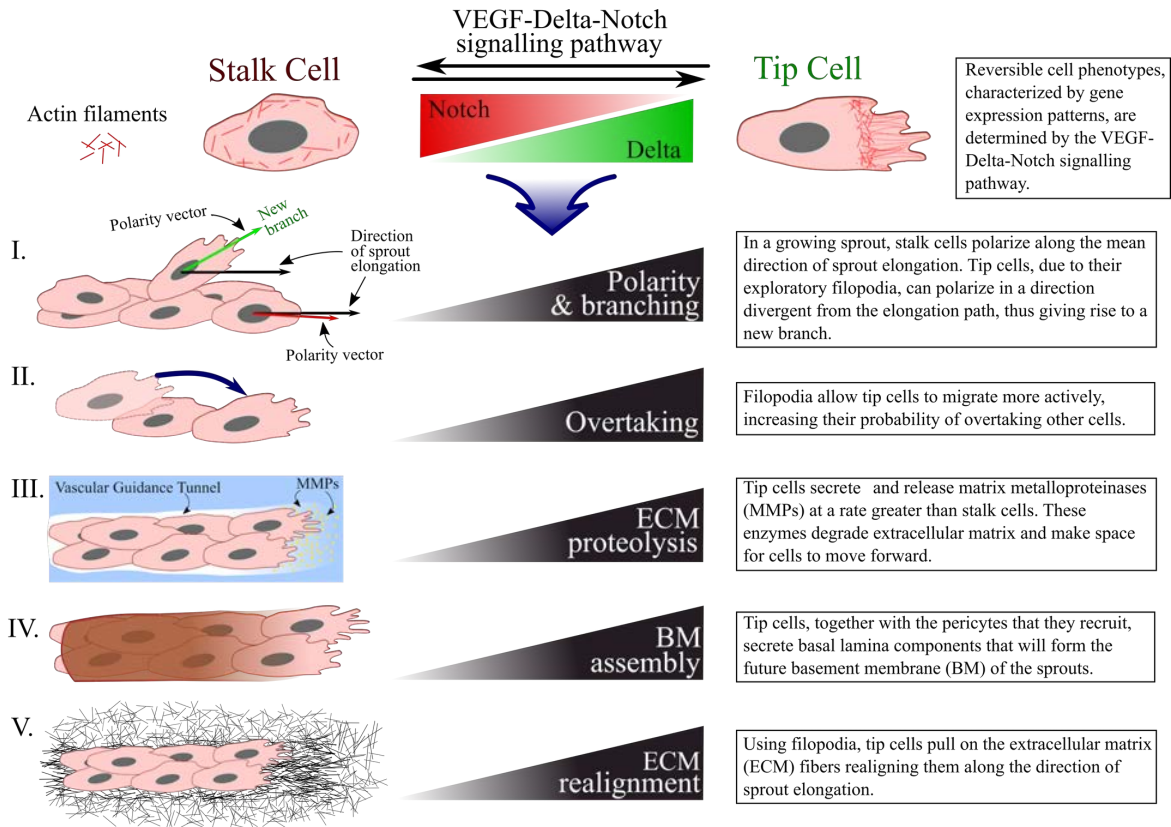
Figure 1.2. An illustration of the distinct roles of EC phenotypes. The gene expression profile of each cell (and its phenotype) is regulated by the VEGF-Delta-Notch signalling pathway. Tip (stalk) cells exhibit high (low) levels of Delta ligand and low (high) levels of Notch receptor. Tip cells are characterised by low proliferative and active migratory behaviour due to their filopodia (thin membrane protrusions which permit tip cells to pull on ECM fibrils to migrate); by contrast, stalk cells have low migratory activity and instead proliferate in order to maintain integrity of elongating sprouts. Cell phenotype (i.e. gene expression profile) influences such processes as I. cell polarity and branching, II. overtaking, III. extracellular matrix (ECM) proteolysis, IV. basement membrane (BM) assembly and V. ECM realignment. The cartoons on the left illustrate each process, whereas the text-boxes on the right describe how they are influenced by tip and stalk cells. For more details see the main text.

ECs alter their gene expression profiles in response to a variety of extracellular cues, such as the structure and composition of the extracellular matrix (ECM), angiogenic factors such as VEGF and changes in cell-cell interactions. Cell phenotype is influenced by contact-dependent cross-talk with neighbouring ECs via the VEGF-Delta-Notch signalling pathway [25]–[27]. VEGF is one of the most common activating external stimuli; Delta and Notch are transmembrane ligands and receptors, respectively, which can trans-bind, (i.e. a ligand on one cell can bind to a receptor on another cell, enabling the two cells to 'communicate'). ECs adjust their gene expression in order to maintain a pattern of two distinct phenotypes, tip and stalk cells (Figure 1.2), in the growing vascular network.

The default phenotype of an EC that has been activated by VEGF is a tip cell [16], [27]. Tip cells, with elevated expression of Delta ligand, VEGF receptor 2 (VEGFR2) and reduced expression of Notch receptor, are characterised by migratory behaviour and low proliferative activity [16] (see Figure 1.2); they extend filopodia, release matrix metalloproteinases (MMPs) that degrade the ECM and, together with the pericytes that they recruit, secrete basal lamina components that stabilise growing vessels. If all ECs moved in such an exploratory fashion, sprout integrity would be lost. In normal angiogenesis, vascular network morphology is achieved when EC proliferation and migration (i.e. the exploration of space by active ECs in response to signalling cues) balance. This balance is mediated by the Delta-Notch signalling pathway, which provides ECs with a contact-dependent mechanism by which they can acquire a stalk cell phenotype [16], [27]. Stalk cells, characterised by low levels of Delta and VEGFR2, and high levels of Notch, migrate along the paths explored by tip cells, and proliferate to maintain connectivity of the elongating sprouts (see Figure 1.2).

Given their distinct behaviours, the spatial distribution of tip and stalk cells affect the structure of the growing vascular network. The processes influenced by cell phenotype are illustrated in Figure 1.2. The ratio of the numbers of tip and stalk cells during sprouting plays a key role in the integrity of the developing vascular network and its functionality. This has been confirmed by experiments in which Notch activity was inhibited or completely

blocked: all cells adopted a tip cell phenotype and a pathological network was formed [9].

EC phenotypes are not static; they are strongly influenced by their local microenvironment (signalling cues, interactions with other ECs, among others) [4], [9]. Furthermore, ECs within sprouts exchange their relative positions via a phenomenon called *cell mixing* [4], [9] (for more details, see section 1.2.4). Every time a cell rearrangement takes place, the cells' microenvironment changes. This, in turn, leads to recurrent (re-)establishment of phenotypes and variations in gene expression within the phenotype. As a consequence, dynamic coupling between cell phenotypes and rearrangements is established.

1.2.3 Cell polarity, migration and cell-ECM interactions

VEGF-induced actin polymerisation and focal adhesion assembly result in substantial cytoskeletal remodelling as required for cell migration [28]. This includes actin remodelling to form filopodia and lamellipodia, stress fibre formation, and focal adhesion turnover [29]. An important consequence of such remodelling is that ECs acquire front-to-rear polarity which determines the direction of their migration [30] (Figure 1.2 I.). Membrane protrusions, such as filopodia and lamellipodia, increase the cell surface area at the leading edge. More VEGF receptors and integrins, which bind to ECM components, become activated at the cell's leading edge, further reinforcing cytoskeleton remodelling and polarisation [31]. This mechanism of directed migration is known as taxis (e.g. chemotaxis, haptotaxis) and allows ECs to sense extracellular cues and migrate towards them. The chemotactic sensitivity of ECs to VEGF leads to the so-called *brush-border* effect where rates of branching and EC densities increase with proximity to the source of the VEGF stimulus. Tip cells are characterised by higher chemotactic sensitivity due to their more developed (than in stalk cells) long filopodia. This also results in more active and exploratory behaviours of tip cells; they can initiate new branches and overtake other ECs (Figure 1.2 I. and II., respectively).

Whilst the local microenvironment affects EC behaviour, EC migration can, in turn, reorganise and remodel the ECM [18]. Prior to assembly of the basement membrane of the

newly formed vessels, the ECM microenvironment consists mostly of collagen I and elastin fibers. Activated ECs secrete matrix type 1 metalloproteinases (MT1-MMPs) that degrade the ECM [17], [19], [32]. This process generates ECM-free tunnels into which the sprouts can elongate [32] (Figure 1.2 III.). As sprouts grow, they assemble a basement membrane which contains, among other things, fibrous components (collagen IV, fibronectin and various laminins [17]) that are secreted by the ECs and whose function is to promote cell-cell and cell-ECM contact and to limit EC migration [19] (Figure 1.2 IV.).

Further matrix reorganisation occurs in response to mechanical forces generated by migrating cells. Several experiments have shown that cells with extended filopodia and lamellipodia form focal adhesions with the ECM components and realign them by pulling in the direction parallel to their motion [31], [33]–[35]. They also pull the fibrils from the local neighbourhood closer to their membranes. As a result, collagen fibrils accumulate and align in the direction of sprout elongation (Figure 1.2 V.). Since cell-followers form focal adhesions with these aligned fibrils they automatically polarise and migrate in the direction of sprout elongation [19]–[21]. In this way sprout integrity is maintained and the coordinated motion of ECs emerges.

1.2.4   Cell rearrangements

It has been long believed that EC phenotype is irreversible and is determined by their fixed positions within growing sprouts [36]. In this model, termed the *snail-trail*, the tip cell phenotype is characteristic of ECs situated at the leading edge of elongating sprouts. Tip cells sense spatial gradients in extracellular cues (e.g. VEGF) and direct the sprout orientation. By contrast, stalk cells trail passively behind tip cells and contribute to sprout elongation via cell proliferation. Cell order is assumed to be maintained at all times, i.e. ECs follow one another, without exchanging their relative positions. A decade ago, new experimental results showed that EC behaviour during angiogenic sprouting is more complex; ECs are now known to overtake each other and rearrange within growing sprouts [4], [9]. This phenomenon is

(A) 0 h

(B) 12 h

(C) 24 h

(D) 36 h
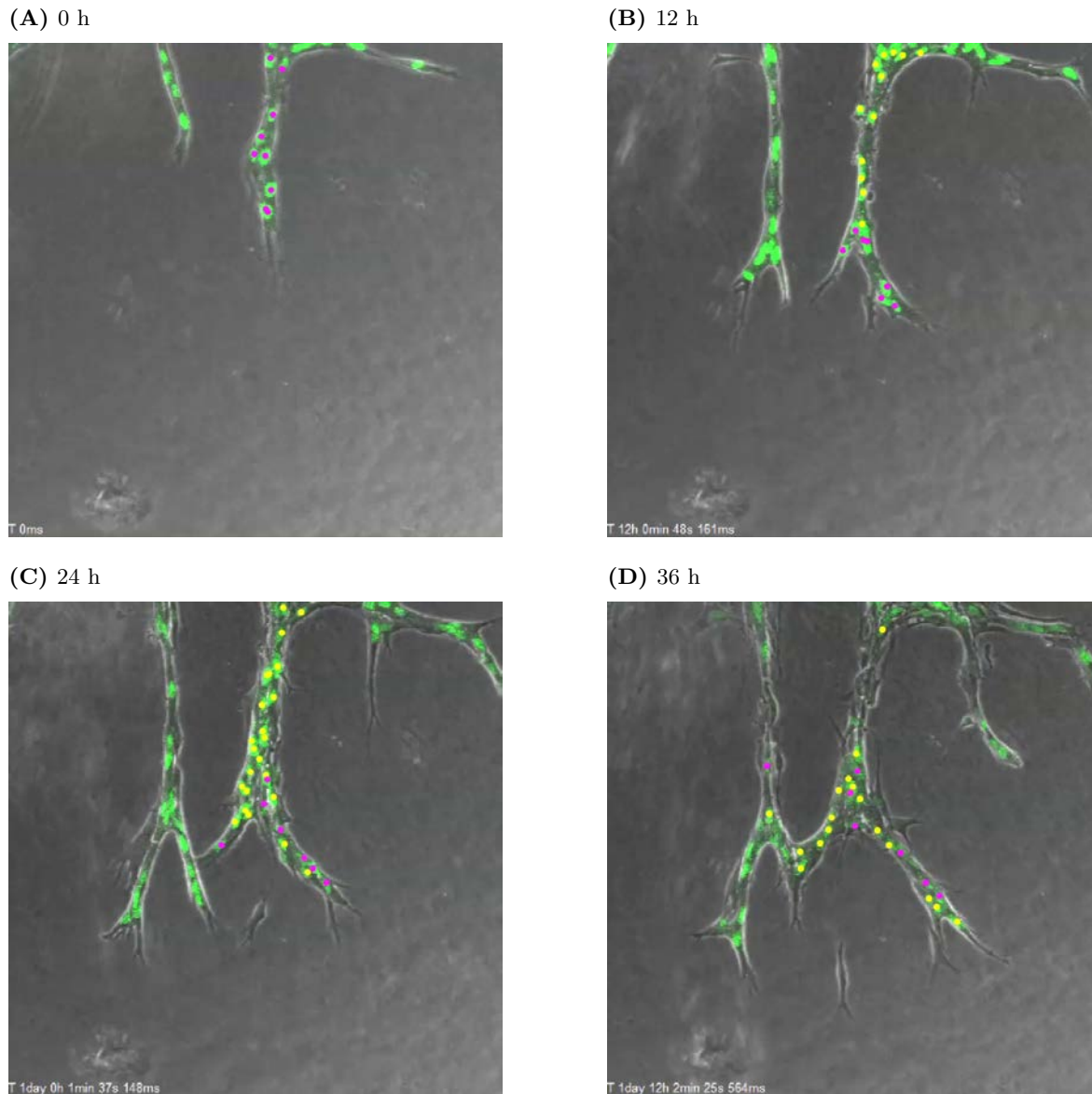
Figure 1.3. Cell rearrangements in *in vitro* angiogenesis. Snapshots of confocal microscopy images from an *in vitro* experiment of angiogenic sprouting in an aortic ring assay embedded in a collagen matrix and stimulated by VEGF. Cell nuclei were labeled with two different colours (magenta and yellow). As time progresses (time is indicated in each panel's title), initial clusters of cells with labels of the same colour become mixed as cells overtake each other and exchange positions. This illustrates the phenomenon of cell rearrangement, or cell mixing, in early angiogenesis. Figure reused from a supplementary movie from [10]. Sugihara, K., Nishiyama, K., Fukuhara, S., Uemura, A., Arima, S., Kobayashi, R., Köhn-Luque, A., Mochizuki, N., Suda, T., Ogawa, H.& Kurihara, H. (2015). Autonomy and non-autonomy of angiogenic cell movements revealed by experiment-driven mathematical modelling. *Cell Reports*, 13(9), 1814-1827 (`https://doi.org/10.1016/j.celrep.2015.10.051`), by permission of the publisher under a Creative Commons Attribution-NonCommercial-No Derivatives License (CC BY NC ND), `https://creativecommons.org/licenses/by-nc-nd/4.0/`.

called *cell rearrangement* or *cell mixing*.

Figure 1.3 (reused from [10]; see also [4] for earlier work of this research group) illustrates this process occurring *in vitro*. In this experiment, ECs, activated by externally supplied VEGF, sprout from an aortic ring assay on a flat collagen substrate. Cell trajectories were tracked using images from confocal microscopy. Cell rearrangements were visualised by labelling EC nuclei with two distinct colours (magenta and yellow in Figure 1.3). Under the snail-trail hypothesis, clusters of cells with the same colour should maintain their integrity over time. However, the results presented in Figure 1.3 show that, in practice, cells exchange positions and clusters become mixed.

In the same series of works [4], [9], the proportion of proliferating cells was found to be negligible on the timescale from hours to days; cell division was localised in the underlying vascular bed (or vascular plexus). Thus, sprout growth and vascular network expansion have been shown to be migration-driven and cell rearrangements have been proposed to be the main driver for early sprouting angiogenesis [3]–[5], [9]. However, our understanding of this phenomenon remains incomplete. The functional role of cell mixing and how it is affected by the gene expression patterns of ECs are unclear, although it is acknowledged that cell rearrangements greatly influence the structure of the vascular network and its functionality [3], [9], [37], [38]. In particular, reduced cell mixing leads to the formation of pathological networks characterised by superimposed aberrant layers of vessels [3].

1.2.5 Cell proliferation and apoptosis

Although the timescale of cell proliferation is longer (approximately 1-4 days) than that of cell migration (of the order of minutes to hours) [39]–[44], it is essential for normal vessel elongation and thickening [16]. Quiescent cells, which line mature vessels, have a low proliferation rate; their primary role is to maintain homeostasis of the blood vessels [15]. At the onset of angiogenesis, activated ECs adopt migratory and proliferative functions. Tip cells have a slow cell cycle, whereas stalk cells (especially at the underlying vascular bed)

actively proliferate [4], [9]. In a recent work [45], this cell behaviour was shown to be due to EC response to VEGF activation (as one of its downstream signalling cascades). Levels of VEGF signalling in stalk cells are optimal for active proliferation, whereas higher levels of VEGF activation in tip cells induce cell cycle arrest [45]. Thus, the VEGF-Delta-Notch signalling pathway controls EC differentiation into tip and stalk cells, and also regulates cell proliferation (although other external cues can modulate EC behaviour, such as mechanical stimuli [29], [46]).

VEGF activation also sustains EC viability during the energetically demanding process of sprouting. In particular, VEGF binding to its receptors on the cell surface inhibits apoptosis (i.e. programmed cell death) and promotes cell survival [47]. Once a new vascular network is formed and previously hypoxic tissues become oxygenised, VEGF levels decrease. This marks the anti-angiogenic switch from the sprouting to a remodelling phase, during which poorly perfused vessels regress [22]. ECs, deprived of the vasculoprotective VEGF signalling, undergo apoptosis so that excessive branches (with inadequate circulation) which compromise vasculature functionality can be eliminated.

1.2.6   Later stages of angiogenesis

For completeness, we provide a brief description of the later stages of angiogenesis, which occur after the initial expansion of a vascular network. This phase is characterised by vascular remodelling, vessel pruning, and vessel stabilisation. Initial networks frequently contain many vessel segments with low or turbulent flow. In order to optimise the delivery of oxygen and nutrients, tortuous and poorly perfused vessels regress when their constituent ECs undergo apoptosis [22], [48] or migrate towards high-flow vessels [8]. Increased blood flow in the remaining vessels contributes to their stabilisation by promoting cell quiescence (laminar shear stress induces expression of Kruppel-like factor 2, KLF2, which slows down cell metabolism) [49]. At the same time, pericytes and smooth muscle cells, recruited by ECs, attach to the outer surface of vascular tubes and induce their maturation by stabilising EC

junctions and promoting assembly of the basement membrane [50].

1.3 Mathematical modelling of random cell migration

Stochastic approaches have been used to mathematically model systems with random, heterogeneous behaviour, including spatially extended systems [51]–[61]. We model cell migration at the cellular scale stochastically to account for random cell motility, cell mixing, and branching dynamics. This approach allows us to compare our model simulations with *in vitro* experiments which, as in any biological system, are noisy.

Within the context of spatially extended systems, stochastic models may be individual-based, or compartment-based. In the former case, the Brownian dynamics of each individual agent (cells, molecules, etc.) are simulated, which becomes computationally expensive as the number of agents increases. Compartment-based approaches are more numerically efficient for simulating small vascular networks containing at most hundreds of cells. In this method the domain is partitioned into non-overlapping compartments, or voxels, and the position of each agent is known up to the voxel scale. Agents within the same voxel are considered indistinguishable and reactions between them occur independently of other compartments. Movement of agents between voxels is modelled as a continuous time random walk (RW). This is also known as the Reaction Diffusion Master Equation (RDME) approach.

A weakness of the RDME approach is that it does not converge to its individual-based Brownian dynamics in dimensions greater than one for compartments with size less than a specific lower bound (of the order of the reaction radius in the Smoluchowski interpretation) [62]. The RDME breaks down as the voxel size tends to zero because the waiting time for multi-molecular reactions becomes infinite. The convergent RDME (cRDME), is an approximation of Doi's model for binary reactions of the form $A + B \rightarrow C$ designed to address this issue [63]. In the cRDME, agents from *different* voxels may interact via multi-molecular reactions if they lie within a predefined *interaction radius*. In this way the artefact of vanishing reaction rates as voxel size tends to zero (i.e. typically smaller than agent size) is avoided.

In this thesis, we formulate intercellular interactions using the cRDME approach (see Chapter 2). We introduce an interaction radius, R_c, within which cells are assumed to interact. This approach also fits naturally with the VEGF-Delta-Notch driven cell cross-talk. We use the Next Subvolume (NSV) method [64], a computationally efficient implementation of the standard Stochastic Simulation Algorithm [65], to simulate RDME/cRDME.

1.4   Hybrid (multiscale) modelling

Biological systems are often highly complex, involving processes that interact across multiple spatial and temporal scales (see Figure 1.4). From a general perspective, the subcellular scale is characterised by intracellular chemistry (e.g. gene expression, signal transduction and receptor/ligand dynamics). Subcellular processes determine behaviour at the cellular scale and may generate emergent properties at the tissue scale. In addition to this upward coupling across spatial scales, downward coupling may occur when extracellular chemicals and biomechanical cues influence the subcellular chemistry/mechanics within a cell. In this way, dynamic interactions, encompassing multiple scales, can occur (Figure 1.4).
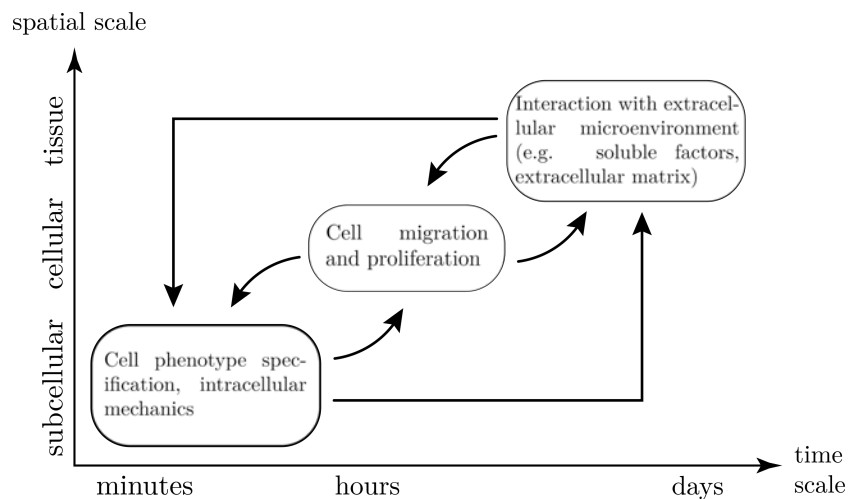
Figure 1.4. A schematic diagram illustrating characteristic spatial and temporal scales of a typical biological process and coupling between them.

From the theoretical perspective, models which consider processes at a single spatial/temporal

scale do not allow for investigation of emergent features which manifest at other scales (for example, collective migration or phenotype patterning which arise from individual cell dynamics and govern tissue scale organisation). Equally, difficulties associated with the interpretation of parameters in phenomenological models make it challenging to fit them meaningfully to biological data. This can hinder model calibration/validation and limits applications of phenomenological models. Multiscale models, which couple processes at different spatial and/or temporal scales, have the potential to overcome these issues [66].

A challenge when formulating multiscale models relates to the number of entities (protein, cells, extracellular components, etc.) that should be included at each scale of interest. Using the same mathematical formalism to model processes concerning entities which vary in number by several orders of magnitude may lead to the omission of essential features or make the models computationally intractable. Hybrid approaches represent a means to overcome problems of this type and, as such, are widely used for multiscale modelling [67], [68]. The central idea is to employ the modelling framework most suitable to each subprocess and then to couple them. For example, the extracellular environment and signalling cues are often modelled deterministically due to the large numbers of proteins involved. On the other hand, cells may be treated as individual entities, equipped with subcellular models that determine their behaviour (e.g. proliferation, cell polarity and migration). This framework has been used to develop multiscale models of cancer (see reviews [67], [69] and references therein), angiogenesis [70], collective cell migration [68], among other examples [71].

Hybrid modelling allows for more efficient model visualisation and facilitates interdisciplinary collaboration between researchers in theoretical and experimental biology [71], [72]. There is also the potential of using high-throughput experimental data to develop more detailed multiscale models. One of the aspects of biological systems that has received little attention in theoretical modelling is the effect of stochasticity on the response of individual entities to external stimuli [68]. Hybrid modelling allows for investigation of this effect on emergent collective behaviour. However, increasing computational complexity can make such

models intractable for large-scale simulations [67].

Angiogenic sprouting involves dynamic interactions at different scales [70]. In this work, we use hybrid modelling to develop a multiscale model that accounts for subcellular signalling of ECs, their heterogeneous behaviours at the cellular scale (cell migration, proliferation and interactions with their microenvironment) and the dynamics of the tissue environment surrounding the cells.

1.5 State of the art

Angiogenic sprouting has been extensively studied from a theoretical perspective in numerous physiological and pathological contexts, including tumour growth (see the reviews [73]–[75]). Early theoretical models typically consisted of systems of partial differential equations (PDEs) for the EC density and growth factors stimulating sprout outgrowth (e.g. [76]–[78]). We provide a brief summary of such *continuum* models in section 1.5.1. Later it was recognised that such a deterministic approach cannot reproduce the branching morphology of real vascular networks (features which are crucial for assessing the functionality of vascular systems in terms of their blood flow and drug delivery). This prompted the development of models in which ECs are treated as individual agents whose trajectories can be tracked, together with the capillaries that they generate (for example, [36], [79]). Models of this type are called *discrete* and include lattice-based, off-lattice and cell-based models. In these models, the external environment is assumed to be static. In practice, however, EC behaviour is highly dependent on the dynamics of the extracellular environment (growth factors, ECM components). Therefore, there are few models which are 'purely' discrete. Typically, theoretical models of angiogenesis use a continuum approach to describe the evolution of the cell microenvironment and couple it to discrete models EC behaviour (e.g. [80]–[83]). These models are referred to as *hybrid* models. Hybrid models use distinct theoretical frameworks to describe specific model components and then couple them together. Hybrid models of angiogenesis can generate branching networks comparable to those observed *in vitro* and *in*

vivo. We review discrete and hybrid models together in section 1.5.2.

Many models of angiogenesis, irrespective of their type, are based on the *snail-trail* assumption. In this approach, EC phenotype is assumed to be irreversible; ECs with the tip phenotype are situated at the leading edge of growing sprouts and respond chemotactically to gradients of signalling cues such as VEGF. All other ECs are viewed as stalk cells that passively follow (i.e. trail) behind tip cells at the leading edge of the sprouts. Cell positions are assumed to be fixed within sprouts and cell rearrangements are neglected.

Here, we review existing mathematical and computational models of angiogenesis. This enables us to illustrate how our modelling approach differs from previous work and to highlight some of its advantages in section 1.6.

For completeness, in Appendix A, we summarise existing mathematical models of subcellular signalling via the VEGF-Delta-Notch pathway.

1.5.1   Continuum models

Snail-trail continuum models

Many early theoretical models of angiogenesis were motivated by studies of tumour growth. The evolution of most solid tumours can be characterised by two phases. Initial tumour growth relies solely on the diffusion of nutrients from the surrounding tissue (avascular tumours). The second phase of vascular tumour growth only occurs *in vivo* and requires successful angiogenesis. In this context, angiogenesis marks the transition from a dormant, avascular tumour to an invasive one which may be capable of metastasis [84], [85]. It is now known that hypoxic tumour cells secrete special chemical compounds (which are known under a common term of tumour angiogenesis growth factors, TAF) which diffuse to the underlying vascular bed and initiate the sprouting of new blood vessels [84], [85]. Early mathematical models of angiogenesis (most of them were continuum) focused on TAF-induced sprout formation via EC migration and proliferation and were motivated by experiments reported

in [86], [87] in which a small tumour fragment, implanted in the rabbit cornea, induced angiogenic sprouting from the underlying limbus. The models were formulated in one spatial dimension and describe radial growth of sprouts towards a tumour fragment located in the centre of the cornea.

One of the first mathematical models of angiogenesis was developed by Deakin [88]. It used PDEs to describe the evolution of TAF and accounted for the chemotactic response of ECs to the evolving TAF distribution. In another model [76], Balding & McElwain noticed that cells at the leading edge of sprouts behave differently from those behind them (although cell phenotype differentiation was unknown at that time). Thus, they formulated their model under the snail-trail hypothesis. Their model accounted for TAF diffusion, sprout tip chemotaxis in response to the spatial distribution of TAF and the increase in capillary density induced by movement of the sprout tips. The model successfully reproduced the brush-border effect, with sprout tip densities increasing as the network approaches the TAF source and vessel regression predicted after removal of TAF.

The work by Balding & McElwain [76] has been extended by several research groups. Byrne & Chaplain [78] also accounted for random migration by sprout tips and their proliferation in regions of high TAF concentrations (in [76] only capillaries behind sprout tips were allowed to proliferate). In other work, Chaplain & Stuart [77] coupled a detailed description of TAF evolution [89] with the model for sprout growth from [76]. They accounted for TAF consumption by ECs and its natural decay. Chaplain [90] then extended this model to two spatial dimensions and performed simulations in a rectangular domain with a circular TAF source at one of its borders. Further model extensions were done in [91] by accounting explicitly for branching and anastomosis (i.e. formation of connections between sprouts). Many of the aforementioned models focused on reproducing the brush-border effect and identifying necessary conditions (e.g. chemotactic strength, proliferation rate) for tumour neovascularisation (when growing capillaries successfully reach the TAF source).

It is now known that (in addition to TAF) EC behaviour also depends on the density

of the surrounding ECM. In particular, ECs, stimulated by TAF, secrete various adhesive substances (fibronectin, different types of collagens). This creates an adhesive gradient which cells can move up via a phenomenon called *haptotaxis.* Later continuum models of angiogenic sprouting included additional PDEs to describe the dynamics of fibronectin and incorporated haptotaxis in the equation for sprout tips. For example, Orme & Chaplain developed a model that accounts for haptotaxis [92], [93] (1D and 2D models, respectively) and investigated how the relative strengths of chemotaxis and haptotaxis affect tumour neovascularisation. They also used their model to investigate the effect of different anti-angiogenic strategies on vessel growth (cytotoxic therapy killing ECs, inhibition of EC mitosis, anti-haptotaxis and anti-chemotaxis treatments).

A more detailed model was formulated by Levine et al. [94] to investigate the onset of sprout growth, when TAF-activated ECs secrete proteolytic enzymes that degrade the basement membrane (BM) surrounding the pre-existing vessel. Their model equations were derived by applying the law of mass action to biochemical reactions for interactions involving VEGF, as a specific type of TAF, and relevant enzymes (proteolytic enzyme and its inhibitor). Their simulation results were in good agreement with experimental data reported in [85] concerning the timing of the onset of sprout extension and the growth rate of the capillary tip.

More recent continuum models have studied angiogenesis in different settings. For example, Aubert et al. [95] developed a model of retinal vascularisation in mice. They considered astrocyte migration from the optic nerve in the retina ahead of ECs, which created a guidance template for vascular network formation due to VEGF secreted by astrocytes. In other work, Flegg and co-workers [96] formulated a model of wound-healing angiogenesis to investigate the ability of hyperbaric oxygen therapy (elevated oxygen supply to the wounds) to aid healing of chronic lesions. They extended the model by Balding & McElwain [76] by accounting for dynamic oxygen supply and investigated several protocols for treatment delivery. In Connor

et al. [97], image analysis of experimental data was performed to extract quantitative information about the cornea vasculature. These data were then used to parametrise a continuum mathematical model based on work reported in [76], [98].

Mechanochemical models

The models described above do not account for the complex structure of the underlying ECM and its interaction with cells. ECs may exert tensile forces on ECM fibrils, which lead to their deformation and displacement [18]. This ECM reorganisation can, in turn, induce passive movement of neighbouring ECs. A mechanical continuum model by Manoussaki et al. [99] confirmed that cell-ECM force interactions could suffice to generate the honeycomb patterns formed by vascular networks *in vitro*. This work was specialised for angiogenesis by Holmes & Sleeman [100]. They combined the model of ECM deformation due to traction forces exerted by cells [99] with a model for sprout growth based on that in [77], [93]. In the resulting 2D model, cell movement is due to cell-ECM interactions (a diffusion tensor given by strains in the ECM and a convection term due to ECM deformation) and chemotactic and haptotactic sensitivity of ECs. The main focus of this work was to investigate the effect of ECM viscoelasticity and its deformation due to EC migration.

The continuum models reviewed above (with the exception of the vasculogenesis model by Manoussaki et al. [99]) do not account for the branching morphology of growing vascular networks. One way to overcome this shortcoming is to treat cells as discrete agents. We review models of this type in the next section.

1.5.2   Discrete and hybrid models

One of the first models to account for the formation of separate sprouts was developed by Stokes & Lauffenburger [101]. Therein, sprout tips were viewed as discrete agents whose velocities satisfied a system of stochastic differential equations. The time evolution of the capillary density of each individual sprout was described by a separate ODE. The authors

also introduced probability-based branching events and allowed connections between sprouts whose trajectories cross (anastomosis) to occur. The parameter values for this model were obtained directly from available experimental data. One of the main goals of the work was to examine the influence of chemotactic strength on the morphology of vascular networks and successful tumour neovascularisation (they considered a rectangular domain with a fixed TAF gradient produced by a circular source). Other examples of stochastic models of angiogenesis include the discrete model by Sleeman & Wallis [79] who focused on EC migration. Their model is formulated as a reinforced random walk for the movement of sprout tips, in which the probabilities for cell migration in a given direction are determined by the chemotactic and haptotactic responses of ECs. The spatial distributions of the TAF and fibronectin were assumed to be static. The aim of this work was to investigate the interplay between chemotactic and haptotactic strengths. An example of an off-lattice model is the work by Plank & Sleeman [82] in which they used a circular random walk that was originally used to describe the dynamics of swimming microorganisms [102]. In their framework, the migration of each sprout tip was characterised by its speed and direction of motion, with the latter described as a random walk on a unit circle. The model also accounts for chemotaxis, haptotaxis, (rule-based) branching, sprout anastomosis and EC proteolytic activity. Simulations were conducted in a tumour environment and various anti-angiogenic strategies were tested.

An alternative approach was developed by Anderson & Chaplain [80]; they first developed a 2D continuum model of angiogenesis and then discretised it in order to obtain a rule-based cellular automaton for sprout growth. In this model, ECs were treated as discrete entities whose migration probabilities depended on their chemotactic and haptotactic sensitivities and random motility. The evolution of TAF and fibronectin was governed by a system of PDEs, as in the original continuum model. The authors also incorporated rule-based branching, anastomosis and cell proliferation. This model has been extended in numerous ways. In [103], numerical simulations were extended to three spatial dimensions. McDougall and coworkers [104] utilised the vascular networks generated by the discretised model by Anderson

& Chaplain [80] to simulate blood flow through the network structures and drug delivery to the tumour. They examined the effects of blood viscosity, vessel radii and network topology on the rate of flow and the amount of fluid (chemotherapeutic drug) reaching the tumour. Their numerical simulations showed that, depending on the treatment strategy and vasculature structure, the drug may not reach the tumour. The efficacy of different treatment strategies was further assessed by Stéphanou et al. [105]. They extended the blood flow model from [104] to 3D and sought to identify conditions under which the amount of chemotherapeutic drug delivered to the tumour was maximised. Their model simulations predicted that vessel pruning (i.e. vessel regression) induced by anti-angiogenic treatment improves drug delivery (due to removal of excessive and blind-ended vessels which obstruct the flow). Thus, they proposed to couple anti-angiogenic treatment and chemotherapy for optimal drug delivery. Later work by this research group includes a model of angiogenic sprouting dynamically coupled with vessel adaptation due to blood flow [106] (dynamic adaptive tumour-induced angiogenesis, DATIA). In this model, vessel perfusion affects network growth instead of being evaluated *a posteriori* (as was done in previous works [104], [105]). In particular, the authors considered adaptations of vessel radii to maintain constant wall shear stress, shear-induced vessel branching and perfusion-dependent anastomosis. They also introduced the dynamics of an enzyme secreted by ECs that degrades the surrounding ECM and thereby promotes vessel elongation. In other work by the research group [107], the DATIA model was extended to account for the effects of pericyte coverage on vessel stabilisation. Then they explored the potential of a treatment that targets pericytes and thereby destabilises blood vessels by inducing capillary pruning.

Vascular remodelling in the context of tumour growth was also investigated by Bartha & Rieger [108]. They developed a 2D probabilistic cellular automaton which accounts for vessel co-option and capillary adaptation due to blood flow. Vessel co-option affects the growth dynamics of avascular tumours: if blood vessels are present in their vicinity, then angiogenic sprouting is not triggered until the co-opted host vasculature regresses, and the

tumour becomes hypoxic. In the model by Bartha & Rieger [108], the co-opted vasculature consists of a square grid of pre-existing vessels surrounding the tumour spheroid. Further vascular adaptation included vessel dilatation/constriction, vessel collapse and regression (due to blood flow) and angiogenic growth of new blood vessels. Model simulations showed that tumour growth is strongly influenced by the structure of the original co-opted vasculature.

More recent work has explored diverse techniques for developing more detailed and/or more numerically tractable models of angiogenesis. For example, Sun and coworkers [109] used finite element methods for efficient numerical simulation of their 2D multiscale model of sprouting. Milde et al. [110] presented the first 3D hybrid model of angiogenesis which explicitly accounted for the complexity of the ECM and the effects of ECM sequestration of growth factors (VEGF) on the sprout growth. An advantage of this approach was that branching, instead of being hard-wired into the model, occurred naturally in response to divergent (from the direction of sprout elongation) extracellular cues (matrix-bound/soluble VEGF and fibronectin) and orientation of ECM fibrils. The efficiency of the hybrid approach in the modelling of angiogenesis was demonstrated by Capasso & Morale [83]. In their model, Langevin equations were used to describe the migration of sprout tips and probability-based rules were implemented for branching and anastomosis. Tissue scale variables, such as concentrations of TAF, fibronectin and proteolytic enzymes, were treated continuously. Spill and coworkers [59] based their 2D on-lattice model on a mesoscopic approach in which cell migration and proliferation were considered stochastic events. This enabled them to derive continuum equations as mean field descriptions of their stochastic model and to identify conditions under which simulations of continuum and discrete models agree. In particular, they showed that comparison between two frameworks is poor when there are low numbers of capillary tips in the system. Norton & Popel used their 3D agent-based model [111] to investigate how the balance between cell migration and proliferation affects the vascular branching structure. Another approach was presented by Perfahl et al. [112]. In their 3D off-lattice mechanistic model, ECs were considered as linearly elastic spheres migrating and

dividing under the influence of the external mechanical stimuli (e.g. chemotactic sensitivity, persistence force, stretch). They showed that chemotaxis is not needed for network formation and that mechanical stimuli could contribute to network formation. The framework of this model permitted a detailed quantification of the network structure in different computational scenarios of varied chemotactic sensitivity and stretch-induced proliferation.

A discrete-to-continuum approach was also (e.g. [59]) used by Pillay and colleagues [36] to determine macroscopic dynamics of angiogenic sprouting from the behaviour of individual ECs. They formulated a discrete cellular automaton that describes two-dimensional sprout growth within the snail-trail modelling framework. Using mean-field approximation, Pillay and coworkers derived from their cellular automaton a 1D continuum model that describes macroscopic sprout growth. This enabled them to perform a systematic comparison between averaged simulation results of their discrete model, the mean-field approximation and the deterministic model by Byrne & Chaplain [78]. They demonstrated that when sprouts in the cellular automaton are allowed to form self-loops (i.e. when a sprout fuses with itself), the agreement between discrete and continuum models is poor. The authors also identify differences between their continuum model derived from microscopic EC behaviour and existing phenomenological models (e.g. [78]). Martinson et al. [113] extended this work by deriving a two-dimensional continuum model which accurately describes microscopic cell behaviour observed in simulations of the discrete snail-trail model by Pillay et al. [36]. To do this, they introduced a multiplicative factor in the equation for the stalk cell (cells-followers within the snail-trail framework) production which corrects the EC density in directions different from the one of the leader cell migration (e.g. due to the sprout bending). Martinson and colleagues showed that their 2D snail-trail continuum model is a valid description of EC microscopic behaviour when the motion of sprout tips is dominated by chemotaxis. They also identify conditions under which their reduced 1D snail-trail description is appropriate to describe cell dynamics observed in the 2D discrete model [36].

Many of the existing theoretical models of angiogenesis were developed by their authors

as custom software programs for the simulation of vascular network growth. This approach hinders cross-comparison of the existing models of angiogenesis and often does not allow for reproduction of the reported results (unless an open-source code is available). Grogan and colleagues addressed this issue by developing an open-access library, called Microvessel Chaste [114], for assembly and simulation of complex multiscale models describing vascular dynamics in different contexts (for example, angiogenesis, tumour growth, oxygen delivery, etc.). Its general framework, based on the comprehensive Python/C++ interface, offers a wide range of building blocks and numerical techniques for the composition of models of vascularised tissues. The Microvessel Chaste library was designed to facilitate model visualisation and analysis, integration of experimental data and efficient model simulation. In [114], Grogan and coworkers applied their Microvessel Chaste library to compose a model of vascular tumour growth as developed by Owen et al. [115]. They performed simulations of the tumour evolution in a vascularised tissue obtained via image analysis from *in vivo* experiments in mice. They also demonstrated the potential of the Microvessel Chaste to perform simulations on complex geometries such as a hemispherical surface of the murine cornea (as was formulated in [97]).

We now continue by providing a brief overview of other classes of hybrid models of angiogenesis.

Cornea vascularisation models

Post-natal vascularisation of the cornea is characterised by angiogenic sprouting from the limbal vessels located at the circumference of the cornea domain. Tong & Yuan [81] formulated a simple hybrid model of sprout formation induced by basic fibroblast growth factor (bFGF, another growth factor capable of stimulating angiogenesis) released from a rectangular pellet implanted into the cornea. Their results showed that the topology of the simulated vascular networks was sensitive to the distribution of bFGF and its rate of uptake by ECs. This work was extended by Harrington et al. [116] where the effects of an externally supplied

inhibitor of angiogenesis were evaluated. A more detailed model of corneal angiogenesis was developed by Jackson & Zheng [117]. Therein, sprout tip motion was implemented with a viscoelastic model for their elongation. Stalk cells, following behind sprout tips in a snail-trail fashion, were assumed to proliferate at a rate depending on the concentration of VEGF and their level of maturation (described by differential equations for each individual cell). Cell maturation was induced by a special type of growth factor, angiopoietins, expressed by pericytes to promote vessel quiescence. One of the main goals of this work was to provide a mechanistic explanation to experimental observations that cell proliferation mostly occurs at the leading edge of the growing vasculature. Their simulation results confirmed that the proposed mechanism of cell division (dependent of the bioavailability of VEGF and the degree of cell maturation) can possibly explain the experimental data. Another cornea vascularisation model was developed by Watson and coworkers [118]; they extended the model by Anderson & Chaplain [80] by coupling it with an equation for astrocytes. These cells migrate outwards from the central optic nerve of the cornea prior to sprout initiation, guided by a gradient of platelet-derived growth factor (PDGF). They express chemical cues (e.g. VEGF) which induce angiogenic sprouting. Thus, the template created by the astrocytes serves as a guidance map for ECs migration. The model also accounted for adaptation of vessel radii and vessel pruning in response to blood flow. Simulation results of this model were compared with available experimental images of retina vascularisation in mice.

MemAgent model by Bentley et al.

In a series of articles [5], [37], [119], Bentley and coworkers developed the first model to account for subcellular VEGF-Delta-Notch signalling in EC crosstalk in the context of angiogenesis. In their *in silico* model, a small set of ECs, positioned linearly on a fixed tubular geometry, are comprised of memAgents (representing small sections of cellular membrane) connected via Hookean springs to form a mesh-like structure of the cell's outer membrane

(memAgent model). Cell communication was maintained via the VEGF-Delta-Notch signalling pathway with additional positive feedback due to filopodia extension (a cell, stimulated by VEGF, can grow filopodia which, in turn, increases VEGF capture by the cell due to the availability of VEGF receptors within these thin protrusions). Their first model [119] focused on the dynamics of cell phenotype patterning (a 'salt-and-pepper' pattern of alternating tip and stalk cells) at the onset of angiogenesis upon VEGF stimulation. The model predicted that filopodia extensions can speed up cell fate selection (which is crucial for an adequate growing vascular network due to phenotype-dependent EC behaviour). Their simulation results also suggest that in high VEGF concentrations ECs synchronise their fates and that these fates may oscillate in time (all tip/stalk cells instead of a salt-and-pepper pattern). This can be explained by the saturation of VEGF receptors with VEGF in which case filopodium extension does not give a particular cell a greater ability to inhibit its neighbours. As a consequence, all cells adopt the same phenotype.

Later work [119] involves extension of the memAgent framework to account for membrane elongation in response to VEGF stimulation and pulling force of filopodia. This allowed the authors to explore how the process of sprout fusion, i.e. anastomosis, affects the stability of the cell phenotype pattern within the sprout in different VEGF environments. Further extensions of the model [5] included cell shuffling within the given tubular domain to investigate the mechanism of cell mixing during angiogenesis. Using computational modelling and experimental data, they identified the Notch/VEGFR-regulated dynamics of EC adhesion as a key driver of EC rearrangements. However, due to the computational complexity of the model, simulations were performed with only 10 ECs. In addition, the fixed tubular geometry of the model did not allow for the exploration of how cell rearrangements affect the vascular morphology. The memAgent model has been also used to generate model predictions (supported by experimental data) in order to investigate dynamic EC competition for the leading cell position [9], the EC division process [120], the influence of EC metabolism on cell rearrangements [7] and the role of EC filopodia as an active perception mechanism [121].

Cellular Potts models

The Cellular Potts Model (CPM) is a generalisation of a cellular automaton in which each agent (cell) is associated with a cluster of identical lattice sites that represent the shape of the cell [122], [123]. Thus, this is a cell-based approach for modelling cellular dynamics. The CPM algorithm is based on a Monte-Carlo approach, in which iterative displacement of the cell interface is implemented to reduce the effective energy of the cellular configuration. Typically, an effective energy is lower for round cell shapes (as compared to elongated cells), strong cell-cell and cell-ECM adhesion (as compared to weak adhesion). Chemotaxis, in this framework, can be implemented, for example, as an increase in the cell velocity for higher concentrations of the stimulating cue.

The CPM framework has been successfully used to model the formation of vascular structures and angiogenesis. In a general setting, CPM models of vascular growth are hybrid since tissue scale variables (growth factors, ECM components) are treated in a deterministic way. The first cell-based CPM model of tumour-induced angiogenesis was developed by Bauer et al. [124]. This work explored the role of the ECM as an obstacle for sprout elongation. The model explicitly accounts for the composition and structure of the ECM which, together with the VEGF dynamics, produces inhomogeneities in the local cell environment and results in such emergent properties as branching and anastomosis (instead of being implemented in a rule-based fashion as in the majority of hybrid/discrete models of angiogenesis). Simulation results of this model included the elongation of a small sprout. A more detailed representation of the ECM structure was incorporated into this model in a follow-up paper [125]. Furthermore, the model was validated against experimental data (average sprout elongation speed, its thickness and cell shape) [125]. This enabled the authors to examine the effects of varying ECM density on sprout integrity and their ability to extend into the matrix. They also explored how the alignment of ECM fibrils affects cell shape and sprout growth. Their simulation results agree with experimental observations [126] (reported later): at low ECM

densities, cell proteolysis inhibits the formation of chord-like sprouts, whereas at high ECM densities proteolytic enzymes secreted by ECs have a pro-angiogenic effect.

The CPM approach has been also used to understand the mechanisms responsible for the formation of characteristic vascular patterns. Merks et al. [127] showed that inhibition of cell chemotactic sensitivity due to contact with neighbouring cells (maintained via VE-cadherin-mediated cell junctions) is a possible mechanism for sprout formation in vasculogenesis and angiogenesis. Another explanation was suggested by van Oers and coworkers [128]. They formulated a CPM model in which the contractile forces exerted by cells can generate strains in the underlying ECM and modulate EC behaviours (durotaxis, cell sensitivity to the ECM rigidity). This set of purely mechanical biological assumptions was shown to suffice to reproduce typical chord-like patterns in the context of vasculogenesis and angiogenesis. The simulation results of this model demonstrated that ECMs of intermediate stiffness favour elongated cell shape and formation of vascular networks, whereas soft (stiff) matrices cause cells to spread out (contract) on the ECM and form cell clusters. Daub & Merks [129] explored another mechanism for vascular network formation based on ECM-guided sprout formation. Their CPM model confirmed that chemotaxis alone suffices to sustain growth of linear sprouts. However, branching network structures are achieved only when the traditional chemotactic response is combined with proteolysis, cell proliferation and haptokinesis (cell ability to modulate their velocity in response to the ECM concentrations). Moreover, they also (as in [125]) confirmed that sprout elongation is faster (slower) on the ECM of intermediate (low/high) concentrations.

Boas & Merks [130] used the CPM methodology to study EC rearrangements within small vascular networks. They investigated how a cell at the leading position in a sprout can be overtaken by another cell, a phenomenon called *cell overtaking*. Their simulation results suggest that cell overtaking occurs in an unregulated fashion, due to the stochastic motion of ECs. Moreover, their findings suggest that the role of the VEGF-Delta-Notch pathway in cell overtaking is not to select a cell with the highest expression of Delta ligand and

VEGFR2, corresponding to the tip phenotype, that will shuffle up towards the sprout tip. Rather, EC subcellular signalling is proposed to ensure that a cell that ends up occupying the leading position in a vessel (due to random cell overtaking) acquires the tip phenotype. In their model, time-dependent ordinary differential equations (ODEs) are used to simulate the dynamics of subcellular signalling pathways (the VEGF-Delta-Notch signalling pathway) within each cell. Cells are assigned a discrete phenotype, tip or stalk, and variations in gene expression levels that might influence the behaviour of the cell are neglected.

A 3D CPM model of angiogenesis in the context of tumour growth was formulated by Shirinifard et al. [131]. Simulations of this multicellular model show how the evolution of the pre-existing vascular grid affects the morphology of growing tumours.

Angiogenesis models in the context of tumour growth

Vascular dynamics have been considered in a number of theoretical models of tumour growth (using techniques different from the CPM approach, e.g. [131]). In a series of works, Alarcón and coworkers focused on the adaptation of vascular networks in tumour environments [132], [133]. They formulated a multiscale hybrid model which takes into account interactions between cancerous and normal cells, blood flow, vasculature remodelling, oxygen transport and VEGF distribution. A nutrient-dependent model of the cell cycle in tumour and stromal cells was formulated at the subcellular scale by a system of ODEs. They prescribed a fixed honeycomb structure for the vascular network, in which vessels adapt their diameter in response to the blood flow and VEGF. The model considers how the way in which blood flow and vascular remodelling are represented impacts the structure (size and morphology) of tumour cells embedded in the vascularised tissue. In subsequent work [134], the authors also took into account vessel dematuration, loss of the basal lamina surrounding vessels which results in vessel leakiness in high VEGF concentrations induced by hypoxic tumour cells. This multiscale model was then used to assess the potential of different therapeutic strategies [134], [135]. In later work, Owen et al. [136] extended the multiscale model by incorporating

vascular remodelling due to angiogenesis and shear-induced vessel pruning. The modelling framework was subsequently extended to 3D simulations by Perfahl et al. [137] in order to investigate conditions under which the simulation results of tumour evolution and its response to treatment can be extrapolated from small to larger (and from 2D to 3D) domains. Furthermore, the authors illustrated how experimentally obtained images of *in vivo*-grown vascular systems can be used as initial configurations for model simulations [137].

Other examples of hybrid multiscale models coupling tumour invasion with tumour-induced angiogenesis include the work by Macklin et al. [138]. This paper combines a detailed model of solid tumour growth with the model for vascular network formation following the work by Anderson & Chaplain [80] with vascular remodelling as in McDougall et al. [106]. Their simulation results highlighted the effects of the evolution of the underlying vasculature on tumour progression. In particular, they showed that the proliferation of tumour cells exerts pressure on the surrounding tissue, which obstructs the flow in the neighbouring blood vessels and impedes effective nutrient delivery to the tumour. Moreover, nutrient delivery is further reduced since growing capillaries tend to surround the tumour spheroid (instead of penetrating it) due to the proteolytic activity of cancerous cells. Phillips and coworkers [139] developed a 2D agent-based model of vascular tumour invasion. Their approach takes into account angiogenic sprouting in response to VEGF stimulation and mechanical interactions with other cells (cancerous and endothelial) and ECM. EC phenotype transitions were implemented in a rule-based manner; quiescent phalanx ECs get activated due to VEGF stimulation and become either stalk cells, or tip cells if positioned at a sufficient distance from other tip cells. Thus, this discrete phenotype distinction does not account for transitions between tip and stalk cell phenotypes. Simulations of the full model demonstrated that physical interactions between ECs and tumour cells led to experimentally observed vessel collapse.

Phase-field models

The phase-field methodology combines a discrete description of sprout tip movement with a continuous representation of the trailing capillary (snail-trail assumption). Sprout tips are viewed as individual agents that migrate in an off-lattice fashion in response to chemical gradients. The trajectories of the sprout tips define the shape of the growing capillaries which are described by the phase-field variable; this variable takes positive values inside blood vessels and 0, or negative values, outside the capillaries (i.e. in the extravascular tissue). The coupling between the continuous representation of capillaries and discrete sprout tips is accomplished by assuming that the phase-field variable is equal to unity where sprout tips are located.

The first phase-field model of angiogenesis was formulated by Travasso et al. [140]. It considers deterministic migration of sprout tips up the gradient of VEGF secreted by hypoxic cells scattered over the domain. The authors utilised this framework to investigate changes in vasculature morphology in the conditions of varying VEGF bioavailability, the velocity of sprout tips and the proliferation rate of stalk cells. Vilanova and coworkers [141] extended this model to account for random motion of sprout tips by using a circular random walk (utilised by Plank & Sleeman [82]). They performed two- and three-dimensional simulations and assessed the connectivity of the resulting vascular networks. Their results demonstrated that network connectivity is lower in 3D than in 2D simulations. Thus, this work highlights the importance of anastomosis for the formation of functional vasculatures. Possible mechanisms of anastomosis were explored in a later work by Moreira-Soares et al. [142]. They considered two hypotheses for the fusion of two sprouts driven by VEGF secreted by hypoxic cells; cells were considered hypoxic if they were located at a certain distance away from (*rule 1*) vessels with blood flow rate different from 0, or (*rule 2*) all vessels. Their simulation results showed that vascular networks generated following *rule 1* have fewer blind-ended vessels and more vessels with blood flow than those generated using *rule 2*. By contrast, simulations in

which cells stop expressing VEGF in the vicinity of a capillary (with or without blood flow, *rule 2*) generated smaller networks, with fewer anastomoses, than those generated following *rule 1*. The authors concluded that the mechanism of VEGF expression by hypoxic cells predetermines the network branching structure to a greater extent than EC proliferation or the velocity of the sprout tips. In later work by Vilanova et al. [143], the model from [141] was extended to account for sprout tip filopodia which can sense not only VEGF gradients but also the basement membrane of neighbouring capillaries. In this way, sprout tips were biased to form anastomosis when they detected another blood vessel or a regressed capillary in their vicinity (i.e. empty collagen sleeves left after vessel regression). This framework allowed the authors to investigate vascular regression caused by a decrease in VEGF levels followed by vasculature regrowth along the empty basement membrane sleeves of the regressed vessels. In other work by this research group, Xu et al. [144] incorporated the phase-field framework (based on [140], [143]) into the tumour environment.

1.6 Problem outline and thesis structure

At the core of the majority of models of angiogenesis lies the *snail-trail* assumption of irreversible cell phenotype and fixed cell positions within sprouts (e.g. [59], [80], [112], [136]–[138], [140], [142], [145], [146]). As such, these models do not account for cell mixing. At the same time, experimental observations suggest that cell rearrangements play a key role in early sprouting angiogenesis [3]–[5], [9]. In particular, reduced cell mixing leads to the formation of pathological networks characterised by superimposed aberrant layers of vessels [3]. Furthermore, in many models, properties such as branching are hardwired via *ad hoc* rules, in which the probability of branching depends on environmental factors [80], [112], [136]–[138], [145]. Chemotactic behaviour is also frequently encoded in theoretical models by explicitly biasing the migration probabilities towards regions of higher VEGF concentrations [59], [80], [112], [136]–[138], [140], [145]. As a result, these models are unable to explain how variations in subcellular signalling, which determine cell phenotype, modify the structure of

the growing network, or how specific mutations might lead to pathological networks.

Several computational models have been proposed to address these issues. For example, the cellular Potts methodology has been successfully used to simulate branching and anastomosis as emergent properties of the model due to local inhomogeneities in the cellular microenvironment [124], [125], [129]. Milde et al. [110] developed a hybrid model that explicitly accounts for the complex ECM structure which, together with dynamic VEGF bioavailability, leads to branching. However, these models ([110], [124], [125], [129]) do not account for the effects of cell phenotype differentiation during angiogenesis.

Cell phenotype specification has been considered in several recent hybrid models. For example, Phillips et al. [139] considered a rule-based phenotype assignment dependent on VEGF levels; quiescent phalanx cells were assumed to differentiate into stalk or tip cells when VEGF levels exceeded a certain threshold. Nonetheless, phenotype patterning was maintained artificially by imposing a fixed distance between tip cells and tip-stalk phenotype transitions were neglected [139]. A similar approach to phenotype patterning, based on fixed distances between tip cells, was used in the phase-field models of angiogenesis by Xu et al. [144] and Moreira-Soares et al. [142].

Cell rearrangement during angiogenic sprouting has been studied by Bentley et al. [5]. Their cell-based model explicitly accounts for EC crosstalk via VEGF-Delta-Notch signalling and dynamic differentiation into tip and stalk cell phenotypes, which determined cellular behaviour. However, cell shuffling is simulated on a fixed tubular domain (imitating cell mixing within a section of a growing sprout). Moreover, due to the computational intensity of the model, only small scale simulations (10 ECs) have been performed. The cellular Potts framework has been used by Boas & Merks to investigate the role of EC phenotype specification in cell rearrangements [130]. ECs are associated with discrete phenotypes (tip or stalk cell) determined by a deterministic model of subcellular signalling. Thus, gene expression profiles and noise-induced phenotype switches, which might be significant for the morphology of growing networks, are neglected.

In this work, we investigate the effects of dynamic phenotype specification and phenotype-driven cell rearrangements on the morphology of growing vascular networks during angiogenesis. The specific objectives of this thesis are the following:

1. *Investigate the effects of dynamic cell rearrangements during angiogenic sprouting on the growth of vascular networks.* To do this, we introduce a multiscale mathematical model of early angiogenesis (i.e. on a time scale of hours). The model accounts for individual cell gene expression patterns associated with the VEGF-Delta-Notch signalling pathway that defines two distinct cell phenotypes. Our model is capable of reproducing the typical behaviour of ECs; branching, chemotactic sensitivity and cell mixing are emergent properties of the model that arise as a result of cell-ECM interactions involving cells with dynamic subcellular gene expression. We then use our calibrated and validated model to quantify cell rearrangement during vascular growth and relate it to the structure of vascular networks generated by cells with mutations in their gene expression. This is the content of Chapter 2.

2. *Develop a coarse-graining method to reduce the computational complexity of our multiscale model, by approximating the stochastic dynamics of the subcellular signalling by a jump process between different phenotypic states.* We develop the coarse-graining method for the general case of a multi-agent system whose internal dynamics are described by a stochastic system with multiple stable steady states. We then illustrate the coarse-graining technique through an example in which EC phenotype is specified via the VEGF-Delta-Notch signalling pathway as introduced at the subcellular scale in the angiogenesis model from Chapter 2. We demonstrate the accuracy of the method and confirm its efficiency in reducing the numerical complexity of the original stochastic model. The coarse-graining method is the subject of Chapter 3.

3. *Incorporate the coarse-grained model of EC phenotype selection into our model of angiogenesis and extend our simulations to longer timescales.* We apply the coarse-grained

technique to reduce the subcellular dynamics of our multiscale model of angiogenesis. This allows us to substantially decrease the computational cost of simulations and to account for the processes of cell proliferation and vessel maturation, both of which act on longer timescales than cell migration. We then perform simulations on the time scales of days to weeks in order to investigate how cell proliferation influences the morphology and expansion of evolving vascular networks. This work is presented in Chapter 4 of this thesis.

Finally, in Chapter 5, we draw conclusions from our findings and discuss possible directions for future work.

Chapter 2

A multiscale model of early angiogenesis

2.1 Summary

We introduce a hybrid two-dimensional multiscale model of angiogenesis, the process by which endothelial cells (ECs) migrate from a pre-existing vascular bed in response to local environmental cues and cell-cell interactions, to create a new vascular network. Recent experimental studies have highlighted a central role of cell rearrangements in the formation of angiogenic networks. Our model accounts for this phenomenon via the heterogeneous response of ECs to their microenvironment. These cell rearrangements, in turn, dynamically remodel the local environment. The model reproduces characteristic features of angiogenic sprouting that include branching, chemotactic sensitivity, the brush border effect, and cell mixing. These properties, rather than being hardwired into the model, emerge naturally from the gene expression patterns of individual cells. After calibrating and validating our model against experimental data, we use it to predict how the structure of the vascular network changes as the baseline gene expression levels of the VEGF-Delta-Notch pathway, and the composition of the extracellular environment, vary. In order to investigate the impact of cell rearrangements on the vascular network structure, we introduce the mixing measure, a scalar metric that quantifies cell mixing as the vascular network grows. We calculate the mixing measure for the simulated vascular networks generated by ECs of different lineages (wild type cells and mutant cells with impaired expression of a specific receptor). Our results show that the time

evolution of the mixing measure is directly correlated to the generic features of the vascular branching pattern, thus, supporting the hypothesis that cell rearrangements play an essential role in sprouting angiogenesis. Furthermore, we predict that lower cell rearrangement leads to an imbalance between branching and sprout elongation. Since the computation of this statistic requires only individual cell trajectories, it can be computed for networks generated in biological experiments, making it a potential biomarker for pathological angiogenesis. This chapter is based on our published work [147].

This chapter is organised as follows. In section 2.2, we summarise the setups and results of several experimental studies which motivated the formulation of our multiscale model. Section 2.3 contains a description of our multiscale model. In section 2.4, we introduce metrics used to analyse vascular network evolution. In section 2.5 we compare our simulation results with data from Arima et al. [4] and Shamloo & Heilshorn [126]. These data were extracted from *in vitro* experiments, and enable us to define a set of basal parameter values for our model. Further model validation is performed against experimental results involving mutant cells, with modified expression of VEGF receptors, carried out by Jakobsson et al. [9]. Finally, we present results on EC mixing quantification and show how it relates to the different branching patterns of the growing vascular networks. We conclude by drawing together our findings in section 2.6.

2.2 Experimental motivation

The model we develop is motivated by *in vitro* experiments in which an aortic ring assay was embedded into a collagen matrix with a uniform VEGF concentration (0, 5 or 50 ng/ml) [4], [10]. Computational analysis of dynamic images, collected using time-lapse microscopy, revealed complex dynamical cell rearrangements within growing sprouts, a phenomenon termed *cell mixing*. The authors concluded that over short periods of time (e.g. 22.4 h averaged over all experiments in [4]) cell rearrangements are the main driver of sprout elongation. Interestingly, successful sprout growth was seen in a uniform distribution of VEGF across the

substrate – sprout elongation velocity was observed to vary as the concentration of the external VEGF was changed, but no VEGF gradient was necessary for coordinated migration of ECs.

Dynamic cell rearrangements within elongating sprouts are a direct consequence of cells continuously updating their phenotype (i.e. adapting their gene expression pattern, depending on their environment [3], [5], [9]). Jakobsson et al. [9] identified the VEGF-Delta-Notch signalling pathway as the key pathway controlling this phenomenon. Using mutant cells heterozygous for VEGFR1 (VEGFR1$^{+/-}$) and VEGFR2 (VEGFR2$^{+/-}$) with halved (compared to wild-type (WT) cells) gene expression of the corresponding VEGF receptor, they investigated how differential levels of VEGF receptors affect the probability that a WT or mutant EC will occupy the leading position in a growing sprout. Embryoid bodies (three-dimensional spherical aggregates of cells) derived from WT cells mixed with one of the populations of mutant cells (50% and 50%) were indistinguishable from those formed by WT cells only, however, the contribution of each cell line to the leading position differed. In particular, VEGFR1$^{+/-}$ (VEGFR2$^{+/-}$) cells demonstrated enhanced (reduced) competition for the leading cell position. The role of the VEGF-Delta-Notch signalling pathway in establishing competitive advantage was reinforced by experiments with the DAPT inhibitor, which abolishes Notch signalling in all EC lineages. Treatment with DAPT, although leading to hyper-sprouting, restored balance in competition for the leading cell position. Motivated by these results and our interest in studying cell rearrangements, we account for the VEGF-Delta-Notch signalling pathway of individual cells in our model.

The coordinated migration of ECs is a result of cell-ECM interactions [20], [29], [33], [34], [148]. Specifically, cell migration depends on the EC ability to degrade ECM proteins via proteolysis in order to form ECM-free vascular guidance tunnels for effective sprout elongation. This was confirmed by experimental results performed by Shamloo & Heilshorn [126]. Therein, ECs were cultured within a microfluidic device with a maintained gradient of VEGF concentration and the response of ECs to variations in ECM components, specifically

collagen, was considered. Their results showed that there is a "sweet spot" of collagen density for the formation of angiogenic sprouts. In low collagen densities, ECs migrate freely into the ECM without forming sprouts; at intermediate concentrations, structures resembling angiogenic sprouts form; at high collagen densities, ECs are unable to migrate into the matrix significantly and form thick short protrusions. These experimental results motivated us to include cell-ECM interactions in our model.

In our mathematical model, we focus on EC migration, and its regulation by local environmental (mechanical and chemical) cues. Due to the short timescales considered in the model, processes such as proliferation, vessel maturation and lumen formation are neglected.

Most *in vitro* experiments are performed on flat substrates in which the depth of the substrate can be considered negligible compared to its length and width [4], [10], [33], [126]. Thus, we formulate our model in a two-dimensional framework.

2.3 Model formulation

2.3.1 Summary of the multiscale model
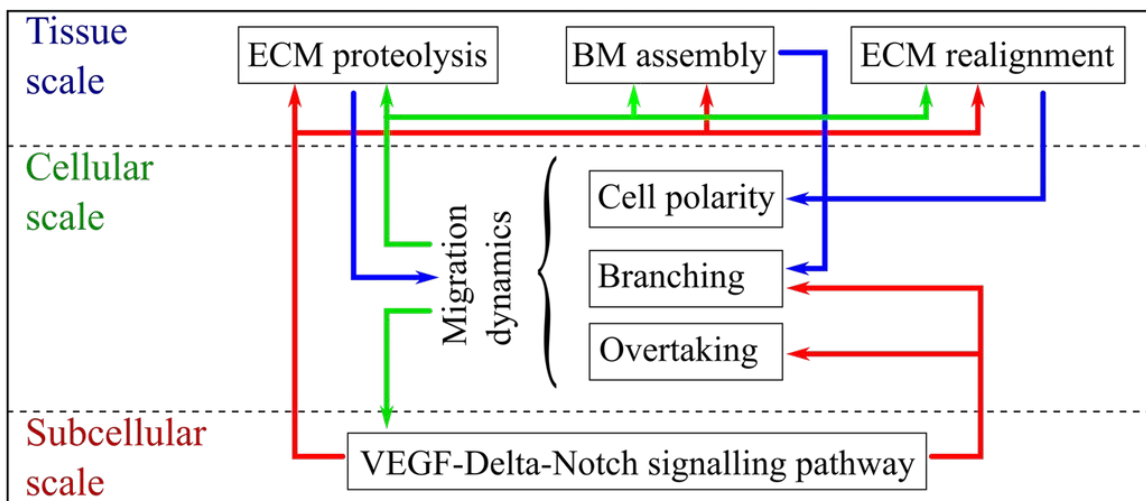
Figure 2.1. The structure of our multiscale model. The diagram illustrates the processes that act at each spatial scale. Arrows illustrate coupling between the scales.

The model we develop is a two-dimensional stochastic multiscale model of migration-driven sprouting angiogenesis. Its structure is shown in Figure 2.1. Briefly, the model operates on three distinct spatial scales:

- The **subcellular scale** defines the gene expression pattern of individual cells. Since ECs contain a finite number of proteins, some level of noise is always present in the system. Thus, we implement a stochastic model of the VEGF-Delta-Notch signalling pathway to describe the temporal dynamics of the number of ligands/receptors for each cell. This pathway is known to produce bistable behaviour. Cells exhibit either high Delta and VEGFR2, and low Notch levels (the tip phenotype) or low Delta and VEGFR2, and high Notch levels (the stalk phenotype). Stochasticity allows random transitions between these phenotypes in regions of bistability, behaviour which cannot be achieved in a deterministic model.

- The **cellular scale** accounts for cell migration. It is formulated as a variant of an on-lattice persistent random walk (PRW) of ECs.

- The **tissue scale** keeps track of the local ECM environment of the cells. Local ODEs track the evolution of the concentrations of the existing ECM and BM components, whereas ECM fibril alignment driven by EC movement is updated using a phenomenological model.

An illustration of the model geometry can be found in Figure 2.2.

In general, an EC has an arbitrary shape which depends on its cell-cell and cell-matrix focal adhesions. In our model we do not keep track of the exact cell shape and assume that cell position is known up to the position of its nucleus. Thus, when referring to a cell position, we refer to the position of its nucleus and assume that the cell has some arbitrary shape centred on the voxel containing its nucleus (see Figure 2.3A). A consequence of this approach is that, since cells can extend membrane protrusions and interact with distinct cells beyond their first neighbours, interactions between cells in our model are non-local. We introduce
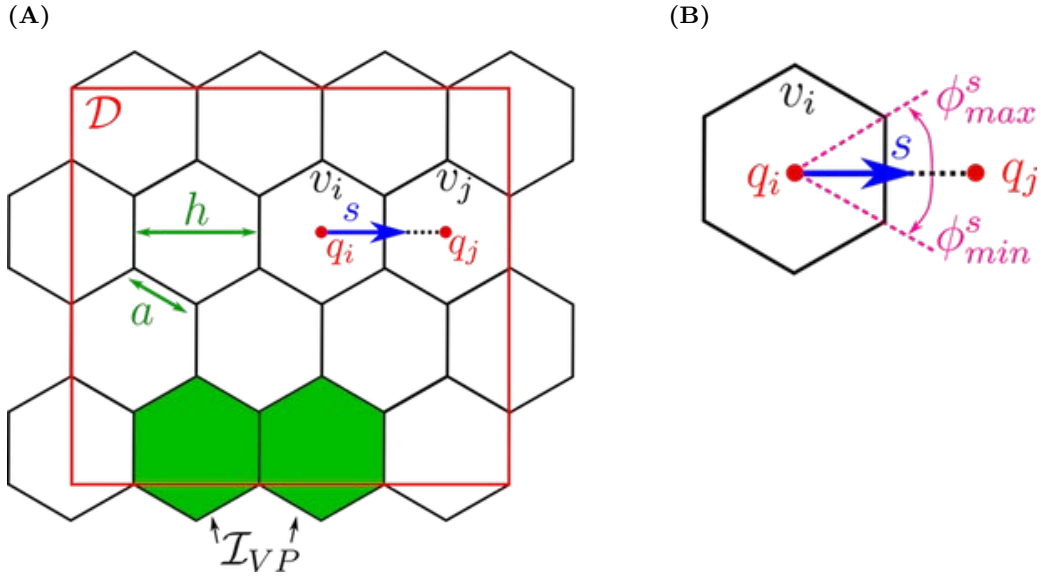
Figure 2.2. Model geometry. (A) To account for cell migration in the framework of a PRW, we cover the domain, $\mathcal{D} \subset \mathbb{R}^2$, by a uniform lattice $\mathcal{L} = \{v_k \ : \ \bigcup_{k=1}^{N_I} v_k \supset \mathcal{D}\}$ of non-overlapping hexagonal voxels, v_k, of width h (or hexagon edge, a, $h = \sqrt{3}a$). We denote by $\mathcal{I} = \{k = (k_x, k_y)^T \ : \ v_k \in \mathcal{L}\}$ the set of 2D indices, with cardinal, $|\mathcal{I}| = N_I$. The coordinates of the centre of voxel v_k are denoted by $q_k = (q_k^x, q_k^y)^T$. We assume that there is a constant supply of ECs to the domain, coming from the vascular plexus. These ECs enter the domain at fixed boundary voxels, defined as a set, $\mathcal{I}_{VP}$ (coloured in green). **(B)** A detailed illustration of an individual voxel, v_i. $s = h^{-1}(q_j - q_i)$ denotes a normalised vector of the migration direction between neighbouring voxels, v_i and v_j. There are at most 6 possible migration directions for each hexagonal voxel. Each migration direction, s, can be characterised by an equivalent angle interval $[\phi_{min}^s, \phi_{max}^s]$.

two interaction radii, R_s and R_c, for the subcellular and cellular scales, respectively, and assume that a cell can interact with any neighbouring cell partially overlapped by a circular neighbourhood of these interaction radii (see Figure 2.3A). In particular, at the subcellular scale trans-binding between a Delta ligand on one cell and a Notch receptor on another cell can occur if the distance between their cell centres is less than the interaction radius, R_s. Thus, the total amount of ligand/receptor (belonging to a neighbour/neighbours) to which a cell is exposed is proportional to the surface area of the overlap region between the circular neighbourhood and the neighbouring voxel/voxels (not necessarily first neighbours). A similar modelling technique is employed at the cellular scale with the interaction radius,

R_c, which we use to account for cell-cell adhesion. These radii are not necessarily equal (although they are of the same order of magnitude) since different types of interactions are considered at each scale.

We perform our numerical simulations over time periods that are commensurate with the duration of *in vitro* experiments (hours) and for which proliferation is negligible [4], [9], [26]. For these reasons the model focuses only on the coordinated migration of ECs and assumes that proliferation occurs only at the vascular plexus [26], the initial vascular bed. This effect is implemented by introducing ECs into the domain at a specific set of boundary voxels, $\mathcal{I}_{VP}$ (see Figure 2.2A).

Since the experimental data we use for model calibration and validation were extracted from experiments carried out with constant VEGF concentration supplied externally, we assume that the distribution of VEGF is maintained at a (prescribed) constant value at all times.

Interested readers will find more detail on model formulation later in this section and in Appendix B.2.

We list the variables of our multi-scale model in Table 2.1.

2.3.2 Subcellular scale

At the subcellular scale we account for the VEGF-Delta-Notch signalling pathway which determines the gene expression pattern (phenotype) of each EC (see Figure 2.3C). This pathway mediates inter-cellular cross-talk and typically produces alternating patterns of tip and stalk cell phenotypes within growing sprouts [25]. In our model, the pathway is simulated via a *bistable* stochastic system which accounts for intrinsic noise and, in particular, noise-induced random transitions between the stable steady states of the system (phenotypes) [149]–[152]. We posit that such phenotypic switches are essential for understanding the complex dynamics of ECs within growing sprouts [4]. Our subcellular model is based on previous

	Variable	Description
Subcellular scale	$\boldsymbol{N} = (N_1, \dots, N_{N_I})$	The distribution of Notch receptor among voxels. If there is no cell nucleus in a voxel v_i, i.e. $E_i = 0$, then $N_i = 0$.
	$\boldsymbol{D} = (D_1, \dots, D_{N_I})$	The distribution of Delta ligand among voxels. If there is no cell nucleus in a voxel v_i, i.e. $E_i = 0$, then $D_i = 0$.
	$\boldsymbol{I} = (I_1, \dots, I_{N_I})$	The distribution of Notch intracellular domain (NICD) among voxels. If there is no cell nucleus in a voxel v_i, i.e. $E_i = 0$, then $I_i = 0$.
	$\boldsymbol{R2} = (R2_1, \dots, R2_{N_I})$	The distribution of VEGFR2 receptor among voxels. If there is no cell nucleus in a voxel v_i, i.e. $E_i = 0$, then $R2_i = 0$.
	$\boldsymbol{R2^*} = \left(R2_1^*, \dots, R2_{N_I}^* \right)$	The distribution of activated VEGFR2 receptor (VEGFR2 bound to extracellular VEGF) among voxels. If there is no cell nucleus in a voxel v_i, i.e. $E_i = 0$, then $R2_i^* = 0$.
Cellular scale	$\boldsymbol{E} = (E_1, \dots, E_{N_I})$	The distribution of EC nuclei among voxels. $E_i = 1$ if a cell nucleus is present in the voxel v_i, $E_i = 0$, otherwise. At most one cell nucleus is allowed per voxel.
	$\boldsymbol{E^N} = \left(E_1^N, \dots, E_{N_I}^N \right)$	The neighbourhood nucleus distribution. This variable is completely defined by the configuration of $\boldsymbol{E}$. Each $E_i^N = \frac{\sum_{j \neq i} \phi_{ij} E_j}{\sum_{j \neq i} \phi_{ij}}$, where $\phi_{ij} = \frac{|v_j \cap \mathcal{B}_{R_c}(i)|}{|v_j|}$, $\mathcal{B}_{R_c}(i)$ is a circular neighbourhood of interaction radius, R_c, centred in the voxel v_i, and $|\cdot|$ denotes area.
Tissue scale	$\boldsymbol{c} = (c_1, \dots, c_{N_I})$	The ECM density, consisting mostly of collagen I and elastin fibers. It is degraded by cells via a process termed *ECM proteolysis* (Figure 1.2 III.). We assume $0 \leq c_i \leq c_{max}$ for all $i \in \mathcal{I}$, where $c_{max} > 0$ is a parameter characterising the maximum density of the ECM.
	$\boldsymbol{m} = (m_1, \dots, m_{N_I})$	The concentration of basal lamina components (collagen IV, fibronectin and various laminins) newly deposited by cells that are used for *BM assembly* (Figure 1.2 IV.). We assume $0 \leq m_i \leq 1$ for all $i \in \mathcal{I}$; $m_i = 0$ if no BM components have been deposited yet, whereas $m_i = 1$ if a BM has been assembled around the sprout segment situated in voxel v_i.
	$\boldsymbol{l} = (l_1, \dots, l_{N_I})$	The orientation landscape (OL) variable representing the *alignment of ECM fibrils* (Figure 1.2 V.) within the voxel. For a hexagonal lattice $l_i = \{l_i^s\}_{s \in \mathcal{S}}$ for all possible jumping directions $s \in \mathcal{S} = \{r, ur, ul, l, dl, dr\}$ (r - right, ur - upward-right, ul - upward-left, l - left, dl - downward-left, dr - downward-right), $s \in \mathbb{R}^2$ (see Figure 2.2). An example of possible orientation landscape configurations is shown in Figure 2.5A.

Table 2.1. (Caption on the next page.)

Table 2.1. The description of the model variables. The variables in the table are organised by spatial scales. Subcellular variables, used to simulate the VEGF-Delta-Notch signalling pathway, define the gene expression pattern of individual cells (their phenotypes). Cellular scale variables define the occupancy of the lattice by ECs. Tissue scale variables define the composition and structure of the ECM. Bold letters denote vector variables specifying variable configuration for the whole lattice; normal font letters correspond to the variables associated with a particular voxel, the index of which is specified by a subscript.

work [153]–[156]. Following [155], [156], we combine the lateral inhibition model of the Delta-Notch signalling pathway introduced in [153], [154] with the VEGF signalling pathway. The Delta-Notch model accounts for cis-inhibition when a Delta ligand and Notch receptor from the same cell inhibit each others' activity. We include this interaction since cis-inhibition has been shown to substantially speed up phenotype specification [157].

Individual cell system

The kinetic reactions acting on individual cells system are illustrated in Figure 2.3D. We account for *trans*-activation of Notch receptor (production of an NICD) when it *trans*-binds to a Delta ligand belonging to a neighbouring cell, D_{ext} (reaction ①a). If a Delta ligand *trans*-binds to a Notch receptor on a neighbouring cell, N_{ext}, it is either endocytotically recycled or degraded (reaction ①b). In this reaction, we assume that the active Notch signal is produced in the neighbouring cell, the dynamics of which are irrelevant for the cell of interest. Once cleaved from the Notch receptor, active Notch signal, NICD, is translocated to the cell nucleus where it down-regulates gene expression of VEGFR2 (reaction ②) and up-regulates gene expression of the Notch receptor (reaction ③). *Cis*-inhibition is accounted for in reaction ④ in which mutual inhibition is assumed for a Delta ligand and a Notch receptor interacting within the same cell. External VEGF, V, can bind to and activate a VEGFR2 (reaction ⑤). This leads to up-regulation of Delta production (reaction ⑥). Reaction ⑦ corresponds to degradation of NICD.

An essential feature of our subcellular model is that it exhibits bistability. To demonstrate this, we derived the mean-field limit equations associated with the kinetic reactions shown

(A)

Interaction radius

(B)

R_s

$y \; (\mu m)$

$x \; (\mu m)$

Weights, α_{ij}

(C)

VEGF
binding
VEGFR2 VEGFR2*

cis-inhibition
∅ ← Delta

Notch

NICD
∅

Cell 1

trans-binding
①a ①b

VEGF
⑤ *binding*
VEGFR2* VEGFR2

Delta *cis-inhibition* ∅
④

Notch ③
⑥

②

NICD
∅ ⑦

Cell 2

(D)

①a $\; N + D_{ext} \rightleftarrows [ND_{ext}] \to I + D_{ext}$

①b $\; D + N_{ext} \rightleftarrows [DN_{ext}] \to D + N_{ext}$
$\qquad\qquad\qquad\qquad\qquad \searrow N_{ext}$

$\qquad H^S(I)$
② $\; \varnothing \quad \rightleftarrows \quad R2$

$\qquad H^S(I)$
③ $\; \varnothing \quad \rightleftarrows \quad N$

④ $\; N + D \rightleftarrows [ND] \to \varnothing$

⑤ $\; R2 + V \to R2^* \to \varnothing$

$\qquad H^S(R2^*)$
⑥ $\; \varnothing \quad \rightleftarrows \quad D$

⑦ $\; I \to \varnothing$

(E)

Tip   Tip, Stalk   Stalk

N

D_{ext}

(F)

Tip   Tip, Stalk   Stalk

V

D_{ext}

(G)

Stalk cell
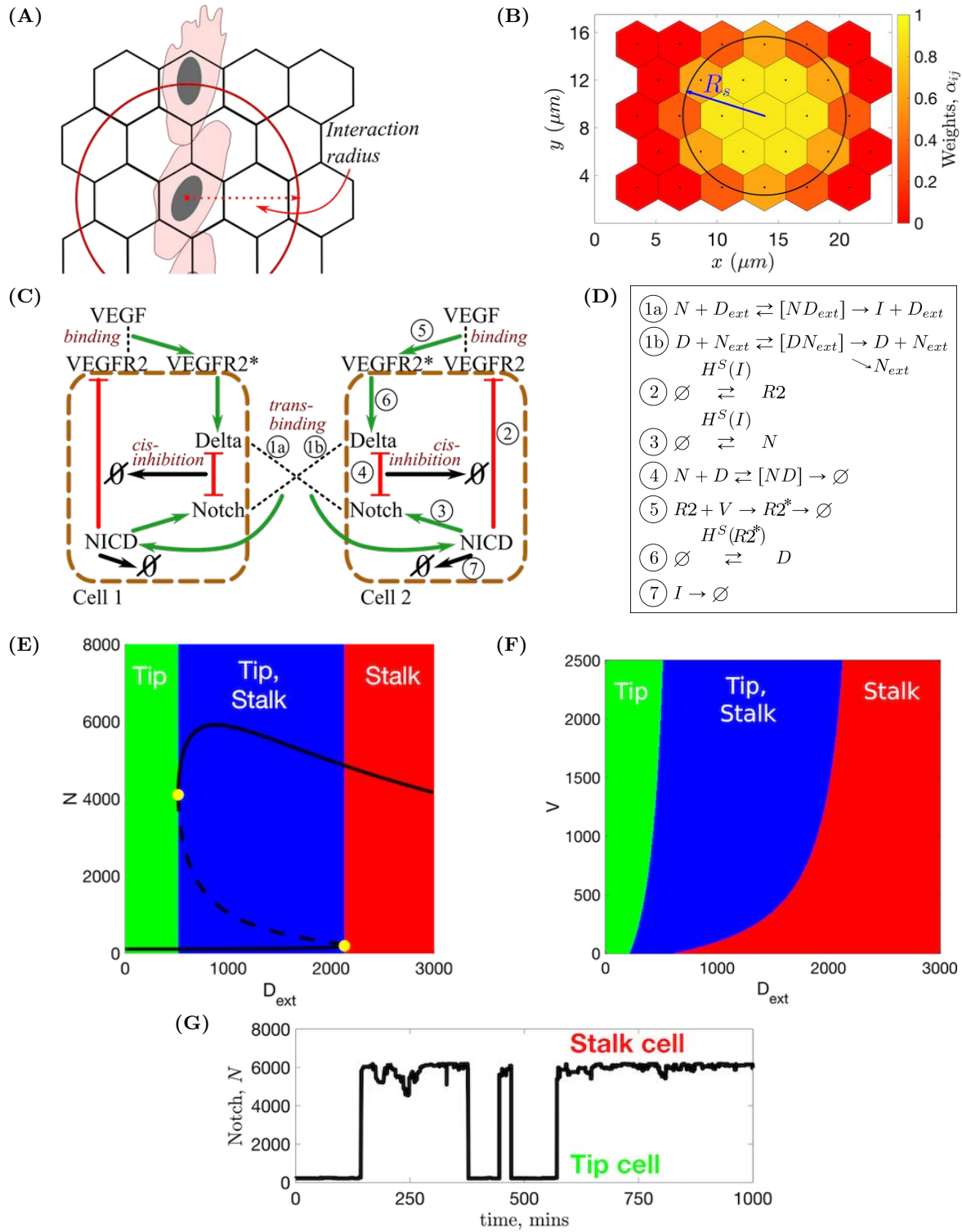
Notch, N

Tip cell

time, mins

Figure 2.3. (Caption on the next page.)

Figure 2.3. Illustrations for the subcellular scale of the model. **(A)** Since we track the position of cells only up to the positions of their nuclei, interactions are assumed to be non-local within some *interaction radius*. The subcellular and cellular scale interaction radii are denoted by R_s and R_c, respectively. **(B)** Illustration of values of the weight coefficients, α_{ij} (see Eq (B.6)). **(C)** Schematic illustration of the VEGF-Delta-Notch signalling pathway. NICD stands for Notch intracellular domain, VEGFR2 for VEGF Receptor 2 and VEGFR2* for activated, i.e. bound to VEGF, VEGFR2. In this case, the local environment of Cell 2 is Cell 1, and D_{ext} and N_{ext} correspond, respectively, to the Delta and Notch concentrations in Cell 1 (and vice versa). Circled numbers correspond to the kinetic reactions listed in **(D)**. **(D)** Kinetic reactions used for the VEGF-Delta-Notch pathway. See Table 2.1 for description of the model variables. $H^S(var)$ indicates that the transition rate of gene expression of a protein is transcriptionally regulated by the signalling variable, var. Here, $H^S(\cdot)$ is the shifted Hill function (see caption of Table 2.2). Simple arrows indicate reactions with constant rates. **(E)** Bifurcation diagram of Notch concentration, N, as a function of external Delta ligand, D_{ext}, corresponding to the system of equations Eq (2.1). Full lines denote stable steady states; dashed lines – unstable steady state; yellow filled dots – saddle-node bifurcation points. **(F)** Phenotype diagram as a function of external Delta, D_{ext}, and external VEGF, V, corresponding to the system of equations Eq (2.1). **(G)** In simulations, the local environment of a cell (Delta and Notch levels in a neighbourhood of the cell, D_{ext} and N_{ext} (Eq (2.6))), dynamically changes with time due to cell migration. This leads to phenotype switches.

in Figure 2.3D (see Eq (2.1) in Table 2.2) and performed a numerical bifurcation analysis (see Table B.7 for a list of the parameter values). The results presented in Figure 2.3E show how the steady state value of the Notch concentration, N, changes as the concentration of external Delta ligand, D_{ext}, varies. For small (large) values of D_{ext}, the system supports a unique steady-state corresponding to the tip (stalk) phenotype. For intermediate values of D_{ext}, the system is bistable: both phenotypes coexist. The combined effect of the external VEGF, V, and D_{ext} on the system is shown in Figure 2.3F. We see that varying V does not alter the qualitative behaviour shown in Figure 2.3E, although the size of the bistable region decreases as V decreases.

Individual cell system (2.1)

$$\frac{\mathrm{d}N}{\mathrm{d}t} = b_N H^S(I; I_0, \lambda_{I,N}, n_N) - \gamma N - k_t D_{ext} N - k_c ND,$$

$$\frac{\mathrm{d}D}{\mathrm{d}t} = b_D H^S(R2^*; R2_0^*, \lambda_{R2^*,D}, n_D) - \gamma D - \eta k_t N_{ext} D - k_c ND,$$

$$\frac{\mathrm{d}I}{\mathrm{d}t} = k_t D_{ext} N - \gamma_e I,$$

$$\frac{\mathrm{d}R2}{\mathrm{d}t} = b_{R2} H^S(I; I_0, \lambda_{I,R2}, n_{R2}) - \gamma R2 - k_v V R2,$$

$$\frac{\mathrm{d}R2^*}{\mathrm{d}t} = k_v V R2 - \gamma_e R2^*,$$

D_{ext}, N_{ext} are constant input parameters.

Multicellular system (2.2)

$$\frac{\mathrm{d}N_i}{\mathrm{d}t} = b_N H^S(I_i; I_0, \lambda_{I,N}, n_N) - \gamma N_i - k_t N_i \overline{D_i} - k_c N_i D_i,$$

$$\frac{\mathrm{d}D_i}{\mathrm{d}t} = b_D H^S(R2_i^*; R2_0^*, \lambda_{R2^*,D}, n_D) - \gamma D_i - \eta k_t D_i \overline{N_i} - k_c N_i D_i,$$

$$\frac{\mathrm{d}I_i}{\mathrm{d}t} = k_t N_i \overline{D_i} - \gamma_e I_i,$$

$$\frac{\mathrm{d}R2_i}{\mathrm{d}t} = b_{R2} H^S(I_i; I_0, \lambda_{I,R2}, n_{R2}) - \gamma R2_i - k_v R2_i V,$$

$$\frac{\mathrm{d}R2_i^*}{\mathrm{d}t} = k_v R2_i V - \gamma_e R2_i^*,$$

$D_{ext} = \overline{D_i}$, $N_{ext} = \overline{N_i}$ are given by Eq (2.6), $i \in \mathcal{I}$.

Table 2.2. Mean-field equations associated with the stochastic system of the VEGF-Delta-Notch signalling pathway for the individual cell system (left column) and the multicellular system (right column). Here $H^S(\cdot)$ is the so-called shifted Hill function [158]. Its functional form is given by
$H^S(X) = H^S\left(X; X_0, \lambda_{X,Y}, n_Y\right) = \frac{1 + \lambda_{X,Y}\left(X/X_0\right)^{n_Y}}{1 + \left(X/X_0\right)^{n_Y}}$, where X_0, $\lambda_{X,Y}$ and n_Y are positive
parameters (see Appendix B.2 for more details). Description and values of parameters can be found in Table B.7.

The stable states of the subcellular system are characterised by distinct gene expression patterns (for example, high (low) Delta level, D, corresponds to tip (stalk) phenotype). Thus, one variable suffices in order to effectively define the phenotypes. We use Delta level, D, as a proxy variable in the following way

$$
\begin{aligned}
\text{tip phenotype:} \quad & D \geq b_D, \\
\text{stalk phenotype:} \quad & \text{otherwise,}
\end{aligned}
\tag{2.3}
$$

where b_D is baseline gene expression of Delta ligand in ECs (see Table B.7).

Multicellular system

In order to account for cell-cell cross-talk via the VEGF-Delta-Notch pathway, we extend the individual cell system (see Figure 2.3D) to a multicellular environment by specifying for each cell the external (i.e. belonging to neighbouring cells) amount of Delta and Notch to which it is exposed. As mentioned above, since cell positions in our model are only known up to the position of their nuclei, we assume non-local interactions between cells within a reaction radius, R_s. Thus, we define the local environment of a cell whose nucleus is situated in voxel v_i as the set of voxels with a non-zero overlap region with a circular neighbourhood of radius R_s centred at voxel v_i, $\mathcal{B}_{R_s}(i)$,

$$
H(i) := \{v_j : v_j \cap \mathcal{B}_{R_s}(i) \neq \emptyset,\ j \neq i,\ j \in \mathcal{I}\}.
\tag{2.4}
$$

The weights, α_{ij}, assigned to each voxel $v_j \in H(i)$, (see Figure 2.3B) are defined as follows

$$
\alpha_{ij} = \frac{|v_j \cap \mathcal{B}_{R_s}(i)|}{|v_j|}, \quad i,\ j \in \mathcal{I},
\tag{2.5}
$$

where $|\cdot|$ denotes 2D area.

The external Delta (Notch) concentration, D_{ext} (N_{ext}), for a cell situated in a voxel v_i is

defined as follows:

$$
\begin{aligned}
D_{ext} = \overline{D_i} &= \frac{\displaystyle\sum_{v_j \ \in \ H(i)} \alpha_{ij} D_j}{\displaystyle\sum_{v_j \ \in \ H(i)} \alpha_{ij}}, \\[2em]
N_{ext} = \overline{N_i} &= \frac{\displaystyle\sum_{v_j \ \in \ H(i)} \alpha_{ij} N_j}{\displaystyle\sum_{v_j \ \in \ H(i)} \alpha_{ij}},
\end{aligned}
\tag{2.6}
$$

where D_j (N_j) denotes the Delta (Notch) concentration in voxel v_j.

Therefore, our multicellular stochastic system at the subcellular scale consists of the same kinetic reactions as in Figure 2.3D formulated for each voxel v_i, $i \in \mathcal{I}$ with D_{ext}, N_{ext} given by (2.6). It is important to note that, in simulations of angiogenic sprouting, the quantities D_{ext} and N_{ext} dynamically change due to cell migration, thus leading to phenotype re-establishment (see Figure 2.3G).

When simulated within a two-dimensional domain, our multicellular system produces an alternating pattern of tip/stalk phenotypes. As the reaction radius, R_s, changes the system dynamics do not change but the proportion of tip and stalk cells does. To illustrate this, we ran simulations of the stochastic multicellular system for a 10×12 regular monolayer of cells for different values of the interaction radius, R_s (see Figure B.15). These simulations revealed that the distance between tip cells increases (i.e. the proportion of tip cells decreases) as R_s increases. We also investigated how phenotype patterning changes within a monolayer as cis-inhibition intensity varies (see Appendix B.2). For low values of the cis-inhibition parameter, κ_c, typical chessboard tip-stalk pattern is produced; as κ_c increases, ECs with tip phenotype can become adjacent to each other, thus increasing the time to patterning, since the lateral inhibition is weakened (see Appendix B.2).

The mean-field equations associated with the multicellular stochastic system are given by

Eq (2.2) in Table 2.2.

More detail on the derivation and analysis of the subcellular model can be found in Appendix B.2.

2.3.3 Cellular scale

At the cellular scale we account for EC migration and overtaking. In more detail, we consider a compartment-based model of a persistent random walk (PRW) [159], in which transition rates depend on the phenotypic state of individual cells and their interactions with ECM components.

We denote by $s = h^{-1}(q_j - q_i) \in \mathcal{S}$ the migration direction, as a unit vector pointing from q_i towards q_j, the centres of neighbouring voxels v_i and v_j, respectively (see Figure 2.2B). In order to formulate the PRW of ECs, we introduce, $\omega(i \to j)$, to denote the probability that a cell moves from voxel v_i to a neighbouring voxel v_j (i.e. along the direction s) where

$$\omega(i \to j) = \underbrace{\widetilde{D_\omega}}_{\substack{\text{diffusion} \\ \text{coeffi-} \\ \text{cient}}} E_i \underbrace{S(c_i)}_{} \overbrace{F(E_i^N)}^{\substack{\text{cell-cell} \\ \text{adhesion}}} \underbrace{\rho_{ij}(D_i)}_{\substack{\text{overtaking} \\ \text{probability}}} \overbrace{\left[\int_0^{2\pi} W^s(\phi) f_{vM}(\phi|\mu,\kappa) \mathrm{d}\phi \right]}^{\text{cell polarity}}. \tag{2.7}$$

where the braces label: "cell occupancy" over E_i, "cell-cell adhesion" over $F(E_i^N)$, "cell polarity" over the integral, "diffusion coefficient" under $\widetilde{D_\omega}$, "ECM density" under $S(c_i)$, "overtaking probability" under $\rho_{ij}(D_i)$.

We explain below each of the terms that appears in Eq (2.7) (see also Figure 2.4 for a graphical illustration and Table 2.1 for a description of the model variables).

Diffusion coefficient. Transition rates in the framework of a PRW must be appropriately scaled with the size of a voxel (depending on the particular lattice used to discretise the domain). For a uniform hexagonal lattice, $\mathcal{L}$, the diffusion coefficient of the transition $\omega(i \to j)$ is scaled as $\widetilde{D_\omega} = D_\omega / h^2$ [160]. Here $h\,[\mu m]$ is the width of a hexagonal voxel (see Figure 2.2) and $D_\omega \left[\frac{\mu m^2}{min} \right]$ is the macroscale diffusion coefficient for the ECs.
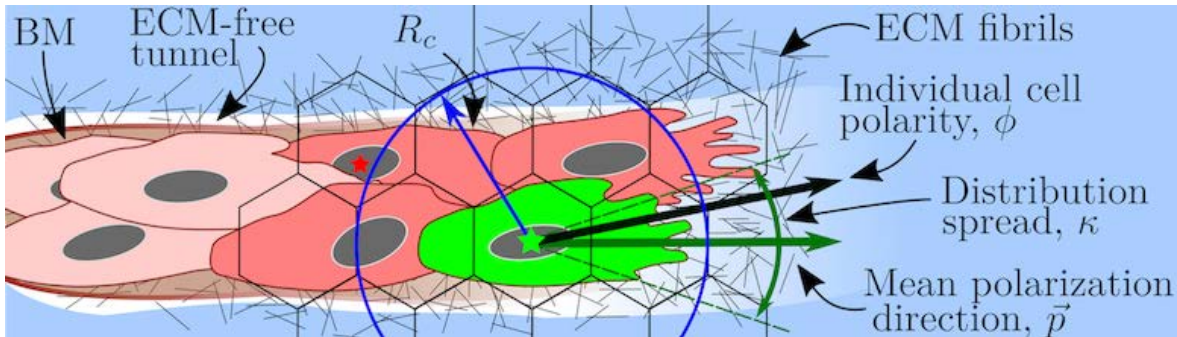
Figure 2.4. A cartoon illustrating cell migration. Migration transition rate
(Eq (2.7)) is illustrated for a cell coloured in green. Its nucleus is marked with a green star.
The motility of this cell depends on the ECM density, c_i, in the voxel where its nucleus is
situated (accounted for by the $S(\cdot)$ function (Eq (2.8))). The green cell forms cell-cell
adhesions with other cells coloured in red. In this work, we assume a circular neighbourhood
for cell-cell interactions within the so-called *interaction radius*, R_c, for the cellular scale
(here it is drawn to have the same value as in our simulations, $R_c = 1.5h$, where h is the
voxel width). This allows cells to interact beyond their immediate neighbours as, for
example, the cell with the nucleus marked by a red star and the focal green cell. Other
geometries (e.g. elliptical neighbourhood aligned with cell polarity vector) are unlikely to
alter the model behaviour significantly since, in sprouting structures, lateral regions of the
circular neighbourhood, which would be ignored by an elliptic neighbourhood, are typically
empty. Cell-cell adhesion is accounted for by the *neighbourhood function*, $F(\cdot)$, Eq (2.9).
The *individual cell polarity*, ϕ, is sampled from the von Mises distribution (Eq (2.12)) with
the mean value given by the *mean polarization direction*, $\vec{p}$ (calculated as a function of local
ECM fibril alignment, l_i, Eq (2.13)). The *distribution spread*, κ, is assumed to depend on
the focal cell phenotype and the concentration of the BM components, Eq (2.14).

Cell occupancy. If a cell nucleus is present in voxel v_i, then $E_i = 1$ (at most one cell
nucleus is allowed per voxel). If the voxel v_i is empty, then $E_i = 0$ and $\omega(i \to j) = 0$.

ECM density. The function $S(c_i)$ accounts for the effect of the local ECM density, c_i, on
cell motility. In general, $S(\cdot)$ is a decreasing function of its argument. We assume further
that ECs cannot move if the ECM concentration exceeds a threshold value, c_{max} ($S(c_i) = 0$
for $c_i \geq c_{max}$). In our simulations we fix

$$S(c_i) = \begin{cases} 1 - \dfrac{c_i}{c_{max}} & \text{if } 0 \le c_i < c_{max} \\[2mm] 0, & \text{otherwise.} \end{cases} \tag{2.8}$$

Cell-cell adhesion. The effect of cell-cell adhesion on cell migration is incorporated via the so-called *neighbourhood function*, $F(E_i^N)$. Its argument, E_i^N, represents the number of ECs in a cell's local neighbourhood (red-coloured cells in Figure 2.4). The functional form of the neighbourhood function was chosen in order to phenomenologically capture the way in which EC behaviour depends on the cell-cell contacts (see Figure 2.5E). In biological experiments, it was shown that when a cell loses contact with its neighbours (laser ablation experiments in [10]) it halts until the following cells reach it. This is captured by the increasing part of $F(E_i^N)$; when the number of neighbours around a cell is below the first threshold, E_{F1}, the probability of cell movement decreases rapidly to zero, thus the migration transition (Eq (2.7)) goes to 0 as well. Similarly, when there are many ECs in a cell's neighbourhood, its movement slows down. This is accounted for by the decreasing part of $F(E_i^N)$ when the number of neighbouring cells exceeds the second threshold value, E_{F2}, cell movement is slowed down and eventually halts in regions of high cell density.

$$F\left(E_i^N\right) = \left(\frac{1}{1 + \exp\left(-s_{F1}(E_i^N - E_{F1})\right)} + \frac{1}{1 + \exp\left(s_{F2}(E_i^N - E_{F2})\right)} - 1 \right)^+, \tag{2.9}$$

where $(x)^+ = max(0, x)$, and the parameters E_{F1}, E_{F2}, s_{F1} and s_{F2} characterise the shape of the curve.

Overtaking probability. This term accounts for cell overtaking and excluded volumes. A jump occurs with overtaking probability, $\rho_{ij}(D_i) = 1$, if the target voxel, v_j, is empty ($E_j = 0$). Otherwise, the cells in voxels v_i and v_j switch their positions with probability $\rho_{ij}(D_i) = p_{switch}(D_i)$. We consider this probability to be phenotype-dependent. In particular,
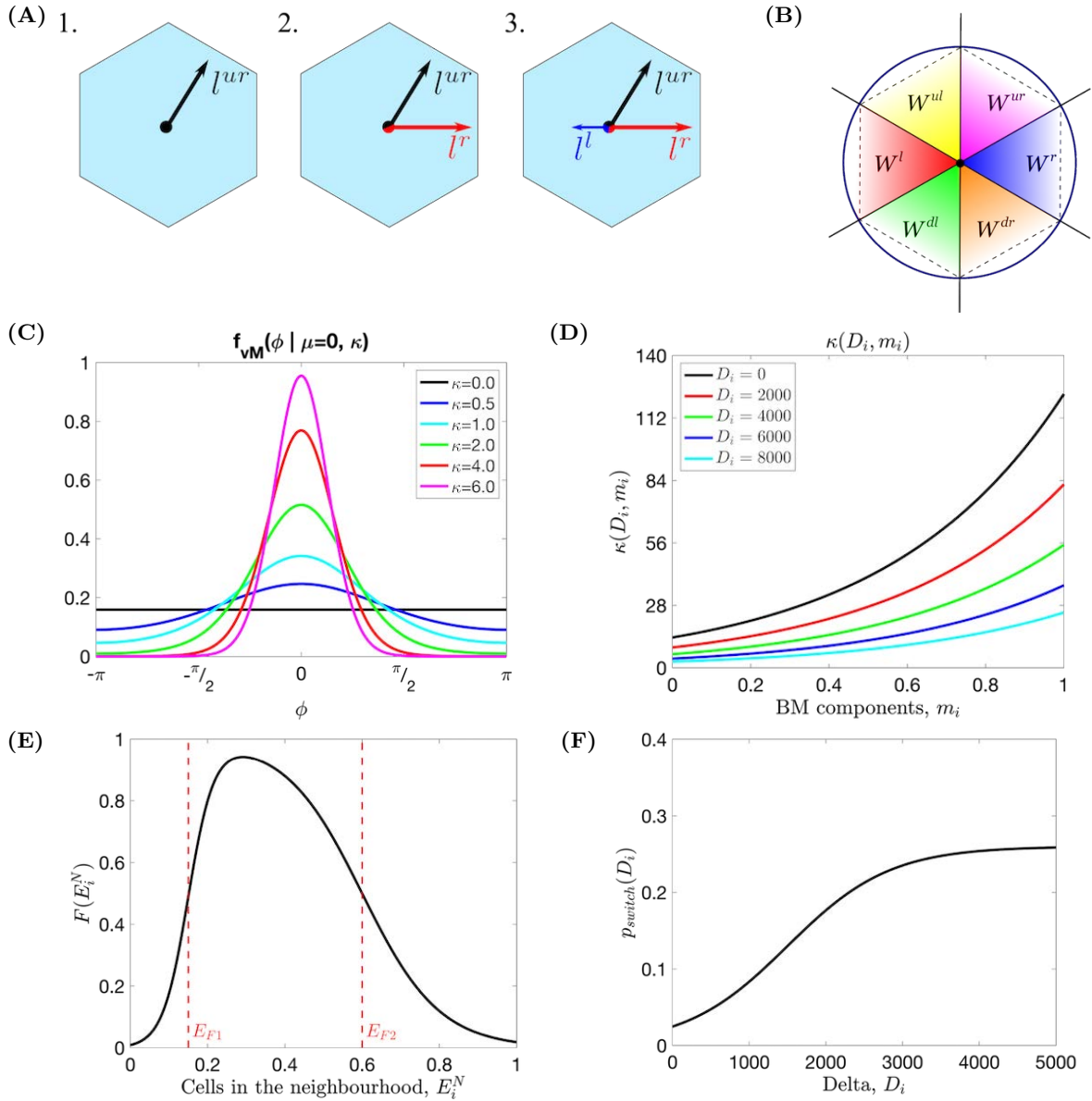
Figure 2.5. (Caption on the next page.)

Figure 2.5. Series of sketches illustrating the components of the cellular scale persistent random walk. (A) An example of the orientation landscape, l, configurations for a hexagonal lattice. **1.** All fibrils are aligned in the upward-right direction; this would be an example of a strongly aligned part of the ECM. **2.** Half of the fibrils are aligned to the right, half in the upward-right direction. This would correspond to a branching point. **3.** As in **2.** but with some additional fibrils aligned in the left direction. **(B)** The window function, $W^s(\phi)$, (Eq (2.15)) has been defined as an indicator function over an angle interval corresponding to each possible migration direction $s \in \mathcal{S}$ (lattice-dependent). The diagram illustrates these intervals for a hexagonal lattice. **(C)** Illustration of the probability distribution function of the von Mises distribution, $f_{vM}(x|\mu, \kappa)$, centred at $\mu = 0$ for different fixed κ (Eq (2.12)). **(D)** Illustration of the κ function as a function of local Delta ligand level, D_i, and concentration of BM components, m_i, (Eq (2.14) with $K = 13.6$, $k_m = 2.2$ and $k_D = 0.0002$) . **(E)** An example of the neighbourhood function, $F(E_i^N)$ (Eq (2.9), with $E_{F1} = 0.15$, $E_{F2} = 0.6$, $s_{F1} = 30$, $s_{F2} = 10$). **(F)** A sketch showing how the switching probability, $p_{switch}(D_i)$, changes with the level of Delta in voxel v_i, D_i (Eq (2.10) with $p_{max} = 0.26$, $s_p = 0.0015$, $D_p=1500$).

we assume that tip cells (see Eq (2.3)) are more motile because their filopodia are stronger (see Figure 1.2 II.). Thus, the switching probability, $p_{switch}(D_i)$, is assumed to be an increasing function of the Delta level, D_i, of the migrating cell

$$\rho_{ij}(D_i) = \begin{cases} 1, & \text{if } E_j = 0, \\ p_{switch}(D_i), & \text{otherwise.} \end{cases} \tag{2.10}$$

where

$$p_{switch}(D_i) = \frac{p_{max}}{1 + \exp(-s_p(D_i - D_p))}, \tag{2.11}$$

the parameters s_p and D_p characterise, respectively, the slope and position of the sigmoid, and p_{max} denotes its maximum value (see Figure 2.5F).

Cell polarity. Prior to migration, cells develop a polarity which depends on their local environment. Following [161], [162], we consider the local cell polarity, ϕ, (see Figure 2.4) to be a random quantity sampled from the von Mises distribution. The probability density function (pdf) of the von Mises distribution reads

$$f_{vM}(\phi|\mu,\kappa) = \frac{\exp\left(\kappa\cos(\phi-\mu)\right)}{2\pi I_0(\kappa)}. \tag{2.12}$$

Its shape is characterised by two parameters: the mean value, μ, and the distribution spread, κ (see Figure 2.5C for a sketch of this pdf for different values of κ). I_0 is the modified Bessel function of the first kind of order 0.

In the context of EC migration, we view μ as the *mean polarisation angle*, and κ as *cell exploratoriness*. We integrate ECM structure and composition and cell phenotype into our cell migration model by assuming that μ and κ depend on these quantities. In particular, we assume that the mean polarisation angle, μ, depends on the ECM fibril alignment which is represented in our model by the orientation landscape variable, l_i (see Table 2.1). From a biological point of view, this is substantiated by experimental observations of cells forming focal adhesions with ECM fibrils and, consequently, aligning along them [148]. We introduce the *mean polarisation direction* vector, $\vec{p} \in \mathbb{R}^2$, and compute μ as its principle argument (see Figure 2.4)

$$\vec{p} = \left(\sum_{dir \in \mathcal{S}} H_{a,n}(l_i^{dir})dir_x, \sum_{dir \in \mathcal{S}} H_{a,n}(l_i^{dir})dir_y\right)^T,$$
$$\mu = Arg(\vec{p}). \tag{2.13}$$

In Eq (2.13) the summation is taken over all possible directions for movement, $dir = (dir_x, dir_y)^T \in \mathcal{S}$ (in a hexagonal lattice there are at most 6 possible directions, see Figure 2.5A). The Hill function, $H_{a,n}(\cdot)$, is used to reflect the natural saturation limit to alignment and deformation of the ECM fibrils, with a and n being fixed positive parameters. Details about how fibril orientation (orientation landscape, l_i) is calculated are given below.

Cell exploratoriness, $\kappa \geq 0$, is directly related to the EC phenotype (see Figure 1.2 I.). If $\kappa \approx 0$, then the effect of polarity on migration is weak, and cells can *explore* many directions

(this behaviour is typical of exploratory tip cells, see Eq (2.3)). By contrast, when $\kappa \gg 1$, the von Mises pdf is concentrated around μ (this behaviour is characteristic of stalk cells, see Eq (2.3)). To account for such phenotype-dependent behaviour, we assume κ to be a monotonic decreasing function of D_i, the Delta level of the migrating cell. Similarly, increased concentration of the BM components deposited by ECs (see Figure 1.2 IV.) reduces the exploratory capability of both tip and stalk cells. We therefore propose κ to be an increasing function of the local concentration of the BM components, m_i. Combining these effects, we arrive at the following functional form for $\kappa = \kappa(D_i, m_i)$:

$$\kappa = \kappa(D_i, m_i) = K \exp(k_m m_i - k_D D_i). \tag{2.14}$$

Here K, k_m, k_D are positive parameters (see Figure 2.5D for a sketch of $\kappa(D_i, m_i)$).

Since our model of cell migration is formulated on a lattice, transition rates of type $\omega(i \to j)$ (jumps from v_i into v_j, in the direction $s \in \mathcal{S}$) are associated with an angle interval $[\phi^s_{min}, \phi^s_{max}]$ (see Figure 2.2B). This corresponds to the angle between the vectors connecting the centre of the voxel v_i with the endpoints of the voxel edge shared by v_i and v_j. For example, in a hexagonal lattice, the right direction, $r \in \mathcal{S}$, is associated with an interval $[\phi^r_{min}, \phi^r_{max}] = [-\pi/6, \pi/6]$. Therefore, we restrict the von Mises pdf, $f_{vM}(\cdot)$, in Eq (2.7) to this interval by multiplying it by a corresponding indicator function, $W^s(\phi)$,

$$W^s(\phi) = \begin{cases} 1, & \text{if } \phi + 2\pi k \in [\phi^s_{min}, \phi^s_{max}], \quad k \in \mathbb{Z}, \\ 0, & \text{otherwise.} \end{cases} \tag{2.15}$$

This function is 2π-periodic due to the fact that its argument is an angle. We refer to $W^s(\phi)$ as the *window function* (see Figure 2.5B).

2.3.4 Tissue scale

We account for the alignment of ECM fibrils, l, density of the ECM, c, and concentration of the basal lamina components, m, (see Table 2.1) in the following way.

Local alignment of the ECM fibrils, l, serves as a scaffold for the orientated migration of ECs [148]. Thus, we refer to l as the *orientation landscape*. Traction forces exerted by migrating ECs realign the ECM fibrils, so that they move closer to the growing sprouts. Furthermore, since tip cells have more filopodia than stalk cells, they exert a greater influence on the orientation landscape [34] (see Figure 1.2 V.). We account for phenotype-dependent ECM realignment by assuming active stretching and accumulation of the fibrils upon cell movement between the voxels $i \rightarrow j$ (in the direction $s \in \mathcal{S}$), i.e. when a transition of type $\omega(i \rightarrow j)$ occurs,

$$
\begin{aligned}
l_i^s &= l_i^s + \Delta_l D_i, \\
l_j^s &= l_j^s + \Delta_l D_i.
\end{aligned}
\tag{2.16}
$$

Here, the parameter $\Delta_l > 0$, which quantifies the linear response of ECM fibrils to cell migration, depends on the substrate stiffness.

Besides active stretching induced by cell locomotion, we also consider passive relaxation of the orientation landscape. We assume that relaxation follows a simple elastic model so that the orientation landscape decays exponentially at a constant rate, η_l,

$$
l_i^s(t + \tau) = l_i^s(t) \exp(-\eta_l \tau),
\tag{2.17}
$$

where τ is the waiting time of the occurred migration transition and the update is done for all voxels $i \in \mathcal{I}$ and all directions $s \in \mathcal{S}$.

The time evolution of the ECM density, c, and BM components, m, is modelled via local ODEs. We assume phenotype-dependent ECM proteolysis induced by ECs (see Figure 1.2

III.). Since tip cells exhibit higher proteolytic activity than stalk cells [163], [164], we assume that the ECM at voxel v_i is degraded at rate $\eta_c(D_i)$, which is an increasing function of its argument

$$\frac{\mathrm{d}c_i}{\mathrm{d}t} = \begin{cases} -\eta_c\left(D_i\right), & \text{if } c_i > 0, \\ 0, & \text{otherwise;} \end{cases} \tag{2.18}$$

$$\eta_c(D_i) = \frac{\eta_{max}}{1 + \exp\left(-s_c(D_i - D_c)\right)}. \tag{2.19}$$

Here, in order to account for the natural saturation in EC proteolytic ability, we assume a sigmoidal functional form for $\eta_c(D_i)$ with positive parameters D_c and s_c (which correspond to the threshold level of Delta for initiation of ECM proteolysis and sharpness of EC response, respectively) and maximum value η_{max}.

Similarly, BM assembly (i.e. deposition of basal lamina components), is assumed to be phenotype-dependent (see Figure 1.2 IV.). Tip cells are known to secrete BM components and to recruit and activate pericytes which secrete basal lamina components around the sprout [163], [164]. Thus we assume that the rate of secretion of BM components, $\gamma_m(D_i)$, is an increasing function of D_i

$$\frac{\mathrm{d}m_i}{\mathrm{d}t} = \begin{cases} \gamma_m(D_i), & \text{if } m_i < 1.0, \\ 0, & \text{otherwise.} \end{cases} \tag{2.20}$$

$$\gamma_m(D_i) = \frac{\gamma_{max}}{1 + \exp\left(-s_m(D_i - D_m)\right)}, \tag{2.21}$$

where, again, a sigmoidal functional form is assumed for $\gamma_m(D_i)$ with positive parameters D_m and s_m (which correspond to the threshold level of Delta for initiation of BM assembly and sharpness of EC response, respectively) and maximum value γ_{max}. Here we assume the

decay of BM components is negligible on the timescale of our simulations.

2.3.5 Multiscale simulation algorithm

Here we provide a brief summary of the algorithm for simulating our multiscale model. A pseudocode of this algorithm is given in Appendix B.3.

After initialisation, initial phenotypes are prescribed by using the multicellular system of the subcellular kinetic reactions of the VEGF-Delta-Notch pathway for each present cell via the Next Subvolume (NSV) method [64] for some fixed final time. This distribution of phenotypes serves as an input to the cellular scale where migration transition rates, $\omega(i \to j)$ (see Eq (2.7)), are calculated. The waiting time for each transition to occur is generated from a Poisson distribution with the intensity given by the corresponding transition rate, and the transition with the smallest waiting time fires, i.e. a cell migration event takes place. The simulation time is incremented by the time step of the fired transition. This is one iteration of the NSV method for the cellular scale. Since cell movement affects the orientation of the ECM fibrils, the orientation landscape variable, $\boldsymbol{l}$, is updated (see Eq (2.16)). To finish the iteration step, fibril relaxation takes place (see Eq (2.17)), and ECM and BM component concentrations, $\boldsymbol{c}$ and $\boldsymbol{m}$, respectively, are updated for the whole domain for the time step of the fired migration transition (see Eq (2.18) and Eq (2.20), respectively). The cell migration event changes the local neighbourhood of some cells. Consequently, re-establishment of cell phenotypes is simulated at the subcellular scale, starting a new iteration of the simulation algorithm. The final time for the simulation of the subcellular scale at each iteration is taken as the waiting time of the last fired transition at the cellular scale (except for the initial phenotype prescription). The algorithm is run until the final simulation time, T_{max}, is reached at the cellular scale (specified for each numerical experiment). The details of the correspondence between real and simulation times are given in Appendix B.1.

2.4 Description of quantitative metrics

In order to calibrate and compare our simulation results to experimental data (see [4], [10]), we computed a number of metrics defined below.

Displacement The displacement statistic is associated with the average distance travelled by a cell in 15 minutes [10].

Orientation The orientation statistic measures the average persistence of cells as they move. It is computed as the average (over ECs in all performed realisations) quantity of ratios of the length of a smoothed trajectory to the actual trajectory travelled by a single cell during simulation [4].

Directionality This metric measures the average proportions of cells moving in the direction of sprout elongation (anterograde), cells moving in the direction opposite to sprout elongation (retrograde), and cells that do not move during 20 minutes (still) [4].

Tip cell proportion This metric is computed as the ratio of cells characterised by tip phenotype (see Eq (2.3)) to the total number of cells in the system at a given time point.

Mixing measure This metric is motivated by the experimental observation that the trajectories of individual ECs, which initially form clusters with their immediate neighbours (see Figure 2.6 for an illustration), at later times diverge so that cells can find themselves at distant regions of the angiogenic vascular network [4], [10]. This metric is introduced to quantify the cell rearrangements. Cell rearrangements are a key driver of sprout elongation during the early stages of vasculature formation and, as such, are directly related to network growth patterns. Later in this work, we will show how the mixing measure varies for different patterns of vascular network formation.
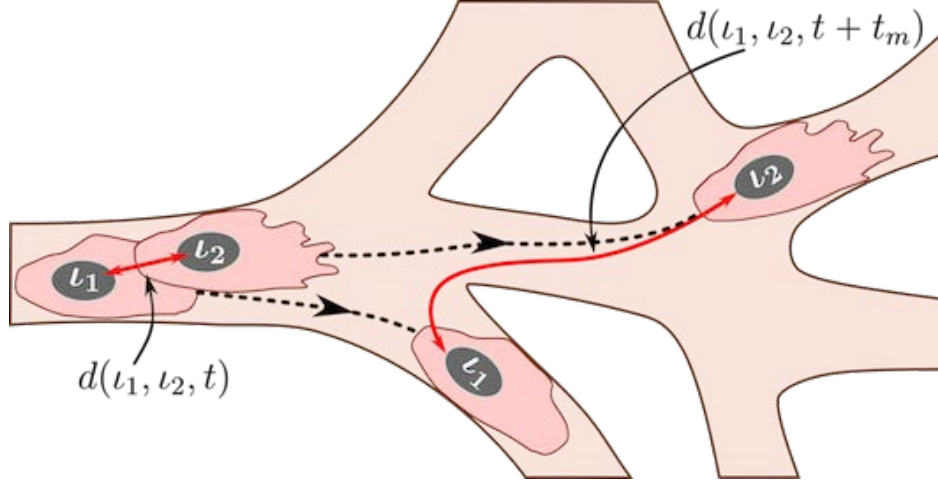
Figure 2.6. An illustration of the mixing measure. Two cells, labelled by ι_1 and ι_2, are located at the positions corresponding to the set $\mathcal{I}_{cluster}$ at time t. We track their trajectories in the simulated vascular network (dashed black lines) during time t_m. The mixing measure is defined as the difference between the distances between these cells at times t and $t + t_m$, $d(\iota_1, \iota_2, t)$ and $d(\iota_1, \iota_2, t + t_m)$, respectively, normalised by the number of cells considered and the maximum distance it is possible to travel in the simulated network. The distance function is defined as a distance within the simulated network (see Appendix B.5 for details).

Briefly, during simulations, we assign a label to each EC, ι, and record its position in the system at time t, $p(\iota, t) \in \mathcal{I}$. We specify a set of voxels that form a cluster of nearest neighbours in the lattice, $\mathcal{I}_{cluster}$. At the end of the simulation, using recorded cell trajectories, we compute how far away (in a pair-wise fashion) cells that were situated at the voxels in $\mathcal{I}_{cluster}$ at time t have moved away from each other during time interval of duration t_m. Normalising this quantity by the cardinal of $\mathcal{I}_{cluster}$, $|\mathcal{I}_{cluster}|$, and the maximum possible travel distance in the system, d_{max}, we obtain the *mixing measure* at time t, $\mathcal{M}(t)$, defined as

$$\mathcal{M}(t) = \frac{1}{|\mathcal{I}_{cluster}| \, d_{max}} \sum_{\substack{\iota_1, \, \iota_2 \text{ such that} \\ p(\iota_1, t)=i, \, p(\iota_2, t)=j \\ i,j \in \mathcal{I}_{cluster}, \, i \neq j}} \Big(d(\iota_1, \iota_2, t + t_m) - d(\iota_1, \iota_2, t) \Big). \tag{2.22}$$

Here $d(\iota_1, \iota_2, t)$ is the distance between cells with labels, ι_1 and ι_2, at time t. It is computed as a distance in a manifold of the simulated vascular network (see Figure 2.6). This is due

to the fact that ECs do not migrate randomly but rather within ECM-free vascular guidance tunnels of the generated vascular network.

The distance, d_{max}, in Eq (2.22), is the maximum distance in the simulated vascular network, defined as follows

$$d_{max} = \max_{\iota_1, \, \iota_2} d(\iota_1, \iota_2, T_{max}), \tag{2.23}$$

where T_{max} is the final simulation time.

Detailed descriptions of all the metrics and computational algorithms that we used are given in Appendix B.5.

2.5   Results

2.5.1   Emergent qualitative features: branching and VEGF sensitivity

Our model exhibits two characteristic features of functional angiogenic structures, namely, branching and chemotactic behaviour. A novel aspect of our multiscale model is that these features are emergent properties of its dynamics rather than being hardwired into the model.

Specifically, branching is a direct consequence of the phenotype-dependent polarity of individual cells. When a stalk cell within a sprout undergoes a phenotype switch and assumes a tip identity, its exploratoriness, increases (i.e. κ, decreases). This enables the cell to develop a polarity angle that departs from the mean elongation direction of the sprout, μ. As a consequence, a new branch forms. In our model, new branches are typically initiated by cells exhibiting the tip cell phenotype (see Movie 2.1). This behaviour is characteristic of ECs observed in biological experiments [9], [11]. Figures 2.7 and 2.8 illustrate the branching phenomenon and stabilisation of the network structure (due to accumulation of BM components deposited by ECs) in single realisations of numerical simulations of the model for uniform VEGF distribution at concentrations of 5 and 50 ng/ml (see also Movies 2.1 and 2.4).
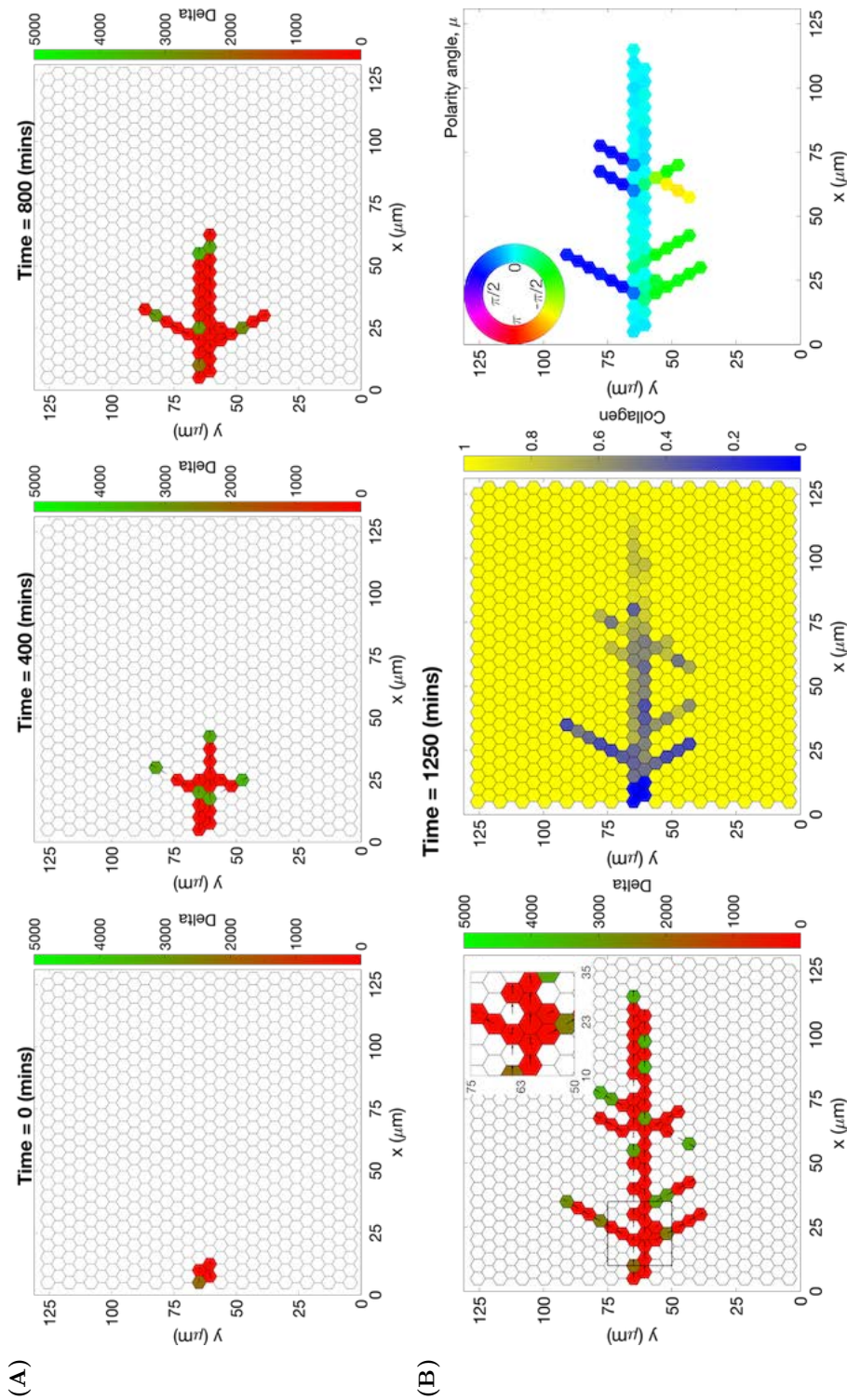
Figure 2.7. An example of an individual vascular network generated during simulation of our model with uniform VEGF = 5 ng/ml. (A) Temporal evolution of a simulated vascular network captured at 0 mins, 400 mins and 800 mins in an individual realisation of our model for uniform VEGF = 5 ng/ml. The colour bar indicates level of Delta, D, (green colour corresponds to tip cells, red – to stalk cells). Arrows indicate the configuration of the orientation landscape, l. **(B)** The final configuration of the simulated vascular network at 1250 mins (corresponds to the final simulation time, $t = T_{max} = 2.5$). The leftmost panel shows the concentration of Delta, D. Higher concentration (green colour) corresponds to tip cell phenotype, low concentration (red colour) – to stalk. On this plot, arrows correspond to the orientation landscape configuration, l. The central panel shows the final concentration of the ECM, c. The rightmost panel shows the final distribution of the polarity angle, μ, variable. Numerical simulation was performed using **Setup 1** from Table B.10. Parameter values are listed in Tables B.7 and B.8 for subcellular and cellular/tissue scales, respectively. For a movie of the numerical simulation, see Movie 2.4, left panel.
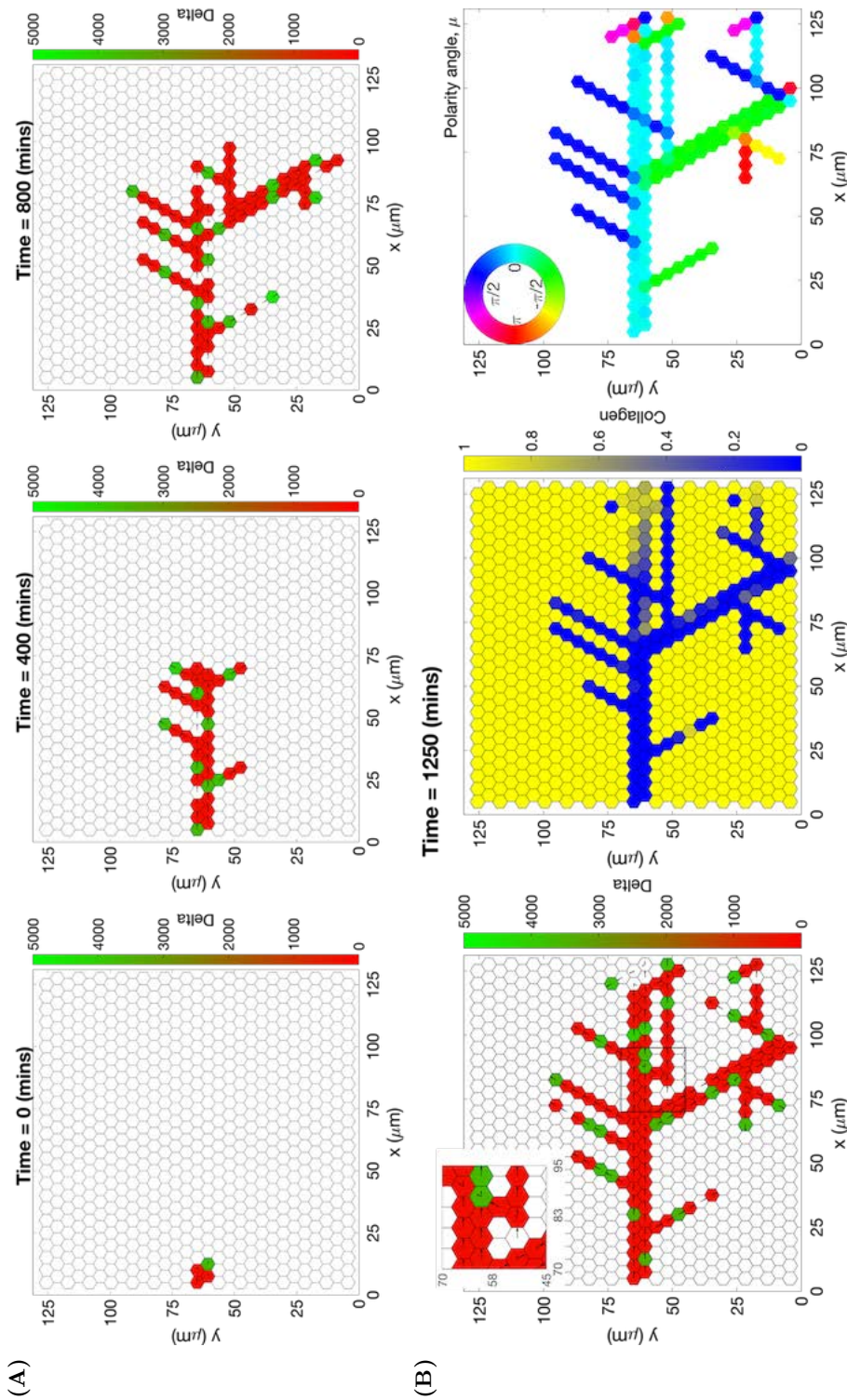
Figure 2.8. An example of an individual vascular network generated during simulation of our model with uniform VEGF = 50 ng/ml. (A) Temporal evolution of a simulated vascular network captured at 0 mins, 400 mins and 800 mins in an individual realisation of our model for uniform VEGF = 50 ng/ml. The colour bar indicates level of Delta, D, (green colour corresponds to tip cells, red − to stalk cells). Arrows indicate the configuration of the orientation landscape, l. **(B)** The final configuration of the simulated vascular network at 1250 mins (corresponds to the final simulation time, $t = T_{max} = 2.5$). The leftmost panel shows the concentration of Delta, D. Higher concentration (green colour) corresponds to tip cell phenotype, low concentration (red colour) − to stalk. On this plot, arrows correspond to the orientation landscape configuration, l. The central panel shows the final concentration of the ECM, c. The rightmost panel shows the final distribution of the polarity angle, μ, variable. Numerical simulation was performed using **Setup 1** from Table B.10. Parameter values are listed in Tables B.7 and B.8 for subcellular and cellular/tissue scales, respectively. For a movie of the numerical simulation, see Movie 2.1.

Note that in all our simulations "gaps" within sprouts can arise since we track the positions of cell nuclei and do not account for their true spatial extent.

Chemotactic sensitivity in our model is a direct consequence of cell interactions with the ECM. In biological experiments, proteolytic activity of cells was observed to increase as expression levels of Delta rise [163], [164]. In our model, increased levels of extracellular VEGF, V, up-regulate subcellular levels of Delta. As a result, an EC's ability to degrade the ECM and invade it at a faster rate is enhanced where VEGF levels are high. This can be seen by comparing networks generated at different uniform VEGF concentrations (see Figures 2.7 and 2.8). The network generated at VEGF=5 ng/ml is small (Figure 2.7B, leftmost plot), and the vascular guidance tunnels created via proteolysis (Figure 2.7B, middle plot) are not fully formed. By contrast, the simulated network for VEGF=50 ng/ml (Figure 2.8B, leftmost plot) has a greater spatial extent, since collagen-free vascular tunnels (Figure 2.8B, middle plot) facilitate cell migration within them, increasing sprouting and cell persistence (see *ECM density* term in Eq (2.7)).

Our model also exhibits the *brush-border* phenomenon [25], [87]. We performed a numerical simulation experiment of sprouting initialised from an initial vessel placed in a matrix with linearly increasing VEGF gradient. Figure 2.9 shows the evolution of the network at different times. The brush-border effect is evident at later times and characterised by increased cell numbers and branches in the top regions of the domain where VEGF levels are high.

2.5.2 Model calibration

Having established that our model exhibits the essential features of branching and chemotactic behaviour observed in experiments, we next compared our simulations with experimental results from [4], [10], [126]. This enabled us to estimate baseline parameter values for processes at the cellular and tissue scales (estimated values of parameters associated with processes acting at the subcellular scale are taken from previous works, see Table B.7).
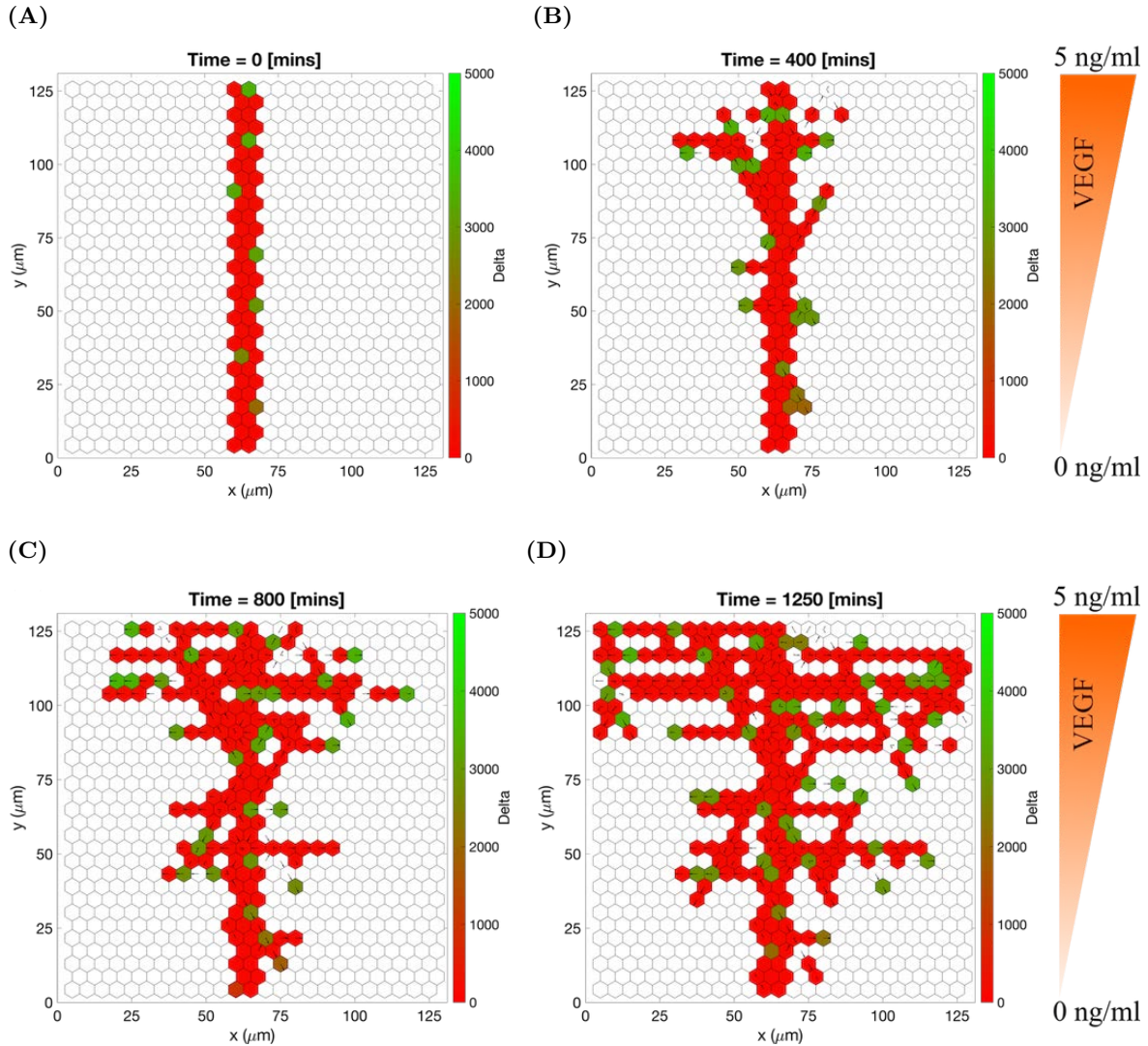
Figure 2.9. Sprouting in static VEGF gradient. Snapshots at different times of a vascular network growing in linear VEGF gradient increasing from VEGF = 0 ng/ml to VEGF = 5 ng/ml. **(A)** Time = 0 mins, initial setup. **(B)** Time = 400 mins, new branches appear from the initial sprout mostly in the upper half of the domain (higher VEGF concentrations). ECs with lower positions have lower Delta level. **(C)** Time = 800 mins, the effect of the VEGF gradient can be seen clearly. **(D)** Time = 1250 mins, the final configuration of the simulated V-shaped (opening towards higher VEGF concentrations) network. Colour bar shows the level of Delta, $\boldsymbol{D}$. Numerical simulation was performed using **Setup 2** from Table B.10 with final simulation time, $T_{max} = 2.5$. Parameter values are listed in Tables B.7 and B.8 for subcellular and cellular/tissue scales, respectively.

We ran 100 model simulations for uniform VEGF concentrations of 0, 5 and 50 ng/ml (**Setup 1**, see Table B.10, with final simulation time, $T_{max} = 2.5$, equivalent to 1250 mins, i.e. ≈ 20.8 h) and computed three metrics, namely, *displacement*, *orientation* and *directionality* (see section 2.4 for definitions) as was done in [4], [10]. The results presented in Figure 2.10 show that our simulations reproduce general trends of angiogenic sprouting reported in [4], [10]. Specifically, regarding the displacement statistic (Figure 2.10A), agreement is very good, except for the inconsistency at displacement = 0 μm, i.e. cells that did not move during the considered time interval (15 minutes). This inconsistency arises because we do not include the vascular bed from which cells migrate (we account for it via a boundary condition; see Figure 2.2A and Appendix B.3). By contrast, in [10], cell displacements from the embedded aortic ring assay were included in the sample (these ECs are mostly quiescent). Similarly, results regarding the orientation statistic (Figure 2.10B and 2.10C) are in good agreement with the experimental results. In particular, in our model ECs are more oriented, i.e. more persistent, in higher VEGF concentrations, which is a feature also observed in [4]. Concerning the directionality statistic (Figures 2.10D to 2.10F), we note that when VEGF=0 ng/ml the numbers of anterograde and retrograde cells in the experiments [4] (Figure 2.10F) and numerical simulations (Figure 2.10E) are approximately equal. In this scenario, ECM proteolysis is slow and cell migration is mostly constrained to existing sprouts. Thus, any anterograde movement is an overtaking event in which the overtaken cell has to perform a retrograde displacement. As the VEGF concentration increases, ECM proteolysis (see Eqs (2.18)-(2.19)) increases and more cells at the leading edge of sprouts can invade the surrounding ECM, elongating the sprouts. This leads to an increase in the ratio of anterograde to retrograde moving cells with the VEGF concentration.

Further evidence of agreement with experimental data is found by performing numerical simulations imitating the experimental setup of [126]. We performed simulations of sprouting from a cell bead embedded into the ECM (see **Setup 3** from Table B.10) with varying collagen density (which corresponds to the initial ECM concentration, c_{max}, in our model)
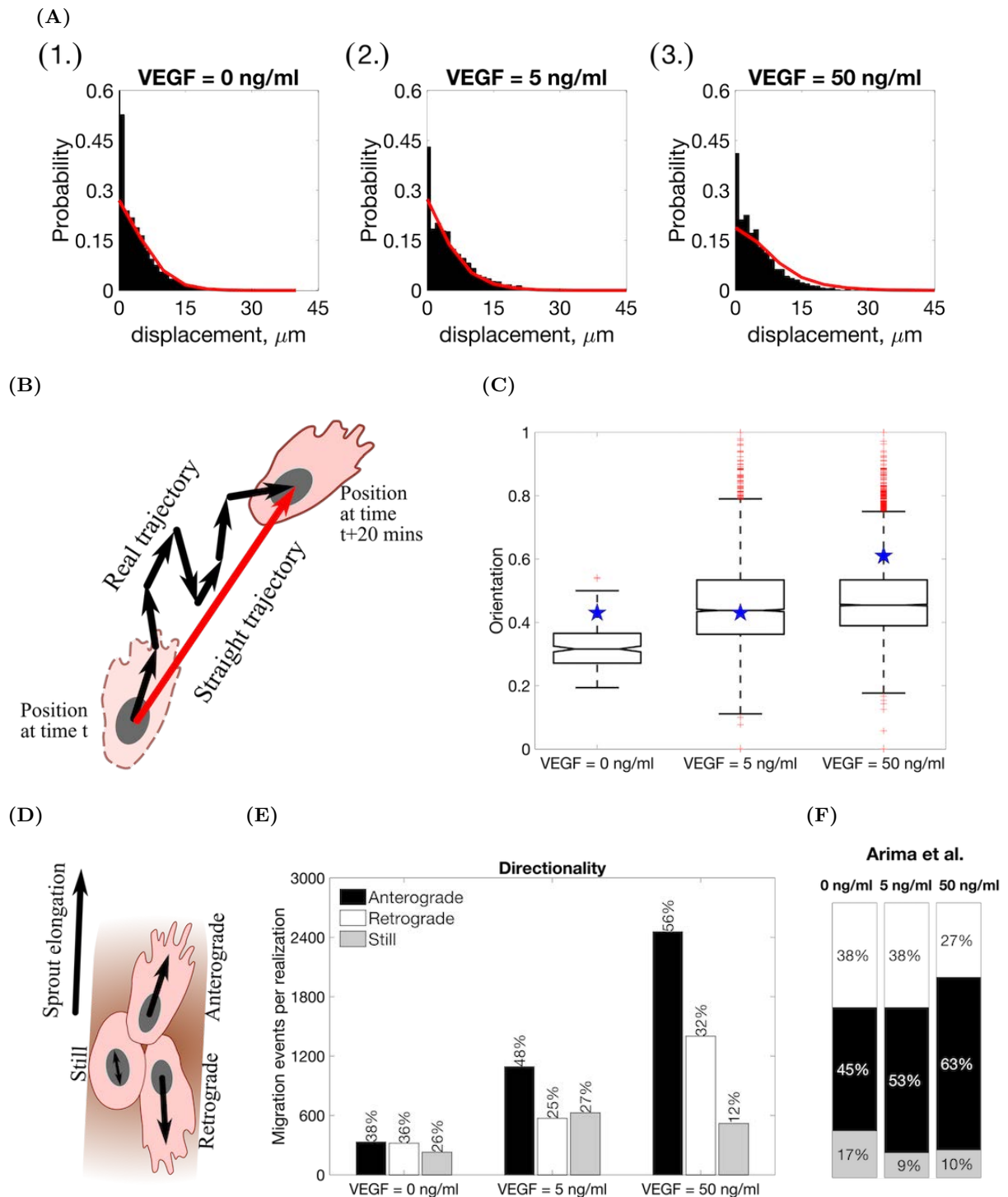
(A)

(1.)

(2.)

(3.)

(B)

(C)

(D)

(E)

(F)

Figure 2.10. (Caption on the next page.)

Figure 2.10. Statistics extracted from simulations of our model. (A) Histograms of cell displacements during a 15 minute time period for **(1.)** VEGF $= 0$ ng/ml, **(2.)** VEGF $= 5$ ng/ml and **(3.)** VEGF $= 50$ ng/ml. Black histograms correspond to the experimental data taken from the Supplementary Material of [10], red lines correspond to displacement curves for each VEGF concentration extracted from our model simulations. **(B)** A cartoon illustrating the orientation statistic, which is defined as a ratio between the net trajectory and the actual trajectory of a cell during simulation. **(C)** Box plots of the orientation statistic extracted from model simulations with VEGF $= 0, 5, 50$ ng/ml. Red crosses indicate box plot outliers. Orientation statistics obtained from experimental data from [4] are shown by blue stars on each box plot. **(D)** A cartoon illustrating the directionality statistic. **(E)** The directionality statistics for model simulations with VEGF $= 0, 5, 50$ ng/ml. **(F)** The directionality statistics extracted from experimental data in [4]. Numerical simulations were performed using **Setup 1** from Table B.10 and $T_{max} = 2.5$. Parameter values are listed in Tables B.7 and B.8 for subcellular and cellular/tissue scales, respectively. All statistics were computed for 100 realisations.

and a static linear VEGF gradient. Results from single realisations of different values of c_{max} are presented in Figure 2.11 (see also Movie 2.2). These results show free cell migration with no preferred direction for low c_{max} values, typical angiogenic morphology for intermediate values of c_{max}, and poorly elongating sprouts for higher values of c_{max}. These findings are consistent with the experimental observations reported in [126]. Furthermore, we note that the "sweet spot" of ECM concentration is related to EC ability to form typical angiogenic sprouting structures rather than to their ability to invade the ECM which decreases as the ECM concentration, c_{max}, increases (see Figure 2.11).

We note that the results presented in this section were generated using a fixed set of parameter values, except for the concentration of VEGF, V, and the concentration of collagen, c_{max}. Henceforth, we use these values as baseline parameter values (see Table B.8).

2.5.3 Model validation

In this section we validate our model by comparing its predictions with experimental results detailing the behaviour of certain VEGF receptor mutant cells (VEGFR2$^{+/-}$ and VEGFR1$^{+/-}$ mutants with halved gene expressions of VEGFR2 and VEGFR1, respectively), studied by Jakobsson et al. in [9] and described in Appendix B.3.
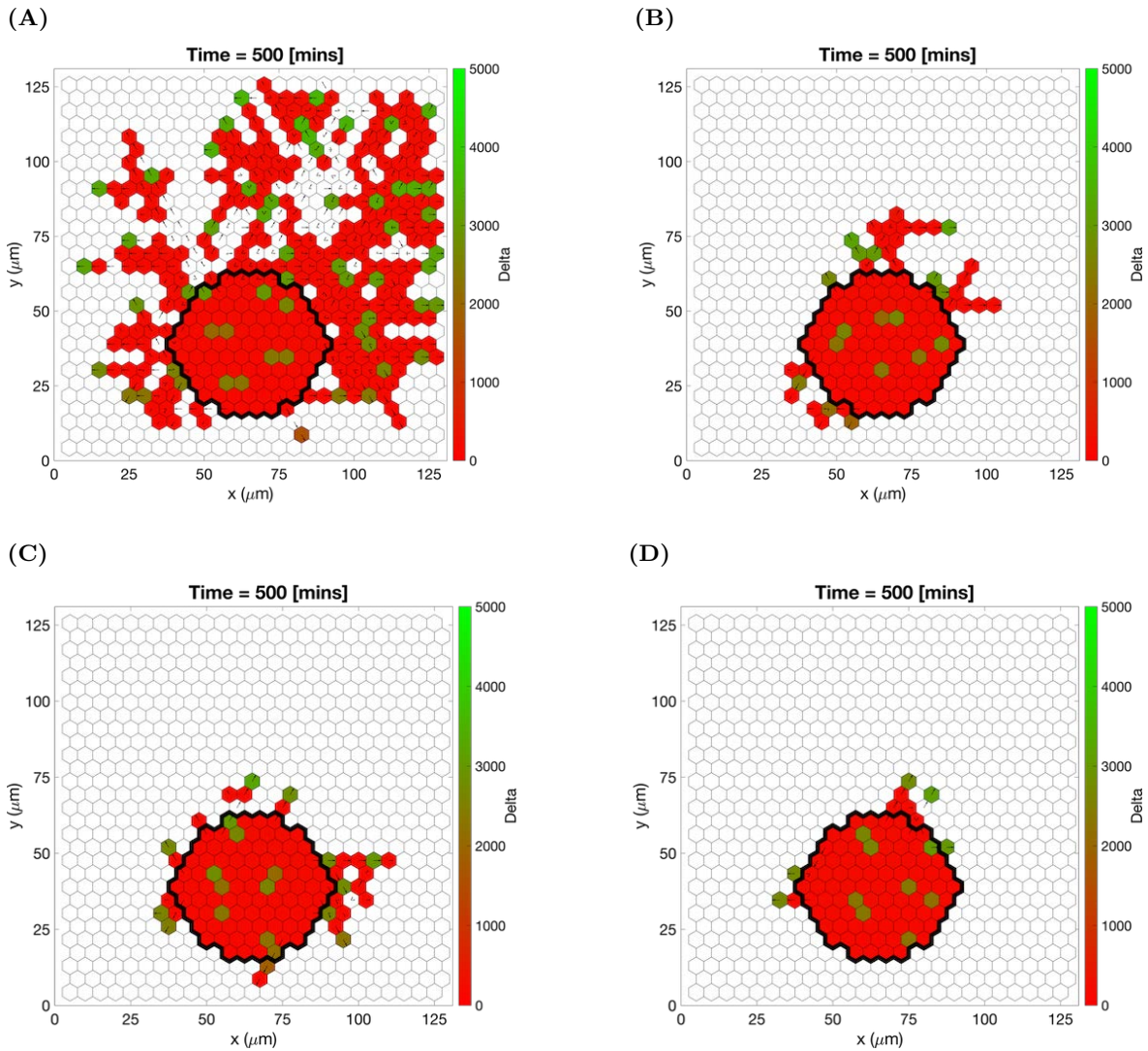
Figure 2.11. Cell migration from a cell bead in substrates of different collagen density. Final configurations of simulated vascular networks at time $T_{max} = 1.0$ (corresponding to 500 minutes) of individual simulations used in reproducing the results of the polarisation experiment in [126]. Maximum collagen density **(A)** $c_{max} = 0.1$, **(B)** $c_{max} = 1.0$, **(C)** $c_{max} = 1.7$, **(D)** $c_{max} = 3.0$. The VEGF linear gradient starts with 0 ng/ml at $y = 0$ and increases up to 5 ng/ml at $y = 125$ μm. Central bead initial and basement membrane conditions, $\mathcal{I}_{BM} = \mathcal{I}_{init}$, are outlined by a black thick line on each plot. Colour bars indicate Delta ligand concentration. Numerical simulations were performed using **Setup 3** from Table B.10. Parameter values are listed in Tables B.7 and B.8 for subcellular and cellular/tissue scales, respectively. For a movie of the numerical simulation, see Movie 2.2.

In order to ascertain whether our model can quantitatively reproduce competition between cells of different lineages (wild type (WT) and mutant cells) for the position of the leading cell in a sprout, we designed a series of numerical experiments which mimic the biological experiments reported in [9]. We start by simulating EC competition within linear sprouts that are devoid of collagen matrix (**Setup 4** in Table B.10), to ensure proteolysis-free random shuffling of cells within the sprout. We randomly initialise the sprout with cells of two chosen types with probability 50% (50% of WT cells and 50% of a specific mutant cell type) (see Figure 2.12, left column). Cells are then allowed to shuffle within the sprout, overtaking each other. For each realisation we record the total amount of time for which WT and mutant cells occupy the position of the leading cell.

As a control, we ran simulations in which two identical cell lines with parameters corresponding to WT lineage were mixed in a 1:1 ratio. As expected, the contribution of each WT cell to the leading cell position was approximately 50% (see Table 2.3).

Experiment	Position 1	Position 2	Ref. value [9]
WT:WT	$51.1 \pm 16.4\%$	$53.3 \pm 20.6\%$	45.8%
WT:VEGFR2$^{+/-}$	$93.6 \pm 7.1\%$	$90.4 \pm 14.8\%$	87.0%
WT:VEGFR1$^{+/-}$	$19.5 \pm 9.8\%$	$20.5 \pm 17.8\%$	30.0%
WT:VEGFR2$^{+/-}$ +DAPT	$51.5 \pm 13.7\%$	$52.9 \pm 17.8\%$	47.0%
WT:VEGFR1$^{+/-}$ +DAPT	$50.3 \pm 14.3\%$	$47.6 \pm 16.7\%$	40.6%

Table 2.3. Contribution of WT cells to the leading cell position when mixed 1:1 (50% : 50%) with another type of cell (equivalent WT or specified mutant). Since as an initial setup of simulations we considered a sprout of width 2 (two voxels), there are two equivalent leading positions (Position 1 and Position 2) (outlined on each plot by cyan lines in Figure 2.12). The results are reported as mean value $\pm$ standard deviation for samples obtained from 100 realisations for each experimental scenario. Numerical setup is as specified in Figure 2.12.

We then performed competition simulations in which WT cells were mixed with the different mutant cell lines in a 1:1 ratio (i.e. mixing 50% of WT cells with 50% of mutant cells). We repeated these numerical experiments in the presence of DAPT inhibitor which abolishes Notch signalling. The results of individual realisations presented in Figure 2.12 (see also
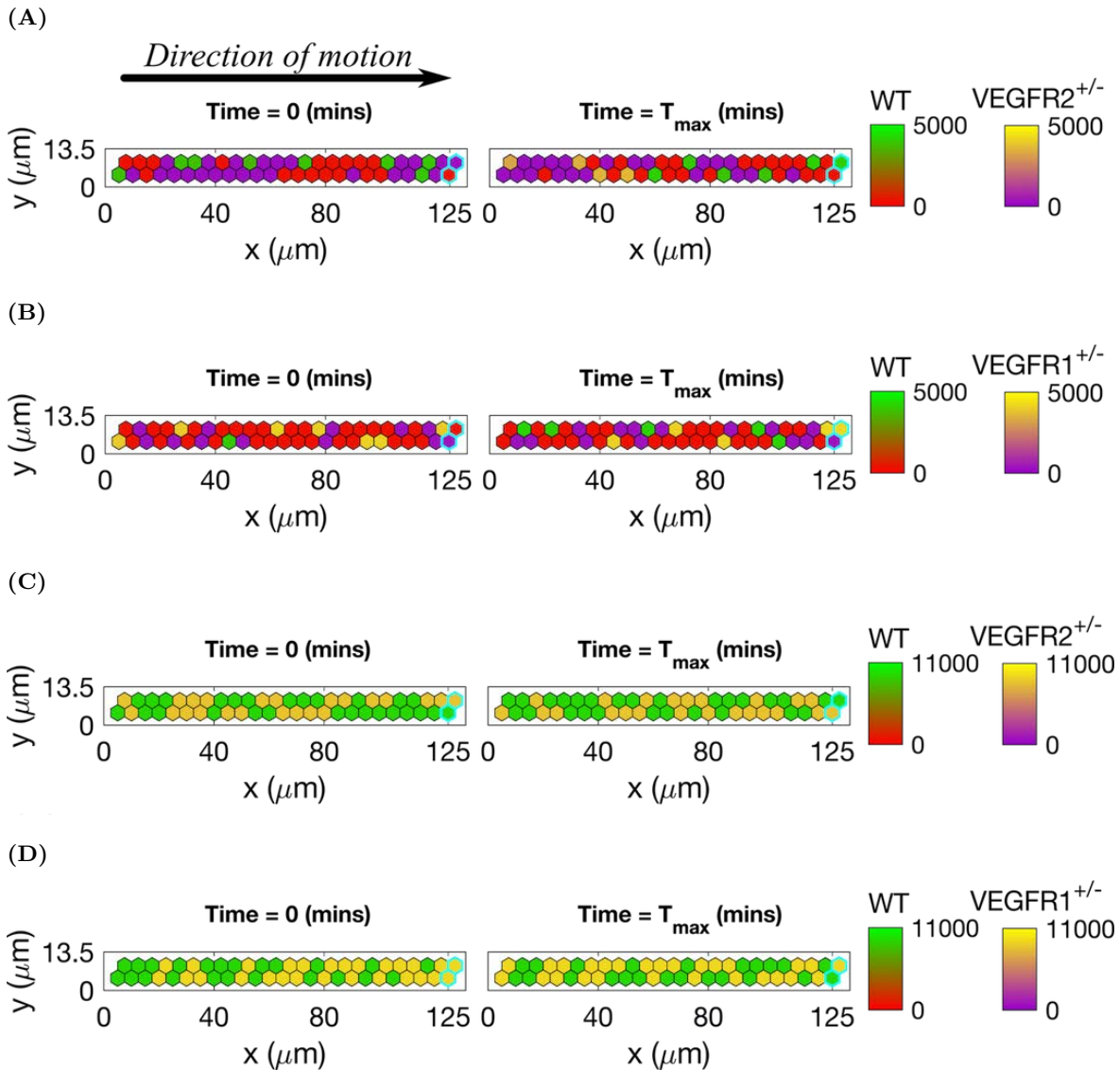
(A)

(B)

(C)

(D)

Figure 2.12. Initial and final configurations of single realisations of cells shuffling within a linear sprout when two given cell lines are mixed 1:1 (50% to 50%). Left column corresponds to the initial (random, 1:1) distribution of cells, right column - to the final one. The colour bar for Delta level of the WT goes from red colour (stalk cell) to green (tip cell), whereas for the mutant cells the colour bar goes from purple colour (stalk cell) to yellow (tip cell). **(A)** 50% of WT cells mixed with 50% of VEGFR2$^{+/-}$ mutant cells, no DAPT treatment. **(B)** 50% of WT cells mixed with 50% of VEGFR1$^{+/-}$ mutant cells, no DAPT treatment. **(C)** 50% of WT cells mixed with 50% of VEGFR2$^{+/-}$ mutant cells, both DAPT-treated. **(D)** 50% of WT cells mixed with 50% of VEGFR1$^{+/-}$ mutant cells, both DAPT-treated. Voxels corresponding to the leading edge of a sprout are outlined by thick cyan lines on each plot. Numerical simulations were performed using **Setup 4** from Table B.10. Parameter values are listed in Tables B.7 and B.8 for subcellular and cellular/tissue scales, respectively, except for the changed parameters for the mutant cells listed in Appendix B.3. Final simulation time, $T_{max} = 50.0$. For a movie of the numerical simulations, see Movie 2.3.

Movie 2.3), illustrate features of the different competition scenarios. For the WT:VEGFR2$^{+/-}$ scenario (see Figure 2.12A) when the mutant cells compete with WT cells, they almost never acquire the tip phenotype. Consequently, they are rapidly overtaken by WT cells and accumulate far from the leading edge of the sprout (outlined in cyan on each plot). The leading cell positions are thus occupied predominately by WT cells. By contrast, in the WT:VEGFR1$^{+/-}$ scenario (Figure 2.12B), mutant cells acquire the tip phenotype more often than WT cells, and thus contribute more significantly to the leading cell position. Treatment with DAPT forces all ECs (WT, VEGFR2$^{+/-}$ and VEGFR1$^{+/-}$) to acquire the tip cell phenotype (which is the default when Notch signalling is abolished [16], [27]). Consequently, in these cases both treated mutants have a 50% likelihood of occupancy of the leading position (Figures 2.12C and 2.12D).

We have also collected statistics from 100 realisations for each scenario and compared the results to the quantitative estimates provided in [9]. The results reported in Table 2.3 show that the contribution of WT cells to the leading cell position in each scenario is in good agreement with experimental values from [9]. In our simulations, VEGFR2$^{+/-}$ cells are less likely to stay at the leading position than WT cells: they occupy the leading position approximately 7% of the time. By contrast, VEGFR1$^{+/-}$ cells occupy the leading cell position approximately 78% of the time. DAPT restored the balance between the cells of different lineages so that they were on average equally mixed. Since the only parameters that we have modified are those used to mimic mutant cell gene expression and DAPT inhibition of Notch signalling (see Appendix B.3) our model provides possible explanation for overtaking dynamics of ECs in angiogenesis.

2.5.4 Sensitivity analysis

To ascertain how variation in the baseline parameter values of our model affects the behaviour of the system, we have performed an extensive sensitivity analysis. Since the subcellular VEGF-Delta-Notch model has already been calibrated and validated independently [156], we

have focused our analysis on the cellular and tissue scale parameters (see Table B.8). Briefly, we have performed our analysis by fixing all the parameters except one at their baseline values, and then vary the focal parameter by $\pm 0.1\%$, $\pm 5\%$, $\pm 10\%$, $\pm 15\%$, and $\pm 20\%$. This procedure is repeated for each of the tissue and cellular scale parameters. In order to quantify the impact of the variation of each parameter on both EC behaviour and network structure we have measured the following quantities:

- anterograde cell proportion (directionality metric);

- orientation;

- displacements;

- number of branching points per 100 μm^2 of vascular network area;

- number of vessel segments;

- vessel segment lengths.

Each of these metrics has been measured over 100 realisations of the multiscale system. For a full account of the details, see Appendix B.8.

The results of our sensitivity analysis are summarised in Figures 2.13 and B.16. Our analysis shows that system behaviour is robust to variations in most of the model parameters considered. This is indicated by the central cluster in Figures 2.13 and B.16, highlighted in magenta, which represents those scenarios that exhibit very small deviations from the baseline behaviour. By contrast, variations of a small number of parameters produce significant deviation from the baseline behaviour (see Table 2.4 and Figures 2.13 and B.16).

Specifically, we observe that an increase in D_m and a decrease in both D_c and K induce excessive branching, with shorter average vessel length (see Figure 2.13, hyper-branching region highlighted in brown). By contrast, a decrease in D_m and an increase in both D_c and K induce less branched networks, with longer average vessel length (see Figure 2.13, hypo-branching region highlighted in grey). These results are in agreement with well-known
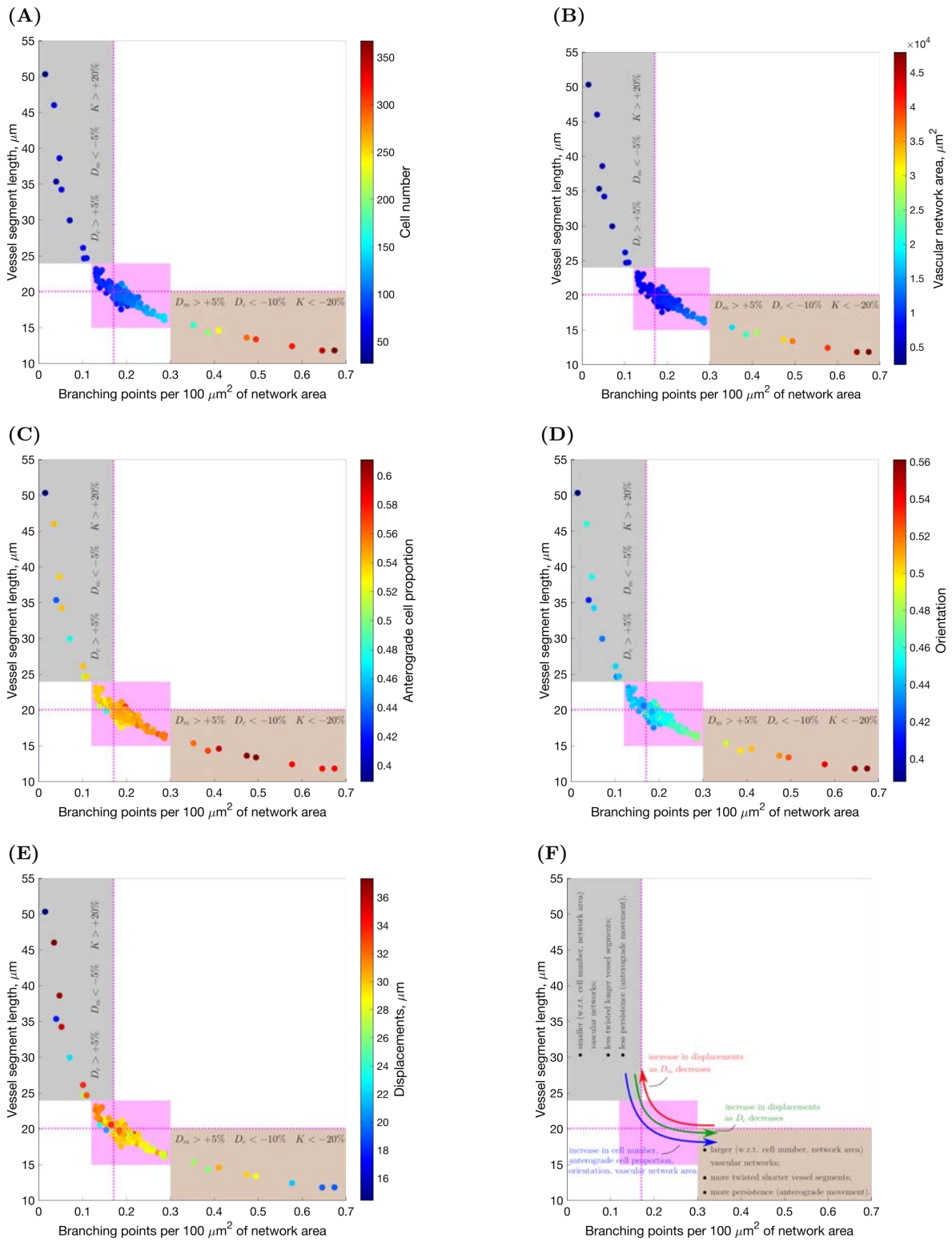
Figure 2.13. (Caption on the next page.)

Figure 2.13. Sensitivity analysis: branching vs. vessel elongation. The results of the sensitivity analysis are represented as scatter plots of the mean number of branching points per 100 μm^2 of vascular network area vs. mean vessel segment length, with colouring indicating mean **(A)** cell number; **(B)** vascular network area; **(C)** anterograde cell proportion; **(D)** orientation and **(E)** displacements. On these plots, dashed magenta lines indicate the point corresponding to the default parameter values (see Table B.8); magenta highlights the region of the main point clustering. The grey-coloured outlier region corresponds to vascular networks with few branching points and long vessel segments (hypo-branching), whereas the brown outlier region is characterised by short vessel segments and greater number of branching points (hyper-branching). Variations of the parameters that push the system towards one of the outlier regions are indicated on each plot. Panel **(F)** provides a general summary of these results. Simulation setup as in **Setup 1**, Table B.9, with $T_{max} = 2.5$. The results are averaged over 100 realisations for each scenario. The subcellular parameters are fixed at their default values in all experiments (see Table B.7).

Par.	Description	Ref. equation	Metrics affected	Effect
D_c	Threshold of level of Delta for initiation of ECM proteolysis	Eq (2.19)	All	Hyper-branching: $D_c \downarrow$; hypo-branching: $D_c \uparrow$
D_m	Threshold of level of Delta for initiation of BM assembly	Eq (2.21)	All	Hypo-branching: $D_m \downarrow$; hyper-branching: $D_m \uparrow$
K	Cell exploratoriness, i.e. controls the variance of the von Mises distribution	Eq (2.14)	All	Hyper-branching: $K \downarrow$; hypo-branching: $K \uparrow$
E_{F1}	Threshold of the level of cell-cell contact necessary for cell movement initiation	Eq (2.9)	Orientation, directionality	Hyper-branching: $E_{F1} \downarrow$
E_{F2}	Threshold of the inhibitory effect of crowding on cell movement	Eq (2.9)	Orientation, directionality	Hypo-branching: $E_{F2} \downarrow$

Table 2.4. Sensitivity analysis: parameters producing significant deviation in system behaviour from the baseline scenario. $\downarrow$ stands for decrease of the focal parameter, $\uparrow$ - increase of the focal parameter.

features of tumour vasculature, where the tumour microenvironment inhibits vessel stabilisation; specifically, it hinders the formation of the basal membrane in tumour vasculature,

yielding aberrant, excessively branched, networks [165]. This phenomenon can be realised by increasing D_m. Furthermore, proteolysis is also up-regulated during tumour-induced angiogenesis due to secretion of MMPs by cancer cells. Proteolysis reduces the resistance experienced by the ECs as they migrate towards the tumour [165]. This effect can be accounted for phenomenologically by a reduction in D_c. Increased stimulation with growth factors that can also bind to VEGF receptors (as in pathological angiogenesis [165], [166]) can reduce the response of the ECs to chemotactic stimuli, due to high occupancy of receptors all over the cell membrane, thus shifting cell behaviour to chemokinesis (non-directional cell migration) [167], [168]. In our model, this transition is controlled by the cell exploratoriness, κ (see Eq (2.14)): for high values of κ (i.e. higher values of K) cell migration is directed along the sprout elongation vector, whereas for small values of κ (i.e. smaller values of K) cells exhibit exploratory behaviour corresponding to chemokinesis.

Our model thus predicts that changes in D_c, D_m and K are likely to occur in tumour-induced angiogenesis. This prediction is supported by current knowledge regarding the effects of the presence of a tumour in the microenvironment [165]–[167].

2.5.5 Model prediction: network structure and cell mixing

We also simulated the growth of vascular networks formed by a single mutant cell line (VEGFR2$^{+/-}$ or VEGFR1$^{+/-}$) in the presence/absence of DAPT and compared our findings with the results from Jakobsson et al. who observed that in the absence of DAPT mutant cells mix with WT cells to form normal networks [9]. By contrast, the addition of DAPT leads to unstructured growth [9]. This is consistent with our simulation results (see Figures B.17-B.20). Specifically, simulations with VEGFR2$^{+/-}$ mutant cells in the absence of DAPT (see Figure B.17 and Movie 2.4) suggest that the rate of network growth of VEGFR2$^{+/-}$ is slower than for their WT counterparts (see Figures 2.7, 2.8 and B.21). Since Delta levels in VEGFR2$^{+/-}$ cells are lower than in WT cells, they are less able to degrade and invade ECM, and deposit BM components than WT cells. This results in slower sprout

elongation and increased branching (see Figure B.21). By contrast, VEGFR1$^{+/-}$ mutant cells possess higher levels of Delta and thus degrade the ECM more efficiently and invade the matrix more quickly than the WT cells (see Figure B.19 and Movie 2.4). Likewise, since the rate of segregation of BM components, γ_m, increases with Delta (Eq (2.21)), VEGFR1$^{+/-}$ cells are more persistent than WT cells. As a result, VEGFR1$^{+/-}$ ECs form less branched networks, with longer sprouts (see Figure B.21). Regarding networks grown with DAPT, since DAPT treatment abolishes all Notch signalling, all cells in the simulations with DAPT acquire the tip cell phenotype (Figures B.19 and B.20), which produces unstructured growth.

Since a cells' ability to compete for the leading position, or, equivalently, cell shuffling, is altered in mutant cells, we sought to understand how cell rearrangements influence the structure of a growing vascular network. To quantify cell rearrangements, we introduce a metric, which we refer to as *mixing measure*, $\mathcal{M}(t)$ (see Eq (2.22)). In Figure 2.14A, we plot the dynamics of the mixing measure, $\mathcal{M}(t)$, obtained by averaging over 100 WT simulations. As the vascular network grows and new sprouts form (see Figure 2.14C), $\mathcal{M}(t)$ increases over time.

The time evolution of the mixing measure varies for different cell lines. For VEGFR2$^{+/-}$ mutant cells it increases more slowly (Figure 2.15A), than for the WT cells (Figure 2.14A). VEGFR2$^{+/-}$ mixing arises more from branching than sprout elongation (see Figure 2.15C). A similar trend is seen for the VEGFR1$^{+/-}$ cells (compared to WT cells) (Figure 2.15A). However, contrary to VEGFR2$^{+/-}$, this is due to high migration persistence of VEGFR1$^{+/-}$ ECs (see Figure 2.15D). A slower increase in the mixing measure for mutant cells correlates with slower stabilisation of tip cell proportion around its steady state in vascular networks formed by mutant cells (see Figures 2.14B and 2.15B for WT and mutant cells, respectively). This supports our hypothesis that cell shuffling is directly related to the phenotypic specifications of ECs. Thus, we note that the cell rearrangement phenomenon is not a cell-autonomous decision but rather a result of contact-dependent EC cross-talk, which leads to EC phenotype specification.
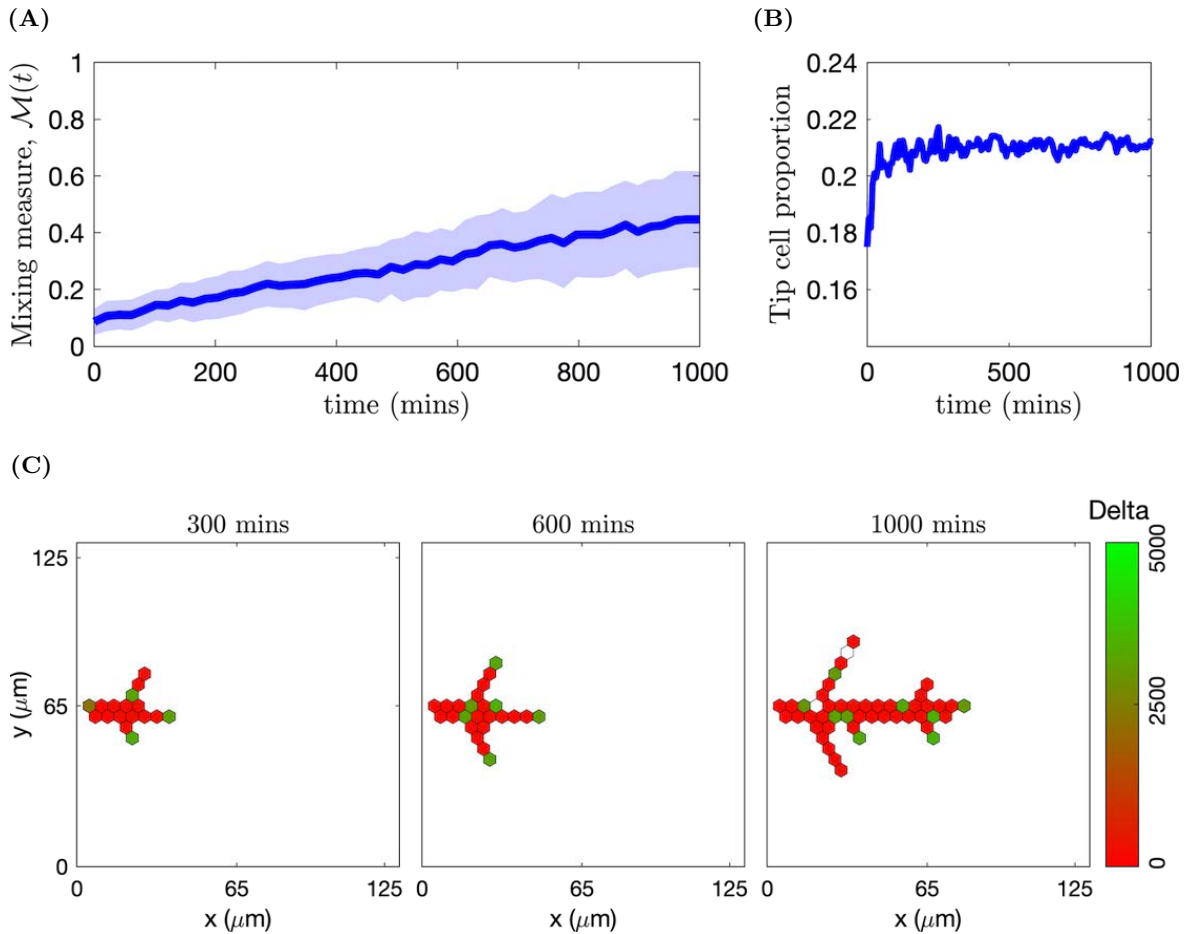
Figure 2.14. Temporal evolution of mixing measure, tip cell proportion and branching structure in a simulated vascular network formed by WT cells. (A) The mixing measure, $M(t)$, as a function of time (the mean value is indicated by a thick line and standard deviation is shown by a colour band). The results are averaged over 100 realisations. **(B)** Evolution of tip cell proportion as a function of time. The results are averaged over 100 realisations. **(C)** Snapshots from a single realisation of our model simulating a vascular network formed by WT cells at 300, 600 and 1000 minutes. Colour bar indicates the level of Delta. The numerical simulation setup used is **Setup 1** from Table B.10 with final simulation time $T_{max} = 2.5$. VEGF distribution was fixed uniformly at 5 ng/ml. Parameter values are listed in Tables B.7 and B.8 for subcellular and cellular/tissue scales, respectively.

(A)

(B)

(C)

VEGFR2$^{+/-}$

(D)
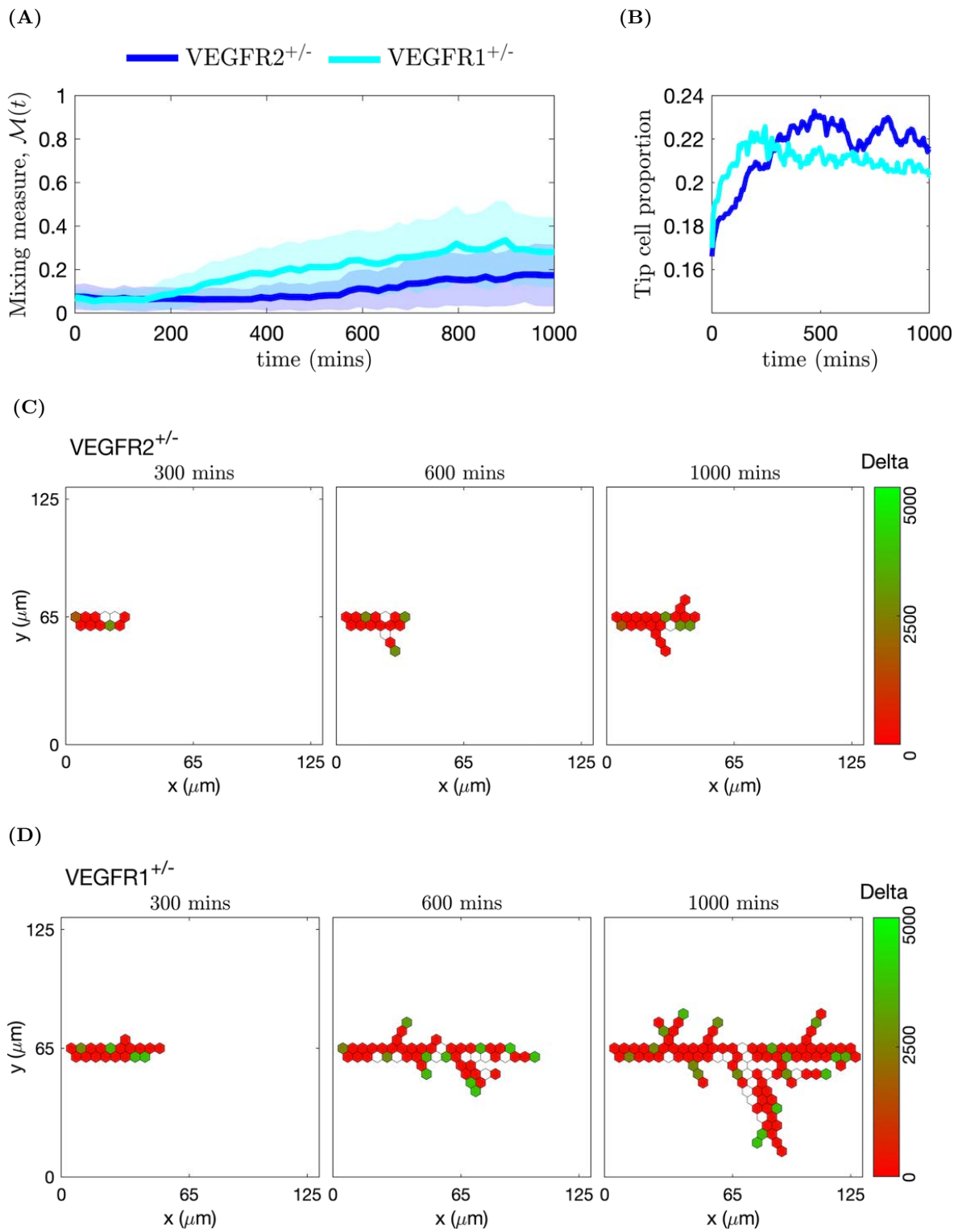
VEGFR1$^{+/-}$

Figure 2.15. (Caption on the next page.)

Figure 2.15. Temporal evolution of mixing measure, tip cell proportion and branching structure in simulated vascular networks formed by VEGFR2$^{+/-}$and VEGFR1$^{+/-}$ mutant cells. (A) The mixing measure, $M(t)$, as a function of time (the mean value is indicated by a thick line and standard deviation is shown by a band of the corresponding colour). The results are averaged over 100 realisations. **(B)** Evolution of tip cell proportion as a function of time. The results are averaged over 100 realisations. **(C)** Snapshots from a single realisation of our model simulating a vascular network formed by VEGFR2$^{+/-}$ mutant cells at 300, 600 and 1000 minutes. Colour bar indicates the level of Delta. **(D)** Snapshots from a single realisation of our model simulating a vascular network formed by VEGFR1$^{+/-}$ mutant cells at 300, 600 and 1000 minutes. Colour bar indicates the level of Delta. The numerical simulation setup used is **Setup 1** from Table B.10 with final simulation time $T_{max} = 2.5$. VEGF distribution was fixed uniformly at 5 ng/ml. Parameter values are listed in Tables B.7 and B.8 for subcellular and cellular/tissue scales, respectively, except of those changed for mutant cells (see Appendix B.3).

In all cases, regardless of the cell type and VEGF concentration, the mixing measure increases towards a steady state value (see Figure B.22, left panels). Furthermore, the steady state value of the mixing measure is independent of cell type ($\mathcal{M}(t) \approx 0.385$ as $t \to \infty$, see Figure B.23). This is a result of the fact that, as the vascular network reaches a sufficient size, cells perform proteolysis-free random shuffling within the manifold of the developed sprouts [32]. The rate of this proteolysis-free random shuffling does not depend on the cell line but rather on the tip-to-stalk ratio in the vasculature, which evolves to a steady state regardless of cell type and VEGF concentration (see Figure B.22, right panels). We conclude that the temporal evolution of the mixing measure characterises the resulting network structure to a larger degree than its steady state.

2.6 Discussion

Here, we developed a multiscale model which integrates individual cell gene expression, EC migration and interaction with the local ECM environment. Our model exhibits characteristic EC behaviour, such as branching and chemotactic sensitivity, as emergent properties instead of being encoded via *ad hoc* rules (as has been traditionally done in the literature). The vascular networks generated by our model are capable of reproducing the general traits

of sprouting angiogenesis: the networks exhibit branching patterns (see Figures 2.7 and 2.8), sprout elongation is enhanced in higher VEGF stimulation (see Figure 2.8) and the brush-border effect can be observed in networks grown in VEGF gradients (see Figure 2.9). Our simulation results are in good quantitative agreement with the characteristic trends of angiogenesis observed in experiments [4], [9], [10], [126] (see Figures 2.10 and 2.11 and Table 2.3).

We then used our model to quantify the phenomenon of cell rearrangement. We defined and introduced a mixing measure, $\mathcal{M}(t)$ (see Figure 2.6), for networks formed by WT cells and VEGFR2$^{+/\text{-}}$ and VEGFR1$^{+/\text{-}}$ mutant cells with impaired gene expression of VEGFR2 and VEGFR1, respectively, used in [9] (see Figures 2.14 and 2.15).

In all cases, in agreement with experimental observations, the mixing measure increases over time, although the specific details of its temporal evolution vary for different cell lines (see Figure B.22). In particular, for mutant cells, we find that mixing is lower due to either poor sprout elongation (VEGFR2$^{+/\text{-}}$ lineage, see Figures 2.15A, 2.15C and B.21) or elevated cell persistency (VEGFR1$^{+/\text{-}}$ lineage, see Figures 2.15A, 2.15D and B.21). WT cells form more functional networks, in the sense of more effective coverage of the domain (and thus future delivery of oxygen/nutrients). This is achieved by a balance between branching and sprout elongation which increases the mixing measure for WT cells. We thus showed that the time evolution of the mixing measure is directly correlated with the generic features of the vascular pattern. This result supports the claim that shuffling and cell mixing are essential for network formation and structure.

We also observe that the mixing measure reaches a steady state (see Figure B.23). We hypothesise that this is directly related to the proportion of tip cells in the network since they are the main driver of cell overtaking. This is substantiated by our results that, while the gene expression of VEGFR1$^{+/\text{-}}$ and VEGFR2$^{+/\text{-}}$ mutant cells exhibits variations, the steady state of the tip cell proportion is the same for all cell lineages (see Figure B.22, right column). Thus, although the branching pattern and effective sprout elongation vary for mutant cells, they generate adequate vascular networks in our simulations (see Figures B.17 and B.18).

We suggest that pathological network formation is directly related to the imbalance in the tip cell proportion (for example, treatment with DAPT, which abolishes Notch signalling and forces all ECs to acquire tip phenotype, leads to hyper-sprouting [9], see Figures B.19 and B.20). Analysing this proportion and what triggers its change might help to understand better what leads to malformations in sprouting angiogenesis. Furthermore, the results of our sensitivity analysis suggest that variations in the parameters that control ECM remodelling (ECM proteolysis and BM assembly) and cell exploratoriness significantly modify vascular network structure (see Figures 2.13 and B.16). This is in agreement with experimental evidence of aberrant vessels with excessive branching in tumour-induced angiogenesis [165]–[167].

We calibrated and validated our model against *in vitro* experiments carried out over a timescale on which cell proliferation and cell death are negligible (only $\approx 5\%$ of cells were undergoing mitosis in the observed time of ≈ 22.4 hours [4]). Whilst cell turnover is neglected in the present study, it will need to be incorporated in any future study that simulates larger vascular networks. To do so, we must first reduce the computational complexity of the model since, in its current implementation, the runtime of a single simulation is up to several hours (computational complexity increases with the number of cells in the system). One way to achieve this is to coarse-grain the subcellular model to a two-state (tip and stalk cell) Markovian system, omitting the dynamics of the intermediate variables [169] (which is the subject of the next Chapter 3). We expect such an approach to reduce the computational complexity of the subcellular model, thus allowing us to run larger scale simulations.

Chapter 3

A method to coarse-grain multi-agent stochastic systems with regions of multistability

3.1 Summary

Hybrid multiscale modelling has emerged as a useful framework for modelling complex biological phenomena. However, when accounting for stochasticity in the internal dynamics of agents, these models frequently become computationally expensive. Traditional techniques to reduce the computational intensity of such models can lead to a reduction in the richness of the dynamics observed, compared to the original system. Here we use large deviation theory to decrease the computational cost of a spatially-extended multi-agent stochastic system with a region of multi-stability by coarse-graining it to a continuous time Markov chain on the state space of stable steady states of the original system. Our technique preserves the original description of the stable steady states of the system and accounts for noise-induced transitions between them. We apply the method to a bistable system modelling phenotype specification of endothelial cells driven by a lateral inhibition mechanism. For this system, we demonstrate how the method may be used to explore different pattern configurations and unveil robust patterns emerging on longer timescales. We then compare the full stochastic, coarse-grained and mean-field descriptions via pattern quantification metrics and in terms of the numerical cost of each method. Our results show that the coarse-grained system exhibits

the lowest computational cost while preserving the rich dynamics of the stochastic system. The method has the potential to reduce the computational complexity of hybrid multiscale models, making them more tractable for analysis, simulation and hypothesis testing. This chapter is based on our published work [170].

The remainder of this chapter is organised as follows. In section 3.2, we explain how our multiscale model of angiogenesis (described in Chapter 2) motivated us to formulate the coarse-graining method. In the following, section 3.3, we summarise large deviation theory. This provides us with the information needed to formulate the coarse-grained model in section 3.4. In section 3.4.1, we start by coarse-graining the individual agent system and checking the accuracy of the method. We then extend the technique to a multi-agent system in section 3.4.2 where we outline a general algorithm for formulating and simulating the coarse-grained model. In section 3.5, we present typical simulation results for the model of the VEGF-Delta-Notch signalling pathway (sections 3.5.1 and 3.5.2) and compare the full stochastic, coarse-grained and mean-field systems via metrics which quantify the spatial patterns formed by the two cell phenotypes and we also compare computational cost of simulations (section 3.5.3). The chapter concludes in section 3.6 with a summary of our findings and suggestions for future research directions.

3.2 Motivation

When modelling a biological process, one has to make choices on how detailed the model should be in order to capture the characteristic features of the system. At the same time, the model should be as simple as possible in order to facilitate its analysis and numerical simulations. The evolution of systems with large numbers of agents (e.g. molecules, cells, species) can be described by the average behaviour of their agents, or their mean-field limits using (ordinary or partial) differential equations ([78], [138], [155]). Dynamical systems theory provides methods and techniques for the analysis and numerical simulations of such systems. This description might become insufficient when the system comprises agents with internal

variables that change in time, thus altering the agents' behaviour, or when the system is not 'large enough' to be described accurately by the mean-field equations. For these systems, stochastic descriptions are employed [152] (for example, continuous time Markov chains, CTMCs, or stochastic differential equations, SDEs). In biological systems, the number of agents is finite and some level of noise is always present which can affect the system dynamics [152]. While exhibiting richer dynamics than deterministic systems, stochastic models are more computationally intensive.

Furthermore, in order to formulate a theoretical model of a biological phenomenon, it is often necessary to account for dynamics that act on different temporal and/or spatial scales [68], [71]. This has led to the development of hybrid multiscale models, in which different modelling techniques may be applied at each scale and then efficient coupling algorithms are used to integrate these models (see, e.g., [67], [72], [171] and references therein). In many of these models, individual entities (cells, species, etc.) are considered as discrete agents which are, themselves, equipped with models for their internal states determining the behaviour (e.g. subcellular signalling, cell cycle, response to extracellular stimuli). Such models have great potential for generating insights into the behaviour of a system (e.g., endothelial cell rearrangements [5], cell differentiation and tissue organisation in intestinal crypts [171], and multiscale cancer modelling [172]). However, they frequently become numerically intractable because of their complexity (e.g. the internal dynamics of agents) [71]. This limits possible applications of these models.

In this thesis, we explain how to reduce the computational complexity of a hybrid model by coarse-graining the internal dynamics of its agents when these are described by a stochastic system with multiple steady states. The method involves applying large deviation theory (LDT) to reduce the dynamics of the stochastic system to a continuous time Markov chain (CTMC) on the state space of its stable steady states. LDT provides a theoretical framework with which to quantify how small time-dependent fluctuations can lead to significant deviations from the mean-field behaviour (*rare events*) such as transitions between stable steady
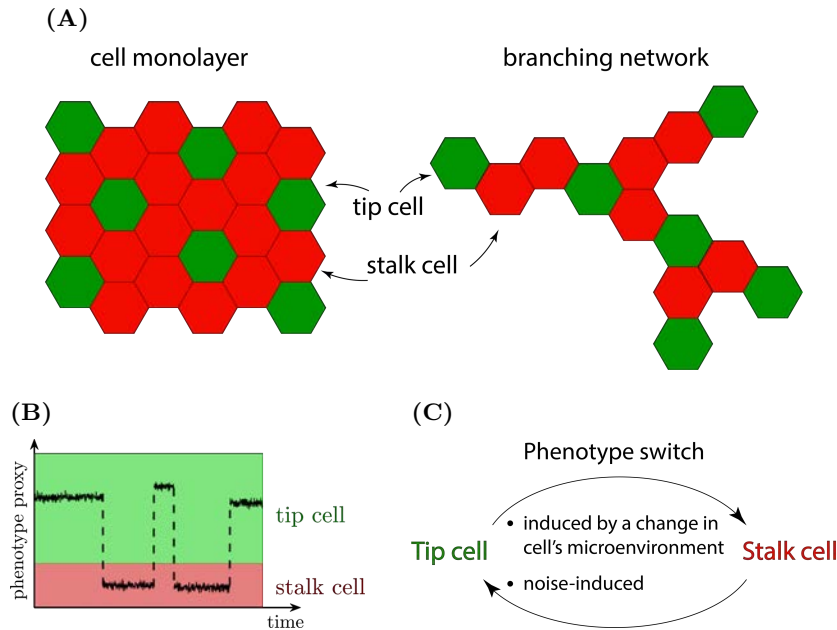
(A)

cell monolayer   branching network

tip cell

stalk cell

(B)   **(C)**

Phenotype switch

tip cell

stalk cell

Tip cell • induced by a change in
cell's microenvironment   **Stalk cell**

• noise-induced

phenotype proxy

time

Figure 3.1. Cell phenotype specification. (A) Phenotype (tip and stalk cells) patterning of ECs induced by a mechanism of lateral inhibition in two different domains: a cell monolayer and a branching network. **(B)** Dynamic time evolution of phenotype adaptation of an individual cell. Using a phenotype proxy, e.g. level of Delta, allows for identification of a continuous cell phenotype. **(C)** Phenotype switches, as in **(B)** (dashed vertical lines), occur due to either a change in a cell's microenvironment or naturally present noise in intracellular signalling.

states which cannot occur in deterministic systems [173]. This approach has previously been used to study rare, noise-induced events in individual stochastic systems [152], [174]–[178], but to our knowledge, this is its first application to a multi-agent model.

In previous Chapter 2, we developed a multiscale model of angiogenesis, the process of growth of new blood vessels from pre-existing ones, which accounts for gene expression patterns (phenotypes) of ECs at the subcellular scale. For prescribed levels of extracellular stimuli (VEGF), the system is either monostable (i.e. only one cell phenotype exists) or bistable (i.e. two stable steady states, cell phenotypes, coexist). Cell phenotype is specified via contact-dependent cross-talk with neighbouring ECs via the VEGF-Delta-Notch signalling pathway [25], [26]. Cells adjust their gene expression in order to maintain a pattern of two distinct phenotypes, tip and stalk cells (see Figures 3.1A and 3.1B). We use the internal level

of Delta as a proxy to distinguish between the phenotypes. The number of transmembrane proteins in this signalling pathway is on the order of thousands for each cell [155]. Therefore, in order to formulate a mathematical model, it is tempting to use deterministic mean-field equations to describe the kinetic reactions of this signalling pathway. However, deterministic descriptions cannot account for noise-induced transitions between stable steady states or, in the case of this signalling pathway, phenotypic switches, which can occur in regions of bistability (see Figures 3.1B and 3.1C). Since branching patterns of vascular networks are affected by the distribution of cells with different phenotypes, such phenotype transitions are potentially significant. Therefore, we modelled the subcellular signalling pathways stochastically (see Appendix B.2), which increased the computational cost of the model. This example illustrates a general problem associated with computational and, in particular, hybrid models: in order to preserve emergent features of the system, such as continuous cell phenotypes and noise-induced phenotype switches, the model becomes computationally intractable for large lattice simulations. Instead of simulating the full system of stochastic kinetic reactions for the cell crosstalk, as was done in our model of angiogenesis (see Chapter 2), the coarse-graining technique reduces the subcellular system dynamics to a jump process involving phenotype switches (i.e. between stable steady states of the system). This allows us to preserve the continuous description of the steady states and noise-induced transitions between them, while substantially reducing the computational effort required for simulation.

We illustrate the coarse-graining method by reference to the subcellular model of the VEGF-Delta-Notch signalling pathway that defines cell phenotype. We perform our simulations for two spatial geometries: a cell monolayer and a branching network (Figure 3.1A). For our model of multicellular VEGF-Delta-Notch signalling, we show typical simulation results of the coarse-grained system which allows us to explore different configurations of spatial patterns in a single realisation of the model (due to phenotypic switches). We then demonstrate how this dynamic exploration of possible patterns may be used to uncover robust patterns emerging at long timescales. We finally compare the spatiotemporal dynamics and

computational cost of the full stochastic CTMC, the coarse-grained and the deterministic mean-field descriptions. Our results show that the coarse-grained model, while preserving the continuous description of cell phenotype and rare events of phenotype switching, is more computationally efficient than the other two systems. Thus, it significantly reduces the computational complexity of the model without sacrificing the rich dynamics of the original stochastic system.

3.3 Theoretical background on large deviation theory

In the presence of noise, small fluctuations can drive significant deviations from mean-field behaviour such as, for example, transitions from one stable steady state to another. These transitions are usually referred to as *rare events* since their likelihood is small. LDT is predicated on the assumption that when rare events occur, the system follows the least unlikely paths. Deviations from these paths occur with very small probability (i.e. smaller than the probability of a rare event). Specifically, Freidlin-Wentzell's theory of large deviations predicts that the deviations are exponentially suppressed [173], making such transitions 'predictable'. LDT provides the means to analyse the frequency of rare events and to identify the maximum likelihood path (minimum action path, MAP) along which these transitions can occur.

A stochastic differential equation (SDE) of a diffusion process, $x^\epsilon \in \mathbb{R}^n$, has the following form

$$\mathrm{d}x^\epsilon(t) = b(x^\epsilon)\mathrm{d}t + \sqrt{\epsilon}\sigma(x^\epsilon)\mathrm{d}W, \tag{3.1}$$

where $b : \mathbb{R}^n \to \mathbb{R}^n$ is a drift vector, $a(x^\epsilon) = (\sigma\sigma^T)(x^\epsilon)$ is a diffusion tensor ($\sigma : \mathbb{R}^n \to \mathbb{R}^n \times \mathbb{R}^m$, m corresponds to the number of kinetic reactions in the system), W is a Wiener process in $\mathbb{R}^m$ and $\epsilon = \Omega^{-1}$ is noise amplitude.

The mean-field limit of Eq (3.1), $x(t) \in \mathbb{R}^n$, solves the following differential equation:

$$\frac{\mathrm{d}x}{\mathrm{d}t} = b(x). \tag{3.2}$$

Assume that Eq (3.2) has two stable steady states, $x_1, x_2 \in \mathbb{R}^n$, whose basins of attraction form a complete partition of $\mathbb{R}^n$. We are interested in transitions from $x_1 \rightarrow x_2$ (and $x_2 \rightarrow x_1$) which cannot be accounted for unless noise is present in the system.

A key player in LDT is the action functional

$$S_T(\psi) = \begin{cases} \int_0^T L(\psi, \dot{\psi}) \, dt, & \text{if } \psi \in C(0, T) \text{ is absolutely continuous and} \\ & \qquad \text{the integral converges,} \\ \\ +\infty, & \qquad \text{otherwise,} \end{cases}$$

which is computed for a transition path $\psi : [0, T] \rightarrow \mathbb{R}^n$ from x_1 to x_2 ($\psi(0) = x_1$ and $\psi(T) = x_2$, T is the transition time). Here, $\dot{\psi}$ denotes the gradient of the transition path, ψ; $L(x, y) = \sup_{\theta \in \mathbb{R}^n} (\langle y, \theta \rangle - H(x, \theta))$ is the large deviation Lagrangian, with $\langle \cdot, \cdot \rangle$ being the Euclidean scalar product in $\mathbb{R}^n$ and $H(x, \theta)$ being the Hamiltonian associated with $L(x, y)$. The particular form of the Hamiltonian depends on the dynamical system under consideration (in Appendix C.1, we explain how to define the Hamiltonian for an SDE such as Eq (3.1) and for a general birth-death CTMC).

The action functional is used to estimate the probability that a trajectory $x^\epsilon(t)$ lies in a narrow neighbourhood, of width $\delta > 0$, of a given path $\psi \in C(0, T)$ (see Figure 3.2 for an illustration):

$$\mathrm{P} \left\{ \sup_{0 \leq t \leq T} \mid x^\epsilon(t) - \psi(t) \mid < \delta \; \middle| \; x^\epsilon(0) = x_1 \right\} \approx \exp\{-\epsilon^{-1} S_T(\psi)\}. \tag{3.3}$$

Since the probability function in Eq (3.3) decreases as the action functional, $S_T(\psi)$, increases, the maximum likelihood path, ψ^*, is the minimiser of $S_T(\cdot)$. This leads naturally to the idea of the quasipotential:
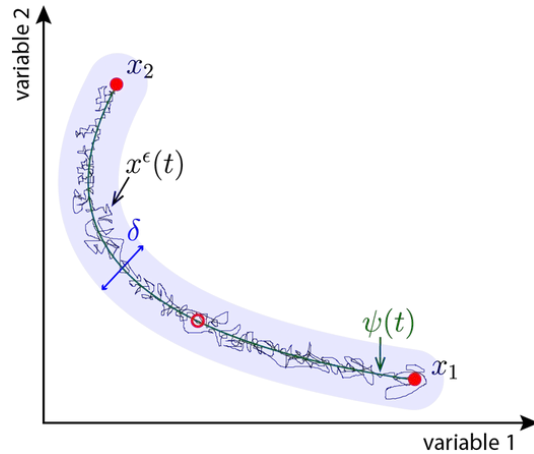
Figure 3.2. An illustration of a transition path between two stable steady states of an arbitrary bistable system. The two stable steady states, x_1 and x_2, are marked by filled red circles; an unstable saddle point is marked by an unfilled red circle. The transition path, $\psi(t)$, from x_1 to x_2 is shown by a thick green line, whereas a single stochastic trajectory, $x^\epsilon(t)$, is indicated by a thin black path. The shaded blue region indicates a δ-neighbourhood around $\psi(t)$ (δ as defined in Eq (3.3)).

$$Q(x_1, x_2) = \inf_{T>0} \inf_{\psi \in \overline{C}_{x_1}^{x_2}(0,T)} S_T(\psi). \tag{3.4}$$

Here $\overline{C}_{x_1}^{x_2}(0,T)$ is the space of absolutely continuous functions $f : [0,T] \to \mathbb{R}^n$ such that $f(0) = x_1$ and $f(T) = x_2$. Roughly speaking, the quasipotential gives an estimate of how 'difficult' it is to move from x_1 to x_2. Thus, the quasipotential value depends on the direction of a transition path and, in general, $Q(x_1, x_2) \neq Q(x_2, x_1)$.

On timescales which are much longer than those associated with relaxation to a stable steady state, the dynamics of Eq (3.1) can be reduced, or *coarse-grained*, to that of a CTMC on the state space of the two stable steady states, $\{x_1, x_2\}$, with transition rates [173], [179]

$$\omega_{x_1 \to x_2} \asymp \exp\left(-\epsilon^{-1}Q(x_1, x_2)\right), \qquad \omega_{x_2 \to x_1} \asymp \exp\left(-\epsilon^{-1}Q(x_2, x_1)\right). \tag{3.5}$$

Here $\asymp$ denotes log-asymptotic equivalence so that $f(\epsilon) \asymp g(\epsilon)$ if and only if $\lim_{\epsilon \to 0} \frac{\log f(\epsilon)}{\log g(\epsilon)} = 1$.

In practice, most double minimisation problems, such as Eq (3.4), do not have a solution for finite $T > 0$. Furthermore, closed-form Lagrangians exist for SDEs of the type defined by Eq (3.1) but not for general birth-death CTMCs. Eq (3.4) can be reformulated in terms of a Hamiltonian system of the form

$$\frac{\mathrm{d}\phi}{\mathrm{d}t} = \frac{\partial H(\phi,\theta)}{\partial\theta}, \qquad \frac{\mathrm{d}\theta}{\mathrm{d}t} = -\frac{\partial H(\phi,\theta)}{\partial\phi}.$$

This problem must be solved as a boundary-value problem, i.e. $\phi(0) = x_1$ and $\phi(T) = x_2$, on an infinite time interval, $T \to \infty$, [180] which makes it a non-trivial numerical problem. Thus, the traditional LDT methods are inapplicable in most cases.

One way to resolve these problems is to reformulate the minimisation problem defined by Eq (3.4) on the space of curves (i.e. transition paths from one stable steady state to another). In [181], Heymann & Vanden-Eijnden proved that the minimisation problem defined by Eq (3.4), is equivalent to

$$Q(x_1, x_2) = \inf_{\phi} \widehat{S}(\phi), \quad \text{with} \quad \widehat{S}(\phi) = \sup_{\substack{\hat{\theta}:[0,1]\to\mathbb{R}^n \\ H(\phi,\hat{\theta})=0}} \int_0^1 \langle \phi', \hat{\theta} \rangle \, d\alpha, \tag{3.6}$$

where $\phi : [0,1] \to \mathbb{R}^n$ is a curve from x_1 to x_2 parametrised by standard arc length.

The geometric reformulation, Eq (3.6), resolves analytically the issue of the infinite time, T, in the original minimisation problem. Furthermore, only the Hamiltonian is needed. In this respect, the method is more general as it can be applied to SDEs, CTMCs and other systems for which the Hamiltonian is known (see Appendix C.1 in Appendix C).

In [181], an algorithm was developed to efficiently compute $Q(x_1, x_2)$ and the corresponding minimiser, ϕ^*, from the geometric reformulation. The algorithm is known as the geometric minimum action method (gMAM) and the minimiser, ϕ^*, of the action functional is referred to as the minimum action path (MAP) (for more details see Appendix C.1).

Once the quasipotential has been computed, the coarse-grained system is given by a

CTMC, with rates defined by Eq (3.5).

3.4 Coarse-graining method

We now illustrate how the theory described in the previous section can be used to coarse-grain a specific hybrid multiscale model, one for which the internal dynamics of the agents are described by multistable stochastic systems. This property is characteristic of, for example, systems driving cell fate (phenotype) determination. We begin by using LDT to formulate a CG model for a system comprising a single agent (here a cell). The subcellular signalling pathway, which we use to illustrate the method, is the VEGF-Delta-Notch pathway (see section 1.2 and Appendix B.2 for details). This pathway regulates phenotypic adaptation via lateral inhibition [182], [183]. This system meets the requirements for application of the CG technique: *(a)* it is bistable; its stable steady states are associated with cellular phenotypes (tip and stalk cells); *(b)* we are interested in its evolution on timescales longer than the typical time for relaxation to an equilibrium since other processes (e.g. cell migration and dynamics of extracellular matrix) act on longer timescales (see Figure 1.4).

We then extend the method to the general case of multi-agent systems. Here the dynamics of each entity is coarse-grained to a CTMC on the state space of its stable states, and coupling between the internal dynamics of individual agents is achieved via the external variables whose dynamics depend on the states of neighbouring agents and/or the time evolution of these variables. We outline below how we apply this method to a monolayer of cells (motivated by phenotype patterning via the core Delta-Notch pathway in cell monolayers [183]) and a branching network (angiogenesis-motivated application, see Chapter 2) that interact via VEGF-Delta-Notch signalling.

3.4.1 Individual agent system

Our algorithm for coarse-graining a stochastic system with a region of multistability involving a single entity is illustrated in Figure 3.3. For the particular case of VEGF-Delta-Notch
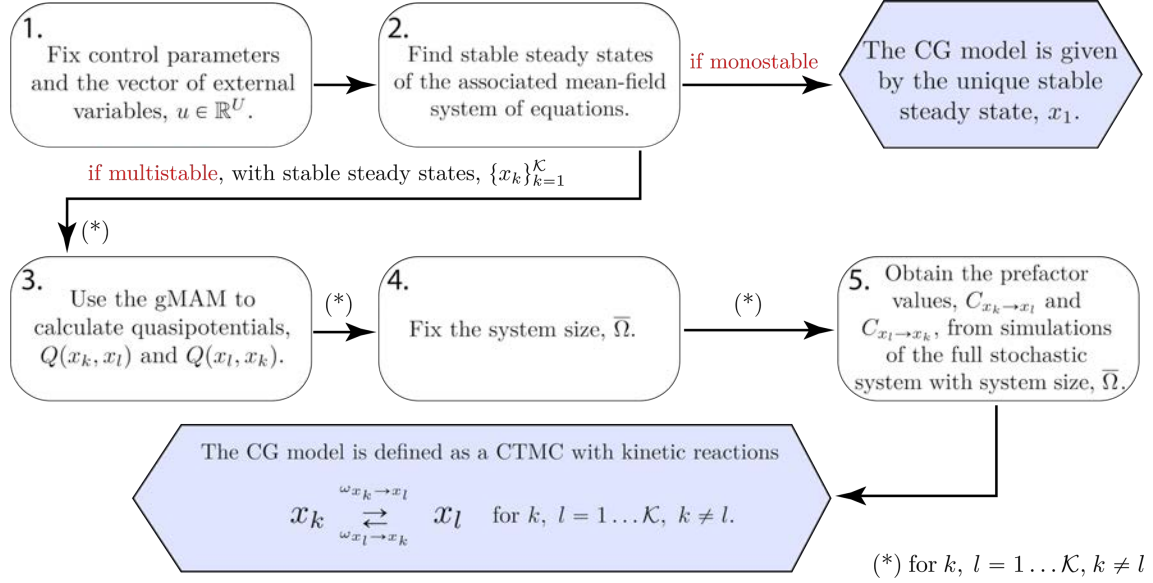
Figure 3.3. A flowchart of the procedure used to coarse-grain a multistable stochastic system for an individual entity. The steady state solutions, quasipotential and prefactor depend on the model parameters and external variables, $u \in \mathbb{R}^U$ (U indicates the dimension of the vector of external variables). Here the transition rates, $\omega_{x_k \to x_l}$, are defined by Eq (3.7), the prefactor, $C_{x_k \to x_l}$, is determined from Eq (3.8b), and $\overline{\Omega}$ is given by Eq (3.9).

signalling, a cell's internal state (phenotype) depends on two model parameters (inputs) corresponding to the extracellular levels of Delta and Notch, $u = (d_{ext}, n_{ext}) \in \mathbb{R}^2$ (corresponding to the levels of Delta and Notch, respectively, that the cell under consideration perceives from the cells in its external microenvironment, see Appendix B.2). We fix the values of the model parameters and the external variables, u (see Table C.1). We then use the mean-field system defined by Eq (B.4) to compute the steady state solutions. For this example, the values of the external variables, u, are chosen so that the system is bistable; the two stable steady states correspond to tip and stalk cell phenotypes, $\{x_1, x_2\} = \{$tip cell, stalk cell$\}$, and the unstable steady state is an unstable saddle. Our goal is to compute the transition rates of the CG system which we approximate as follows:

$$\omega_{x_k \to x_l} \approx C_{x_k \to x_l} \exp\left(-\Omega Q(x_k, x_l)\right), \quad k, \ l \in \{1, 2\}, \ k \neq l. \tag{3.7}$$

We note that the prefactor, $C_{x_k \to x_l}$, arises from the asymptotic equivalence relation defined by Eq (3.5) [152], [173], [184]. The system size is given by $\Omega = \epsilon^{-1}$, where ϵ is the noise level.

We use the gMAM to compute the quasipotential values and corresponding paths (MAPs) for transitions between the tip and stalk phenotypes (for more details, see Appendix C.3). An illustrative example is shown in Figure 3.4, where we compare the MAPs and sample paths of the full stochastic CTMC for an individual cell (see also Table B.1 in Appendix B.2). Several characteristic features of the phenotype transitions are noteworthy. First, the dynamics of the MAP can be split into two parts: the transition from the steady state of origin to the saddle point (for example, from the stalk cell phenotype to the saddle point, indicated by the blue circle in Figure 3.4A) which is possible due to the presence of noise. The main contribution to the quasipotential comes from this transition. The MAP from the unstable saddle point to the stable steady state of destination (from the saddle point indicated by the blue circle to the tip cell phenotype in Figure 3.4A) follows the fastest route given by the deterministic heteroclinic orbit connecting the steady states (i.e. the unstable saddle and the stable tip cell state). For systems that possess a single unstable saddle point and no other limit sets such as periodic orbits, it is possible to show that the MAP crosses the separatrix at the unique saddle point (see e.g. [173], [180], [185] and references therein). Thus, Figure 3.4 confirms the accuracy of the implemented gMAM for the system of interest. The second noteworthy feature of the phenotype transitions is that, as the level of noise, ϵ, decreases, the stochastic sample path follows the MAP more closely (compare Figures 3.4A and 3.4B for which $\Omega = \epsilon^{-1} = 70$ and $\Omega = \epsilon^{-1} = 450$, respectively). In addition, Figure C.2 illustrates the corresponding transition tubes (tubular neighbourhoods around the MAPs within which transitions between steady states occur) for these phenotype transitions.

To fully determine the CG transition rates, the prefactor value, $C_{x_k \to x_l}$, must be estimated.

(A) system size, $\Omega = 70$ (noise level, $\epsilon = 1/\Omega \approx 0.014$)

(B) system size, $\Omega = 450$ (noise level, $\epsilon = 1/\Omega \approx 0.002$)
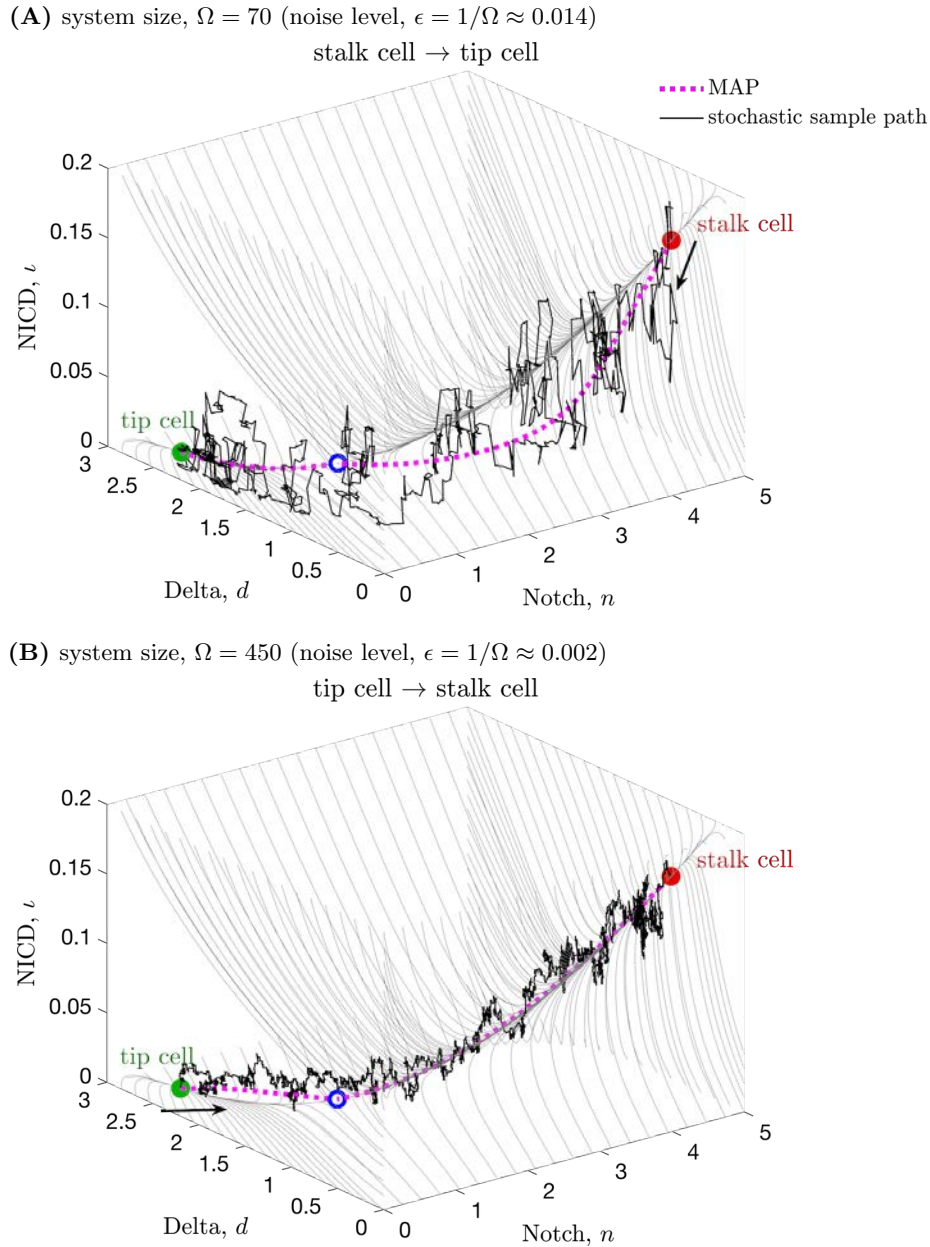
Figure 3.4. An illustration of the minimum action paths (MAPs) and stochastic sample paths for transitions between the tip and stalk cell phenotypes. We computed the MAPs (indicated by the dotted magenta lines) for the subcellular VEGF-Delta-Notch system in an individual cell using the gMAM for transitions from **(A)** stalk to tip cell and **(B)** tip to stalk cell. The stochastic sample paths obtained by simulating the full stochastic CTMC model (Table B.1) with the system sizes **(A)** $\Omega = 70$, **(B)** $\Omega = 450$, are plotted in black. The thin grey lines indicate streamlines of the corresponding mean-field system (Eq (B.4)). The tip (stalk) cell stable steady state is indicated by a green (red) filled circle; the unstable saddle by a blue unfilled circle. The plots represent three-dimensional projections of the full five-dimensional system as defined by Eq (B.4). Parameter values are fixed as indicated in Table C.1.

From Eq (3.7), for $k,\ l \in \{1, 2\}\,,\ k \neq l$, we have

$$\log\langle T^{\Omega}_{x_k \to x_l}\rangle \approx \Omega Q(x_k, x_l) - \log C_{x_k \to x_l}\ , \tag{3.8a}$$

$$\log C_{x_k \to x_l} \approx \Omega Q(x_k, x_l) - \log\langle T^{\Omega}_{x_k \to x_l}\rangle\ , \tag{3.8b}$$

where $\langle T^{\Omega}_{x_k \to x_l}\rangle = 1/\omega_{x_k \to x_l}$ is the mean passage time between the stable steady states, x_k and x_l (tip and stalk cell phenotypes), for a fixed value of the system size, Ω. $\langle T^{\Omega}_{x_k \to x_l}\rangle$ can be determined from direct simulation of the full stochastic model using the reaction kinetics given in Table B.1.

An accurate estimate of the quasipotential (as obtained via the gMAM) allows us to obtain the prefactor given the mean passage time, $\langle T^{\Omega}_{x_k \to x_l}\rangle$, for a single value of the system size, Ω. However, the approximate relation in Eq (3.8) is valid in the limit $\Omega \to \infty$ (see Figure 3.5). Thus, Ω should be chosen sufficiently large to achieve convergence in Eq (3.8) and, at the same time, not too large in order to ensure that transitions between the phenotypes occur in a computationally feasible time, since the waiting times for transitions between stable steady states increase exponentially as Ω grows. Specifically, since larger values of the quasipotential, $Q(x_k, x_l)$, in Eq (3.8) lead to longer mean passage times, a maximum simulation time, $\widehat{T}$, can be determined computationally by simulating the original stochastic system for the values of the external variables, u, for which the quasipotential is large (either $Q(x_k, x_l)$ or $Q(x_l, x_k)$). For the VEGF-Delta-Notch signalling pathway, the quasipotential is characterised by larger values close to the border of the bistability region. Thus, we performed several realisations of the full stochastic system, choosing several values of u for which at least one of the quasipotentials is large, and recorded the maximum simulation time, $\widehat{T}$, and the average prefactor estimate obtained, $\bar{C}$. The corresponding system size, $\overline{\Omega}$, is then approximated as follows:
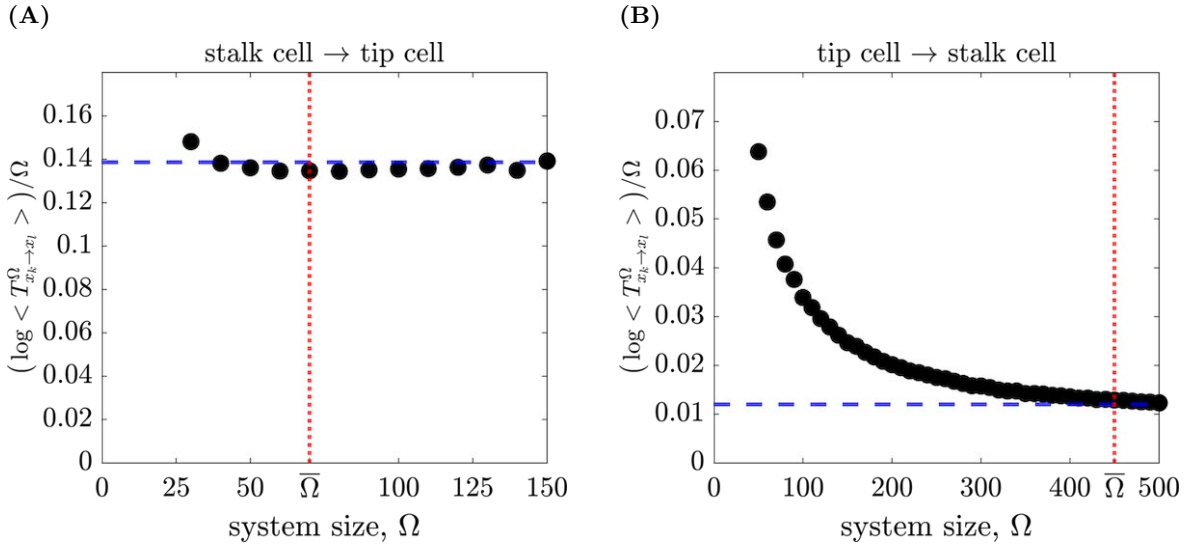
Figure 3.5. Convergence of the quasipotential, $Q(x_k, x_l)$, as the system size, Ω, increases. We ran 1000 realisations of the stochastic VEGF-Delta-Notch model for an individual cell (see Table B.1) for fixed values of $d_{ext} = 0.2$, $n_{ext} = 0.5$ and increasing system size, Ω. We plotted the convergence to the quasipotential value **(A)** $Q(\text{stalk}, \text{tip})$ and **(B)** $Q(\text{tip}, \text{stalk})$ as a function of Ω (black circle markers). For these parameter values, transitions from the stalk to tip cell phenotype are less likely to occur (higher noise levels, $\epsilon = \Omega^{-1}$, and/or longer transition times are needed) than transitions from the tip to stalk cell phenotype (see Eq (3.8a)). Therefore, the perturbations of this random event are smaller and convergence is reached for higher values of noise. This is why lower values of Ω in **(A)** suffice to accurately determine the prefactor value from Eq (3.8). The blue dashed lines indicate the value of the corresponding quasipotential computed via the gMAM; the red dotted lines indicate $\overline{\Omega}$ from Eq (3.9). All other parameter values are fixed as indicated in Table C.1.

$$\overline{\Omega} \approx \frac{\log \widehat{T} + \log \bar{C}}{Q(x_k, x_l)}. \tag{3.9}$$

Then the prefactor, $C_{x_k \to x_l}$, can be approximated using Eq (3.8b) with $\Omega = \overline{\Omega}$.

From Eq (3.8a), we know that $\log\langle T^{\Omega}_{x_k \to x_l}\rangle$ is a linear function of Ω whose slope and intercept are given by the quasipotential, $Q(x_k, x_l)$, and $(-\log C_{x_k \to x_l})$, respectively. Thus, in order to check the accuracy of our estimate for the system size, $\overline{\Omega}$, (Eq (3.9)) we compared linear fitting of data obtained from the full stochastic CTMC model for increasing Ω

with the estimate obtained from the gMAM quasipotential and the prefactor extracted from simulations with system size, $\overline{\Omega}$. The results presented in Figure 3.6 show that the estimates converge as Ω increases, confirming the accuracy of the two methods.
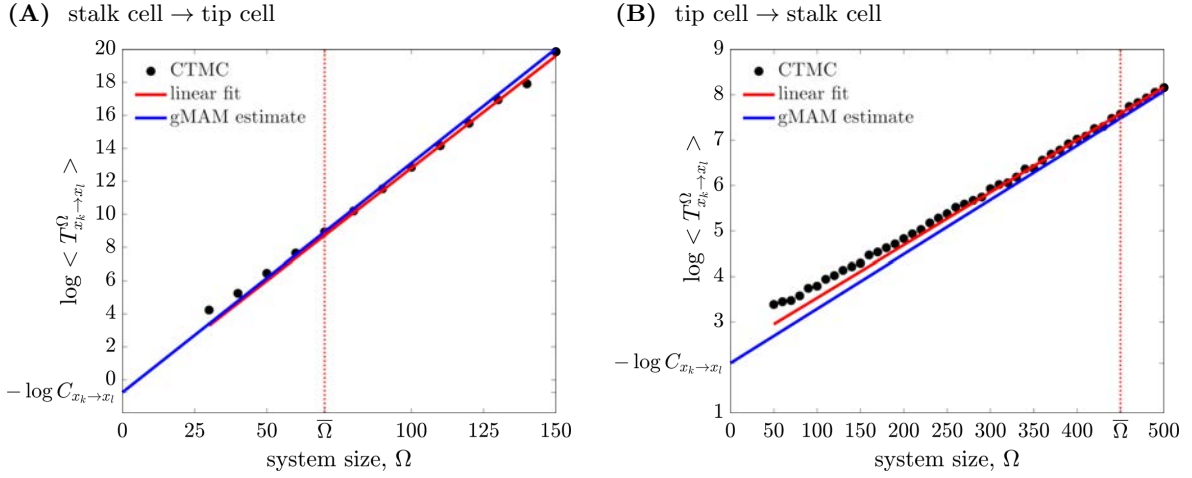

Figure 3.6. Prefactor estimation. Comparison of prefactor estimates obtained from simulations of the full stochastic CTMC model (black circles) and estimates obtained using the gMAM-quasipotential and mean passage times for a single value of the system size, $\overline{\Omega}$ (blue line), see Eq (3.8a). The linear fit of the full stochastic data (red line) was performed for values of Ω such that the corresponding sample $\left\{ T_{x_k \to x_l}^{\Omega} \right\}$ is exponentially distributed (high levels of noise might affect the distribution of these transitions). Panel **(A)** corresponds to the transition from stalk to tip cell phenotype; panel **(B)** corresponds to the transition from tip to stalk cell phenotype. The red dotted lines indicate $\overline{\Omega}$ from Eq (3.9). All other parameter values are fixed as indicated in Table C.1.

To summarise, we coarse-grain the stochastic VEGF-Delta-Notch dynamics as follows (see Figure 3.3):

I Fix the model parameter values and the vector of external variables, u, which, for this system, is given by the extracellular levels of Delta and Notch, $u = (d_{ext}, n_{ext})$.

II Compute the steady states of the corresponding mean-field system (Eq (B.4)).

III Formulate the CG model:

i If, for the given $u = (d_{ext}, n_{ext})$, the system is monostable (either tip or stalk cell steady state exists), then the quasipotential value to arrive at this state is 0. The value of the other quasipotential can be assumed infinite (since the system is monostable, this transition is impossible). For example, if the only stable steady state is the tip cell, then $Q(\text{stalk}, \text{tip}) = 0$ and $Q(\text{tip}, \text{stalk}) = \infty$. The CG model is defined by its unique stable steady state.

ii If the system is within the bistable regime (both tip and stalk cell steady states are stable), then the CG model is defined as a CTMC on the state space of $\{x_k, x_l\} = \{\text{tip, stalk}\}$. The transition rates are given by Eq (3.7). The quasipotential, $Q(x_k, x_l)$, is approximated using the gMAM; the prefactor value, $C_{x_k \to x_l}$, is obtained via Eq (3.8b) from stochastic simulations of the full VEGF-Delta-Notch model for a fixed value of the system size, $\overline{\Omega}$, defined by Eq (3.9).

IV The CG model can be simulated using any variant of the SSA, such as, for example, the classical Gillespie algorithm [65].

The above method generalises naturally for systems with an arbitrary number of stable steady states (see Figure 3.3). In this case, the quasipotential and the corresponding prefactor must be approximated for each pair of stable steady states. The method can also be applied to systems which possess other attractors, e.g. limit cycles [173], [175].

3.4.2 Multi-agent system

In this section, we show how the CG method can be applied to multi-agent systems with a region of multistability. In this case, the dynamics of *each* agent is coarse-grained to that of a CTMC between its stable steady states for given values of the external variables, u, which establish the coupling between the internal dynamics of individual agents (u depends on the state of agents in the local environment of the focal agent and/or time, and defines its internal state, e.g. phenotype). If the dynamics of an individual agent are independent of its
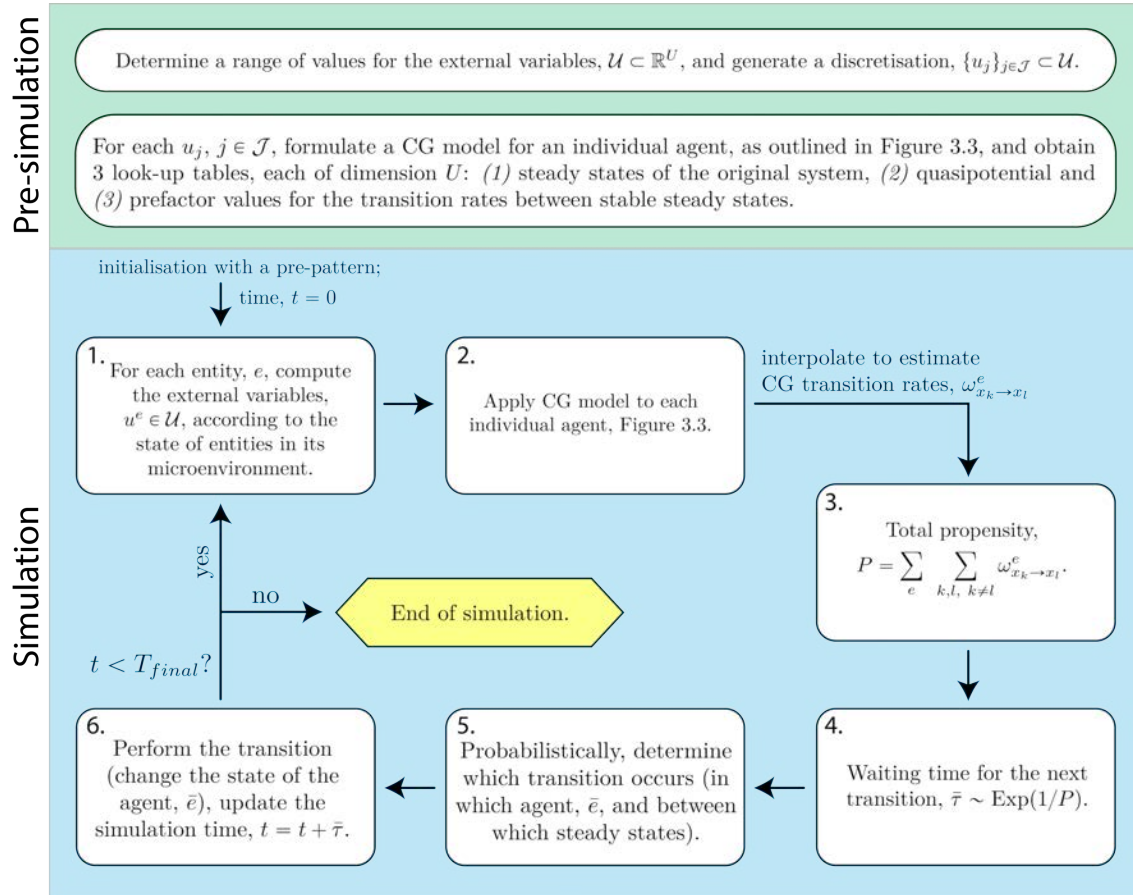
Figure 3.7. A flowchart of the procedure to coarse-grain a multi-agent stochastic system with a region of multistability. A pseudocode of the simulation algorithm for the multi-agent CG model is presented in Appendix C.4. The *simulation* part of the diagram illustrates an iteration of the Gillespie algorithm for simulation of multi-agent CG systems. Here T_{final} stands for the final simulation time; $\text{Exp}(\lambda)$ is an exponential distribution of intensity, λ.

neighbours and time (i.e. the values of the external variables are constant) then we use the CG method described in section 3.4.1 (see also Figure 3.3). A suitable range of values for the external variables, $u \in \mathcal{U}$, where $\mathcal{U} \subset \mathbb{R}^U$, can be determined by simulating the original multiscale model. Here U indicates the dimension of the vector of external variables, u. In order to reduce the computational cost in the multi-agent CG system, it is convenient to calculate *a priori* look-up tables for the steady states, quasipotential and prefactor values for a discretisation, $\{u_j\}_{j \in \mathcal{J}} \subset \mathcal{U}$ (here, j indexes entries in the generated discretisation; $\mathcal{J}$ is

the size of the discretisation). Interpolation routines can then be used to establish an input-output relationship between an arbitrary $u \in \mathcal{U}$ and the values of the corresponding steady states and the transition rates between them. Therefore, we split the general CG method for multi-agent systems into two steps (see Figure 3.7):

(i) **Pre-simulation:** calculate look-up tables for the system steady states, quasipotential and prefactor values for each entry in a discretisation, $\{u_j\}_{j \in \mathcal{J}}$, for a range of values of the external variables, $\mathcal{U} \subset \mathbb{R}^U$.

(ii) **Simulation:** the CG model is simulated (via, e.g., the Gillespie algorithm) as a CTMC on a state space defined by the steady states of all of its entities, with the coupling maintained via the external variables, u, updated at each simulation step according to entities' local environments and/or time.

We now provide more details on the pre-simulation and simulation steps.

Pre-simulation: look-up tables

Pre-computed look-up tables of system steady states, quasipotential and prefactor values are used to interpolate the values of the system steady states and the CG transition rates between them for an arbitrary set of values of the external variables, $u \in \mathcal{U}$, without calculating them explicitly at each step during simulations of the CG model. By an accurate estimation of the range of the external variables, $\mathcal{U}$, we ensure that these look-up tables need to be computed only once, prior to the simulation of the CG system. In a general setting, the dimension of each table is equal to U, the dimension of the vector of external variables.

The steady states must be computed numerically for each entry u_j in the discretisation, $\{u_j\}_{j \in \mathcal{J}}$, using the mean-field limit for an individual entity (as described in section 3.4.1). For values of u_j that fall within the multistability region, the quasipotential is computed via the gMAM in a pair-wise manner, for each pair of stable steady states, $\{x_k\}_{k=1}^{\mathcal{K}}$. The last look-up

table corresponds to the prefactor, $C_{x_k \to x_l}$, x_k, $x_l \in 1 \dots \mathcal{K}$, which must be approximated for each u_j within the multistability region. The prefactor values are obtained from Eq (3.8b) as before, using the mean passage times, $\langle T^{\Omega}_{x_k \to x_l} \rangle$, which are determined by simulating the full stochastic model with the system size, $\Omega = \overline{\Omega}$, defined by Eq (3.9).

Simulation algorithm

Once all the look-up tables have been computed, the multi-agent CG system can be simulated as a standard Gillespie algorithm (or one of its variants, e.g., Next Subvolume method [64]) in which the total propensity, P, at each time step is computed as a sum of transitions, $\omega^e_{x_k \to x_l}$, for each entity, e, to switch its (stable) state (see Figure 3.7). The steady states corresponding to each entity (and the transition rates between them) for the exact value of the external variables, $u^e \in \mathcal{U}$, (u^e has to be computed for each entity, e, according to its microenvironment) are interpolated via appropriate numerical routines. We present pseudocode for the simulation procedure in Appendix C.4.

Note that our CG method does not account for the initial, relatively short (compared to the LDT timescale), relaxation time during which the system relaxes onto the timescale on which the CG approximation is valid. Thus, it is necessary to obtain an initial stable steady state configuration, i.e to *pre-pattern* the system, using either the full stochastic CTMC or the mean-field model (see Figure 3.7 and line 5 in Algorithm 8). The final simulation time for the pre-patterning should be large enough to ensure that the system relaxes to an equilibrium. Since this procedure is performed only once, it does not affect the computational complexity of the CG simulations. We have chosen to use the mean-field system to pre-pattern our simulations since it is less time-consuming and the stochasticity (i.e. transitions between phenotypes) is preserved later in the CG simulation loop.

3.5 Results

For illustrative purposes, we consider the specific example of spatial phenotype patterning via the Delta-Notch lateral inhibition mechanism in response to an external signalling cue (VEGF). First, we provide more details about our implementation of the CG model and present typical simulation results and the robust patterns that emerge at long times. We then discuss the relative merits of the CG method, using a variety of metrics to compare its performance with the original stochastic and mean-field systems. We used the Next Subvolume method [64] (see Appendix B.4) for simulations of the full stochastic CTMC and the Euler-Lagrange method (explicit scheme) for the numerical integration of the mean-field equations.

3.5.1 Application to EC phenotype specification

The multicellular VEGF-Delta-Notch (i.e. the Delta-Notch signalling pathway coupled with external VEGF stimulation) model is bistable (see Appendix B.2). When simulated in a two-dimensional geometry, it produces 'salt-and-pepper' patterns in which the phenotypes of neighbouring cells alternate between tip and stalk cell states (see Appendix B.2). For this model, cross-talk between individual cells is achieved via external variables, d_{ext} and n_{ext}, which represent the non-dimensional levels of Delta and Notch, respectively, summed over cells in a circular neighbourhood with a fixed interaction radius, R_s (see Figure 2.3B and Appendix B.2). Hence, for this system, $u = (d_{ext}, n_{ext})$ defines a cell's internal state (phenotype) and the dimension of the pre-computed look-up tables is 2 (see section 3.4.2). We determined a suitable range, $\mathcal{U} = [0, d_{ext}^{max}] \times [0, n_{ext}^{max}] \subset \mathbb{R}^2$, for these variables by running 100 realisations of the multiscale model of angiogenesis (see Chapter 2; the number of realisations depends on the model of interest).

We then generated a regular discretisation of $\mathcal{U}$, $\{u_j\}_{j \in \mathcal{J}}$, with a grid 100×100. For each u_j in this grid, we computed the steady states for the mean-field limit defined by Eq (B.4)

using non-linear solvers from the C++ GNU Scientific Library (GSL). We note that, once the steady states of the full system have been computed, the subcellular variables ι, $r2$ and $r2^*$, corresponding to the Notch intracellular domain, VEGF receptor 2 (VEGFR2) and VEGF-VEGFR2 complexes, respectively, (see definitions in Appendix B.2) are redundant; it is not necessary to track these variables because the input-output relationship between $u = (d_{ext}, n_{ext})$, and the steady states completely defines the configuration of the system.

For values of u_j that fall within the bistability region, we computed the quasipotential values of the transitions between phenotypes (see Figure 3.8), using the gMAM (see Appendix C.1). We also used the full stochastic system to check those values of the quasipotential for which a phenotype switch is more likely to occur. As expected, most phenotype transitions occur close to the boundary of the bistability region, where values of the quasipotential are lower. For example, Figures 3.8A and 3.8B show a sample path of the full stochastic system for an individual cell during a simulation of the multi-agent model of angiogenesis (Chapter 2). The cell undergoes a noise-induced switch from a tip to a stalk cell phenotype. Figures 3.8C and 3.8D show the same sample path projected onto the quasipotential surfaces. These plots show that phenotypic switches are more likely to occur when the values of external Delta and Notch, (d_{ext}, n_{ext}), are such that the quasipotential, $Q(x_1, x_2) = Q(\text{tip}, \text{stalk})$, is small.

We constructed a look-up table of prefactor values, $C_{x_k \to x_l}$, x_k, $x_l \in \{\text{tip, stalk}\}$, by approximating the mean passage times, $\langle T^{\overline{\Omega}}_{x_k \to x_l} \rangle$, (sample size of 1000 realisations) for an individual cell to switch its phenotype from simulations of the full stochastic CTMC (Table B.1) with the system size, $\overline{\Omega}$, given by Eq (3.9).

We then implemented the CG model in C++ using Algorithm 8 in Appendix C.4. In order to establish an input-output relationship between an arbitrary $u = (d_{ext}, n_{ext})$ and the corresponding cell phenotypes and transition rates, we used bilinear interpolation routines from the C++ GNU Scientific Library (GSL) (*gsl_interp2d* routines). The model was then simulated using the standard Gillespie algorithm. We used no-flux boundary conditions to
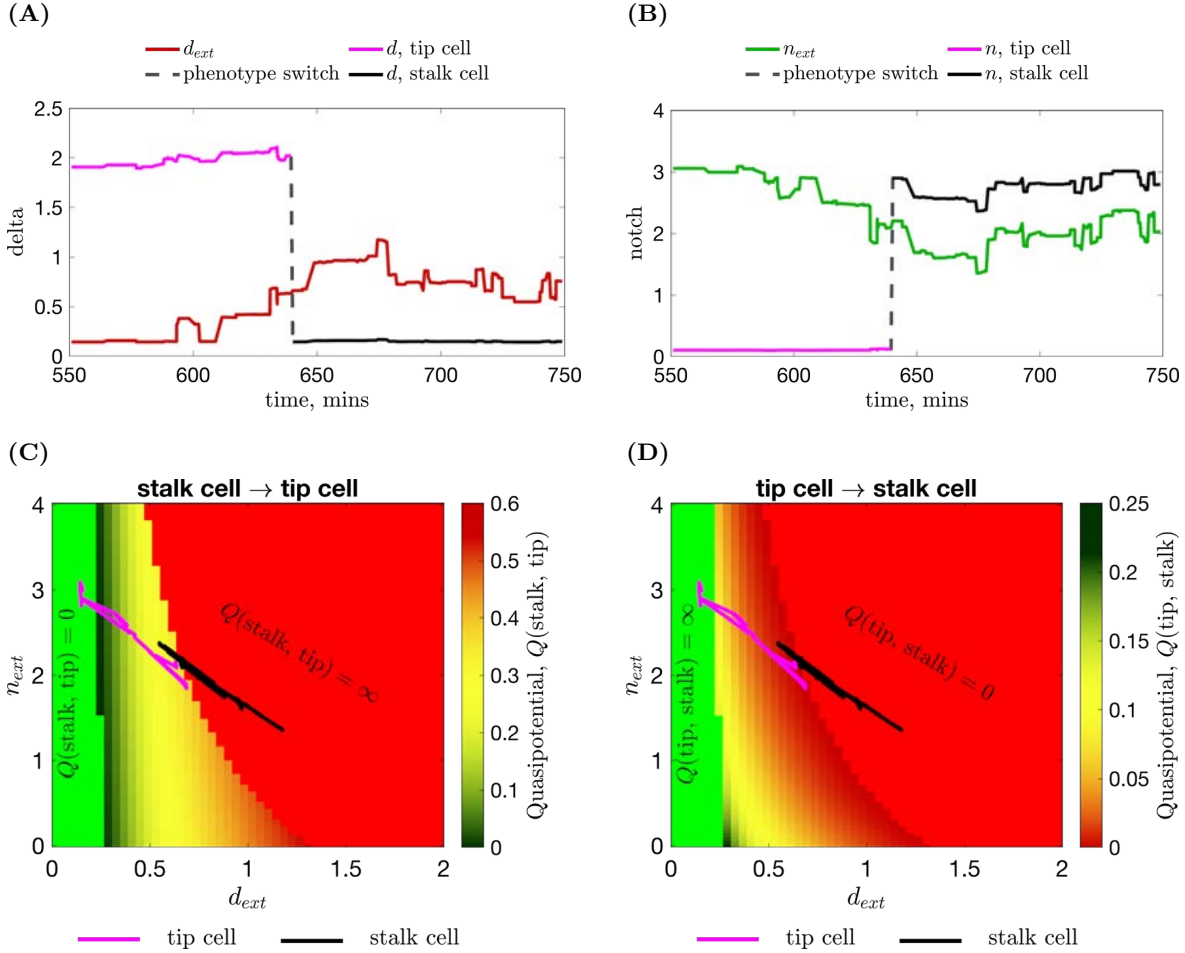
Figure 3.8. An illustration of the quasipotential surfaces. Upper panels: a noise-induced transition from tip (in magenta) to stalk cell (in black) phenotype of a single cell during a simulation of the angiogenesis model (Chapter 2) plotted as a function of the focal cell's **(A)** Delta and **(B)** Notch levels. The external Delta, d_{ext}, (Notch, n_{ext}) for the focal cell is computed as a weighted sum of the Delta (Notch) levels of its neighbours as defined by Eq (B.9). Lower panels: 2D projections of the quasipotential surfaces **(C)** $Q(\text{stalk}, \text{tip})$ and **(D)** $Q(\text{tip}, \text{stalk})$ as functions of d_{ext} and n_{ext}. The monostability region in which the unique stable steady state corresponds to a tip (stalk) cell is coloured green (red). The colour bar indicates the value of the corresponding quasipotential. The trajectory (as in panels **(A)** and **(B)**) plotted on the quasipotential surfaces (in **(C)** and **(D)**), illustrates that phenotype switches are more likely to occur for lower values of the quasipotential. Parameter values are fixed as indicated in Table C.1.

compute for each cell the extracellular levels of Delta and Notch in all our simulations.

3.5.2 Spatial phenotype patterning in the CG system

In order to illustrate the CG model, we first ran numerical simulations on a small cell mono-layer (10×12 voxels). The results presented in Figures 3.9A to 3.9D show how the distribution of tip and stalk cells changes over time during a typical CG realisation (see also Movie 3.1). Starting from an initial pre-pattern (Figure 3.9A), noise-induced phenotype transitions enable the system to explore different pattern configurations for the given geometry, while the proportion of tip cells remains on average constant (see Figure 3.9E).

The mean proportion of tip cells (and, thus, the spatial pattern) during simulations of the CG system depends on the interaction radius, R_s. For values of R_s corresponding to nearest-neighbours interaction ($R_s \leq 1.5h$, where h is the voxel width), we observe classical patterns of alternating tip and stalk cells (i.e. the so-called salt-and-pepper pattern [182]; see Figure C.4A). As R_s increases, the number of stalk cells that may be inhibited by a focal tip cell increases, causing the proportion of tip cells in the spatial patterns to decrease (Appendix B.2). Thus, for larger values of R_s ($R_s > 1.5h$), tip cells are separated by larger distances (see Figures C.4B to C.4D). These results for CG simulations are consistent with those obtained for the full multicellular stochastic model of the VEGF-Delta-Notch signalling pathway (Chapter 2). The ability of the CG system to explore different spatial patterns increases as the size of the interaction radius, R_s, grows, and the corresponding emerging patterns are more diverse (see Figures 3.9A to 3.9D and C.4B to C.4D).

It is noteworthy that spatial patterns explored in simulations of the CG model differ in their robustness to noise. In particular, the mean passage time for a phenotype switch, and, thus, a change in the pattern, to occur, which is equal to the inverse of the total propensity, P, depends on the values of the quasipotential, $Q(x_k, x_l)$, for all entities in the system. Here, the total propensity, P, for a phenotype switch event is defined as a sum of transition rates, $\omega^e_{x_k \to x_l}$, for each cell with index, e, to change its state from x_k to x_l, see Figure 3.7. When,
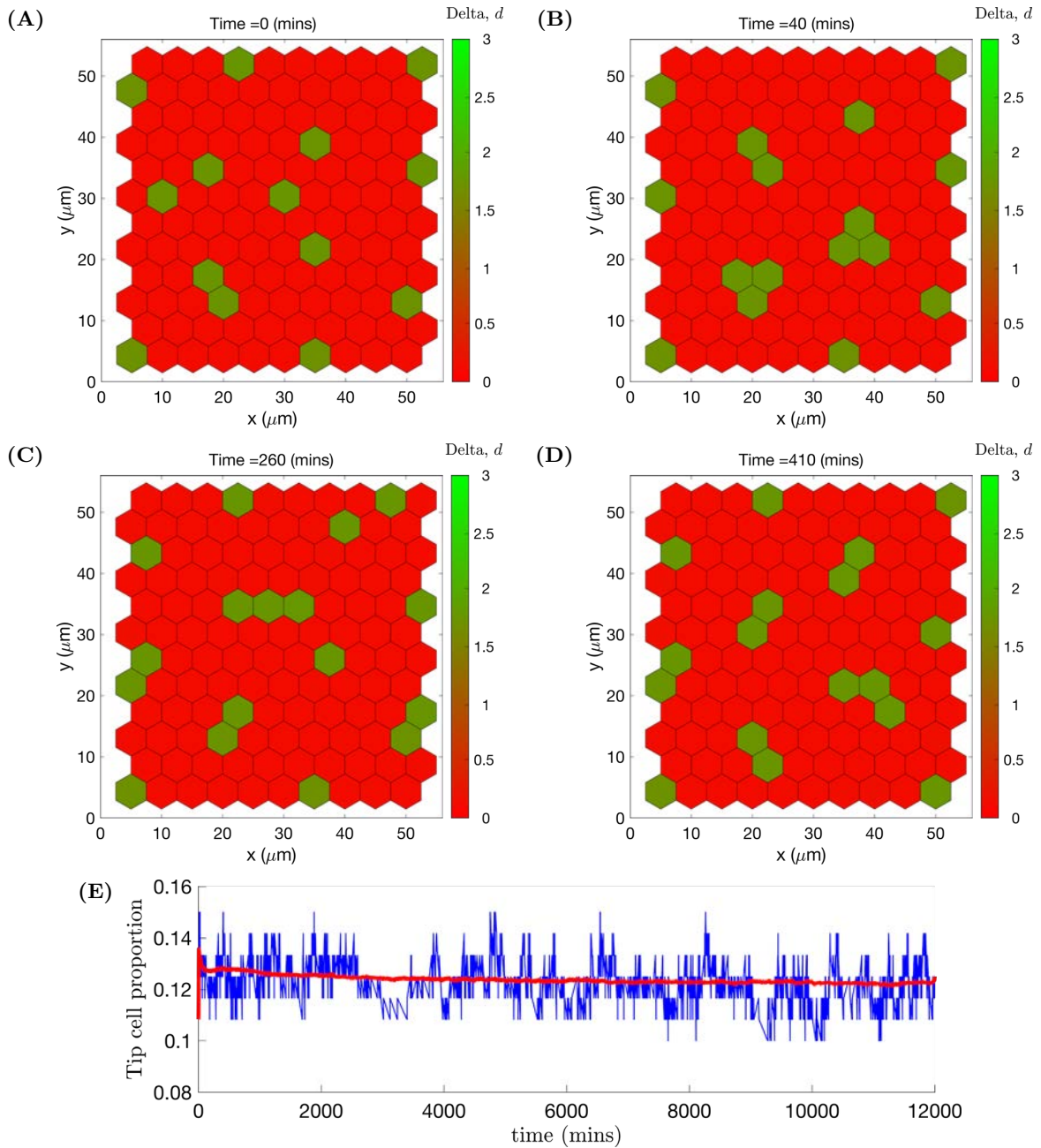
Figure 3.9. Different pattern configurations explored by the CG model. (A)-(D) Series of plots showing how the distribution of cell phenotypes changes over time during a single simulation of the CG model. The colour bar indicates the level of Delta. **(A)** $t = 0$; **(B)** $t = 40$; **(C)** $t = 260$; **(D)** $t = 410$ minutes. **(E)** Time evolution of the tip cell proportion (defined as a ratio of cells with the tip cell phenotype to the total cell number) for a single simulation of the CG model (blue line) and averaged over 1000 realisations (red line). For these simulations, the interaction radius and system size were fixed at $R_s = 15\mu m$ and $\Omega = 100$, respectively; the values of the remaining parameters were fixed as indicated in Table C.1.

via random exploration, the system finds a configuration for which the values of $Q(x_k, x_l)$ are larger, the waiting time for a phenotype switch increases and the configuration is more resilient to further changes.

This feature of the CG method facilitates exploration of new robust spatial patterns which cannot practically be achieved using other numerical frameworks: *(i)* simulations of the full stochastic model are too computationally intensive, which makes the exploration of these patterns infeasible because of the longer timescales needed; *(ii)* the deterministic framework does not allow for transitions between stable steady states, which makes this exploration impossible; *(iii)* the complexity of analytic methods needed to verify the stability of a pattern of a system with non-local interactions does not permit exploration of complex pattern configurations [186].

We now present simulation results which illustrate the ability of the CG method to uncover new spatial patterns for the VEGF-Delta-Notch system at long times. We fixed the interaction radius at $R_s = 3.0h = 15\mu m$ ($h = 5\mu m$ is the voxel width), so that interactions occur between cells that are first and second order neighbours in the lattice; the noise amplitude was fixed at $\epsilon = \Omega^{-1} = 0.001$. We ran a CG simulation on a medium size monolayer of cells (see Figure 3.10A and Movie 3.2). Starting from the initial pre-pattern, the CG model explores various patterns until it eventually settles on a more robust configuration (shown in Figure 3.10A). In order to confirm our prediction regarding pattern robustness, we plotted the temporal evolution of the total propensity of the lattice, P, in Figure 3.10B. As its value decreases, $P \rightarrow 0$, the mean waiting time for a change in the spatial pattern becomes infinite, which accounts for the robustness of the emerging pattern. We also considered the dynamics of an individual cell (its position in the monolayer is highlighted by a cyan line in Figure 3.10A). Figure 3.10C shows how the phenotype of this cell changes over time: at early times, the cell switches between tip and stalk phenotypes (low (high) values of subcellular Delta, d, correspond to stalk (tip) phenotype). As the spatial pattern settles to a robust configuration, the cell's environment, i.e. the levels of Delta of its neighbours, d_{ext}, stop
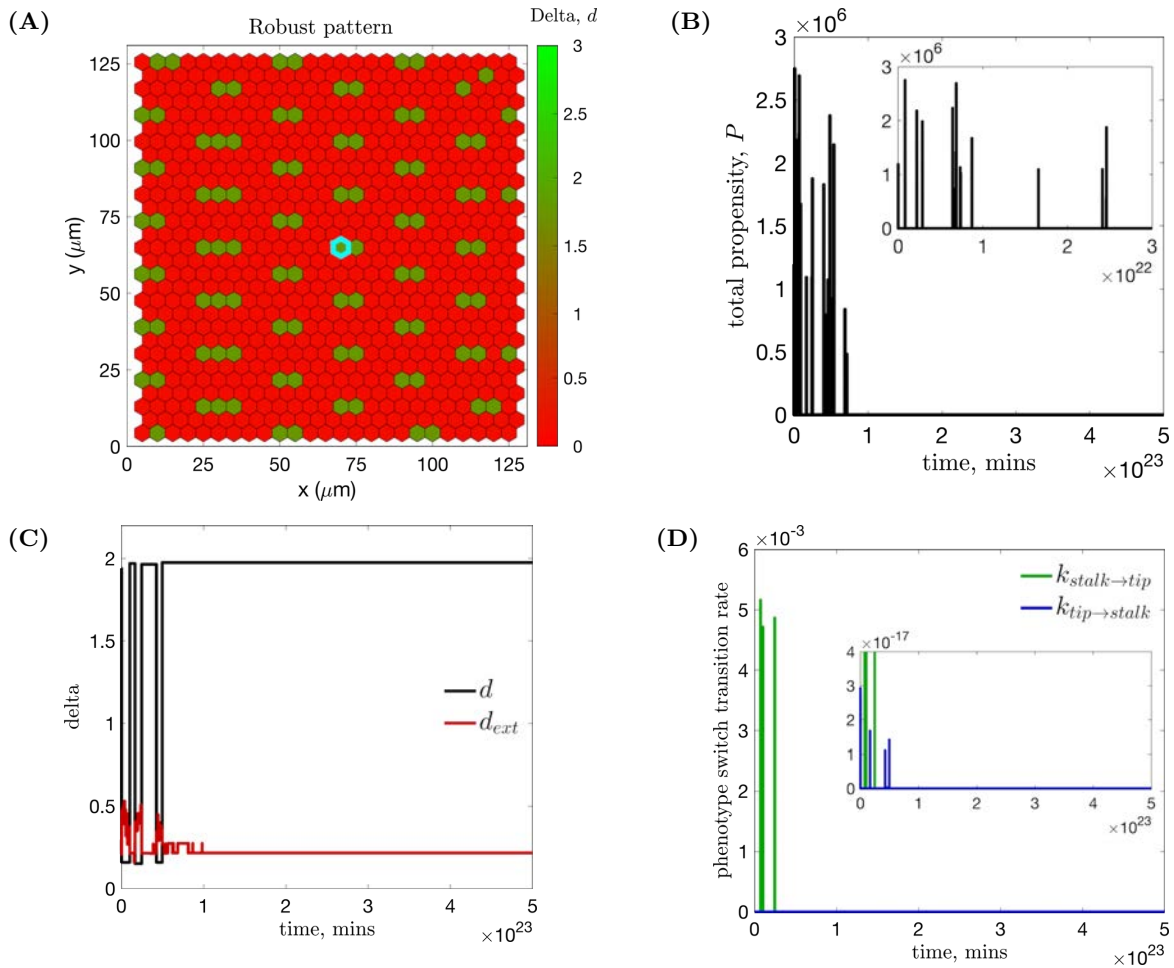
Figure 3.10. Emergence of robust pattern configurations in simulations of the CG model. At long times, via exploration of different pattern configurations, the dynamics of the CG system evolve to a robust pattern in which any further phenotype switches are unlikely. **(A)** A typical emergent pattern for a single realisation of the CG model (the colour bar indicates the level of Delta, d, for each cell). **(B)** The time evolution of the total propensity, P, for a phenotype switch to occur. Cells in the border rim (three-cell width) are excluded from P since, due to the model geometry, they do not possess a 'robust' configuration of neighbours. As P decreases to 0, the waiting time for a phenotype switch to occur approaches infinity, and the pattern becomes more robust to change. **(C)-(D)** The dynamics of an individual cell (outlined in cyan in **(A)**) during this simulation. **(C)** Temporal evolution of the internal level of Delta, d, (defining cell phenotype: high (low) values of d correspond to tip (stalk) cell phenotype) and that in its microenvironment, d_{ext}. **(D)** Temporal evolution of transition rates for a phenotype switch for this cell. We note that the large difference in the order of values for transition rates for the total propensity, P, of the lattice ($O(10^6)$), plot **(B)**, and for an individual cell ($O(10^{-17}) - O(10^{-3})$), plot **(D)**, comes from the contribution to P of transition rates for cells which are, for the given values of the external variables, on the border of the bistability region (see Figure 3.8). For these simulations, the interaction radius and system size were fixed at $R_s = 15\mu m$ and $\Omega = 1000$, respectively; the values of all remaining parameters were fixed as indicated in Table C.1.

changing and the cell acquires a tip phenotype that remains unchanged for the rest of the simulation. The transition rates for phenotype switches for this cell (Figure 3.10D) exhibit similar dynamics to the total propensity, P, of the whole lattice (Figure 3.10B).

Our CG simulation results show that this robust pattern configuration is not unique. However, we note that the spatial patterns tend to have a regular structure; for example, tip cells may be organised in similar clusters comprising two or three cells as in the pattern shown in Figure 3.10A. These configurations have lower values of the total propensity, P. Cells on the border of the lattice undergo phenotype switches (see Movie 3.2), since they cannot attain this 'more robust' combination of neighbours for the given geometry (since we use no-flux boundary conditions in our simulations).

3.5.3 Comparison of the full stochastic, CG and mean-field descriptions

We compared the dynamics of the multicellular VEGF-Delta-Notch model using three frameworks:

(i) **full stochastic CTMC** in which each cell's dynamics is given by the set of kinetic reaction rates listed in Table B.1 of Appendix B.2;

(ii) **CG description** formulated as in section 3.5.1;

(iii) **deterministic mean-field description** in which each cell is equipped with a set of deterministic ODEs (see Eq (B.9) in Appendix B.2).

Simulated (using any of these frameworks) on a 2D domain, the model produces a characteristic pattern of ECs with two cell phenotypes (see, for example, Figures 3.9 and C.4). Since the CG approximation describes the long-term behaviour of the system, when its evolution is dominated by the timescale associated with phenotypic switches, it does not account for the initial relaxation onto a quasi-steady state pattern. Thus, the three frameworks cannot be compared with respect to their behaviour at early evolution times. Instead, we quantified the final pattern and the computational cost of simulations. The final simulation time, $t = T_{final}$,

was chosen sufficiently large to ensure that a steady state pattern had been established for the mean-field simulations (since stochastic systems do not have a steady state pattern in a classical sense). In order to systematically compare the three frameworks, we used the same final simulation time, $t = T_{final}$, for the other two systems.

We used the following set of metrics to compare the dynamics of the three mathematical descriptions (see also Appendix C.5):

- **tip cell proportion**, which is defined as the ratio of the number of cells with tip cell phenotype to the total number of cells in the system;

- **distribution of tip cell clusters**, which provides a breakdown of sizes of tip cell clusters (adjacent cells with tip cell phenotype, e.g., a single tip cell, two adjacent tip cells, etc.) in a steady pattern configuration;

- **computational cost**, which is defined as the average CPU time (in seconds) to perform a single realisation of model simulation.

Since the pre-calculated look-up tables for the CG simulations (section 3.4.2) were computed for a fixed set of model parameters (see Table C.1), we held them fixed for all simulations. However, the cell-to-cell interaction radius, R_s, which is used in the multicellular simulations to determine for each cell, e, the vector of extracellular variables, $u^e = (d_{ext}^e, n_{ext}^e)$, may vary. In our simulations, we used $R_s \in \{5, 7.5, 10, 12.5, 15\}$ μm which correspond to experimental observations of the distance over which cell-to-cell interaction can occur in endothelial cells [34] (which corresponds to up to three cells in the interaction circle). Nonetheless, from a theoretical point of view, this quantity can take any value greater than the half-width of a voxel, $R_s > 0.5h$, where h is the voxel width (we fix $h = 5\mu m$ in our simulations). In addition, for the full stochastic CTMC and CG descriptions, we vary the noise amplitude, $\epsilon = 1/\Omega$, by changing the system size parameter, Ω. We used $\Omega \in \{50, 100, 200, 500, 1000\}$. The larger the value of Ω, the closer will be the dynamics of a stochastic system to its mean-field description. For each numerical setup (R_s and Ω), we ran 100 realisations.

We considered two simulation geometries: a 2D cell monolayer and a branching network.

Setup 1: a cell monolayer We first ran numerical simulations on a cell monolayer (see Figure C.5). This spatial geometry was motivated by the biological process of cell fate specification induced by lateral inhibition via Delta-Notch signalling in flat domains. Examples of such cell fate specification include bristle patterning in *Drosophila* notum [187]–[189], and differentiation of neural precursors in neurogenesis [190] (see [183], [191] and references therein for other examples). The fixed stationary distribution of the VEGF serves as an external stimulus which enhances lateral inhibition via Delta-Notch signalling. We chose VEGF as an illustrative example, although, depending on the specific system, other extracellular signals will provide cell stimulus.

We began by considering the dynamics of the tip cell proportion for this spatial geometry (see Figure 3.11A). Consistent with the previous results (Chapter 2), for all simulation frameworks (i.e. the full stochastic (CTMC), CG, and mean-field descriptions), the tip cell proportion decreases as the cell interaction radius, R_s, increases. Figure 3.11A confirms that, as expected, differences in this metric between the three systems decrease as the level of noise is reduced (i.e. as Ω increases). In particular, for high noise levels (i.e. lower values of Ω), the patterns generated by the stochastic systems (full CTMC and CG frameworks) are more diverse, and the tip cell proportions differ from those for the associated mean-field description. We note that each cell is not an isolated system, its dynamics are affected by the noisy behaviour of its neighbours and the model geometry. This explains why we observe variations in the tip cell proportion for lower values of Ω for the full CTMC and CG frameworks. We also note that the dynamics of the tip cell proportion for the mean-field system (red lines) are identical in all subplots in Figure 3.11A since noise is absent in deterministic systems (i.e. the system size parameter, Ω, is irrelevant).

We also quantified the size distribution of the tip cell clusters associated with the final patterns established on the cell monolayers. Since the dynamics of the three systems converge
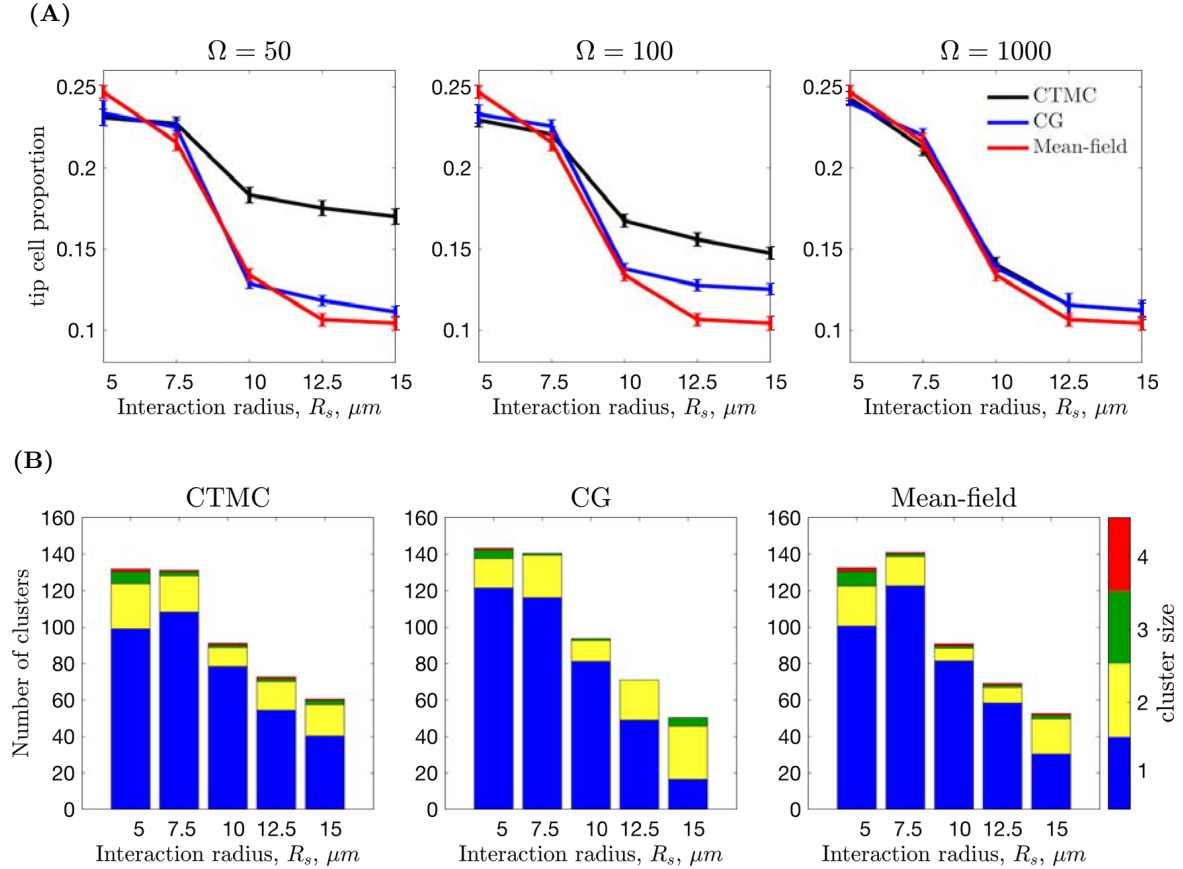
(A)

(B)

Figure 3.11. Comparison of the dynamics of the multicellular VEGF-Delta-Notch model simulated on a cell monolayer using the full stochastic (CTMC), CG, and mean-field descriptions. (A) The tip cell proportion as a function of the cell-to-cell interaction radius, R_s, for varying noise amplitude, $\epsilon = 1/\Omega$ (the value of Ω is indicated in the title of each plot), for the full stochastic CTMC (black), CG (blue) and mean-field (red) descriptions. To explore different possible patterns in the deterministic mean-field system, we created a small initial perturbation to the initial configuration (Figure C.5). **(B)** A series of bar plots showing how the long-time distribution of tip cell clusters changes as the interaction radius, R_s, varies for the full stochastic CTMC (left panel), CG (middle panel), and mean-field (right panel) systems. The number of single tip cells in the final pattern (i.e. at a fixed final simulation time) is shown in blue; the number of clusters with 2, 3, and 4 adjacent tip cells is shown in yellow, green, and red, respectively. For these simulations, we fixed $\Omega = 1000$ ($\epsilon = 0.001$). The results are averaged over 100 realisations. The remaining parameter values were fixed as indicated in Table C.1.

for larger values of the system size, Ω (as shown in Figure 3.11A), Figure 3.11B shows results for this metric computed for simulations with $\Omega = 1000$. The distributions are in good quantitative agreement for the three systems. The discrepancy for simulations with larger cell interaction radius (e.g. $R_s = 15\mu m$) arises because (for this value of Ω) the CG system is more likely to explore long timescale patterns which have a more 'regular' structure and are more robust to noise (cells with tip cell phenotype organised in similar clusters, see section 3.5.2).

Setup 2: a branching network We next considered a more complex spatial geometry of a small branching network (see Figure C.6) extracted from a simulation of a hybrid model of angiogenesis (Chapter 2). Figure C.7 shows a series of patterns explored by the CG system at different time points during a typical simulation for this configuration (for the full simulation, see Movie 3.3).

For this spatial configuration, we compared the three simulation frameworks using the same metrics as for the cell monolayer. The results for the tip cell proportion are presented in Figure C.8A. We find that the number of possible patterns generated by lateral inhibition is lower for the branching network geometry than for the cell monolayer (see Figure C.7). Consequently, the tip cell proportions converge for smaller values of Ω (compare Figures 3.11A and C.8A). We also note that, since, in the network configuration, cells have fewer neighbours, the values of this metric are higher than those computed for a cell monolayer.

Figure C.8B shows the size distribution of tip cell clusters for simulations on the branching network. We note that, for this configuration, isolated tip cells (i.e. cells not adjacent to another tip cell) are predominant in the final spatial patterns and the patterns generated by the three frameworks are comparable.

Regarding the computational cost (see technical specifications of computers used in File 3.1), the CG method showed a great reduction in the average CPU time compared to the original stochastic system when performing a single realisation (see Figure 3.12). Whereas the

numerical cost of simulations of the full stochastic system (Figure 3.12, left panels) increases exponentially as the system size, Ω, grows, simulations of the CG system decrease in average computational time as Ω increases (Figure 3.12, middle panels). This is because, as the noise level decreases (i.e. Ω increases), fewer transitions occur in a CG simulation for a fixed final simulation time. Interestingly, the CG simulations are also faster (see Figure 3.12, right panels) than the numerical integration scheme used for the mean-field system (we used the explicit scheme for the Euler-Lagrange method, although other schemes for numerical integration may show better performance). This scheme required evaluation of the non-linear right-hand-side of the mean-field equations (see Eq B.9 in Appendix B.2) at each time step for every voxel in the lattice, whereas for the CG simulations only one voxel undergoes a change (i.e. a phenotype switch) at each iteration and an update is required only for a local neighbourhood of this voxel. Therefore, fewer updates are required in the CG system (which are further decreased as Ω grows). In addition, the transition rates for phenotype switches needed for CG updates are interpolated directly using the pre-calculated look-up tables (see section 3.4.2) which reduces the amount of computations required (as compared to the evaluation of the right-hand-side of the deterministic system). This explains why the mean CPU time for CG simulations is smaller (except for high noise levels, $\Omega = 50$) than for the numerical scheme we used for the associated deterministic system (see Figure 3.12, middle and right panels).

To summarise, the CG method, while preserving stochasticity of transitions between cell phenotypes and producing spatial patterns comparable to those generated using the original stochastic and mean-field descriptions, significantly reduces computational time of simulations.

3.6 Discussion

Hybrid (multiscale) models of complex biological phenomena are often computationally in-efficient, which hinders their potential utility. To address this issue, we have developed a
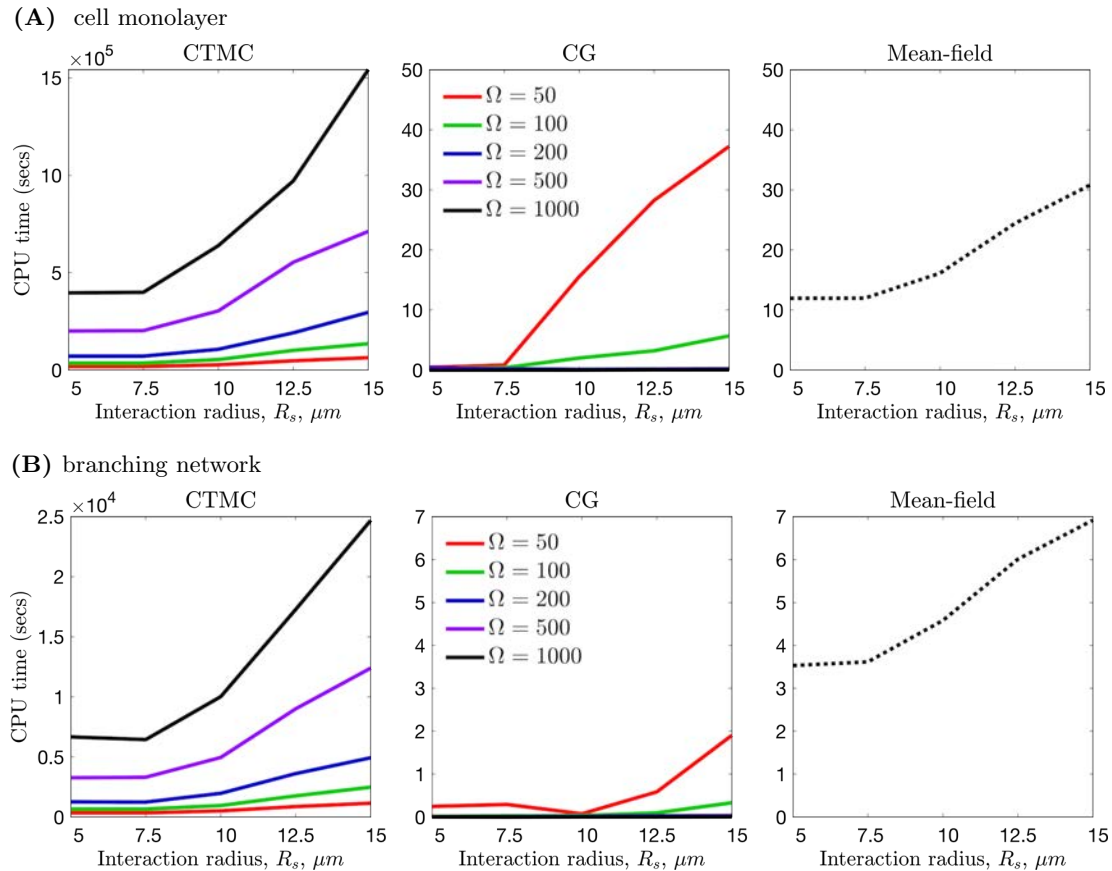
(A) cell monolayer

(B) branching network

Figure 3.12. Comparison of the mean CPU times to simulate the multicellular VEGF-Delta-Notch model. The plots show how the average (100 realisations) CPU times (in seconds) to perform a single realization using the full stochastic CTMC (left panels), CG (middle panels), and mean-field (right panels) descriptions changes as the cell-to-cell interaction radius, R_s, and the system size, Ω, vary. The colour code indicates the system size, Ω (shown as insets in the middle panels); the mean-field description (dotted black line) corresponds to the limit $\Omega \to \infty$. The simulation setup was **(A)** a medium size cell monolayer, and **(B)** a small branching network. For both spatial geometries, the average CPU time for simulating the full stochastic CTMC is several orders of magnitude larger that those for CG and mean-field descriptions. For these simulations, the parameter values were fixed as indicated in Table C.1.

coarse-graining (CG) method that reduces the numerical cost of simulations of multi-agent stochastic systems with multiple stable steady states. The CG technique is based on large deviation theory that allows to reduce the dynamics of a stochastic system to a jump process (i.e. a continuous time Markov chain) on a discrete state space which comprises the stable steady states of all agents in the system. The CG system operates on a timescale on which transitions between these steady states take place. This allows the method to be applied to models whose dynamics act on timescales longer than the typical timescale for relaxation to an equilibrium (e.g., molecular or subcellular processes act on longer timescales when compared to higher spatial scales such as cell migration, dynamics of extracellular cues, etc.). Our results show good qualitative and quantitative agreement between CG simulations and other simulation methods (Figures 3.11 and C.8). Furthermore, the CG algorithm is numerically more efficient in terms of CPU time even when compared with the corresponding mean-field simulations (see Figure 3.12). Likewise, the CG framework allows exploration of new emergent properties of the system, such as long timescale patterns in multicellular systems (Figure 3.10).

The implementation of the CG method requires pre-calculation of several look-up tables (for stable steady state solutions of the system that is being coarse-grained, quasipotential values for transitions between them and the corresponding prefactor of these transitions) which are used later in simulations. To do this, the values of model parameters must be fixed (except for the external variables). However, in order to perform sensitivity analysis with respect to any specific parameter, this parameter may be added to the set of external variables (thus, adding a new dimension to the look-up tables). Since the procedure of pre-calculating the look-up tables is done once, prior to model simulation, it does not increase the numerical cost of the algorithm. Likewise, the computational cost of computing the quasipotential via the geometric minimum action method (gMAM) is independent of the system size, Ω, and an estimate for the required prefactor can be obtained from simulations of the full stochastic model for a single value of the system size parameter, Ω, for which we provided an accurate

estimate (see Eq (3.9) and Figure 3.6). Then the CG model can be efficiently simulated using the standard Gillespie algorithm for any value of Ω (or, equivalently, noise level, $\epsilon = 1/\Omega$).

After introducing the CG method (section 3.4), we applied it to a multi-agent model of phenotypic specification of cells via the VEGF-Delta-Notch signalling pathway. For this system, we demonstrated how the spatial patterning of cells with different phenotypes changes as CG transitions between these steady states (phenotypes) occur (Figure 3.9). We then confirmed that the patterns generated by the CG system are quantitatively similar to steady state configurations of the original stochastic system and the associated mean-field limit for this model (see Figures 3.11 and C.8). We conclude that the CG method preserves the continuous cell phenotypes and stochasticity of the original system, while reducing the computational cost of simulations by several orders of magnitude (as compared to the numerical cost of simulations of the full stochastic system, see Figure 3.12).

In this chapter, we used the VEGF-Delta-Notch model to illustrate the benefits of the CG method. We note, however, that the CG method can be applied to a wider class of multi-agent models in which the behaviour of the agents is regulated by stochastic models with multiple stable attractors (e.g. steady states, limit cycles) and whose dynamics are controlled by external cues (e.g. morphogens, growth factors, levels of specific ligands/receptors in neighbouring cells, etc.). Examples of systems with subcellular dynamics which satisfy the requirements for application of the CG method include fate specification of cells in intestinal crypts [171], [192], epithelial to mesenchymal phenotypic transition (and its reverse) in cancer invasion [193] and development [194], cell differentiation in neurogenesis [190], and a general class of models describing cell decision switches [151]. These models are multistable and the timescale of simulations is longer than the timescale of the relevant subcellular signalling pathway. Nonetheless, the spectrum of models which are suitable for coarse-graining via the CG algorithm is not restricted to intracellular signalling pathways in animal cells; other examples include vegetation patterning in arid ecosystems [195] or plant morphogenesis mediated via the auxin hormone [196], [197]. The exact implementation of the CG system

for the aforementioned models is beyond the scope of this thesis.

Chapter 4

Large-scale simulations of the multiscale model of angiogenesis

4.1 Summary

In this chapter, we extend our multiscale model of angiogenic sprouting so that it can simulate longer timescales of days to weeks. To do so, we use the CG method to reduce the computational complexity of the subcellular components of the model, which determine cell phenotype specification. We confirm the validity of this model reduction by comparing metrics extracted from simulations of the original and CG phenotype models. We also incorporate into our model processes that operate on longer timescales, such as cell proliferation and vessel maturation. The implementation of these processes is based on available experimental data. This allows us to perform large-scale simulations and investigate the effects of varying cell cycle speed on vasculature expansion. Our simulation results agree with experimental observations, which show that the duration of the cell cycle affects the supply of cells into the growing network due to proliferation and not migration. In particular, faster cell cycles lead to larger vascular networks. Nonetheless, the branching structure, characterised by the average number of branching points per fixed network area and average vessel length, is preserved for different proliferation rates. The large-scale simulations allow us to further validate our model by comparing distances between cell nuclei in our simulations with data extracted from experimental images. To sum up, we illustrate the potential of the CG method for decreasing the computational complexity of hybrid multiscale models by applying it to

our angiogenesis model. This framework allows us to perform simulations on the timescale associated with angiogenic sprouting *in vivo* and to explore vasculature growth in different (numerical) scenarios.

This chapter is organised as follows. We first motivate the application of the CG method to our multiscale model of angiogenesis in section 4.2. In section 4.3, we incorporate CG phenotype specification into the subcellular scale of the angiogenesis model and validate it by comparing the statistics extracted for the coarse-grained and original models. We then extend the model by incorporating cell proliferation and vessel maturation in sections 4.4 and 4.5, respectively. The results of our numerical simulations are reported in section 4.6. Therein, we demonstrate that vessel maturation is necessary for the formation of vascular networks (section 4.6.1), investigate the effects of varying cell proliferation rates on vasculature growth (section 4.6.2) and perform further model validation by comparing distributions of cell nuclei within networks to experimental data (section 4.6.3). Finally, we summarise our findings and discuss possible directions for future work in section 4.7.

4.2   Motivation

In Chapter 2, we formulated a multiscale model of angiogenesis which allowed us to accurately capture complex EC behaviour during the early stages of vasculature outgrowth. A key component of the model is dynamic cell crosstalk via the VEGF-Delta-Notch signalling pathway. ECs adapt their subcellular gene expression pattern to changes in their local microenvironment, which results in heterogeneous EC behaviour determining the branching structure of the growing vasculature. In order to capture noise-induced phenotype transitions (see Figure 3.1), the subcellular EC signalling was implemented stochastically. This led to an increase in the computational complexity of the model and did not permit simulation of larger vascular networks. We concluded that we must reduce the numerical cost of our model in order to simulate the formation of larger networks over longer timescales.

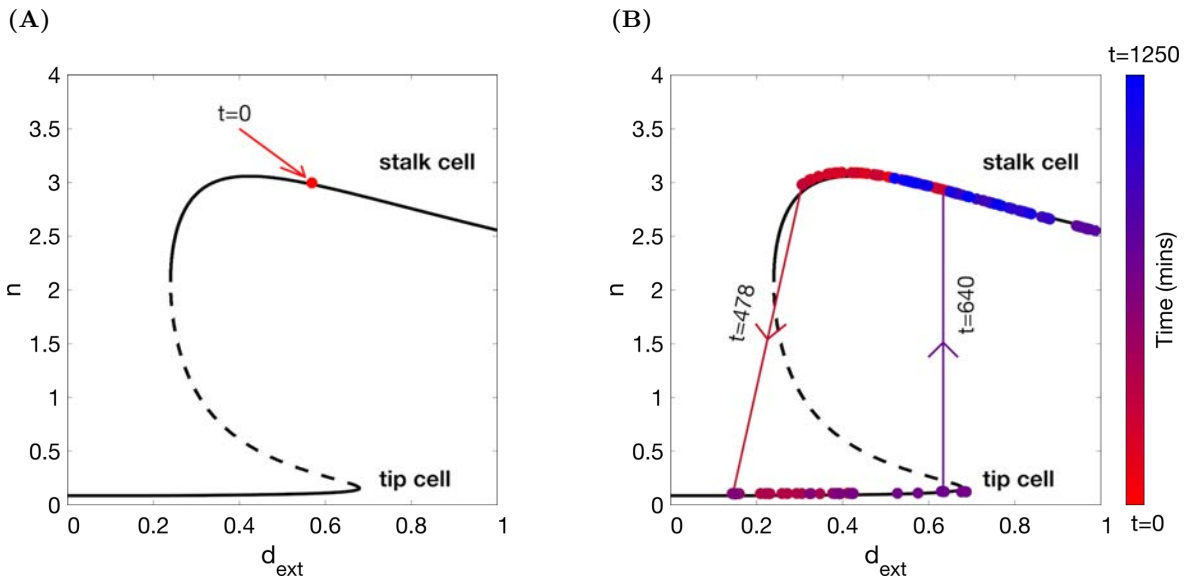One way to decrease the computational cost of our model is to coarse-grain the subcellular

Figure 4.1. An illustration of phenotype switches during a simulation of our multiscale model of angiogenesis. Notch concentration, n, of a representative cell **(A)** at the beginning of simulation ($t = 0$); **(B)** during simulation of the multiscale angiogenesis model (Chapter 2) as the function of the cell's extracellular Delta signal, d_{ext}. The black lines on both panels correspond to a bifurcation curve (as in Figure B.3B) for a fixed value of n_{ext} (although this value changes together with d_{ext} in the simulations of our angiogenesis model, the bifurcation curve does not change significantly, so just one curve was plotted for simplicity). Arrows indicate phenotype switch transitions for the representative cell with the corresponding times. The colour bar represents simulation time.

model of EC signalling which determines cell phenotype, using the coarse-graining (CG) method formulated in Chapter 3. The VEGF-Delta-Notch signalling pathway acts on a shorter timescale than other processes (e.g. cell migration, cell-ECM interaction at the tissue scale; see Chapter 2) involved in our multiscale model which allows us to use this method. The CG technique reduces the full stochastic model of phenotypic specification to a Markov chain model on a state space of EC phenotypes (tip and stalk cell) thus substantially reducing the computational complexity of the subcellular scale.

First, we provide an illustration which motivates the application of the CG method to our hybrid model of angiogenesis. In Figure 4.1B, we plot the non-dimensional Notch concentration of an individual cell during a single realisation of the angiogenesis model. The arrows

on this plot indicate the times at which the focal cell switches its phenotype. For example, a phenotype switch from stalk to tip at $t = 478$ minutes indicates that, during the simulation, the neighbourhood of the focal cell (given by external, i.e. belonging to neighbouring cells, levels of Delta and Notch, $\{d_{ext}, n_{ext}\}$) changed and the cell adjusted its phenotype accordingly. However, the phenotype switch, from tip to stalk, at $t = 640$ minutes is noise-induced since the cell's neighbourhood (i.e. d_{ext}) did not change at that time. Phenotype transitions of this type cannot be accounted for by the deterministic mean-field limit whereas the CG method allows for their precise quantification. Likewise, Figure 4.1B confirms that fluctuations away from the mean-field steady state values are small since the simulated trajectory of the focal cell (circled markers) lies in a narrow neighbourhood around the deterministic bifurcation curve. This strengthens the case for the application of large deviation theory to coarse-grain the dynamics of this system.

Coarse-graining of subcellular EC signalling allows us to simulate the model for longer times (in Chapter 2, final simulation time was ≈ 20 h). If we increase the timescale of our simulations then we need to take into account cell proliferation, which occurs on the timescale of days (EC cell cycles have been estimated to vary from 12 h to 4 days [42]–[44], [198], [199]). On the other hand, activation of ECs by VEGF increases their ability to survive and protects them from undergoing programmed cell death (apoptosis) [200]. In the later stages of angiogenesis, when levels of pro-angiogenic stimuli (such as VEGF) decrease because the newly formed vasculature oxygenates the tissue, an anti-angiogenic switch marks the transition from the sprouting to the remodelling phase [22]. Vasculature remodelling occurs via systematic pruning of blind-ended and tortuous vessels by inducing cell apoptosis [22], [48]. Since we limit our model to the sprouting phase of angiogenesis (characterised by active cell migration and proliferation), at this stage of our work, we neglect EC death in what follows.

Our multiscale model of angiogenesis was initially motivated by a series of short-time (hours) *in vitro* experiments [4], [10], [126]. The large-scale simulations (on the timescale of

days to weeks) that we aim to perform in this chapter resemble more closely the evolution of vascular growth *in vivo* (e.g. postnatal vascularisation of retina in mice [26]). However, in a living system, other processes that have been neglected in our model influence the growth of the vascular network. Examples of such processes include the onset of blood flow, which remodels the initial branching network and induces cell quiescence in mature vessels [2], [22], EC interactions with smooth muscle cells (pericytes and murine cells) which promote vessel stabilisation [2], [22], and changes in the distribution of VEGF as the vasculature expands [201]–[203]. Our goal in this chapter is to extend our model simulations to the timescale of days and to determine whether we can simulate functional branching networks at this scale by taking into account only cell migration and proliferation.

4.3 Incorporating the CG system into the multiscale model of angiogenesis

In Chapter 3, we showed examples of spatial phenotype patterning produced by the CG system for the VEGF-Delta-Notch signalling pathway when a constant VEGF concentration was imposed across the domain (i.e. a cell's state is determined by the external levels of Delta and Notch, (d_{ext}, n_{ext}), of its cell neighbours). In Chapter 2, we used our angiogenesis model to perform simulations in response to fixed uniform concentration profiles of VEGF and also VEGF gradients. In these simulations, cell phenotype is determined by a set of external variables, $u = (d_{ext}, n_{ext}, v_{ext})$, where v_{ext} indicates the local level of VEGF detected by an EC. We conclude that we must include VEGF concentration in the set of external variables for the CG system (i.e. the dimension, U, of the vector of external variables is 3; $u \in \mathbb{R}^3$) and pre-calculate CG look-up tables (see section 3.4.2) for a range of values of the VEGF concentration. Since in Chapter 2 we used fixed VEGF levels of 0, 5, and 50 ng/ml, a suitable range for VEGF is $[0, 50]$ ng/ml (which corresponds to $[0, v_{ext}^{max}] = [0, 12.5]$ in non-dimensional values, see Table B.2). Thus, the range for the complete set of external variables is $\mathcal{U} = [0, d_{ext}^{max}] \times [0, n_{ext}^{max}] \times [0, v_{ext}^{max}] \subset \mathbb{R}^3$, where d_{ext} and n_{ext} are fixed at the values used in Chapter 3 (see Table C.1). We now use trilinear interpolation routines (implemented in

C++) to establish an input-output relationship between an arbitrary $u = (d_{ext}, n_{ext}, v_{ext})$, the corresponding cell phenotypes and transitions between them.

Figure 4.2 shows how the quasipotential corresponding to transitions from stalk to tip cell, Q(stalk,tip), varies as the values of VEGF increase (for equivalent plots for the transition from tip to stalk cell see Figure D.2). These plots show that after initial cell activation by VEGF (which corresponds to an expansion of the bistability region, see Figures 4.2A and 4.2B), the quasipotential values decrease to facilitate the transition from stalk to tip cell (see Figures 4.2C and 4.2D). Since the tip cell phenotype is more active, this might contribute to a more rapid expansion of vascular networks for higher VEGF levels (as we saw in our simulations in Chapter 2; see section 2.5.1 and Figures 2.7 to 2.9).

The coarse-grained (CG) VEGF-Delta-Notch system replaces the original stochastic system of cell phenotype specification at the subcellular scale of the angiogenesis model. The rest of the model and computational setups are as in Chapter 2 (for further details, see Appendix D.1). Simulations are performed as explained in Algorithm 1 (Appendix B.3) except that, on line 8, cell phenotypes are now updated by running the CG system for VEGF-Delta-Notch signalling until the corresponding final simulation time, τ, is reached. Therefore, depending on the value of their transition rates, cells can undergo phenotype switches within the given final time. Henceforth, we refer to our multiscale model of angiogenesis, with the CG system for EC phenotype specification, as the *CG phenotype model.*

4.3.1 Comparison to the CTMC benchmark

First, we compared the CG phenotype model with the original model of angiogenesis by running small-scale simulations and comparing the statistics defined in Chapter 2. We began by performing single realisations of the CG phenotype model for fixed uniform VEGF distributions of 5 and 50 ng/ml and compared them with the simulations of the original model from Chapter 2 (see Figures 2.7 and 2.8). In Figure 4.3 we compare the final configurations of networks generated by the original (left panels) and CG phenotype (right panels) models
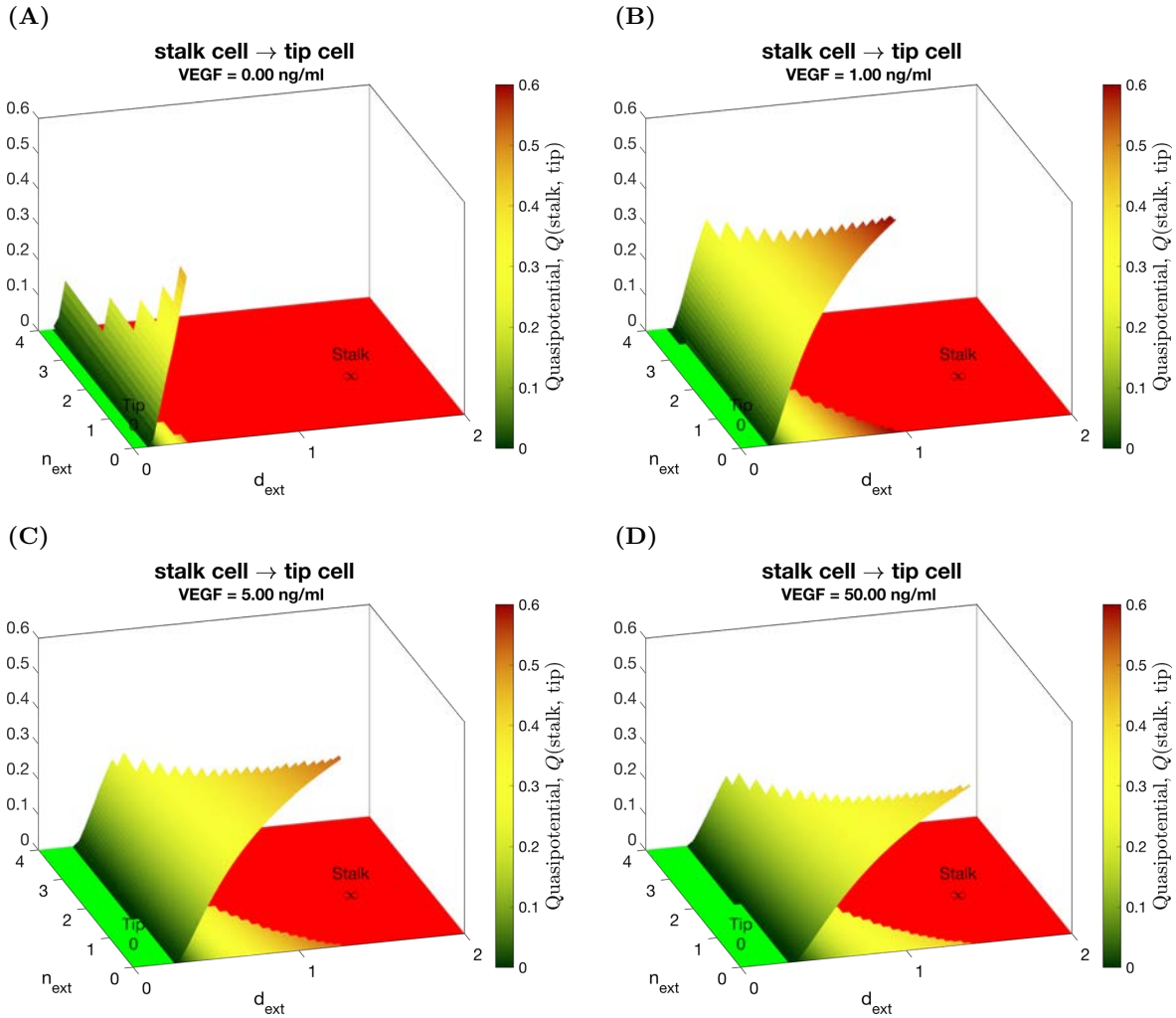
Figure 4.2. An illustration of the evolution of the quasipotential surface for the transition from stalk to tip cell for increasing VEGF levels. Quasipotential surfaces, $Q(\text{stalk}, \text{tip})$, for VEGF concentrations equal to **(A)** 0, **(B)** 1, **(C)** 5 and **(D)** 50 ng/ml (to facilitate interpretation, we indicate dimensional values of VEGF). The monostable region in which the unique stable steady state corresponds to a tip (stalk) cell is coloured in green (red) and the corresponding quasipotential, $Q(\text{stalk,tip}) = 0$ ($Q(\text{stalk,tip}) = \infty$). The colour bar indicates the value of the quasipotential. An animation of the evolution of the quasipotential, $Q(\text{stalk,tip})$, for the complete range of VEGF, $[0, 50]$ ng/ml, is shown in Movie 4.1.
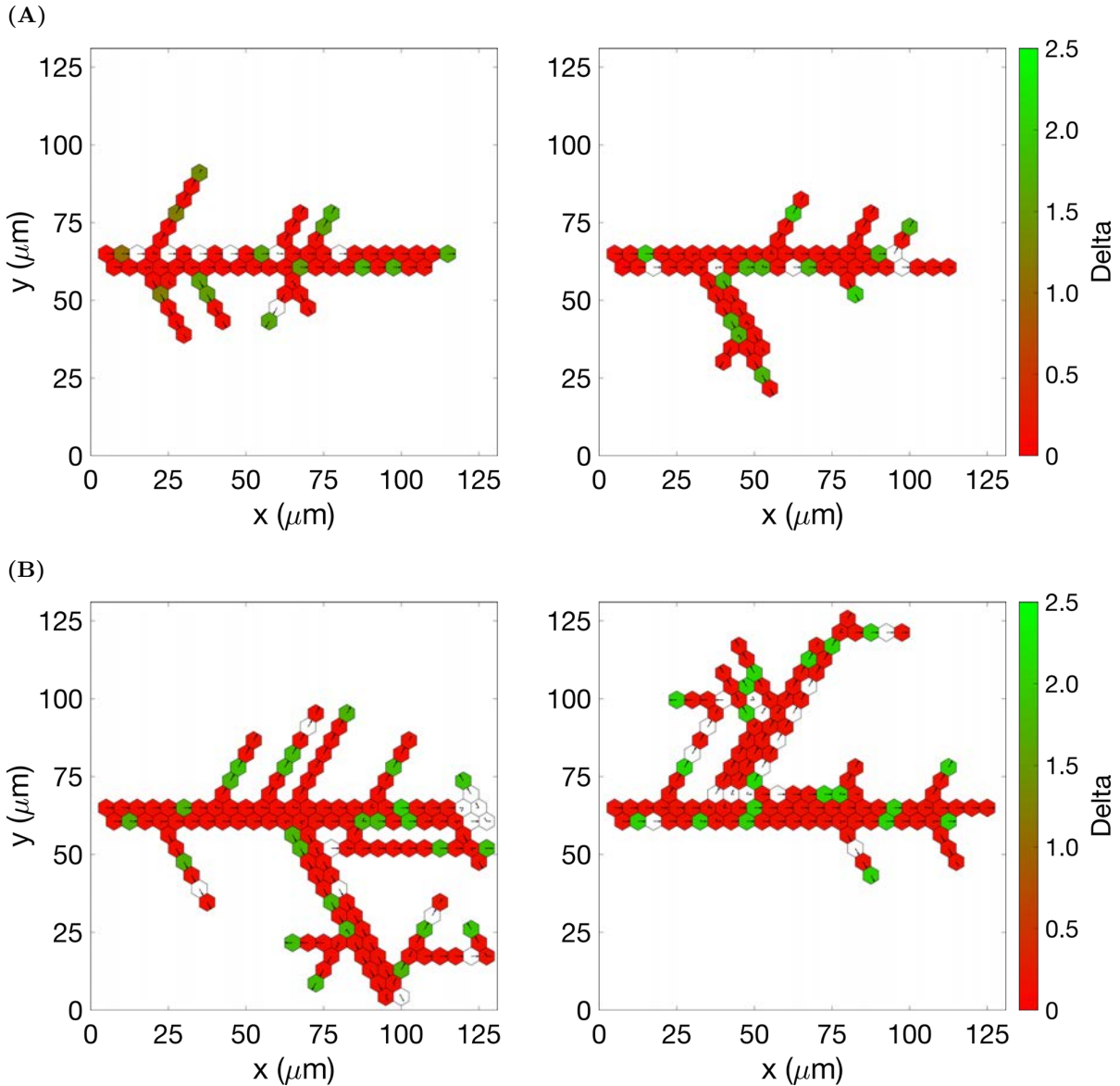
**Figure 4.3. Comparison of vascular networks generated by single realisations of
the original and CG phenotype models.** Final configurations of vascular networks
generated by the original (left panels) and CG phenotype (right panels) models for VEGF
levels of **(A)** 5 ng/ml and **(B)** 50 ng/ml. The colour bar indicates non-dimensional Delta
levels, $\boldsymbol{d}$, (green colour corresponds to tip cells, red – to stalk cells). Arrows indicate the
configuration of the orientation landscape, $\boldsymbol{l}$. Numerical simulation was performed using
Setup 1 from Table B.10 with final simulation time, $T_{max} = 2.5$. Parameter values are
listed in Tables B.7 and B.8 for subcellular and cellular/tissue scales, respectively. For a
movie of the numerical simulation corresponding to panel **(A)**, see Movie 4.2.

(see Movie 4.2 for an animation comparing the numerical simulations for VEGF levels of 5 ng/ml, which corresponds to Figure 4.3A). A preliminary inspection reveals that both models generate comparable branching structures (we remark that the simulations are stochastic and, therefore, each network is unique).

For a more systematic comparison, we performed 100 realisations of the CG phenotype model for VEGF levels of 5 and 50 ng/ml and extracted the same statistics as in Chapter 2: displacement, orientation and directionality (Figure 2.10); mixing measure (Figure 2.14); network quantification metrics (Appendix B.7 and Figure B.21). In Figures 4.4 and 4.5, we compare these statistics for the original and CG phenotype models for VEGF levels of 5 ng/ml (for VEGF levels of 50 ng/ml, see Figures D.3 and D.4, respectively). We confirm that there is good agreement between the metrics extracted from simulations of both models. From Figure 4.5, we note further that the network quantification metrics of the CG phenotype model have smaller variance than those of the original angiogenesis model. This is because when we coarse-grain the subcellular signalling, in the CG phenotype model, we neglect the full dynamics of phenotype switches. By contrast, since phenotype switches are binary events, transient behaviour is neglected, causing a reduction in the variance of the metrics.

4.4 Cell proliferation

In order to extend our simulations from timescales of hours (as in Chapter 2) to days, we must include cell proliferation in our model. We implement EC proliferation in accordance with existing experimental data (see below for details). Briefly, our model of proliferation consists of four main components:

(i) **the cell cycle duration**, which depends on EC activation via VEGF [45];

(ii) **the influence of the external microenvironment** (extracellular matrix, ECM, and components of basement membrane, BM) on cell division [204];

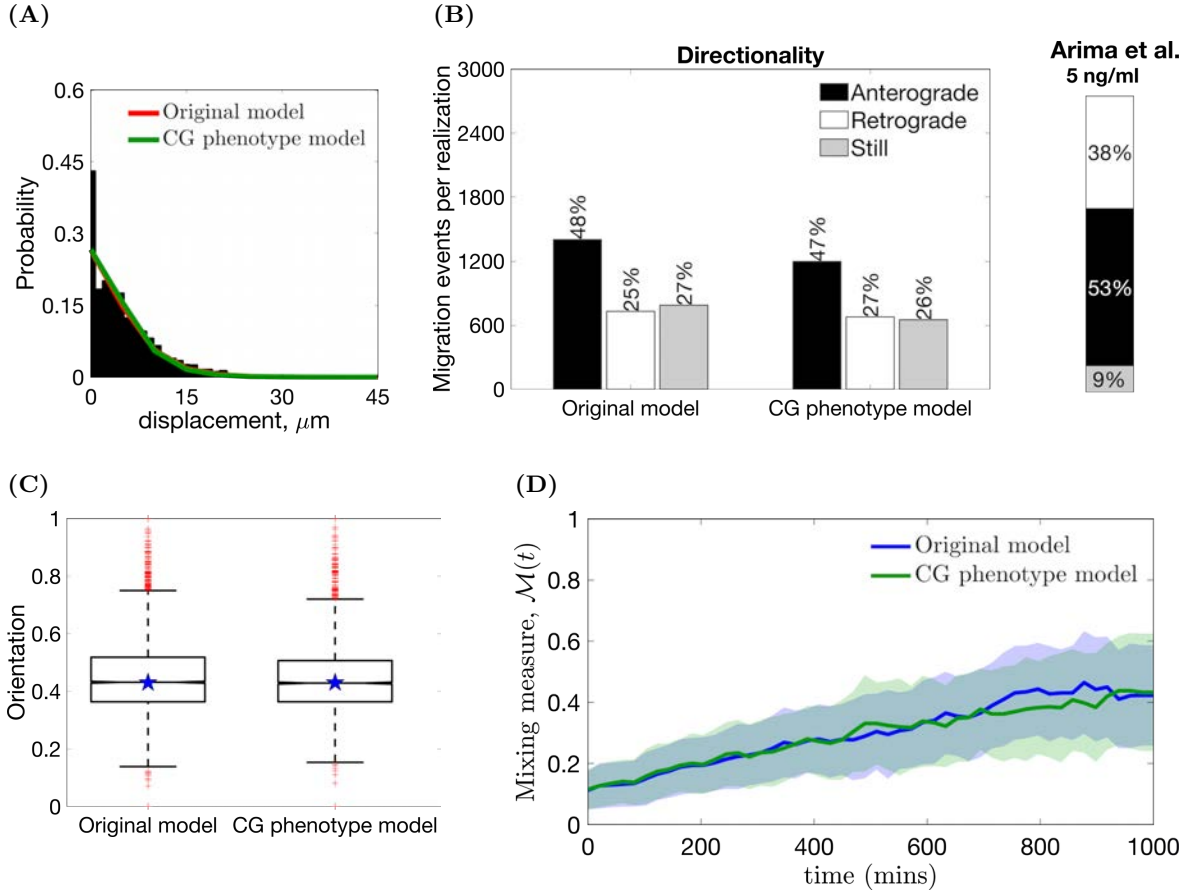(iii) **the location of the daughter cells** with respect to their parent cell [198];

Figure 4.4. Comparison of statistics extracted from simulations of the original and CG phenotype models for VEGF = 5 ng/ml. **(A)** Cell displacements during a 15 minute time period for VEGF = 5 ng/ml. The black histogram corresponds to the experimental data taken from the Supplementary Material of [10], the red (green) line corresponds to the displacement curve for simulations of the original (CG phenotype) model. **(B)** The directionality statistics for simulations of both models for VEGF = 5 ng/ml (left panel); the directionality statistics extracted from experimental data in [4] (right panel). **(C)** Box plots of the orientation statistic extracted from simulations of both models for VEGF = 5 ng/ml. Red crosses indicate box plot outliers. Orientation statistics obtained from experimental data from [4] are shown by blue stars on each box plot. **(D)** Temporal evolution of mixing measure, $\mathcal{M}(t)$, as a function of time for VEGF = 5 ng/ml (the mean value is indicated by a thick line and standard deviation is shown by a colour band). All statistics were computed for 100 realisations. Numerical simulations were performed using **Setup 1** from Table B.10 and $T_{max} = 2.5$. Parameter values are listed in Tables B.7 and B.8 for subcellular and cellular/tissue scales, respectively.
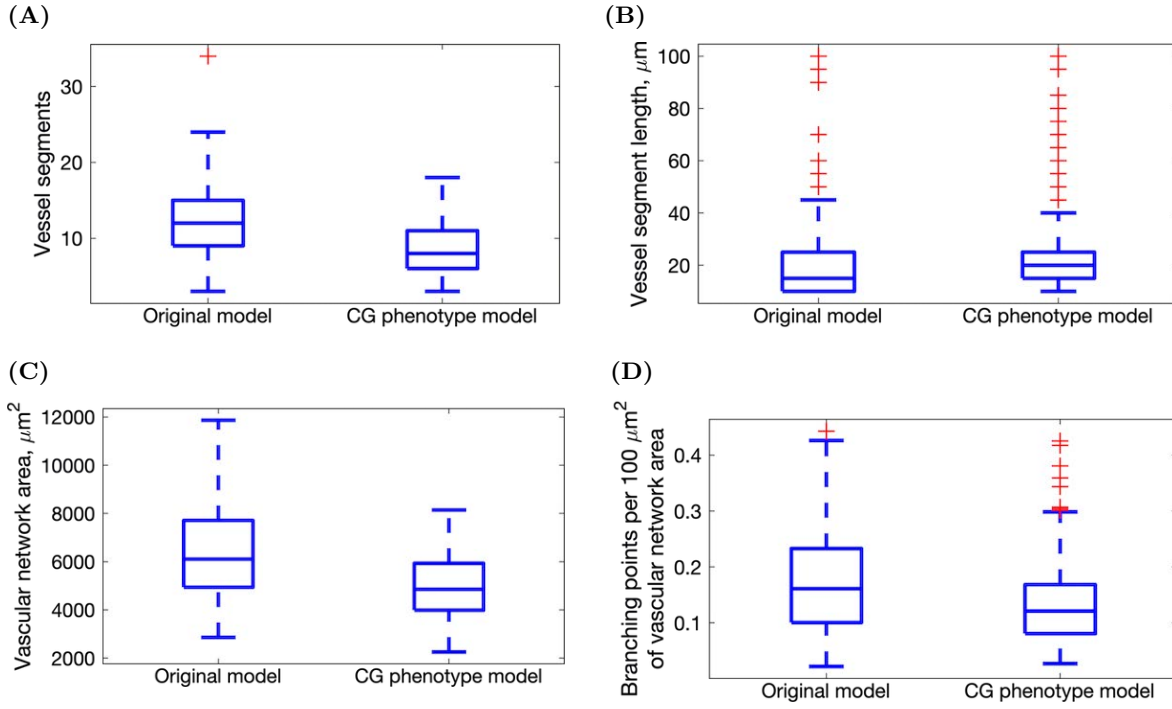
Figure 4.5. Comparison of metrics for quantification of vascular network structure for the original and CG phenotype models for VEGF = 5 ng/ml. (A) Number of vessel segments. **(B)** Vessel segment length (μm). **(C)** Vascular network area (μm^2). **(D)** Number of branching points per 100 μm^2 of vascular network area. Details of the definitions of these metrics can be found in Appendix B.5. In each box plot, the central line indicates the median, and the horizontal edges of the box represent the 25th and 75th percentiles (for the bottom and top edges, respectively). The outliers are indicated by red cross symbols. The numerical simulation setup used is **Setup 1** from Table B.10 with final simulation time $T_{max} = 2.5$. Parameter values are listed in Tables B.7 and B.8 for subcellular and cellular/tissue scales, respectively. Results are averaged over 100 realisations.

(iv) **asymmetric cell division** which accounts for non-uniform splitting of the components of the VEGF-Delta-Notch signalling pathway between the daughter cells [120].

4.4.1 Cell cycle duration

First, we performed a literature search in order to determine a suitable range of cell cycle times in ECs. Figure 4.6A summarises the durations of the cell cycle times reported in the

literature for ECs (the values are plotted as given in the corresponding reference indicated in the figure caption). We notice that the reported times vary for different EC types (e.g. microvascular endothelial cells, MEC, human umbilical vein endothelial cells, HUVEC) and within the same EC type for different experimental setups (these were distinct for each of the studies reported in Figure 4.6A). Based on these data, we assume that the EC cell cycle time varies in the range of $12 - 96$ hours.

4.4.2 Bell-shaped response of cell proliferation to VEGF activation

A key pathway controlling EC proliferation rate is the MAPK/ERK signalling pathway (mitogen-activated protein kinases, MAPK, also known as extracellular signal-regulated kinases, ERK). This pathway is activated following VEGF binding to VEGFR2 and controls the G1/S-phase transition of cell cycle, thus inducing cell proliferation [205]. According to this model, tip cells have a higher rate of proliferation than stalk cells since they have higher levels of activated VEGFR2. However, this contradicts experimental results which show that tip cells do not proliferate rapidly [4], [26], [27].

This issue was addressed in a recent study by Pontes-Quero et al. [45]. The results of their *in vivo* experiments in mice showed that there is a bell-shaped response of EC proliferation rate upon stimulation by VEGF (for an illustration, see Figure 4.6B). More specifically, quiescent cells (i.e. EC lining blood vessels before the onset of angiogenesis and differentiation into stalk and tip cell phenotype) are not activated (or have low activation) by VEGF and, thus, have low proliferation rates. During the early stages of angiogenic sprouting, MAPK/ERK signalling is increased due to higher levels of VEGFR2 activation by VEGF. Stalk cells (which have lower levels of activated VEGFR2 than tip cells) are stimulated to proliferate rapidly in order to support the growing network. On the other hand, high MAPK/ERK signalling induced by elevated VEGFR2 signalling in tip cells triggers expression of a cell cycle inhibitor, p21, which arrests cell cycle progress in tip cells and promotes their migration and sprouting. This can be represented by a bell-shaped response
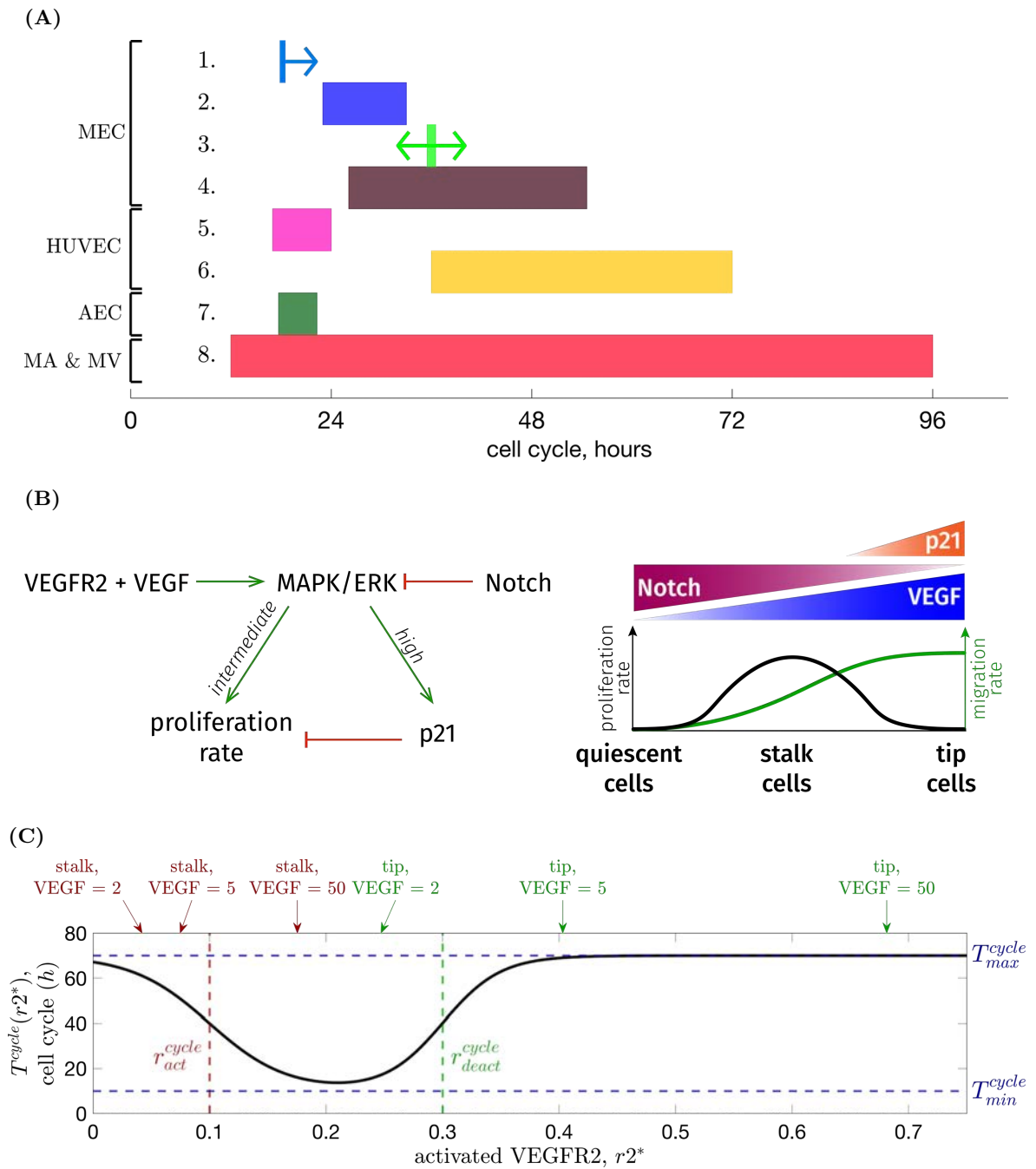
(A)

(B)

(C)

Figure 4.6. (Caption on the next page.)

Figure 4.6. EC cell cycle. (A) Duration of EC cell cycle reported in the literature. All values are indicated in hours and are plotted as given in the corresponding references. We used the following abbreviations to indicate EC types: microvascular endothelial cell (MEC), human umbilical vein endothelial cell (HUVEC), aortic endothelial cell (AEC), mesenteric artery (MA) and mesenteric vein (MV) EC. **1.** minimum cell cycle, $17.8 \ h$ [39]; **2.** $23 - 33 \ h$ [40]; **3.** mean cell cycle, $36 \ h$ [42]; **4.** $26.1 - 54.6 \ h$ [41]; **5.** $17 - 24 \ h$ [199]; **6.** $36 - 72 \ h$ [44]; **7.** $17.7 - 22.3 \ h$ [41]; **8.** $12 - 96 \ h$ [43]. **(B)** Illustration of signalling pathways involved in regulation of EC proliferation rate. A key pathway controlling activation of cell proliferation, MAPK/ERK, is activated by VEGF signalling. On the other hand, Notch signalling inhibits MAPK/ERK activity. The balance between the activity of these two pathways (as in stalk cells) induces cell proliferation. However, high MAPK/ERK activity of tip cells triggers expression of a cell cycle inhibitor, p21, which arrests the cell cycle. This leads to a bell-shaped response of EC proliferation to stimulation by VEGF. The level of EC activation by VEGF (represented by the $r2^*$ variable in our model) can be used as a proxy to capture EC proliferation variability. **(C)** An example of a function describing the bell-shaped response of EC cell cycle duration, $T^{cycle}(r2^*)$, described by Eq (4.1) with $r_{act}^{cycle} = 0.1$, $r_{deact}^{cycle} = 0.3$, $s_{act} = 30$, $s_{deact} = 40$, $T_{min}^{cycle} = 10$, $T_{max}^{cycle} = 70$. On the horizontal axis above the plot, we indicate characteristic levels of VEGF activation ($r2^*$ variable) for stalk and tip cells for varying VEGF levels (ng/ml) in our model of angiogenesis.

of EC proliferation upon activation by VEGF.

We use the level of activated VEGFR2 within a cell ($r2^*$ variable) as a proxy to capture the bell-shaped activation of cell proliferation in EC. We use the following expression to describe the duration of the cell cycle, $T^{cycle}(r2^*)$:

$$T^{cycle}(r2^*) = T_{min}^{cycle} + \left(T_{max}^{cycle} - T_{min}^{cycle} \right) \left(F_{sig}(r2^*; r_{act}^{cycle}, s_{act}) + F_{sig}(r2^*; r_{deact}^{cycle}, -s_{deact}) \right),$$
(4.1)

where $F_{sig}(r2^*; r, s) = (1 + \exp(s(r2^* - r)))^{-1}$ is a sigmoid function, characterised by a threshold, r, and a slope, s. The first (second) sigmoid in Eq (4.1), $F_{sig}(r2^*; r_{act}^{cycle}, s_{act})$ ($F_{sig}(r2^*; r_{deact}^{cycle}, -s_{deact})$), acts to decrease (increase) the duration of the cell cycle (see Figure 4.6C for an illustration). T_{min}^{cycle} and T_{max}^{cycle} are the minimum and maximum cell cycle durations, respectively.

In order to calibrate this function with our model of subcellular signalling, we ran several

realisations of the angiogenesis model for different fixed values of the VEGF concentrations and recorded the values of VEGFR2 activation, $r2^*$, for tip and stalk cells. We indicate these values for specific values of VEGF in Figure 4.6C (horizontal axis above the plot). Then, the threshold and slope parameters, r_{act}^{cycle}, r_{deact}^{cycle}, s_{act} and s_{deact}, respectively, were chosen so that the fastest cell cycle corresponds to stalk cells, while tip cells and ECs with low VEGF activation have longer cell cycles. T_{min}^{cycle} and T_{max}^{cycle} are assumed to vary within $12 - 96$ hours (Figure 4.6A).

4.4.3 Influence of external microenvironment

ECM density   In the same way that ECM density affects cell migration (Chapter 2), we assume that the rate of cell division increases as the ECM concentration decreases (since more space is available for cell division). To take this into account, we assume that the cell proliferation rate is proportional to the function $S(c_i)$ given by Eq (2.8) (this function describes the fraction of ECM-free space in a voxel v_i).

BM inhibition   Deposition of BM components is known to inhibit vascular network expansion and promote cell quiescence (this effect being mediated by BM fragments such as endostatin or arresten) [204], [206], [207]. Thus, we assume that the cell proliferation rate decreases sharply to 0 when the BM concentration, m_i, is close to 1 (which represents vessel maturation in our phenomenological model). We account for this effect by introducing the function, $F_{BM}(m_i)$, which has the following form:

$$F_{BM}(m_i) = \frac{1}{1 + \exp(s_{BM}(m_i - m_{BM}))}. \tag{4.2}$$

Here, the parameters, m_{BM} and s_{BM} characterise the position and slope, respectively, of this sigmoid function.

4.4.4 Proliferation rate

By combining external (ECM and BM) and internal (VEGF activation) factors influencing EC division, we arrive at the following expression for the proliferation rate, $\omega_{prol}(i)$, of a cell in a voxel v_i:

$$\omega_{prol}(i) = \frac{1}{T^{cycle}(r2_i^*)} S(c_i) F_{BM}(m_i).$$

(4.3)

The cellular scale of our model now accounts for migration (the transition rate is given by Eq (2.7)) and proliferation (Eq 4.3) events which occur stochastically, in the framework of a persistent random walk. When a proliferation event occurs, the parent EC splits into two daughter cells. The placement of daughter cells and splitting of the cellular proteins are described below.

4.4.5 Location of daughter cells

The orientation of the plane of EC division determines the positions of the two daughter cells during cytokinesis (the final stage of cell division during which the cytoplasm of the parent cell splits between the two daughter cells). In angiogenesis, daughter cell placement directly influences the morphology of the growing vessels ([198] and Figure 4.7A). When a parent EC divides perpendicular to the vessel elongation direction (i.e. the vessel's longer axis), daughter cell positioning contributes to vessel elongation (Figure 4.7A). On the other hand, if the division plane is parallel to the vessel's elongation direction then the vessel thickens or a new branch is initiated. Since the early stages of angiogenic expansion are characterised by rapid vessel growth, ECs typically divide in the direction perpendicular to vessel elongation [198].

In order to account for the influence of the orientation of the division plane, we used *in vivo* experimental data reported in [198] (Figure 5B in [198]) to determine the positions of daughter cells upon division (Figure 4.7B). Figure 4.7C illustrates of how we implemented EC
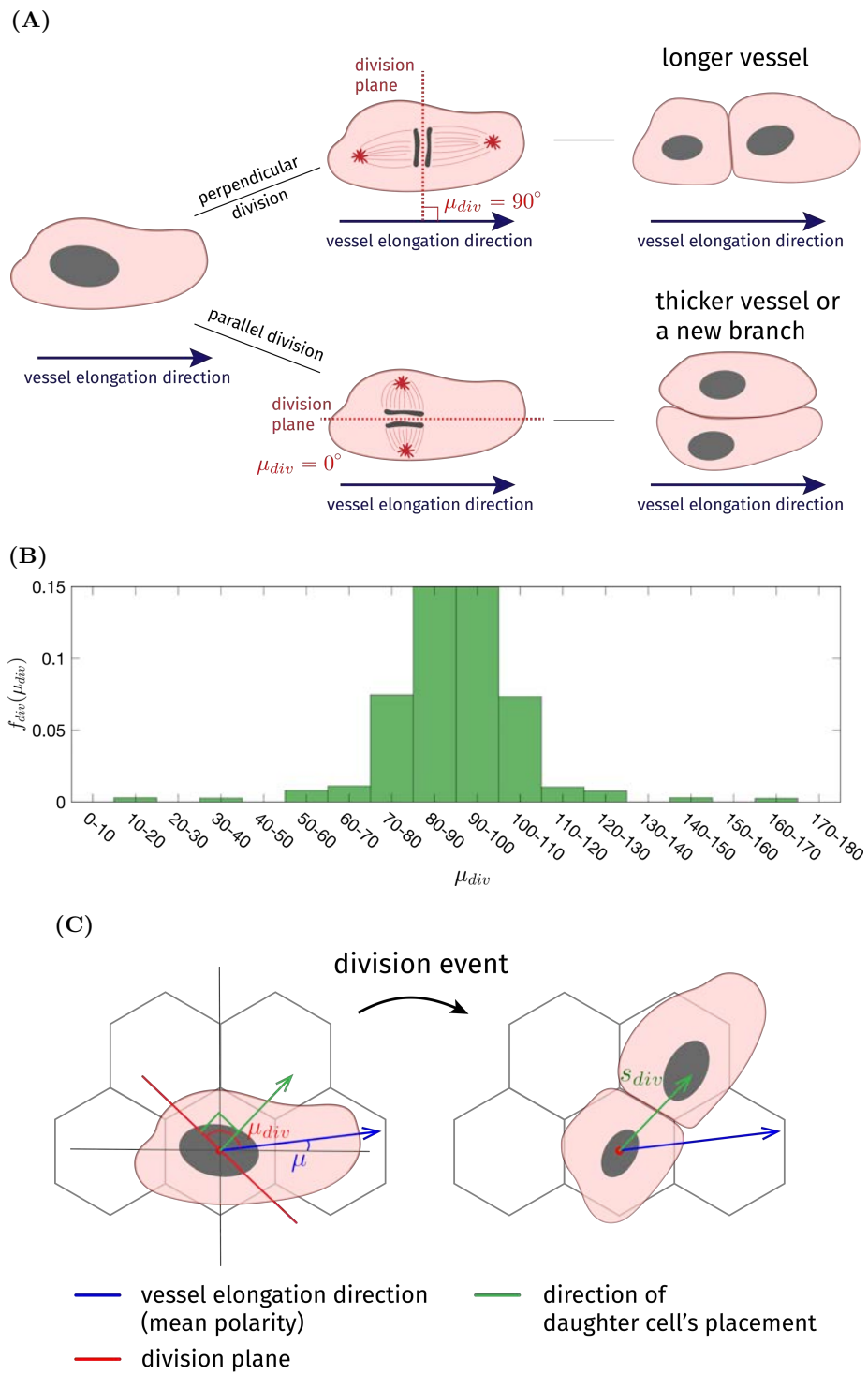
(A)

(B)

(C)

Figure 4.7. (Caption on the next page.)

Figure 4.7. Series of diagrams showing how EC proliferation is implemented.
(A) An illustration of how the orientation of the division plane (the plane of EC cytokinesis) influences vessel morphogenesis [198]. When the division plane is perpendicular to the direction of vessel elongation (upper branch), the two daughter cells contribute to vessel elongation. However, when the planes of cytokinesis and vessel elongation are parallel to each other (lower branch), the daughter cells are positioned laterally and cell division either thickens the vessel, or a new branch is initiated. **(B)** *In vivo* experimental data taken from experiments on postnatal retina vascularisation in rats (Figure 5B from [198]). The histogram shows the probability that the division plane angle lies in a particular interval (each bar is of 10° width). Here, $\mu_{div} = 90°$ corresponds to perpendicular division and $\mu_{div} = 0°$ and $\mu_{div} = 180°$ to parallel division. The probability distribution, $f_{div}(\mu_{div})$, is symmetric about $\mu_{div} = 180°$ (here, we only sketch it for $\mu_{div} \in [0°, 180°]$). We used these data in our model to determine the position of the second daughter cell after a proliferation event. **(C)** A cartoon showing the positioning of daughter cells after division. One of the daughter cells is placed at the lattice site of the parent EC; the second daughter EC is positioned at a lattice site in the direction, s_{div}, (green line) perpendicular to the division plane (red line). For further explanation see the main text. In this illustration, the second daughter cell is placed in a voxel which does not coincide with the axis of vessel elongation. This is an example of a less frequent (according to distribution, $f_{div}(\mu_{div})$) event when cell division initiates a new branch [198].

proliferation events. The direction of vessel elongation, or mean polarity angle, μ, is defined in Eq (2.13) of Chapter 2 (mean polarity vector is calculated as a vector sum of weighted contributions of all explored migration directions for the lattice site of interest). We restate Eq (2.13) for the reader's convenience:

$$\vec{p} = \left(\sum_{dir \in \mathcal{S}} H_{a,n}(l_i^{dir}) dir_x, \sum_{dir \in \mathcal{S}} H_{a,n}(l_i^{dir}) dir_y \right)^T,$$

$$\mu = Arg(\vec{p}). \tag{2.13}$$

Then an angle, μ_{div}, is sampled from the probability distribution, $f_{div}(\mu_{div})$, taken from the experimental data [198] (as shown in Figure 4.7B). The sum of these two angles, $(\mu + \mu_{div})$, defines the division plane for EC cytokinesis. One of the daughter cells is then positioned at the same lattice site as the parent EC and the second daughter cell is placed at a neighbouring lattice site perpendicular to the division plane, i.e. in the direction given by the angle $(\mu + \mu_{div} - 90°)$.

Mathematically, if a proliferation event happens in voxel v_i, the first daughter EC is placed in voxel v_i. The second EC is located in voxel $v_{j_{div}}$, where j_{div} is defined by the division direction, $s_{div} = h^{-1}(q_{j_{div}} - q_i)$, as follows:

$$s_{div} \in \mathcal{S} \text{ is such that } W^{s_{div}}(\mu + \mu_{div} - {}^\pi/_2) = 1. \tag{4.4}$$

Here, $W^s(\cdot)$ is the window function defined in Eq (2.15) (see also Figure 2.2 for a reminder of the model geometry). We restate Eq (2.15) for the reader's convenience:

$$W^s(\phi) = \begin{cases} 1, & \text{if } \phi + 2\pi k \in [\phi^s_{min}, \phi^s_{max}], \quad k \in \mathbb{Z}, \\ 0, & \text{otherwise.} \end{cases} \tag{2.15}$$

If this lattice site is occupied by another EC (i.e. $E_{j_{div}} = 1$), we assume that cell proliferation exerts pressure on neighbouring cells and forces them to move to make space for the daughter EC. Thus, ECs situated in voxels in direction s_{div} from the voxel v_i are moved in the same direction until an empty lattice site is found. Since the transition rate for proliferation events (Eq (4.3)) is proportional to $F_{BM}(m_i)$ (Eq (4.2) which describes inhibition of cell proliferation by BM components), proliferation events occur more frequently at the angiogenic front characterised by lower cell densities (as compared to mature vessels). Thus, in practice, few cells have to be moved because of cell proliferation.

Finally, since EC movement exerts traction forces on the ECM fibrils and since the division direction defines the future migration direction of ECs [198], we increment the orientated landscape (OL) variable, $\boldsymbol{l}$, (this variable defines the orientation of ECM fibrils, see Table 2.1) in the division direction, s_{div}, in all the lattice sites which were modified during a proliferation event:

$$l_i^{s_{div}} = l_i^{s_{div}} + \Delta_l D_0 d_i,$$

$$l_{j_{div}}^{s_{div}} = l_{j_{div}}^{s_{div}} + \Delta_l D_0 d_{j_{div}},$$

$$l_k^{s_{div}} = l_k^{s_{div}} + \Delta_l D_0 d_k \quad \text{for all ECs which were moved to a new voxel } v_k$$

(4.5)

$$\text{during the proliferation event.}$$

This update is performed only when a proliferation event occurs (not on each simulation time step) and is similar to the one defined in Eq (2.16) for EC migration; there we incremented the OL variable in the direction of cell movement. Here we used the conversion factor, D_0, (see Table B.2) to define the update in terms of non-dimensional Delta levels. We restate Eq (2.16) for the reader's convenience:

$$l_i^s = l_i^s + \Delta_l D_i,$$

$$l_j^s = l_j^s + \Delta_l D_i.$$

(2.16)

4.4.6   Asymmetric cell division

ECs are known to divide asymmetrically [120] which means that the signalling components of the VEGF-Delta-Notch pathway are partitioned unequally between daughter cells. Specifically, a daughter cell situated closer to the sprout tip obtains a greater proportion of cellular proteins. This fraction has been estimated to be around $60 - 70\%$ of the parental EC components [120]. In [120], it was hypothesised that unequal partitioning of cell components between daughter ECs accelerates cell phenotype specification after division (cell fate determination that relies on the VEGF-Delta-Notch pathway alone takes longer when both daughter ECs have approximately equal amounts of cellular components [157]).

According to these experimental data, we split the VEGF-Delta-Notch components of the parent cell situated in voxel v_i, $X_i^p = (n_i, d_i, \iota_i, r2_i, r2_i^*)$, in the following way:

$$X_{j_{div}} = (0.65 + \xi)X_i^p, \quad \text{where } \xi \in \text{Unif}[-0.05, 0.05],$$

$$X_i = X_i^p - X_{j_{div}}.$$

(4.6)

Here, $\text{Unif}[a, b]$ is the uniform distribution on the interval $[a, b]$. Thus, in Eq (4.6), the daughter cell, positioned closer to the sprout tip (leading cell at voxel $v_{j_{div}}$) receives 65% ($\pm 5\%$ noise) of the parent cell proteins and the second daughter cell (trailing cell at voxel v_i) receives the rest of the cellular components.

To sum up, our model for cell division is incorporated at the cellular scale of the angiogenesis model with proliferation events occurring at the transition rate given by Eq (4.3). On cell division, the parent EC splits asymmetrically in the direction determined by the division plane angle, this angle being sampled from explicitly determined distribution. Figure D.5 (in Appendix D.2) shows how a division event happens during model simulations.

4.5 Vessel maturation

Since our aim is to simulate vascular network formation on a timescale of days, we must extend our model to account for dynamic processes such as baseline BM assembly and inhibition of cell migration by BM components. These processes become significant on longer timescales than those considered in Chapter 2 where their contribution could be neglected.

Baseline BM assembly In Chapter 2, the variable, $\boldsymbol{m}$, describes the concentration of basement membrane (BM) components secreted by ECs. We assumed that tip cells secrete these components at higher rate than stalk cells (see Eq (2.21)). We restate Eq (2.21) for the reader's convenience:

$$\gamma_m(D_i) = \frac{\gamma_{max}}{1 + \exp\left(-s_m(D_i - D_m)\right)}.$$

(2.21)

Here, we also account for BM self-assembly induced by the presence of ECs [207], [208] and stimulation of uniform BM assembly by pericytes (these cells migrate to newly formed sprouts and form an outer coating which stabilises the vessel) [209]. We augment Eq (2.21) by including an additional rate of slow BM assembly due to these two processes:

$$\gamma_m(d_i) = \gamma_{min}E_i + \frac{\gamma_{max} - \gamma_{min}}{1 + \exp\left(-s_m(D_0 d_i - D_m)\right)}. \tag{4.7}$$

Here, γ_{min} represents the rate of slow BM assembly at lattice sites where ECs are present (i.e. $E_i = 1$).

BM inhibition of cell migration It is known that the formation of BM promotes cell quiescence and limits EC proliferation and migration [18], [204], [210]. In Eq (4.2), we account for inhibition of EC proliferation by BM components. Here, we also account for changes in cell motility caused by changes in BM components. We suppose that the diffusion coefficient, D, in voxel v_i, introduced in Eq (2.7), is a linearly decreasing (from the maximum diffusion coefficient, D_{max}, to the minimum, D_{min}) function of $m_i \in [0, 1]$, the BM concentration in voxel v_i:

$$D(m_i) = D_{max} + (D_{min} - D_{max})m_i. \tag{4.8}$$

4.6 Results

4.6.1 Importance of vessel maturation on vasculature expansion

We have extended the initial CG phenotype model by incorporating processes associated with angiogenic sprouting that take place on a timescale of days. In particular, we now account for:

(a) baseline BM assembly (Eq (4.7));

(b) cell proliferation (section 4.4 and Eq (4.3));

(c) BM inhibition of cell migration (Eq (4.8)).

In order to assess their effects, we first performed individual realisations of our model including each effect one by one. We performed simulations on a larger domain of 1000^2 μm^2, with a VEGF gradient of $1-10$ ng/ml increasing linearly in the direction of the x-axis. Using this setup, we first performed an individual realisation of the initial CG phenotype model (as described in section 4.3.1). Figure 4.8A shows the final configuration of this simulation at $t = 15$ days. We note that the uniform radial expansion of the network resembles a cell monolayer rather than a branching vascular network. Since in this simulation we did not include baseline BM assembly, enhanced cell migration (which decreases with BM formation, Eq (2.14)) enabled cells to expand in a radial fashion by initiating new branches. By accounting for baseline BM assembly (Figure 4.8B), we could partially recover the structure of a growing vascular network since branching was limited by uniform vessel maturation. In Figure 4.8C we show the final configuration of a simulation in which we also included cell proliferation. The additional source of cells enabled greater radial expansion of the network although certain regions lacked a normal branching structure. A clear branching structure was recovered when the inhibitory effects of BM formation on cell motility were included (Figure 4.8D). Based on these preliminary simulation results, we conclude that vessel maturation caused by baseline BM assembly and its inhibition of cell migration is essential for the formation of a realistic branching network on longer timescales.

4.6.2 Effect of cell proliferation on vasculature expansion

In order to understand how cell proliferation influences the growth of vascular networks, we considered several proliferation setups (see Table D.2) with different lower and upper bounds for the cell cycle duration (T_{min}^{cycle} and T_{max}^{cycle}, respectively, in Eq (4.1)). In Figure 4.9, we present configurations of simulated vascular networks in a linear VEGF gradient of $1 - 10$ ng/ml for each of the proliferation setups (see Figure D.6 for simulations in a VEGF gradient of $1-5$ ng/ml). We observe increasing network expansion as the cell cycle duration decreases
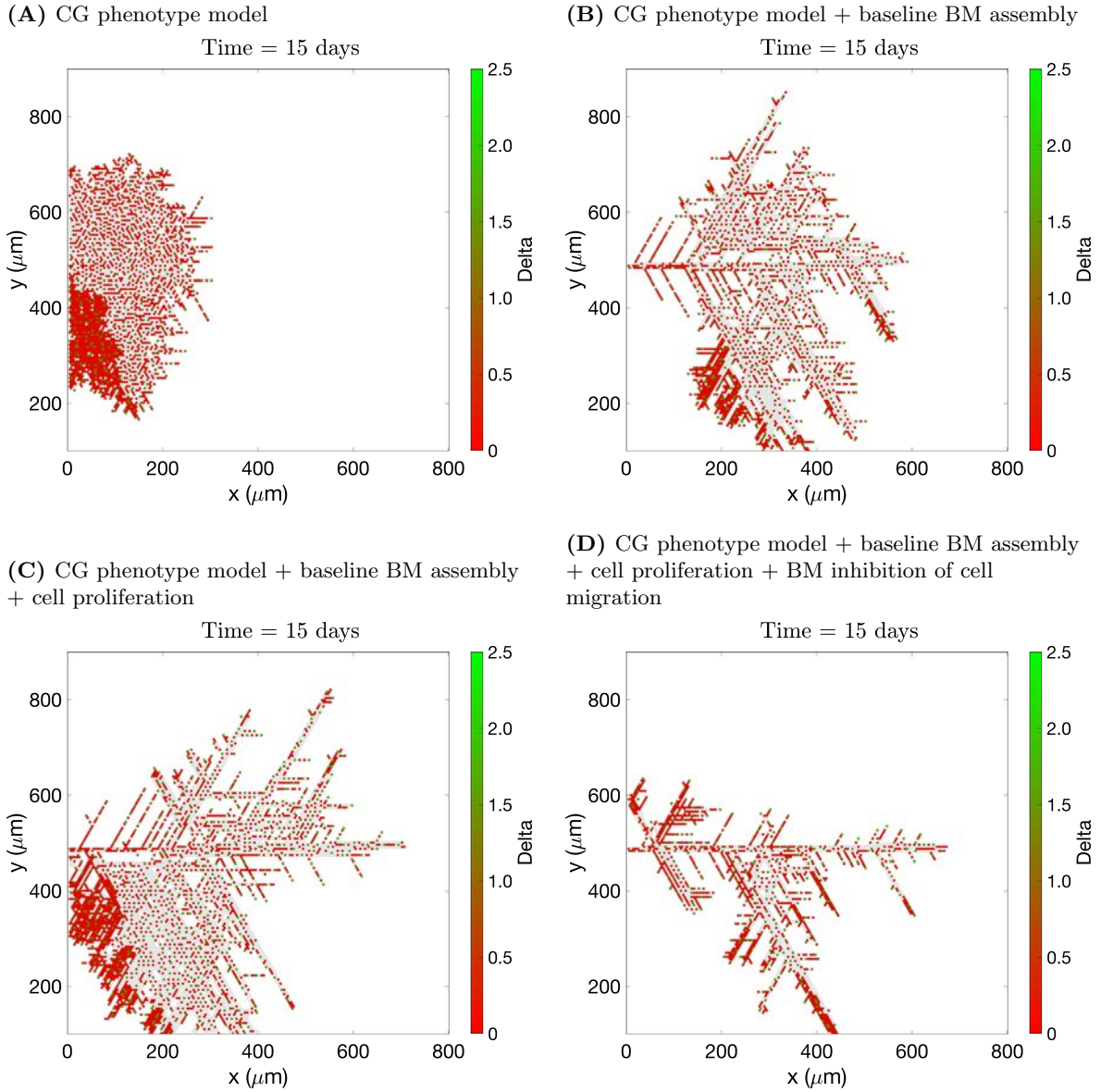
(A) CG phenotype model

(B) CG phenotype model + baseline BM assembly

(C) CG phenotype model + baseline BM assembly
+ cell proliferation

(D) CG phenotype model + baseline BM assembly
+ cell proliferation + BM inhibition of cell
migration

Figure 4.8. The importance of vessel maturation on vascular network expansion.
Single realisations of our model on a large domain of 1000^2 μm^2 in a VEGF gradient of
$1 - 10$ ng/ml that increases linearly in the direction of the x-axis. Simulation setup: **(A)**
initial CG phenotype model; **(B)** initial CG phenotype model + baseline BM assembly
(Eq (4.7)); **(C)** initial CG phenotype model + baseline BM assembly + cell proliferation
(section 4.4); **(D)** initial CG phenotype model + baseline BM assembly + cell proliferation
+ BM inhibition of cell migration (Eq (4.8)). Numerical simulations were performed using
large-scale setup 1 from Table D.3 with final simulation time $T_{max} = 44.0$. Parameter values
are listed in Table D.1. For simulations without cell proliferation, we fixed $\omega_{prol}(i) = 0$ for
all i; for simulations with cell proliferation, we used proliferation setup 8 from Table D.2.
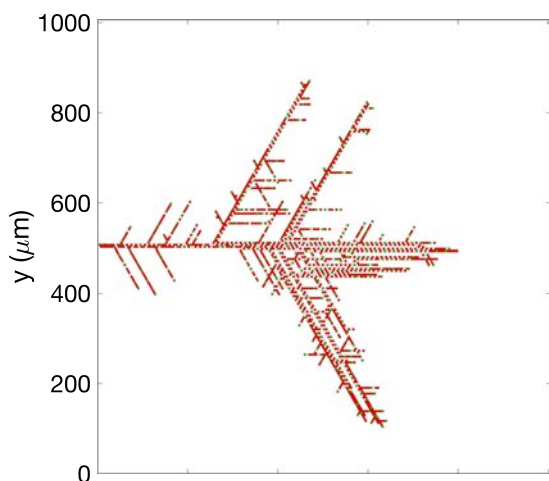
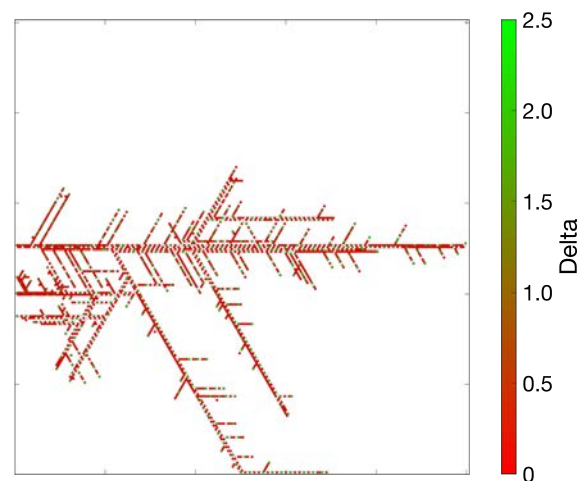**(A) Proliferation setup 1**: cell cycle, $30 - 90$ h
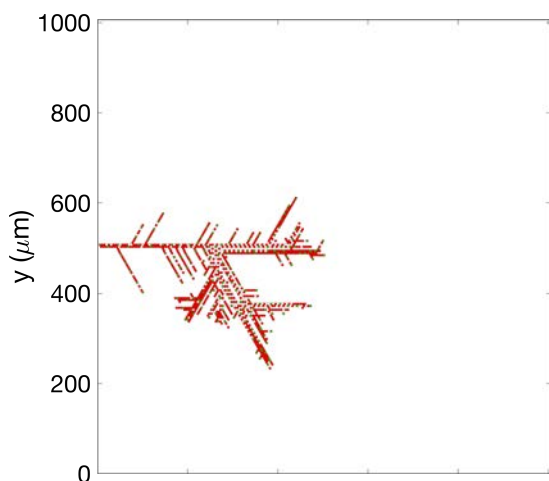
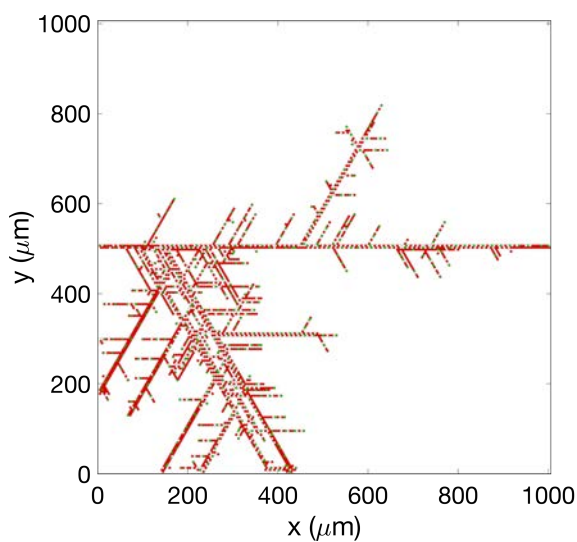**(B) Proliferation setup 2**: cell cycle, $30 - 60$ h
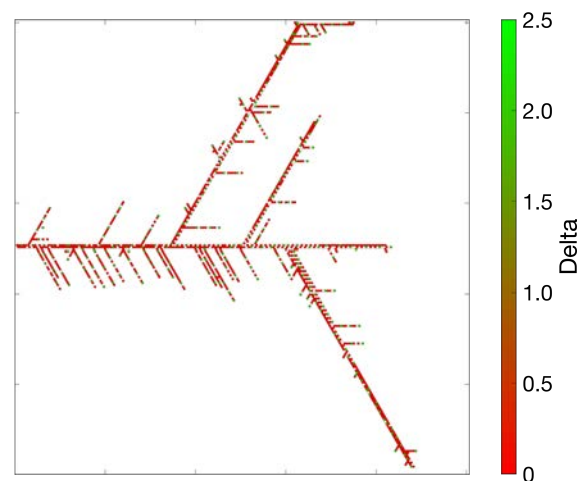
(C) Proliferation setup 3: cell cycle, $20 - 50$ h

(D) Proliferation setup 4: cell cycle, $20 - 40$ h

(E) Proliferation setup 5: cell cycle, $20 - 30$ h

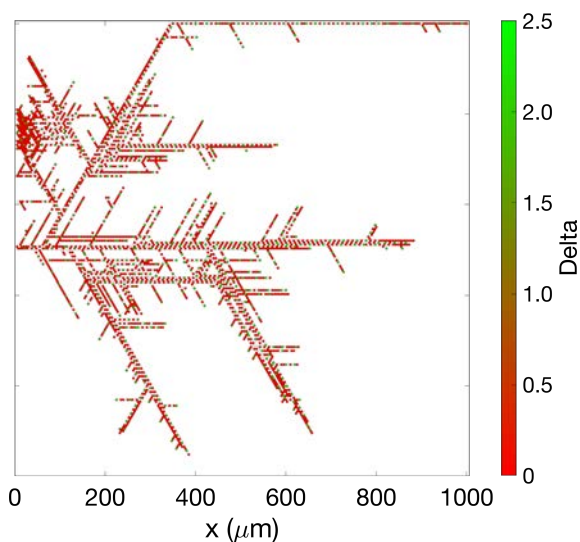**(F) Proliferation setup 6**: cell cycle, $15 - 25$ h

Figure 4.9. (Continuation on the next page.)

(G) Proliferation setup 7: cell cycle, $12 - 25$ h   **(H) Proliferation setup 8**: cell cycle, $12 - 20$ h
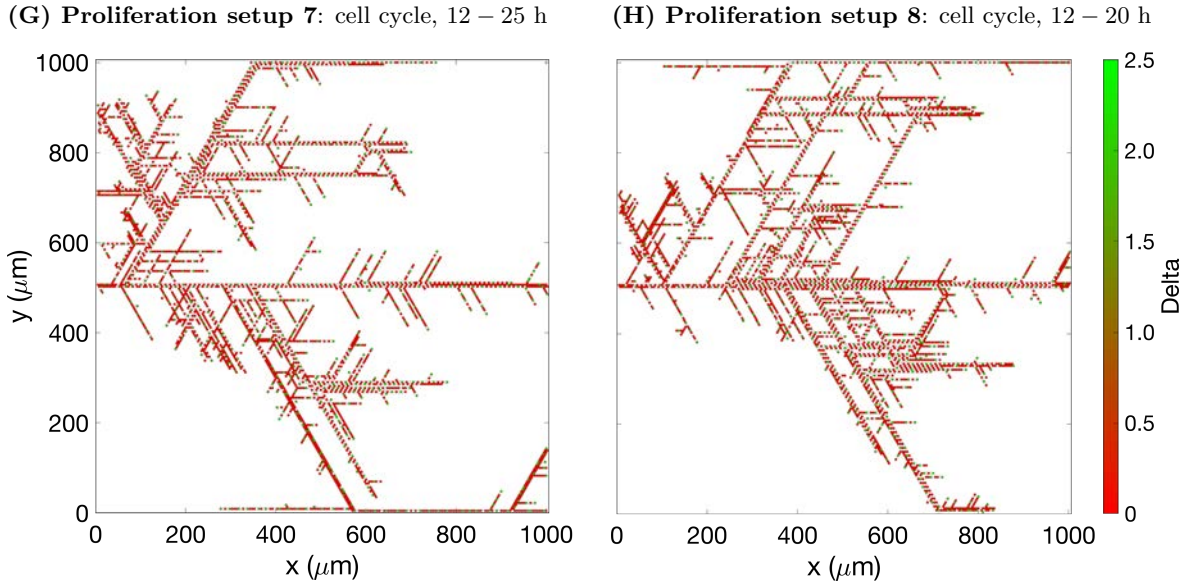
Figure 4.9. Effects of cell proliferation on vasculature expansion. Single realisations of our model on a large domain of 1000^2 μm^2 in a linear VEGF gradient of $1 - 10$ ng/ml increasing in the direction of the x-axis (i.e. VEGF increases from left to right). Proliferation setups (see Table D.2) determining cell cycle duration are indicated in the title of each panel. Numerical simulations were performed using large-scale setup 1 from Table D.3. Parameter values are listed in Table D.1 and the final simulation time was fixed at $T_{max} = 72.0$ (equivalent to 25 days in real time units). For movies of the numerical simulation corresponding to panels **(A)** and **(H)**, see Movie 4.3 and Movie 4.4, respectively.

(proliferation setups are numbered in descending order with respect to cell cycle duration).

Since these simulations were performed with a fixed linear gradient of VEGF (increasing from left to right), vascular network expansion increases more rapidly in regions of higher VEGF concentration (see Movie 4.3 and Movie 4.4). A preliminary inspection suggests that the branching patterns (i.e. distances between branching points or, equivalently, vessel segment length) are not affected by variations in the cell cycle duration (determined by proliferation setups 1-8 in Table D.2).

For a more systematic comparison of simulations with different cell cycle durations, we performed 100 realisations of our model for each proliferation setup and extracted several quantification metrics. Recall that in Chapter 2, cells were supplied to the networks only

(A)

(B)

(C)

(D)
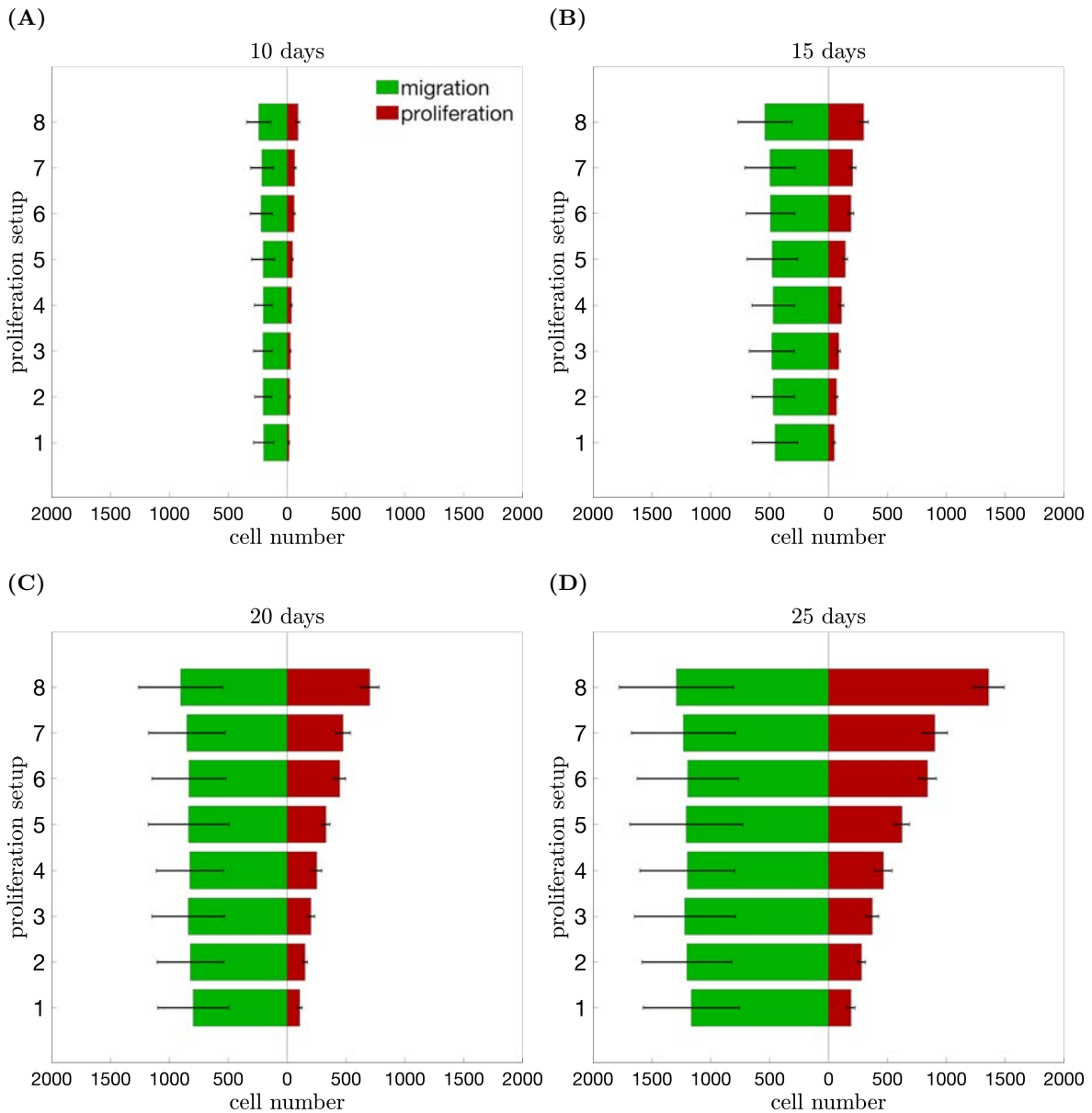
Figure 4.10. Proliferation contribution to the overall cell supply into the network for simulations in VEGF gradient, where VEGF level increases from 1 to 10 ng/ml. The bar plot provides a breakdown of cell supply into growing vasculatures by contribution due to migration from the sprout base (shown in green) and cell proliferation (shown in red) at **(A)** 10 days; **(A)** 15 days; **(A)** 20 days; **(A)** 25 days. The black error bars indicate the standard deviation. The vertical axis indicates proliferation setups (see Table D.2); the horizontal axis shows mean cell number. All results are averaged over 100 realisations. Numerical simulations were performed using large-scale setup 1 from Table D.3. Parameter values are listed in Table D.1.

at the base of growing sprouts in response to cell migration (as a boundary condition, see Appendix B.3). In our large-scale simulations, cell numbers also increase via cell proliferation. We introduced a new metric, called *proliferation contribution*, which characterises the percentage of cells created by cell proliferation up to a given time. The results, averaged over 100 realisations for simulations with VEGF gradient of 1-10 ng/ml, are presented in Figure 4.10 (see Figure D.7 for VEGF gradient of 1-5 ng/ml). We observe that the supply of ECs into the networks is slow during the early stages of the simulations (Figures 4.10A-4.10B and D.7A-D.7B) since, for the chosen initial conditions (see Table D.3), the initial sprouts are located in regions with low VEGF concentrations. Over time, as the network expands, and cells reach regions with higher VEGF concentrations (VEGF gradient increases in the direction of the x-axis), the cell supply increases (Figures 4.10C-4.10D and D.7C-D.7D). We note that the number of cells supplied to the network as a result of cell migration (green colour in Figure 4.10) does not vary significantly for different proliferation setups. However, as expected, the contribution from proliferation (red colour in Figure 4.10) increases as the cell cycle duration decreases. More specifically, the average contribution due to cell proliferation (by the end of numerical simulations) in proliferation setup 1 (cell cycle of 30-90 h) is 14.1%. This proportion doubles for proliferation setup 4 (cell cycle of 20-40 h), to 28.1%. For proliferation setup 8 (cell cycle of 12-20 h), approximately half of new cells are supplied via cell proliferation (51.9%). Thus, the more rapid network expansion noted in Figures 4.9 and D.6 for higher proliferation rates (higher proliferation setup number) is dominated by cell proliferation, as we might expect.

The above findings are consistent with experimental results reported in [211]. The authors investigated the role of mitochondrial respiration on postnatal retinal angiogenesis in mice. They showed that impaired function of EC mitochondria affects cell proliferation but not migration (mitochondrial respiration plays a vital role in producing the building blocks for macromolecule biosynthesis needed for cell proliferation). Vascular networks with slower proliferation rates due to impaired mitochondrial respiration exhibited less radial expansion,

reduced cell numbers and lower numbers of branching points per mm^2 [211]. Interestingly, no change was observed in average vessel segment lengths ECs with impaired mitochondrial respiration (treated with an inhibitor of respiratory capacity) as compared to normal cells. Similarly, in our simulations, varying only the cell proliferation rate does not significantly affect cell supply into the network due to cell migration (Figures 4.10 and D.7) but it does affect the rate of radial expansion of the networks (Figures 4.9 and D.6).

In order to investigate further the effect of varying the cell proliferation rate on the structure of vascular networks, we extracted the following metrics (Appendix B.7): average number of vessel segments (Figures 4.11A and D.8A), mean vessel segment length (Figures 4.11B and D.8B), average vascular area (Figures 4.11C and D.8C) and mean number of branching points per 100 μm^2 of vascular network area (Figures 4.11D and D.8D). These results confirm that an increased cell proliferation rate leads to the formation of larger vascular networks, in terms of area (Figures 4.11C and D.8C), the number of vessel segments (Figures 4.11A and D.8A) and the average number of branching points (Figures 4.11D and D.8D). On the other hand, and in agreement with [211], changes in cell proliferation rates do not significantly affect the mean length of vessel segments (Figures 4.11B and D.8B). Similar results were obtained by Perfahl and colleagues using their off-lattice computational model of vascular growth [112]. Their model accounted for the mechanical sensitivity of individual cells which related the progress of the cell cycle with the stretch experienced by the cell. As such, greater mechanical sensitivity leads to shorter cell cycle durations. Perfahl and coworkers showed that increased cell proliferation rates (due to greater sensitivity to stretch) resulted in vascular networks with larger total network lengths and larger numbers of branching points [112].

4.6.3 Quantification of distances between cell nuclei

A key aspect in the formulation of our model which allowed us to perform large-scale simulations is our assumption that cell positions are defined by the position of cell nuclei and the exact shape of a cell is not needed to simulate non-local cell-cell interactions (see Figure 2.3A).
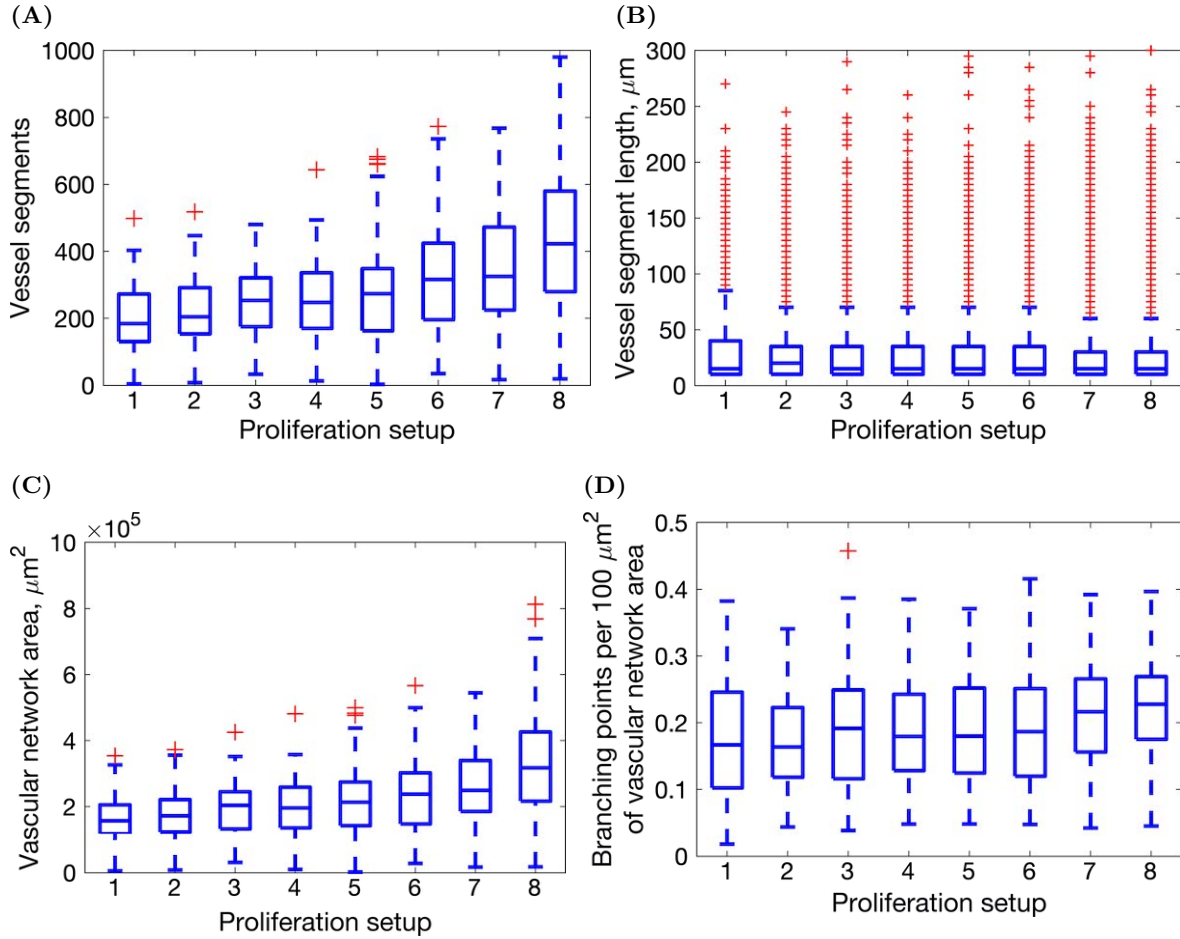
Figure 4.11. Network quantification metrics for large-scale simulations in VEGF gradient, where VEGF level increases from 1 to 10 ng/ml. (A) Number of vessel segments. **(B)** Vessel segment length (μm). **(C)** Vascular network area (μm^2). **(D)** Number of branching points per 100 μm^2 of vascular network area. Details of the definitions of these metrics can be found in Appendix B.5. In each box plot, the central line indicates the median, and the horizontal edges of the box represent the 25th and 75th percentiles (for the bottom and top edges, respectively). The outliers are indicated by the red cross symbols. All results are averaged over 100 realisations. Proliferation setups are listed in Table D.2. Numerical simulations were performed using large-scale setup 1 from Table D.3. Parameter values are listed in Table D.1 and final simulation time was fixed at $T_{max} = 72.0$ (equivalent to 25 days in real time units).

(A)

(B)

(C)

(D)

(E)

(F)

Figure 4.12. (Caption on the next page.)
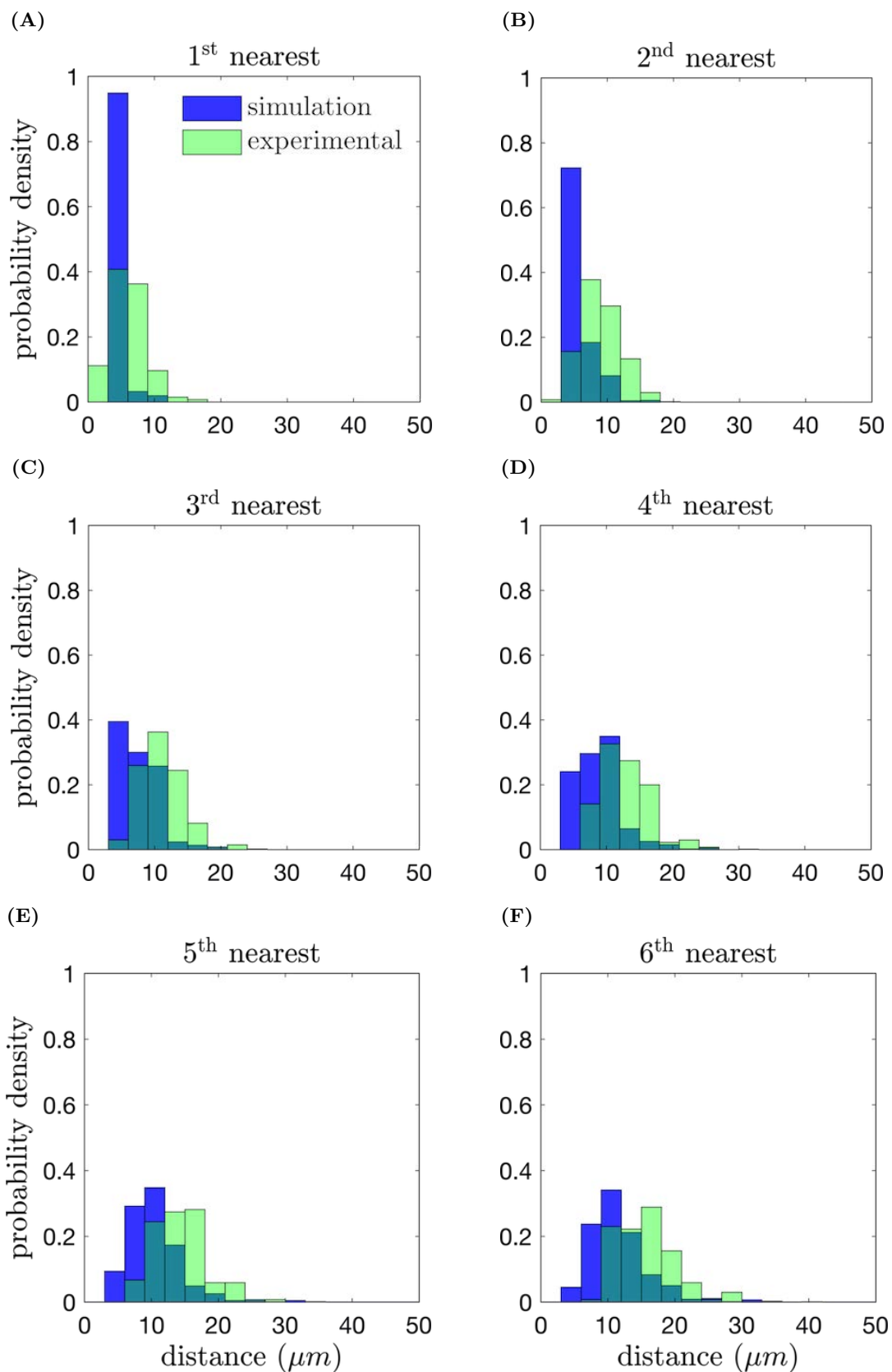
Figure 4.12. A comparison of distributions of distances between cell nuclei obtained from simulations of our model and experimental data. Distributions of distances extracted from our simulations are indicated in blue. Distributions corresponding to experimental data (obtained from Fig. 3c (control) in [3]) are shown in green. The panels correspond to the distance to the **(A)** nearest; **(B)** 2nd nearest; **(C)** 3rd nearest; **(D)** 4th nearest; **(E)** 5th nearest; **(F)** 6th nearest neighbouring cell from a focal cell. Simulation results are averaged over 100 realisations. The experimental results obtained from [3] are averaged over 135 cells. Numerical simulations were performed using large-scale setup 1 from Table D.3 and proliferation setup 8 from Table D.2. Parameter values are listed in Table D.1 and the final simulation time was fixed at $T_{max} = 72.0$ (equivalent to 25 days in real time units).

This approach naturally allows for gaps between cell positions (i.e. locations of their nuclei) within growing sprouts (see, for example, Figures 4.3 and 4.9). This assumption is corroborated by experimental images (e.g. [3], [45], [212], [213]) which confirm that cell nuclei are frequently located at a certain distance from each other (greater than the size of a cell nucleus diameter). In order to test the validity of this assumption, we compared the distributions of distances between cell nuclei in our large-scale simulations with independent experimental results [3], [45], [212], [213]. Since higher proliferation rates lead to larger vascular networks and potentially larger distances between cell nuclei (compare different proliferation setups in Figure 4.9), we performed this comparison for proliferation setup 8 (which corresponds to the shortest cell cycle time considered, i.e. 12-20 hours).

The results of this comparison are shown in Figure 4.12. Since two cells located side by side may have a larger gap behind or in front of them (e.g. Figure 4.9H), we quantified distances to nearest cell neighbours (Figure 4.12A) and also to 2nd-6th nearest cell neighbours (Figures 4.12B to 4.12F, respectively). The experimental data in Figure 4.12 were obtained from [3] (for distributions extracted from other experiments see Figure D.9). The results presented in Figure 4.12 show good quantitative agreement between the distributions of distances between cell nuclei obtained from our simulations and the experimental data. Nonetheless, we note that the distributions depend on the experimental setup (see Figure D.9).

We also investigated whether different initial conditions might affect cell separation distances. In biological vascular networks (e.g. in retina), angiogenic outgrowth is usually initiated by several main sprouts which subsequently branch and form connections between themselves (anastomose). We performed simulations initialised with three main sprouts (see Appendix D.1 for the initial simulation setup and Movie 4.5 for an animation of a representative simulation) and again compared the distribution of cell separation distances with experimental data. The results presented in Figure D.10 confirm that the initial conditions do not affect this metric. We explain this result by the fact that cell behaviour in our model is determined by the local microenvironment (migration transition defined in Eq (2.7) and proliferation transition defined in Eq (4.3)). In particular, cell migration is restricted by the function $F(E_i^N)$ controlling cell-cell adhesion (see Eq (2.9)). Its bell-shaped form does not allow movement of the focal cell when its local neighbourhood contains too few, or too many, cells (see Figure 2.5E for an illustration). This maintains a certain distribution of cells within the network. Thus, global changes (such as the initial number of sprouts) do not affect cell behaviour and the distributions of cell separation distances are preserved.

4.7 Discussion

In this chapter, we extended the multiscale model of angiogenesis from Chapter 2 in order to increase the simulation timescale from hours (which is characteristic of *in vitro* experiments) to the timescale of days or weeks (which corresponds to the timescale of *in vivo* experiments). We achieved this by incorporating the CG model of EC signalling (formulated in Chapter 3) at the subcellular scale in the angiogenesis model. The CG phenotype model allowed us to substantially decrease the computational complexity of model simulations (Figure 3.12) while maintaining good agreement with the original model (Figures 4.3 to 4.5).

In order to perform simulations on longer timescales, we additionally took into account cell proliferation (section 4.4) and vessel maturation (section 4.5). The implementation of cell proliferation model was based on existing experimental data on EC cell cycle duration

(Figure 4.6), the location of the daughter cells (Figure 4.7) and asymmetric cell division (section 4.4.6). By performing computational experiments for a number of scenarios, we showed how cell division and vessel maturation contribute to the formation of a branching network structure on longer timescales (Figure 4.8). In particular, in the absence of vessel maturation and cell proliferation, the cell front tends to expand radially in a uniform fashion and the sprout formation is reduced (Figures 4.8A to 4.8C).

Our detailed, experimentally-based implementation of cell division allowed us to investigate the effect of varying the cell proliferation rate on vascular network formation (see Figures 4.9 and D.6 for representative simulation results). Our simulation results suggest that changes in cell cycle duration do not affect the number of cells supplied into the network as a result of cell migration (Figures 4.10 and D.7). On the other hand, shorter cell cycle times increase the supply of cells into the vasculature (Figures 4.10 and D.7) and give rise to vascular networks with larger surface areas, larger numbers of vessel segments and larger numbers of branching points per unit area of vascular network (Figures 4.11A, 4.11C and 4.11D, respectively). The model also predicts that the average length of vessel sprouts does not change significantly as the cell proliferation rate varies (Figure 4.11B). These model predictions are consistent with the experimental data reported in [211] where the authors were able to reduce the EC proliferation rate without affecting cell migration.

We further validated our model by quantifying the distances between cell nuclei (i.e. cell position is known up to the lattice site in which its nucleus is located) in our simulated networks and compared the resulting distributions with the experimental data reported in [3], [45], [212], [213]. Our results are in good agreement with the distributions from the experimental data (Figure 4.12), although distances between cells may vary depending on local microenvironment conditions (Figure D.9). Moreover, we showed that the distribution of distances between cells in our model is not affected by global changes in the domain, such as the number of main sprouts in the system (Figure D.10). This confirms our model assumption that cell behaviour, defined by its local microenvironment (cell migration, section 2.3.3, and

proliferation, section 4.4.4), suffices to sustain the formation of a vascular network.

The CG phenotype model allowed us to perform simulations of early (before vasculature remodelling) angiogenesis on larger spatial and timescales. This framework enables us to study vascular network formation on timescales associated with angiogenesis *in vivo*. A weakness of the CG approach is that model parameters (of the CG scale) are fixed by the CG formulation of the subcellular signalling. Thus, these parameters cannot be varied in a straightforward fashion; by contrast, in Chapter 2, we could investigate the behaviour of mutant cells with impaired signalling of VEGF receptors. For each variation in subcellular signalling, a new CG model has to be formulated, which requires the pre-calculation of several look-up tables (see Chapter 3). The computational effort of doing this in our implementation was of an order ranging from several days to a week. We also note that the CG method enables us to perform simulations with cells whose internal dynamics are described using distinct frameworks; CG description of the subcellular signalling in a subset of ECs can be coupled to the original stochastic model in another subset of ECs (e.g. when some mutant cells are introduced in the existing network).

In future work, we aim to extend our model to account for cell-ECM interactions and vessel maturation in a more mechanistically-based way, as compared to our current implementation which employs phenomenological descriptions of these processes. Another goal is to perform a more comprehensive comparison of our simulation results on longer timescales with available experimental data (we expect more suitable experimental data to be available in the future).

Chapter 5

Conclusions and future work

Angiogenic sprouting plays a vital role in embryonic development and in the evolution of such pathologies as cancer, diabetes and atherosclerosis [1], [2]. For example, tumour-induced angiogenesis is classified as one of the hallmarks of cancer; growth of solid tumours and metastasis depend on the formation of new vascular networks via angiogenic sprouting [166]. Although it has been extensively studied from experimental and theoretical perspectives, our understanding of angiogenesis is incomplete. In particular, it has been long believed that EC behaviour (i.e. its phenotype) during sprouting is predetermined by the fixed position of the cell within the sprout; ECs positioned at sprout tips were associated with a migratory phenotype responsible for guiding sprout elongation, whereas ECs trailing behind sprout tips were assumed to maintain sprout integrity by proliferation. In this *snail-trail* model of angiogenesis, cell phenotype was assumed irreversible. Recent biological experiments demonstrated that ECs rearrange within growing sprouts and their phenotypes are dynamically adjusted in response to variations in the local microenvironment [4], [9], [10]. As such, early sprout elongation was shown to be driven by cell rearrangements and not cell proliferation [4]. By contrast, the snail-trail model of angiogenesis assumes that sprout elongation is dominated by cell proliferation. The functional role of cell mixing remains unclear [3], [4], [9]. Most mathematical and computational models of angiogenesis are formulated in terms of the snail-trail framework for sprout growth (section 1.5). These models cannot be used to investigate

the effects of cell mixing on the morphology of growing vascular networks. Thus, a more detailed model of complex EC behaviour is needed to study this phenomenon.

In this thesis, we formulated a new multiscale model of sprouting angiogenesis and validated it against experimental data (Chapter 2). This model takes into account gene expression of ECs mediated via the VEGF-Delta-Notch signalling pathway, cell rearrangement and EC interactions with the surrounding environment. Our model, with naturally emerging branching and EC chemotactic sensitivity to VEGF, allowed us to investigate how changes in intracellular signalling and local cell environment influence the dynamics of cell mixing and also to study the impact of cell mixing on the emerging network structure. Our results demonstrate that there is lower cell mixing in networks formed by cells with impaired VEGF signalling (VEGFR1$^{+/-}$ and VEGFR2$^{+/-}$ mutant ECs) than in networks formed by normal ECs. This suggests that specific cell gene expression patterns are needed to maintain a certain level of cell rearrangement. When the amount of cell shuffling decreases due to changes in gene expression dynamics, the vascular network structure changes. In particular, our results indicate that the balance between sprout elongation and branching, which is essential for vascular formation, is altered in mutant networks. Thus, we propose that cell rearrangement during angiogenesis helps to establish a balance between vessel extension and branching in the following way:

1. Cell phenotype adaptation occurs on a slower timescale than cell rearrangement. Thus, when a cell with a specific phenotype (and its phenotype-dependent behaviour) overtakes ECs in its vicinity and migrates to another location within the sprout, it may alter the branching structure of the network before it becomes inhibited by its neighbours and changes its phenotype (Figure 5.1A).

2. Cell rearrangements contribute to ECM remodelling. For example, traction forces exerted by migrating ECs on the ECM align its fibrils in the direction of sprout elongation (Figure 5.1B). This stabilises the network and reduces the probability of excessive
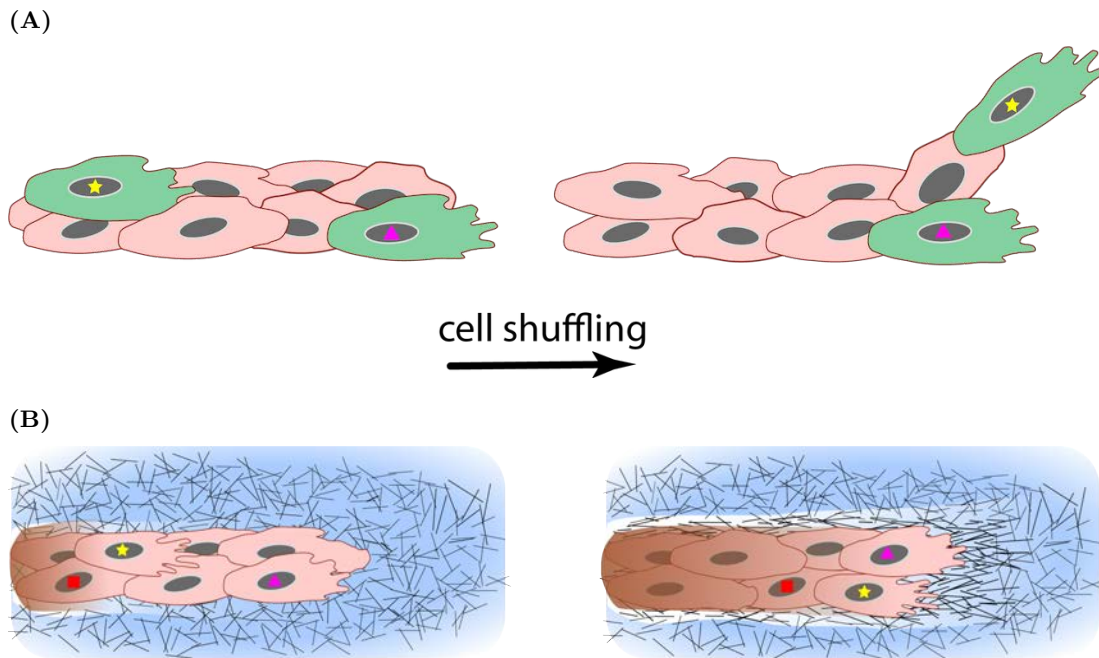
Figure 5.1. Illustrations of the role of cell rearrangements during angiogenic sprouting. (A) Since cell phenotype adaptation acts on a longer timescale than cell migration, a tip cell (its nucleus is indicated by a yellow star) can change its position by overtaking neighbouring ECs and initiate a new branch before becoming inhibited by another tip cell (its nucleus is indicated by a magenta triangle). **(B)** Cell shuffling (note the positions of ECs labeled with a red square, a yellow star and a magenta triangle) leads to ECM remodelling: alignment of the matrix fibrils, formation of vascular guidance tunnels (in blue) and deposition of BM components (in brown). This promotes vessel stabilisation.

branching.

The mixing metric proposed in this thesis is, to our knowledge, the first attempt to quantify cell rearrangements in a theoretical model of angiogenesis. Since only individual cell trajectories are needed to compute this statistic, it can also be extracted from experimental data. This, together with our prediction that cell mixing intensity is directly related to vascular network structure, makes the mixing measure a potential marker for pathological angiogenesis. We plan to test our model predictions regarding the role of cell rearrangement in future biological experiments.

Furthermore, although we used a specific formulation for our subcellular model, the same

modelling approach can be applied to more or less detailed systems (e.g. recent works [214], [215]) provided they generate the phenotypic patterning of ECs that is typical of vascular networks. This flexibility allows us to use our model to test various experimental hypotheses and to make predictions, for example, regarding mechanisms driving pathological network formation.

We initially performed simulations of migration-driven growth of small vascular networks. In order to investigate how cell proliferation (operating on longer timescales) contributes to vascular growth, we first reduced the computational complexity of our multiscale model of angiogenesis. We developed a method that coarse-grains a stochastic system which describes the internal dynamics of agents in a multiscale model to a Markov jump process between the stable steady states of the stochastic system (Chapter 3). This technique is based on large deviation theory and, to our knowledge, is the first time this theory has been used to coarse-grain coupled multi-agent systems. We illustrated our coarse-graining method by applying it to the subcellular signalling of endothelial cells in our angiogenesis model.

The framework of hybrid multiscale modelling enables formulation of more detailed descriptions of biological systems. This facilitates model validation against experimental data and improves interpretability of model simulations (as compared to phenomenological models). However, a drawback of models of this type is their high computational cost. The CG method paves the way for a systematic reduction of a general class of hybrid models in which agent behaviour is described by a stochastic system with multiple metastable states. The CG technique preserves the original description of the agents' internal states (as a continuous variable instead of making it discrete) and stochasticity of noise-induced behavioural switches, while considerably reducing the numerical cost of these models. Thus, it enables investigation of system behaviour on longer timescales than is possible with other frameworks (e.g. full stochastic simulations or deterministic equations). The CG method is especially useful for hybrid models of biological processes, since the behaviour of cells and other biological species is often represented by decision-making systems (i.e. with multiple stable steady

states) in response to external stimuli.

We demonstrated the potential of the CG method in Chapter 4, where we used it to coarse-grain a stochastic model of a subcellular signalling pathway in ECs. This allowed us to substantially reduce the computational cost of simulation of our hybrid model of angiogenesis. We then extended our model to account for cell proliferation. The CG framework enabled us to investigate angiogenic sprouting on timescales associated with angiogenesis *in vivo*. We used it to examine the effects of varying the cell proliferation rate on the morphology of growing vascular networks.

Our model of angiogenesis can be further extended in several ways. In its current implementation, the branching structure of simulated networks is constrained by the hexagonal lattice. Although vascular networks are frequently characterised by honeycomb branching patterns [216], [217] (i.e. the angle between vessel segments is close to that in a hexagonal lattice), we plan to extend our model to account for off-lattice cell migration. To do this, we will formulate a mechanistic, rather than a phenomenological, description of ECM structure and its remodelling due to interactions with ECs. We also aim to extend our model to account for vascular remodelling due to blood flow. In addition, it would be interesting to perform model simulations in three dimensions.

As future work, we also aim to explore the potential for using our CG method to identify robust patterns in biological systems that are capable of generating spatial patterns of species (or cells) with distinct behaviours.

To summarise, this work *(a)* shows how multiscale models can be validated against experimental data and, in so doing, increase understanding of complex biological phenomena, such as angiogenesis and *(b)* advances the field of theoretical modelling by developing a coarse-graining method that reduces the computational cost of simulating multiscale hybrid models.

Bibliography

[1] P. Carmeliet, "Angiogenesis in life, disease and medicine", *Nature*, vol. 438, no. 7070, pp. 932–936, 2005.

[2] M. Potente and P. Carmeliet, "The link between angiogenesis and endothelial metabolism", *Annual Review of Physiology*, vol. 79, pp. 43–66, 2017.

[3] A. Angulo-Urarte, P. Casado, S. D. Castillo, P. Kobialka, M. P. Kotini, A. M. Figueiredo, P. Castel, V. Rajeeve, M. Mila-Guasch, J. Millan, C. Wiesner, H. Serra, L. Muixi, O. Casanovas, F. Viñals, M. Affolter, H. Gerhardt, S. Huveneers, H.-G. Belting, P. R. Cutillas, and M. Graupera, "Endothelial cell rearrangements during vascular patterning require pi3-kinase-mediated inhibition of actomyosin contractility", *Nature Communications*, vol. 9, no. 1, p. 4826, 2018.

[4] S. Arima, K. Nishiyama, T. Ko, Y. Arima, Y. Hakozaki, K. Sugihara, H. Koseki, Y. Uchijima, Y. Kurihara, and H. Kurihara, "Angiogenic morphogenesis driven by dynamic and heterogeneous collective endothelial cell movement", *Development*, vol. 138, no. 21, pp. 4763–4776, 2011.

[5] K. Bentley, C. A. Franco, A. Philippides, R. Blanco, M. Dierkes, V. Gebala, F. Stanchi, M. Jones, I. M. Aspalter, G. Cagna, S. Westrom, L. Claesson-Welsh, D. Vestweber, and H. Gerhardt, "The role of differential ve-cadherin dynamics in cell rearrangement during angiogenesis", *Nature Cell Biology*, vol. 16, no. 309, pp. 309–321, 2014.

[6] K. De Bock, M. Georgiadou, S. Schoors, A. Kuchnio, B. W. Wong, A. R. Cantelmo, A. Quaegebeur, B. Ghesquiere, S. Cauwenberghs, G. Eelen, *et al.*, "Role of pfkfb3-driven glycolysis in vessel sprouting", *Cell*, vol. 154, no. 3, pp. 651–663, 2013.

[7] B. Cruys, B. W. Wong, A. Kuchnio, D. Verdegem, A. R. Cantelmo, L.-C. Conradi, S. Vandekeere, A. Bouche, I. Cornelissen, S. Vinckier, R. M. H. Merks, E. Dejana, H. Gerhardt, M. Dewerchin, K. Bentley, and P. Carmeliet, "Glycolytic regulation of cell rearrangement in angiogenesis", *Nature Communications*, vol. 7, p. 12 240, 2016.

[8] C. A. Franco, M. L. Jones, M. O. Bernabeu, I. Geudens, T. Mathivet, A. Rosa, F. M. Lopes, A. P. Lima, A. Ragab, R. T. Collins, *et al.*, "Dynamic endothelial cell rearrangements drive developmental vessel regression", *PLoS Biology*, vol. 13, no. 4, 2015.

[9] L. Jakobsson, C. A. Franco, K. Bentley, R. T. Collins, B. Ponsioen, I. M. Aspalter, I. Rosewell, M. Busse, G. Thurston, A. Medvinsky, *et al.*, "Endothelial cells dynamically compete for the tip cell position during angiogenic sprouting", *Nature Cell Biology*, vol. 12, no. 10, p. 943, 2010.

[10] K. Sugihara, K. Nishiyama, S. Fukuhara, A. Uemura, S. Arima, R. Kobayashi, A. Köhn-Luque, N. Mochizuki, T. Suda, H. Ogawa, *et al.*, "Autonomy and non-autonomy of angiogenic cell movements revealed by experiment-driven mathematical modeling", *Cell Reports*, vol. 13, no. 9, pp. 1814–1827, 2015.

[11] B. Ubezio, R. A. Blanco, I. Geudens, F. Stanchi, T. Mathivet, M. L. Jones, A. Ragab, K. Bentley, and H. Gerhardt, "Synchronization of endothelial dll4-notch dynamics switch blood vessels from branching to expansion", *ELife*, vol. 5, e12167, 2016.

[12] R. Vega, M. Carretero, R. D. Travasso, and L. L. Bonilla, "Notch signaling and taxis mechanims regulate early stage angiogenesis: A mathematical and computational model", *PLoS Computational Biology*, vol. 16, no. 1, e1006919, 2020.

[13] P. H. Burri, R. Hlushchuk, and V. Djonov, "Intussusceptive angiogenesis: Its emergence, its characteristics, and its significance", *Developmental Dynamics: an official publication of the American Association of Anatomists*, vol. 231, no. 3, pp. 474–488, 2004.

[14] S. J. Mentzer and M. A. Konerding, "Intussusceptive angiogenesis: Expansion and remodeling of microvascular networks", *Angiogenesis*, vol. 17, no. 3, pp. 499–509, 2014.

[15] G. Eelen, P. de Zeeuw, L. Treps, U. Harjes, B. W. Wong, and P. Carmeliet, "Endothelial cell metabolism", *Physiological Reviews*, vol. 98, no. 1, pp. 3–58, 2018.

[16] L.-K. Phng and H. Gerhardt, "Angiogenesis: A team effort coordinated by notch", *Developmental Cell*, vol. 16, no. 2, pp. 196–208, 2009.

[17] U. R. Michaelis, "Mechanisms of endothelial cell migration", *Cellular and Molecular Life Sciences*, vol. 71, no. 21, pp. 4131–4148, 2014.

[18] D. R. Senger and G. E. Davis, "Angiogenesis", *Cold Spring Harbor Perspectives in Biology*, vol. 3, no. 8, a005090, 2011.

[19] J. Sottile, "Regulation of angiogenesis by extracellular matrix", *Biochimica et Biophysica Acta (BBA)-Reviews on Cancer*, vol. 1654, no. 1, pp. 13–22, 2004.

[20] M. G. McCoy, J. M. Wei, S. Choi, J. P. Goerger, W. Zipfel, and C. Fischbach, "Collagen fiber orientation regulates 3d vascular network formation and alignment", *ACS Biomaterials Science & Engineering*, vol. 4, no. 8, pp. 2967–2976, 2018.

[21] N. M. Myer and K. A. Myers, "Clasp1 regulates endothelial cell branching morphology and directed migration", *Biology Open*, vol. 6, no. 10, pp. 1502–1515, 2017.

[22] M. S. Wietecha, W. L. Cerny, and L. A. DiPietro, "Mechanisms of vessel regression: Toward an understanding of the resolution of angiogenesis", *New Perspectives in Regeneration*, pp. 3–32, 2012.

[23] I. Geudens and H. Gerhardt, "Coordinating cell behaviour during blood vessel formation", *Development*, vol. 138, no. 21, pp. 4569–4583, 2011.

[24] A. Mukwaya, L. Jensen, and N. Lagali, "Relapse of pathological angiogenesis: Functional role of the basement membrane and potential treatment strategies", *Experimental & Molecular Medicine*, vol. 53, no. 2, pp. 189–201, 2021.

[25] R. Blanco and H. Gerhardt, "Vegf and notch in tip and stalk cell selection", *Cold Spring Harbor Perspectives in Medicine*, vol. 3, no. 1, a006569, 2013.

[26] H. Gerhardt, M. Golding, M. Fruttiger, C. Ruhrberg, A. Lundkvist, A. Abramsson, M. Jeltsch, C. Mitchell, K. Alitalo, D. Shima, *et al.*, "Vegf guides angiogenic sprouting utilizing endothelial tip cell filopodia", *The Journal of Cell Biology*, vol. 161, no. 6, pp. 1163–1177, 2003.

[27] M. Hellström, L.-K. Phng, J. J. Hofmann, E. Wallgard, L. Coultas, P. Lindblom, J. Alva, A.-K. Nilsson, L. Karlsson, N. Gaiano, *et al.*, "Dll4 signalling through notch1 regulates formation of tip cells during angiogenesis", *Nature*, vol. 445, no. 7129, pp. 776–780, 2007.

[28] S. Rousseau, F. Houle, H. Kotanides, L. Witte, J. Waltenberger, J. Landry, and J. Huot, "Vascular endothelial growth factor (vegf)-driven actin-based motility is mediated by vegfr2 and requires concerted activation of stress-activated protein kinase 2 (sapk2/p38) and geldanamycin-sensitive phosphorylation of focal adhesion kinase", *Journal of Biological Chemistry*, vol. 275, no. 14, pp. 10 661–10 672, 2000.

[29] L. Lamalice, F. Le Boeuf, and J. Huot, "Endothelial cell migration during angiogenesis", *Circulation Research*, vol. 100, no. 6, pp. 782–794, 2007.

[30] T. Watanabe, J. Noritake, and K. Kaibuchi, "Regulation of microtubules in cell migration", *Trends in Cell Biology*, vol. 15, no. 2, pp. 76–83, 2005.

[31] C. A. Reinhart-King, M. Dembo, and D. A. Hammer, "The dynamics and mechanics of endothelial cell spreading", *Biophysical Journal*, vol. 89, no. 1, pp. 676–689, 2005.

[32] A. N. Stratman, W. B. Saunders, A. Sacharidou, W. Koh, K. E. Fisher, D. C. Zawieja, M. J. Davis, and G. E. Davis, "Endothelial cell lumen and vascular guidance tunnel formation requires mt1-mmp–dependent proteolysis in 3-dimensional collagen matrices", *Blood*, vol. 114, no. 2, pp. 237–247, 2009.

[33] N. D. Kirkpatrick, S. Andreou, J. B. Hoying, and U. Utzinger, "Live imaging of collagen remodeling during angiogenesis", *American Journal of Physiology-Heart and Circulatory Physiology*, vol. 292, no. 6, H3198–H3206, 2007.

[34] Y. Du, S. C. Herath, Q.-g. Wang, D.-a. Wang, H. H. Asada, and P. C. Chen, "Three-dimensional characterization of mechanical interactions between endothelial cells and extracellular matrix during angiogenic sprouting", *Scientific Reports*, vol. 6, p. 21 362, 2016.

[35] R. S. Sopher, H. Tokash, S. Natan, M. Sharabi, O. Shelah, O. Tchaicheeyan, and A. Lesman, "Nonlinear elasticity of the ecm fibers facilitates efficient intercellular communication", *Biophysical Journal*, vol. 115, no. 7, pp. 1357–1370, 2018.

[36] S. Pillay, H. M. Byrne, and P. K. Maini, "Modeling angiogenesis: A discrete to continuum description", *Physical Review E*, vol. 95, p. 012 410, 2017.

[37] K. Bentley, G. Mariggi, H. Gerhardt, and P. A. Bates, "Tipping the balance: Robustness of tip cell selection, migration and fusion in angiogenesis", *PLoS Computational Biology*, vol. 5, pp. 1–19, 2009.

[38] W. Chen, P. Xia, H. Wang, J. Tu, X. Liang, X. Zhang, and L. Li, "The endothelial tip-stalk cell selection and shuffling during angiogenesis", *Journal of Cell Communication and Signaling*, pp. 1–11, 2019.

[39] K. Herz, A. Becker, C. Shi, M. Ema, S. Takahashi, M. Potente, M. Hesse, B. K. Fleischmann, and D. Wenzel, "Visualization of endothelial cell cycle dynamics in mouse using the flt-1/egfp-anillin system", *Angiogenesis*, vol. 21, no. 2, pp. 349–361, 2018.

[40] B. Zheng, G. Li, W. C. Chen, B. M. Deasy, J. B. Pollett, B. Sun, L. Drowley, B. Gharaibeh, A. Usas, B. Péault, *et al.*, "Human myogenic endothelial cells exhibit chondrogenic and osteogenic potentials at the clonal level", *Journal of Orthopaedic Research*, vol. 31, no. 7, pp. 1089–1095, 2013.

[41] D. Form, B. Pratt, and J. Madri, "Endothelial cell proliferation during angiogenesis. in vitro modulation by basement membrane components.", *Laboratory Investigation; a Journal of Technical Methods and Pathology*, vol. 55, no. 5, pp. 521–530, 1986.

[42] C. A. Frye and C. W. Patrick, "Isolation and culture of rat microvascular endothelial cells", *In Vitro Cellular & Developmental Biology-Animal*, vol. 38, no. 4, pp. 208–212, 2002.

[43] M. D. Snead, A. Papapetropoulos, G. O. Carrier, and J. D. Catravas, "Isolation and culture of endothelial cells from the mesenteric vascular bed", *Methods in Cell Science*, vol. 17, no. 4, pp. 257–262, 1995.

[44] A. Anagnostou, E. S. Lee, N. Kessimian, R. Levinson, and M. Steiner, "Erythropoietin has a mitogenic and positive chemotactic effect on endothelial cells.", *Proceedings of the National Academy of Sciences*, vol. 87, no. 15, pp. 5978–5982, 1990.

[45] S. Pontes-Quero, M. Fernández-Chacón, W. Luo, F. F. Lunella, V. Casquero-Garcia, I. Garcia-Gonzalez, A. Hermoso, S. F. Rocha, M. Bansal, and R. Benedito, "High mitogenic stimulation arrests angiogenesis", *Nature Communications*, vol. 10, no. 1, pp. 1–16, 2019.

[46] A. Lesman, D. Rosenfeld, S. Landau, and S. Levenberg, "Mechanical regulation of vascular network formation in engineered matrices", *Advanced Drug Delivery Reviews*, vol. 96, pp. 176–182, 2016.

[47] E. Chavakis and S. Dimmeler, "Regulation of endothelial cell survival and apoptosis during angiogenesis", *Arteriosclerosis, Thrombosis, and Vascular Biology*, vol. 22, no. 6, pp. 887–893, 2002.

[48] E. C. Watson, Z. L. Grant, and L. Coultas, "Endothelial cell apoptosis in angiogenesis and vessel regression", *Cellular and Molecular Life Sciences*, vol. 74, no. 24, pp. 4387–4403, 2017.

[49] A. Zecchin, J. Kalucka, C. Dubois, and P. Carmeliet, "How endothelial cells adapt their metabolism to form vessels in tumors", *Frontiers in Immunology*, vol. 8, p. 1750, 2017.

[50] G. Bergers and S. Song, "The role of pericytes in blood-vessel formation and maintenance", *Neuro-Oncology*, vol. 7, no. 4, pp. 452–464, 2005.

[51] A. B. Stundzia and C. J. Lumsden, "Stochastic simulation of coupled reaction–diffusion processes", *Journal of Computational Physics*, vol. 127, no. 1, pp. 196–207, 1996.

[52] M. Howard and A. D. Rutenberg, "Pattern formation inside bacteria: Fluctuations due to the low copy number of proteins", *Physical Review Letters*, vol. 90, no. 12, p. 128 102, 2003.

[53] E. Moro, "Hybrid method for simulating front propagation in reaction-diffusion systems", *Phys. Rev. E.*, vol. 69, 060101(R), 2004.

[54] D. Bernstein, "Simulating mesoscopic reaction-diffusion systems using the gillespie algorithm", *Physical Review E*, vol. 71, no. 4, p. 041 103, 2005.

[55] S. Engblom, L. Ferm, A. Hellander, and P. Lötstedt, "Simulation of stochastic reaction-diffusion processes on unstructured meshes", *SIAM Journal on Scientific Computing*, vol. 31, no. 3, pp. 1774–1797, 2009.

[56] M. B. Flegg, S. J. Chapman, and R. Erban, "The two-regime method for optimizing stochastic reaction–diffusion simulations", *Journal of the Royal Society Interface*, vol. 9, no. 70, pp. 859–868, 2012.

[57] A Hellander, S Hellander, and P Lotstedt, "Coupled mesoscopic and microscopic simulation of reaction-diffusion processes in mixed dimensions", *Multiscale Model. Sim.*, vol. 10, pp. 585–611, 2012.

[58] B. Franz, M. B. Flegg, S. J. Chapman, and R. Erban, "Multiscale reaction-diffusion algorithms: Pde-assisted brownian dynamics", *SIAM Journal on Applied Mathematics*, vol. 73, no. 3, pp. 1224–1247, 2013.

[59] F. Spill, P. Guerrero, T. Alarcon, P. K. Maini, and H. M. Byrne, "Mesoscopic and continuum modelling of angiogenesis", *Journal of Mathematical Biology*, vol. 70, no. 3, pp. 485–532, 2015.

[60] P. Guerrero, H. M. Byrne, P. K. Maini, and T. Alarcón, "From invasion to latency: Intracellular noise and cell motility as key controls of the competition between resource-limited cellular populations", *J. Math. Biol.*, vol. 72, pp. 123–156, 2015.

[61] C. A. Yates and M. B. Flegg, "The pseudo-compartment method for coupling partial differential equation and compartment-based models of diffusion", *Journal of The Royal Society Interface*, vol. 12, no. 106, 2015, ISSN: 1742-5689.

[62] D. T. Gillespie, L. R. Petzold, and E. Seitaridou, "Validity conditions for stochastic chemical kinetics in diffusion-limited systems", *The Journal of Chemical Physics*, vol. 140, no. 5, 02B604_1, 2014.

[63] S. A. Isaacson, "A convergent reaction-diffusion master equation", *The Journal of Chemical Physics*, vol. 139, no. 5, p. 054 101, 2013.

[64] J. Elf and M. Ehrenberg, "Spontaneous separation of bi-stable biochemical systems into spatial domains of opposite phases", *Systems Biology*, vol. 1, no. 2, pp. 230–236, 2004.

[65] D. T. Gillespie, "A general method for numerically simulating the stochastic time evolution of coupled chemical reactions", *Journal of Computational Physics*, vol. 22, no. 4, pp. 403–434, 1976.

[66] S. Bernard, "How to build a multiscale model in biology", *Acta Biotheoretica*, vol. 61, no. 3, pp. 291–303, 2013.

[67] T. S. Deisboeck, Z. Wang, P. Macklin, and V. Cristini, "Multiscale cancer modeling", *Annual Review of Biomedical Engineering*, vol. 13, pp. 127–155, 2011.

[68] A. Deutsch, P. Friedl, L. Preziosi, and G. Theraulaz, *Multi-scale analysis and modelling of collective migration in biological systems*, 2020.

[69] K. A. Rejniak and A. R. Anderson, "State of the art in computational modelling of cancer", *Mathematical Medicine and Biology: A Journal of the IMA*, vol. 29, no. 1, pp. 1–2, 2012.

[70] T. Heck, M.-M. Vaeyens, and H. Van Oosterwyck, "Computational models of sprouting angiogenesis and cell migration: Towards multiscale mechanochemical models of angiogenesis", *Mathematical Modelling of Natural Phenomena*, vol. 10, no. 1, pp. 108–141, 2015.

[71] R. Bardini, G. Politano, A. Benso, and S. Di Carlo, "Multi-level and hybrid modelling approaches for systems biology", *Computational and Structural Biotechnology Journal*, vol. 15, pp. 396–402, 2017.

[72] J. M. Osborne, A Walter, S. Kershaw, G. Mirams, A. Fletcher, P Pathmanathan, D Gavaghan, O. Jensen, P. Maini, and H. Byrne, "A hybrid approach to multi-scale modelling of cancer", *Philosophical Transactions of the Royal Society A: Mathematical, Physical and Engineering Sciences*, vol. 368, no. 1930, pp. 5013–5028, 2010.

[73] M. Scianna, C. Bell, and L. Preziosi, "A review of mathematical models for the formation of vascular networks", *Journal of Theoretical Biology*, vol. 333, pp. 174–209, 2013.

[74] G. Vilanova, I. Colominas, and H. Gomez, "Computational modeling of tumor-induced angiogenesis", *Archives of Computational Methods in Engineering*, vol. 24, no. 4, pp. 1071–1102, 2017.

[75] N. V. Mantzaris, S. Webb, and H. G. Othmer, "Mathematical modeling of tumor-induced angiogenesis", *Journal of Mathematical Biology*, vol. 49, no. 2, pp. 111–187, 2004.

[76] D. Balding and D. McElwain, "A mathematical model of tumour-induced capillary growth", *Journal of Theoretical Biology*, vol. 114, no. 1, pp. 53 –73, 1985, ISSN: 0022-5193.

[77] M. A. Chaplain and A. M. Stuart, "A model mechanism for the chemotactic response of endothelial cells to tumour angiogenesis factor", *Mathematical Medicine and Biology: A Journal of the IMA*, vol. 10, no. 3, pp. 149–168, 1993.

[78] H. Byrne and M. Chaplain, "Mathematical models for tumour angiogenesis: Numerical simulations and nonlinear wave solutions", *Bulletin of Mathematical Biology*, vol. 57, no. 3, pp. 461 –486, 1995, ISSN: 0092-8240.

[79] B Sleeman and I. Wallis, "Tumour induced angiogenesis as a reinforced random walk: Modelling capillary network formation without endothelial cell proliferation", *Mathematical and Computer Modelling*, vol. 36, no. 3, pp. 339–358, 2002.

[80] A. R. A. Anderson and M. A. J. Chaplain, "Continuous and discrete mathematical models of tumor-induced angiogenesis", *Bulletin of Mathematical Biology*, vol. 60, pp. 857–899, 1998.

[81] S. Tong and F. Yuan, "Numerical simulations of angiogenesis in the cornea", *Microvascular Research*, vol. 61, no. 1, pp. 14–27, 2001.

[82] M. Plank and B. Sleeman, "Lattice and non-lattice models of tumour angiogenesis", *Bulletin of Mathematical Biology*, vol. 66, no. 6, pp. 1785–1819, 2004.

[83] V. Capasso and D. Morale, "Stochastic modelling of tumour-induced angiogenesis", *Journal of Mathematical Biology*, vol. 58, no. 1, pp. 219–233, 2009.

[84] J. Folkman, "Tumor angiogenesis", *Advances in Cancer Research*, vol. 19, pp. 331–358, 1974.

[85] ——, "The vascularization of tumors", *Scientific American*, vol. 234, no. 5, pp. 58–73, 1976.

[86] M. A. Gimbrone Jr, R. S. Cotran, S. B. Leapman, and J. Folkman, "Tumor growth and neovascularization: An experimental model using the rabbit cornea", *Journal of the National Cancer Institute*, vol. 52, no. 2, pp. 413–427, 1974.

[87] V. Muthukkaruppan and R Auerbach, "Angiogenesis in the mouse cornea", *Science*, vol. 205, no. 4413, pp. 1416–1418, 1979.

[88] A. Deakin, "Model for initial vascular patterns in melanoma transplants.", *Growth*, vol. 40, no. 2, pp. 191–201, 1976.

[89] M. A. Chaplain and A. M. Stuart, "A mathematical model for the diffusion of tumour angiogenesis factor into the surrounding host tissue", *Mathematical Medicine and Biology: A Journal of the IMA*, vol. 8, no. 3, pp. 191–220, 1991.

[90] M. Chaplain, "The mathematical modelling of tumour angiogenesis and invasion", *Acta Biotheoretica*, vol. 43, no. 4, pp. 387–402, 1995.

[91] ——, "Avascular growth, angiogenesis and vascular growth in solid tumours: The mathematical modelling of the stages of tumour development", *Mathematical and Computer Modelling*, vol. 23, no. 6, pp. 47–87, 1996.

[92] M. Orme and M. Chaplain, "A mathematical model of the first steps of tumour-related angiogenesis: Capillary sprout formation and secondary branching", *Mathematical Medicine and Biology: A Journal of the IMA*, vol. 13, no. 2, pp. 73–98, 1996.

[93] ——, "Two-dimensional models of tumour angiogenesis and anti-angiogenesis strategies", *Mathematical Medicine and Biology: A Journal of the IMA*, vol. 14, no. 3, pp. 189–205, 1997.

[94] H. A. Levine, S. Pamuk, B. D. Sleeman, and M. Nilsen-Hamilton, "Mathematical modeling of capillary formation and development in tumor angiogenesis: Penetration into the stroma", *Bulletin of Mathematical Biology*, vol. 63, no. 5, pp. 801–863, 2001.

[95] M Aubert, M. Chaplain, S. McDougall, A Devlin, and C. Mitchell, "A continuum mathematical model of the developing murine retinal vasculature", *Bulletin of Mathematical Biology*, vol. 73, no. 10, pp. 2430–2451, 2011.

[96] J. A. Flegg, D. L. McElwain, H. M. Byrne, and I. W. Turner, "A three species model to simulate application of hyperbaric oxygen therapy to chronic wounds", *PLoS Computational Biology*, vol. 5, no. 7, e1000451, 2009.

[97] A. J. Connor, R. P. Nowak, E. Lorenzon, M. Thomas, F. Herting, S. Hoert, T. Quaiser, E. Shochat, J. Pitt-Francis, J. Cooper, *et al.*, "An integrated approach to quantitative modelling in angiogenesis research", *Journal of The Royal Society Interface*, vol. 12, no. 110, p. 20 150 546, 2015.

[98] H. Byrne and M. Chaplain, "Explicit solutions of a simplified model of capillary sprout growth during tumor angiogenesis", *Applied Mathematics Letters*, vol. 9, no. 1, pp. 69–74, 1996.

[99] D Manoussaki, S. Lubkin, R. Vemon, and J. Murray, "A mechanical model for the formation of vascular networks in vitro", *Acta Biotheoretica*, vol. 44, no. 3, pp. 271–282, 1996.

[100] M. Holmes and B. Sleeman, "A mathematical model of tumour angiogenesis incorporating cellular traction and viscoelastic effects", *Journal of Theoretical Biology*, vol. 202, no. 2, pp. 95–112, 2000.

[101] C. L. Stokes and D. A. Lauffenburger, "Analysis of the roles of microvessel endothelial cell random motility and chemotaxis in angiogenesis", *Journal of Theoretical Biology*, vol. 152, no. 3, pp. 377–403, 1991.

[102] N. Hill and D.-P. Häder, "A biased random walk model for the trajectories of swimming microorganisms", *Journal of Theoretical Biology*, vol. 186, no. 4, pp. 503–526, 1997.

[103] M. A. Chaplain, "Mathematical modelling of angiogenesis", *Journal of Neuro-Oncology*, vol. 50, no. 1, pp. 37–51, 2000.

[104] S. R. McDougall, A. Anderson, M. Chaplain, and J. Sherratt, "Mathematical modelling of flow through vascular networks: Implications for tumour-induced angiogenesis and chemotherapy strategies", *Bulletin of Mathematical Biology*, vol. 64, no. 4, pp. 673–702, 2002.

[105] A. Stephanou, S. R. McDougall, A. R. Anderson, and M. A. Chaplain, "Mathematical modelling of flow in 2d and 3d vascular networks: Applications to anti-angiogenic and chemotherapeutic drug strategies", *Mathematical and Computer Modelling*, vol. 41, no. 10, pp. 1137–1156, 2005.

[106] S. R. McDougall, A. R. Anderson, and M. A. Chaplain, "Mathematical modelling of dynamic adaptive tumour-induced angiogenesis: Clinical implications and therapeutic targeting strategies", *Journal of Theoretical Biology*, vol. 241, no. 3, pp. 564–589, 2006.

[107] S. R. McDougall, M. A. Chaplain, A. Stéphanou, and A. R. Anderson, "Modelling the impact of pericyte migration and coverage of vessels on the efficacy of vascular disrupting agents", *Mathematical Modelling of Natural Phenomena*, vol. 5, no. 1, pp. 163–202, 2010.

[108]   K. Bartha and H. Rieger, "Vascular network remodeling via vessel cooption, regression and growth in tumors", *Journal of Theoretical Biology*, vol. 241, no. 4, pp. 903–918, 2006, ISSN: 0022-5193.

[109]   S. Sun, M. F. Wheeler, M. Obeyesekere, and C. Patrick Jr, "Multiscale angiogenesis modeling using mixed finite element methods", *Multiscale Modeling & Simulation*, vol. 4, no. 4, pp. 1137–1167, 2005.

[110]   F. Milde, M. Bergdorf, and P. Koumoutsakos, "A hybrid model for three-dimensional simulations of sprouting angiogenesis", *Biophysical Journal*, vol. 95, no. 7, pp. 3146–3160, 2008.

[111]   K.-A. Norton and A. S. Popel, "Effects of endothelial cell proliferation and migration rates in a computational model of sprouting angiogenesis", *Scientific Reports*, vol. 6, no. 1, pp. 1–10, 2016.

[112]   H. Perfahl, B. D. Hughes, T. Alarcón, P. K. Maini, M. C. Lloyd, M. Reuss, and H. M. Byrne, "3d hybrid modelling of vascular network formation", *Journal of Theoretical Biology*, vol. 414, pp. 254–268, 2017.

[113]   W. D. Martinson, H. M. Byrne, and P. K. Maini, "Evaluating snail-trail frameworks for leader-follower behavior with agent-based modeling", *Physical Review E*, vol. 102, no. 6, p. 062 417, 2020.

[114]   J. A. Grogan, A. J. Connor, B. Markelc, R. J. Muschel, P. K. Maini, H. M. Byrne, and J. M. Pitt-Francis, "Microvessel chaste: An open library for spatial modeling of vascularized tissues", *Biophysical Journal*, vol. 112, no. 9, pp. 1767–1772, 2017.

[115]   M. R. Owen, I. J. Stamper, M. Muthana, G. W. Richardson, J. Dobson, C. E. Lewis, and H. M. Byrne, "Mathematical modeling predicts synergistic antitumor effects of combining a macrophage-based, hypoxia-targeted gene therapy with chemotherapy", *Cancer Research*, vol. 71, no. 8, pp. 2826–2837, 2011.

[116]   H. A. Harrington, M Maier, L Naidoo, N. Whitaker, and P. G. Kevrekidis, "A hybrid model for tumor-induced angiogenesis in the cornea in the presence of inhibitors", *Mathematical and Computer Modelling*, vol. 46, no. 3-4, pp. 513–524, 2007.

[117]   T. Jackson and X. Zheng, "A cell-based model of endothelial cell migration, proliferation and maturation during corneal angiogenesis", *Bulletin of Mathematical Biology*, vol. 72, no. 4, pp. 830–868, 2010.

[118]   M. Watson, S. McDougall, M. Chaplain, A. Devlin, and C. Mitchell, "Dynamics of angiogenesis during murine retinal development: A coupled in vivo and in silico study", *Journal of The Royal Society Interface*, vol. 9, no. 74, pp. 2351–2364, 2012.

[119]   K. Bentley, H. Gerhardt, and P. A. Bates, "Agent-based simulation of notch-mediated tip cell selection in angiogenic sprout initialisation", *Journal of Theoretical Biology*, vol. 250, no. 1, pp. 25–36, 2008.

[120]   G. Costa, K. I. Harrington, H. E. Lovegrove, D. J. Page, S. Chakravartula, K. Bentley, and S. P. Herbert, "Asymmetric division coordinates collective cell migration in angiogenesis", *Nature Cell Biology*, vol. 18, no. 12, pp. 1292–1301, 2016.

[121]   B. Zakirov, G. Charalambous, R. Thuret, I. M. Aspalter, K. Van-Vuuren, T. Mead, K. Harrington, E. R. Regan, S. P. Herbert, and K. Bentley, "Active perception during angiogenesis: Filopodia speed up notch selection of tip cells in silico and in vivo", *Philosophical Transactions of the Royal Society B*, vol. 376, no. 1821, p. 20 190 753, 2021.

[122]   F. Graner and J. A. Glazier, "Simulation of biological cell sorting using a two-dimensional extended potts model", *Physical Review Letters*, vol. 69, no. 13, p. 2013, 1992.

[123]   J. A. Glazier and F. Graner, "Simulation of the differential adhesion driven rearrangement of biological cells", *Physical Review E*, vol. 47, no. 3, p. 2128, 1993.

[124]   A. L. Bauer, T. L. Jackson, and Y. Jiang, "A cell-based model exhibiting branching and anastomosis during tumor-induced angiogenesis", *Biophysical Journal*, vol. 92, no. 9, pp. 3105–3121, 2007.

[125]   ——, "Topography of extracellular matrix mediates vascular morphogenesis and migration speeds in angiogenesis", *PLoS Computational Biology*, vol. 5, no. 7, e1000445, 2009.

[126] A. Shamloo and S. C. Heilshorn, "Matrix density mediates polarization and lumen formation of endothelial sprouts in vegf gradients", *Lab on a Chip*, vol. 10, no. 22, pp. 3061–3068, 2010.

[127] R. M. Merks, E. D. Perryn, A. Shirinifard, and J. A. Glazier, "Contact-inhibited chemotaxis in de novo and sprouting blood-vessel growth", *PLoS Computational Biology*, vol. 4, no. 9, e1000163, 2008.

[128] R. F. M. van Oers, E. G. Rens, D. J. LaValley, C. A. Reinhart-King, and R. M. H. Merks, "Mechanical cell-matrix feedback explains pairwise and collective endothelial cell behavior in vitro", *PLoS Computational Biology*, vol. 10, no. 8, pp. 1–14, Aug. 2014.

[129] J. T. Daub and R. M. Merks, "A cell-based model of extracellular-matrix-guided endothelial cell migration during angiogenesis", *Bulletin of Mathematical Biology*, vol. 75, no. 8, pp. 1377–1399, 2013.

[130] S. E. M. Boas and R. M. H. Merks, "Tip cell overtaking occurs as a side effect of sprouting in computational models of angiogenesis", *BMC Systems Biology*, vol. 9, no. 1, p. 86, 2015.

[131] A. Shirinifard, J. S. Gens, B. L. Zaitlen, N. J. Popławski, M. Swat, and J. A. Glazier, "3d multi-cell simulation of tumor growth and angiogenesis", *PloS One*, vol. 4, no. 10, e7190, 2009.

[132] T. Alarcón, H. M. Byrne, and P. K. Maini, "A cellular automaton model for tumour growth in inhomogeneous environment", *Journal of Theoretical Biology*, vol. 225, no. 2, pp. 257–274, 2003.

[133] ——, "A multiple scale model of tumour growth", *Multiscale Model. Sim.*, vol. 3, pp. 440–475, 2005.

[134] T. Alarcón, M. R. Owen, H. M. Byrne, and P. K. Maini, "Multiscale modelling of tumour growth and therapy: The influence of vessel normalisation on chemotherapy", *Computational and Mathematical Methods in Medicine*, vol. 7, no. 2-3, pp. 85–119, 2006.

[135] H. M. Byrne, M. R. Owen, T. Alarcon, J. Murphy, and P. K. Maini, "Modelling the response of vascular tumours to chemotherapy: A multiscale approach", *Mathematical Models and Methods in Applied Sciences*, vol. 16, no. supp01, pp. 1219–1241, 2006.

[136] M. R. Owen, T. Alarcón, H. M. Byrne, and P. K. Maini, "Angiogenesis and vascular remodelling in normal and cancerous tissues", *J. Math. Biol.*, vol. 58, pp. 689–721, 2009.

[137] H. Perfahl, H. M. Byrne, T. Chen, V. Estrella, T. Alarcón, A. Lapin, R. A. Gatenby, R. J. Gillies, M. C. Lloyd, P. K. Maini, M. Reuss, and M. R. Owen, "Multiscale Modelling of Vascular Tumour Growth in 3D: The Roles of Domain Size and Boundary Conditions", *PLoS One*, vol. 6, e14790, 2011.

[138] P Macklin, S McDougall, A. R. A. Anderson, M. A. J. Chaplain, V Cristini, and J Lowengrub, "Multiscale modelling and non-linear simulation of vascular tumour growth", *J. Math. Biol.*, vol. 58, pp. 765–798, 2009.

[139] C. M. Phillips, E. A. Lima, R. T. Woodall, A. Brock, and T. E. Yankeelov, "A hybrid model of tumor growth and angiogenesis: In silico experiments", *Plos One*, vol. 15, no. 4, e0231137, 2020.

[140] R. D. M. Travasso, E Corvera Poiré, M Castro, J. C. Rodriguez-Manzaneque, and A. Hernandez-Machado., "Tumour angiogenesis and vascular patterning: a mathematical model", *PLoS One*, vol. 6, e19989, 2011.

[141] G. Vilanova, I. Colominas, and H. Gomez, "Coupling of discrete random walks and continuous modeling for three-dimensional tumor-induced angiogenesis", *Computational Mechanics*, vol. 53, no. 3, pp. 449–464, 2014.

[142] M. Moreira-Soares, R. Coimbra, L. Rebelo, J. Carvalho, and R. D. M. Travasso, "Angiogenic factors produced by hypoxic cells are a leading driver of anastomoses in sprouting angiogenesis – a computational study", *Scientific Reports*, vol. 8, p. 8726, 2018.

[143] G. Vilanova, I. Colominas, and H. Gomez, "A mathematical model of tumour angiogenesis: Growth, regression and regrowth", *Journal of The Royal Society Interface*, vol. 14, no. 126, p. 20 160 918, 2017.

[144] J. Xu, G. Vilanova, and H. Gomez, "A mathematical model coupling tumour growth and angiogenesis", *PLoS One*, vol. 11, e0149422, 2016.

[145] J. S. Lowengrub, H. B. Frieboes, F Jin, Y. L. Chuang, X Li, P Macklin, S. M. Wise, and V Cristini, "Non-linear modelling of cancer: bridging the gap between cells and tumours", *Nonlinearity*, vol. 23, R1–R91, 2010.

[146] M. Chaplain, S. McDougall, and A. Anderson, "Mathematical modelling of tumor-induced angiogenesis", *Annual Review of Biomedical Engineering*, vol. 8, no. 1, pp. 233–257, 2006, PMID: 16834556.

[147] D. Stepanova, H. M. Byrne, P. K. Maini, and T. Alarcón, "A multiscale model of complex endothelial cell dynamics in early angiogenesis", *PLoS Computational Biology*, vol. 17, no. 1, e1008055, 2021.

[148] E. H. Sage and R. B. Vernon, "Regulation of angiogenesis by extracellular matrix: The growth and the glue.", *Journal of Hypertension. Supplement: Official Journal of the International Society of Hypertension*, vol. 12, no. 10, S145–52, 1994.

[149] C. W. Gardiner, "The escape time in nonpotential systems", *J. Stat. Phys.*, vol. 30, pp. 157–177, 1983.

[150] R. S. Maier and D. L. Stein, "A scaling theory of bifurcations in the symmetric weak-noise escape problem", *J. Stat. Phys.*, vol. 83, pp. 291–357, 1996.

[151] R. Guantes and J. F. Poyatos, "Multistable Decision Switches for Flexible Control of Epigenetic Differentiation", *PLoS Computational Biology*, vol. 4, no. 11, 2008.

[152] R. Perez-Carrasco, P. Guerrero, J. Briscoe, and K. M. Page, "Intrinsic noise profoundly alters the dynamics and steady state of the morphogen controlled bistable genetic switches", *PLoS Computational Biology*, vol. 12, e1005154, 2016.

[153] D. Sprinzak, A. Lakhanpal, L. LeBon, L. A. Santat, M. E. Fontes, G. A. Anderson, J. Garcia-Ojalvo, and M. B. Elowitz, "Cis-interactions between notch and delta generate mutually exclusive signalling states", *Nature*, vol. 465, no. 7294, p. 86, 2010.

[154] D. Sprinzak, A. Lakhanpal, L. LeBon, J. Garcia-Ojalvo, and M. B. Elowitz, "Mutual inactivation of notch receptors and ligands facilitates developmental patterning", *PLoS Computational Biology*, vol. 7, no. 6, e1002069, 2011.

[155] M. Boareto, M. K. Jolly, M. Lu, J. N. Onuchic, C. Clementi, and E. Ben-Jacob, "Jagged–delta asymmetry in notch signaling can give rise to a sender/receiver hybrid phenotype", *Proceedings of the National Academy of Sciences*, vol. 112, no. 5, E402–E409, 2015.

[156] M. Boareto, M. K. Jolly, E. Ben-Jacob, and J. N. Onuchic, "Jagged mediates differences in normal and tumor angiogenesis by affecting tip-stalk fate decision", *Proceedings of the National Academy of Sciences*, vol. 112, no. 29, E3836–E3844, 2015.

[157] L. Venkatraman, E. R. Regan, and K. Bentley, "Time to decide? dynamical analysis predicts partial tip/stalk patterning states arise during angiogenesis", *PLoS One*, vol. 11, pp. 1–23, 2016.

[158] M. Lu, M. K. Jolly, H. Levine, J. N. Onuchic, and E. Ben-Jacob, "Microrna-based regulation of epithelial–hybrid–mesenchymal fate determination", *Proceedings of the National Academy of Sciences*, vol. 110, no. 45, pp. 18 144–18 149, 2013.

[159] E. A. Codling, M. J. Plank, and S. Benhamou, "Random walk models in biology", *Journal of the Royal Society Interface*, vol. 5, no. 25, pp. 813–834, 2008.

[160] A. P. J. Jansen, *An introduction to kinetic Monte Carlo simulations of surface reactions*. Springer, 2012, vol. 856.

[161] K. J. Painter and T. Hillen, "Navigating the flow: Individual and continuum models for homing in flowing environments", *Journal of the Royal Society Interface*, vol. 12, no. 112, p. 20 150 647, 2015.

[162] T. Hillen, K. J. Painter, A. C. Swan, and A. D. Murtha, "Moments of von mises and fisher distributions and applications", *Mathematical Biosciences & Engineering*, vol. 14, p. 673, 2017.

[163] R. del Toro, C. Prahst, T. Mathivet, G. Siegfried, J. S. Kaminker, B. Larrivee, C. Breant, A. Duarte, N. Takakura, A. Fukamizu, *et al.*, "Identification and functional analysis of endothelial tip cell–enriched genes", *Blood*, vol. 116, no. 19, pp. 4025–4033, 2010.

[164]   M. J. Siemerink, I. Klaassen, C. J. Van Noorden, and R. O. Schlingemann, "Endothelial tip cells in ocular angiogenesis: Potential target for anti-angiogenesis therapy", *Journal of Histochemistry & Cytochemistry*, vol. 61, no. 2, pp. 101–115, 2013.

[165]   M. Papetti and I. M. Herman, "Mechanisms of normal and tumor-derived angiogenesis", *American Journal of Physiology-Cell Physiology*, vol. 282, no. 5, pp. C947–C970, 2002.

[166]   M. K. Gupta and R.-Y. Qin, "Mechanism and its regulation of tumor-induced angiogenesis", *World Journal of Gastroenterology: WJG*, vol. 9, no. 6, p. 1144, 2003.

[167]   M. Plank and B. Sleeman, "Tumour-induced angiogenesis: A review", *Journal of Theoretical Medicine*, vol. 5, no. 3-4, pp. 137–153, 2003.

[168]   I. Barkefors, S. Le Jan, L. Jakobsson, E. Hejll, G. Carlson, H. Johansson, J. Jarvius, J. W. Park, N. L. Jeon, and J. Kreuger, "Endothelial cell migration in stable gradients of vascular endothelial growth factor a and fibroblast growth factor 2 effects on chemotaxis and chemokinesis", *Journal of Biological Chemistry*, vol. 283, no. 20, pp. 13 905–13 912, 2008.

[169]   M. I. Dykman, T. Horita, and J. Ross, "Statistical distribution and stochastic resonance in a periodically driven chemical system", *The Journal of Chemical Physics*, vol. 103, no. 3, pp. 966–972, 1995.

[170]   D. Stepanova, H. M. Byrne, P. K. Maini, and T. Alarcón, "A method to coarse-grain multi-agent stochastic systems with regions of multistability", *arXiv preprint arXiv:2105.03398*, 2021.

[171]   P. Buske, J. Galle, N. Barker, G. Aust, H. Clevers, and M. Loeffler, "A comprehensive model of the spatio-temporal stem cell and tissue organisation in the intestinal crypt", *PLoS Computational Biology*, vol. 7, no. 1, e1001045, 2011.

[172]   M. A. Chaplain, "Multiscale modelling of cancer: Micro-, meso- and macro-scales of growth and spread", in *Approaching Complex Diseases*, Springer, 2020, pp. 149–168.

[173]   M. I. Freidlin and A. D. Wentzell, "Random perturbations", in *Random perturbations of dynamical systems*, Springer, 1998, pp. 15–43.

[174]   R. de la Cruz, P. Guerrero, J. Calvo, and T. Alarcón, "Coarse-graining and hybrid methods for efficient simulation of stochastic multi-scale models of tumour growth", *Journal of Computational Physics*, vol. 350, pp. 974–991, 2017.

[175]   R. De La Cruz, R. Perez-Carrasco, P. Guerrero, T. Alarcon, and K. M. Page, "Minimum action path theory reveals the details of stochastic transitions out of oscillatory states", *Physical Review Letters*, vol. 120, no. 12, p. 128 102, 2018.

[176]   M. I. Dykman, E. Mori, J. Ross, and P. Hunt, "Large fluctuations and optimal paths in chemical kinetics", *The Journal of Chemical Physics*, vol. 100, no. 8, pp. 5735–5750, 1994.

[177]   G. L. Poppe Jr, "Physical applications of the geometric minimum action method", 2018.

[178]   D. M. Roma, R. A. O'Flanagan, A. E. Ruckenstein, A. M. Sengupta, and R. Mukhopadhyay, "Optimal path to epigenetic switching", *Physical Review E*, vol. 71, no. 1, p. 011 902, 2005.

[179]   H. Touchette, "The large deviation approach to statistical mechanics", *Physics Reports*, vol. 478, no. 1-3, pp. 1–69, 2009.

[180]   T. Grafke, T. Schäfer, and E. Vanden-Eijnden, "Long term effects of small random perturbations on dynamical systems: Theoretical and computational tools", in *Recent Progress and Modern Challenges in Applied Mathematics, Modeling and Computational Science*, Springer, 2017, pp. 17–55.

[181]   M. Heymann and E. Vanden-Eijnden, "The geometric minimum action method: A least action principle on the space of curves", *Communications on Pure and Applied Mathematics: A Journal Issued by the Courant Institute of Mathematical Sciences*, vol. 61, no. 8, pp. 1052–1117, 2008.

[182]   J. R. Collier, N. A. Monk, P. K. Maini, and J. H. Lewis, "Pattern formation by lateral inhibition with feedback: A mathematical model of delta-notch intercellular signalling", *Journal of Theoretical Biology*, vol. 183, no. 4, pp. 429–446, 1996.

[183] N. A. Monk, J. A. Sherratt, and M. R. Owen, "Spatiotemporal patterning in models of juxtacrine intercellular signalling with feedback", *Mathematical Models for Biological Pattern Formation*, pp. 165–192, 2001.

[184] C. Lv, X. Li, F. Li, and T. Li, "Constructing the energy landscape for genetic switching system driven by intrinsic noise", *PLoS One*, vol. 9, no. 2, e88167, 2014.

[185] M. Tao, "Hyperbolic periodic orbits in nongradient systems and small-noise-induced metastable transitions", *Physica D: Nonlinear Phenomena*, vol. 363, pp. 1–17, 2018.

[186] R. D. O'Dea and J. R. King, "Continuum limits of pattern formation in hexagonal-cell monolayers", *Journal of Mathematical Biology*, vol. 64, no. 3, pp. 579–610, 2012.

[187] M. Cohen, M. Georgiou, N. L. Stevenson, M. Miodownik, and B. Baum, "Dynamic filopodia transmit intermittent delta-notch signaling to drive pattern refinement during lateral inhibition", *Developmental Cell*, vol. 19, no. 1, pp. 78–89, 2010.

[188] G. L. Hunter, Z. Hadjivasiliou, H. Bonin, L. He, N. Perrimon, G. Charras, and B. Baum, "Coordinated control of notch/delta signalling and cell cycle progression drives lateral inhibition-mediated tissue patterning", *Development*, vol. 143, no. 13, pp. 2305–2310, 2016.

[189] F. Corson, L. Couturier, H. Rouault, K. Mazouni, and F. Schweisguth, "Self-organized notch dynamics generate stereotyped sensory organ patterns in drosophila", *Science*, vol. 356, no. 6337, 2017.

[190] P. Formosa-Jordan, M. Ibañes, S. Ares, and J.-M. Frade, "Lateral inhibition and neurogenesis: Novel aspects in motion", *International Journal of Developmental Biology*, vol. 57, no. 5, pp. 341–350, 2013.

[191] F. Bocci, J. N. Onuchic, and M. K. Jolly, "Understanding the principles of pattern formation driven by notch signaling by integrating experiments and theoretical models", *Frontiers in Physiology*, vol. 11, 2020.

[192] S. K. Kay, H. A. Harrington, S. Shepherd, K. Brennan, T. Dale, J. M. Osborne, D. J. Gavaghan, and H. M. Byrne, "The role of the hes1 crosstalk hub in notch-wnt interactions of the intestinal crypt", *PLoS Computational Biology*, vol. 13, no. 2, e1005400, 2017.

[193] M. K. Jolly, M. Boareto, B. Huang, D. Jia, M. Lu, E. Ben-Jacob, J. N. Onuchic, and H. Levine, "Implications of the hybrid epithelial/mesenchymal phenotype in metastasis", *Frontiers in Oncology*, vol. 5, p. 155, 2015.

[194] Y. Sha, D. Haensel, G. Gutierrez, H. Du, X. Dai, and Q. Nie, "Intermediate cell states in epithelial-to-mesenchymal transition", *Physical Biology*, vol. 16, no. 2, p. 021 001, 2019.

[195] S. Kéfi, M. B. Eppinga, P. C. de Ruiter, and M. Rietkerk, "Bistability and regular spatial patterns in arid ecosystems", *Theoretical Ecology*, vol. 3, no. 4, pp. 257–269, 2010.

[196] V. Baldazzi, N. Bertin, H. de Jong, and M. Génard, "Towards multiscale plant models: Integrating cellular networks", *Trends in Plant Science*, vol. 17, no. 12, pp. 728–736, 2012.

[197] E. Farcot, C. Lavedrine, and T. Vernoux, "A modular analysis of the auxin signalling network", *PLoS One*, vol. 10, no. 3, e0122231, 2015.

[198] G. Zeng, S. M. Taylor, J. R. McColm, N. C. Kappas, J. B. Kearney, L. H. Williams, M. E. Hartnett, and V. L. Bautch, "Orientation of endothelial cell division is regulated by vegf signaling during blood vessel formation", *Blood*, vol. 109, no. 4, pp. 1345–1352, 2007.

[199] V. Marin, G. Kaplanski, S. Gres, C. Farnarier, and P. Bongrand, "Endothelial cell culture: Protocol to obtain and cultivate human umbilical endothelial cells", *Journal of Immunological Methods*, vol. 254, no. 1-2, pp. 183–190, 2001.

[200] S. Dimmeler and A. M. Zeiher, "Endothelial cell apoptosis in angiogenesis and vessel regression", *Circulation Research*, vol. 87, no. 6, pp. 434–439, 2000.

[201] N. Ferrara, "Binding to the extracellular matrix and proteolytic processing: Two key mechanisms regulating vascular endothelial growth factor action", *Molecular Biology of the Cell*, vol. 21, no. 5, pp. 687–690, 2010.

[202] G. S. Schultz and A. Wysocki, "Interactions between extracellular matrix and growth factors in wound healing", *Wound Repair and Regeneration*, vol. 17, no. 2, pp. 153–162, 2009.

[203] C. Bonnans, J. Chou, and Z. Werb, "Remodelling the extracellular matrix in development and disease", *Nature Reviews Molecular Cell Biology*, vol. 15, no. 12, pp. 786–801, 2014.

[204] A. Neve, F. P. Cantatore, N. Maruotti, A. Corrado, and D. Ribatti, "Extracellular matrix modulates angiogenesis in physiological and pathological conditions", *BioMed Research International*, vol. 2014, 2014.

[205] H. Lavoie, J. Gagnon, and M. Therrien, "Erk signalling: A master regulator of cell behaviour, life and fate", *Nature Reviews Molecular Cell Biology*, vol. 21, no. 10, pp. 607–632, 2020.

[206] S. E. Bell, A. Mavila, R. Salazar, K. J. Bayless, S. Kanagala, S. A. Maxwell, and G. E. Davis, "Differential gene expression during capillary morphogenesis in 3d collagen matrices: Regulated expression of genes involved in basement membrane matrix assembly, cell cycle progression, cellular differentiation and g-protein signaling", *Journal of Cell Science*, vol. 114, no. 15, pp. 2755–2773, 2001.

[207] R. Kalluri, "Basement membranes: Structure, assembly and role in tumour angiogenesis", *Nature Reviews Cancer*, vol. 3, no. 6, pp. 422–433, 2003.

[208] E. Hohenester and P. D. Yurchenco, "Laminins in basement membrane assembly", *Cell Adhesion & Migration*, vol. 7, no. 1, pp. 56–63, 2013.

[209] A. N. Stratman, K. M. Malotte, R. D. Mahan, M. J. Davis, and G. E. Davis, "Pericyte recruitment during vasculogenic tube assembly stimulates endothelial basement membrane matrix formation", *Blood, The Journal of the American Society of Hematology*, vol. 114, no. 24, pp. 5091–5101, 2009.

[210] S. Ergün, N. Kilic, J.-H. Wurmbach, A. Ebrahimnejad, M. Fernando, S. Sevinc, E. Kilic, F. Chalajour, W. Fiedler, H. Lauke, *et al.*, "Endostatin inhibits angiogenesis by stabilization of newly formed endothelial tubes", *Angiogenesis*, vol. 4, no. 3, pp. 193–206, 2001.

[211] L. P. Diebold, H. J. Gil, P. Gao, C. A. Martinez, S. E. Weinberg, and N. S. Chandel, "Mitochondrial complex iii is necessary for endothelial cell proliferation during angiogenesis", *Nature Metabolism*, vol. 1, no. 1, pp. 158–171, 2019.

[212] H. Park, H. Yamamoto, L. Mohn, L. Ambühl, K. Kanai, I. Schmidt, K.-P. Kim, A. Fraccaroli, S. Feil, H. J. Junge, *et al.*, "Integrin-linked kinase controls retinal angiogenesis and is linked to wnt signaling and exudative vitreoretinopathy", *Nature Communications*, vol. 10, no. 1, pp. 1–14, 2019.

[213] A. Rattner, J. Williams, J. Nathans, *et al.*, "Roles of hifs and vegf in angiogenesis in the retina and brain", *The Journal of Clinical Investigation*, vol. 129, no. 9, pp. 3807–3820, 2019.

[214] D. Antfolk, M. Sjöqvist, F. Cheng, K. Isoniemi, C. L. Duran, A. Rivero-Muller, C. Antila, R. Niemi, S. Landor, C. V. Bouten, *et al.*, "Selective regulation of notch ligands during angiogenesis is mediated by vimentin", *Proceedings of the National Academy of Sciences*, vol. 114, no. 23, E4574–E4581, 2017.

[215] T.-Y. Kang, F. Bocci, M. K. Jolly, H. Levine, J. N. Onuchic, and A. Levchenko, "Pericytes enable effective angiogenesis in the presence of proinflammatory signals", *Proceedings of the National Academy of Sciences*, vol. 116, no. 47, pp. 23 551–23 561, 2019.

[216] D. Nagata, M. Mogi, and K. Walsh, "Amp-activated protein kinase (ampk) signaling in endothelial cells is essential for angiogenesis in response to hypoxic stress", *Journal of Biological Chemistry*, vol. 278, no. 33, pp. 31 000–31 006, 2003.

[217] H.-J. Park, Y. Zhang, S. P. Georgescu, K. L. Johnson, D. Kong, and J. B. Galper, "Human umbilical vein endothelial cells and human dermal microvascular endothelial cells offer new insights into the relationship between lipid metabolism and angiogenesis", *Stem Cell Reviews*, vol. 2, no. 2, pp. 93–101, 2006.

[218] K. Bentley, K. Harrington, and E. Regan, "Can active perception generate bistability? heterogeneous collective dynamics and vascular patterning", in *Artificial Life Conference Proceedings 14*, MIT Press, 2014, pp. 328–335.

[219] Y. L. Koon, S. Zhang, M. B. Rahmat, C. G. Koh, and K.-H. Chiam, "Enhanced delta-notch lateral inhibition model incorporating intracellular notch heterogeneity and tension-dependent rate of delta-notch binding that reproduces sprouting angiogenesis patterns", *Scientific Reports*, vol. 8, no. 1, pp. 1–15, 2018.

[220] B. Debir, C. Meaney, M. Kohandel, and M. B. Unlu, "The role of calcium oscillations in the phenotype selection in endothelial cells", *Scientific Reports*, vol. 11, no. 1, pp. 1–12, 2021.

[221] A. Atri, J. Amundson, D. Clapham, and J. Sneyd, "A single-pool model for intracellular calcium oscillations and waves in the xenopus laevis oocyte", *Biophysical Journal*, vol. 65, no. 4, pp. 1727–1739, 1993.

[222] T. H. Cormen, C. E. Leiserson, R. L. Rivest, and C. Stein, *Introduction to algorithms.* MIT press, 2009.

[223] M. E. Fortini and D. Bilder, "Endocytic regulation of notch signaling", *Current Opinion in Genetics & Development*, vol. 19, no. 4, pp. 323–328, 2009.